LA-4888-PR

A PROGRESS REPORT

*c. 3*

Status Report of the

# LASL Controlled Thermonuclear Research Program

for a 12-Month Period Ending October 1971

**los alamos
scientific laboratory**
of the University of California
LOS ALAMOS, NEW MEXICO 87544

This report presents the status of the LASL Controlled Thermonuclear
Research program. Previous annual status reports in this series, all unclas-
sified, are:

LA-4351-MS                                    LA-4585-MS

**los alamos**
**scientific laboratory**
of the University of California
LOS ALAMOS, NEW MEXICO 87544

Status Report of the

# LASL Controlled Thermonuclear Research Program

for a 12-Month Period Ending October 1971

Compiled by

H. T. Motz

# CONTENTS

# I. Introduction

(J. L. Tuck)

One third (120°) of the toroidal $\theta$ pinch (Scyllac), the largest component of Los Alamos CTR Program, became operational at 1/2 power in April. This constitutes the first test of a high-$\beta$ toroidal equilibrium system, consisting of driven helical $\ell = 1$ coils and static $\ell = 0$ lands and grooves on the inner surface of the $\theta$-pinch compression coil.

It was immediately found that an equilibrium position of the $\theta$ pinch did occur and that it was very responsive to the current in the $\ell = 1$ coils, so that it could be moved in and out radially in the plane of the torus, a very satisfactory result in accord with the theoretical predictions. Less satisfactory was the discovery that after a period of 3 to 5 $\mu$sec, the hot plasma reached the wall. After much work, this contact was traced to ballooning of the compressed plasma opposite the grooves of the $\ell = 0$ field. Once known, it was deduced that this was due to an interaction between the $\ell = 1$ and the $\ell = 0$ systems, such that the $\ell = 1$ field was increased at the grooves. Steps to reduce the interaction have influenced the plasma in the desired direction, ballooning is less (possibly absent), and the high-$\beta$ plasma exhibits a lifetime of 8 $\mu$sec, terminated by an m = 1 motion to the wall. This latter may be the theoretically predicted Freidberg-Weitzner instability for which feedback stabilization measures have been under development for the last year. The latter will be installed in early 1972.

So far then, in this new field of high-$\beta$ toroidal equilibrium, the experiments could be said to be yielding results more or less in accordance with expectations, something which has happened very rarely in experimental plasma physics.

The construction of the linear $\theta$ pinch, which will have a 5-m uniform section with 1/4-m mirror sections at each end, powered in all by seven condenser modules, is expected to be out of the hands of the construction crews this calendar year. Experiments can be expected to start in early 1972.

Toward the reactor feasibility experiment, the cryogenic and superconducting magnetic energy storage and switching study has been initiated this year in the cryogenics group. The development of *reversible* magnetic switching is in the concept stage. This is an essential step in the progress towards a power producing reactor, since a positive power balance could never be achieved in a *dissipative* switched pulsed system.

As had been said before, the Z-pinch geometry is unique and interesting. With the addition of a longitudinal magnetic field, it resembles, superficially, a Tokamak. But in fact, there the resemblance ends. When one looks at the plasma density confined in ZT-1 it is about 100 times more than a Tokamak. This could give stabilized Z pinches a considerable edge in principle over Tokamaks when discussing reactor economics. ZT-1 became operational this year. For a time the behavior was disappointing since stability was less than had been hoped. One shot was obtained in October that, for some reason, showed a high degree of stability. For some weeks thereafter this result could not be duplicated. Now two more highly satisfactory shots have been obtained,

and the cause of the improvement is beginning to be pinned down. The previous unstable behavior appears to have been related to plasma disturbances left behind from the preionization, which are amplified in the main pinch. The future looks encouraging.

The quadrupole injection experiment, after 3 years, has reached its termination date as set up by the CTR Standing Committee and has ceased operation. The decision was based on the pressure of more reactor-worthy projects and that it was more appropriate to study this multipolar geometry, despite its having had some of its origins in this laboratory, at a laboratory specializing in it. As often happens in events of this kind, this has occurred at a time when the experiment for the first time is not only justifying itself, but yielding results of an encouraging, even startling nature. It is certainly true to say that really hot plasma has been trapped with 50% efficiency, and for a time whose upper limit is unknown but shows, at half power in the magnetic well, little decay over the period from 40 to 100 $\mu$sec. The confinement time could well extend to milliseconds. (This is at $\sim$1 keV ion temperature, remember.) All this was done with a nonlevitated coil fed from the outside by magnetically guarded conductors. Already, it must be taken as demonstrated that magnetic shielding works without contributing a serious plasma loss in a multipole geometry for the 100 $\mu$sec observation time, in contradiction to theoretical calculations.

Speaking of the multipolar geometry as a reactor, it might well appear to some a cruel joke for nature to require a large object to be a) surrounded on all sides by an enormously hot, radiating plasma, yet b) be both at liquid helium temperature and inaccessible. As Einstein once said: "Nature may be difficult but never malicious". But once the coil becomes accessible, everything changes, water can even be circulated through the coil, and a multipole reactor becomes imaginable (if rather unwieldy, by virtue of the presence of the scale determining a I-m-thick blanket around the coil). The injected quadrupole results are, according to its operators, considerably beyond anything that has been hitherto achieved with multipoles. It seems too late to revive the experiment, but its transfer (minus condenser bank) to a laboratory working on multipoles is recommended.

The Scylla $\theta$ pinch was founded long ago on the idea of shocking a plasma to 100 eV or so (ion temperature), and raising this to a kilovolt or so by adiabatic compression. The implication for a reactor is that the hot plasma would be compressed to a small fraction of the compression coil radius so that the magnetic field, whose volume is large compared with the plasma volume, is used inefficiently. The shock and separated shock $\theta$-pinch studies have the aim of improving efficiency, by making the shock heating (condenser) large, say to 5 keV, but the adiabatic compression small (magnetic energy storage), then the reactor plasma can fill a large fraction of the compression coil area.

In past years, the merits of computer simulation of plasma have been discussed at some length in the introduction. It has now become self-evident that the technique has amply justified itself; nonlinear plasma theory with the aid of computer plasma simulation is now a mature subject. On the quasi-experimental aspects of computer plasma simulation, it has also been demonstrated that valid plasma-physical experiments can be made without ever stepping outside the computer laboratory.

# II. THETA-PINCH PROGRAM

## A. Summary of θ-Pinch Activities (F. L. Ribe)

Since the last report (see LA-4585-MS, pp. 2 through 24) testing of the Scyllac 5-m toroidal sector capacitor bank was completed (see Sec. II-B of this report). The device had its first plasma at one-half capacitor bank energy in April 1971 and results on the $\ell = 1,0$ toroidal equilibrium were obtained for the June 1971 IAEA Conference on Plasma Physics and CTR at Madison, Wisconsin. The salient result presented there was that the combination of $\ell = 1$ helical fields, furnished by capacitor-driven coils, and asymmetrizing, bumpy $\ell = 0$ fields, formed by rectangular grooves in the compression coil, did overcome the toroidal force of major curvature, approximately as described theoretically by Ribe, Rosenbluth, and Weitzner. The peak plasma $\beta$ was $\sim 0.8$, the ion temperature $\sim 1$ keV, and the density $\sim 2.3 \times 10^{16}$ cm$^{-3}$. However, the plasma lifetime and neutron emission, as seen in the regions (the *lands*), between grooves were limited to 3 to 5 $\mu$sec, at which time a general flash of light across the quartz discharge tube was seen. This was found to be a "ballooning" effect (or z dependence of the plasma sideward motion) in which the plasma hit the tube wall in the region of each groove. Examination of the $\ell = 1$ fields showed them to be 35% stronger in the region of the 18-mm-deep grooves. This electrical effect was anticipated in the original design; its considerable consequences for plasma behavior were not. Reduction of the groove depth to 9 mm reduced the z dependence of the $\ell = 1$ field amplitude to 14% and had a dramatic effect in largely eliminating the plasma ballooning. A toroidal equilibrium is now observed with m = 1 (sideward) motion that is nearly the same in the regions of lands and grooves, giving a plasma lifetime, before hitting the wall, of 8 $\mu$sec. Further adjustments of the $\ell = 1$ and $\ell = 0$ fields will be carried out in an attempt to reach the end-loss-limited containment time of 12 to 15 $\mu$sec and to optimize MHD stability (see Sec. II-C).

On Scylla IV-3, a linear experiment, a quantitative demonstration was made of the $\ell = 1,0$ interference force basic to the Scyllac toroidal equilibrium and to feedback control of the m = 1 instability. This MHD instability, which is the only one observed, has been extensively studied in the linear system with $\ell = 1$ fields. It has a long wavelength (k $\approx 0$) and its growth rate agrees with the predictions of the Weitzner-Freidberg theory which

uses the new large $\delta_1$, small (ha) ordering (see Sec. II-D). Considerable engineering effort has been required to design and fabricate the necessary components to produce the $\ell = 0$ and $\ell = 1$ fields (see Sec. II-E). Modeling measurements were required to scale designs and test electrical behavior (see Sec. II-F).

The extensive electronics of the feedback system for stabilizing the m = 1 instability in Scylla IV and Scyllac have been successfully bench-tested, and the first module (of 20) is being installed on Scylla IV-3 for a plasma test of MHD feedback stabilization. The feedback circuit of each module consists of low-level outputs from optical plasma position detectors feeding through solid-state analog arithmetic circuits, various intermediate amplifiers, and finally ending in a 10 to 15 MW pulsed power amplifier which drives the feedback $\ell = 0$ coils. The fields of these coils control the plasma's m = 1 motion (see Sec. II-G).

The 7-m linear Scyllac device is nearing completion. Construction crafts and technicians will have completed their assembly and wiring by Christmas. Engineering checkout has progressed through four of the seven capacitor racks. Physics experiments on the central five meters are expected to begin in late January 1972, while checkout of the last two (mirror) racks is finished on the night shift. Full 7-rack experiments with 2:1 mirrors are expected to begin in the early part of March (see Sec. II-H).

The diagnostics for the first Scyllac toroidal sector experiments have been well-established techniques which were developed and used in previous work. The techniques include: 1) streak cameras to measure plasma motion; 2) coupled–cavity gas-laser interferometry to measure plasma density; 3) double magnetic loop to measure excluded flux; and 4) plasma luminosity detectors to measure plasma profile (see Sec. II-I). Other diagnostic techniques, including side-on interferometry and Thomson scattering, are under development (see Sec. II-J). The Scyllac computer has become essential in the monitoring of faults, operational parameters, and diagnostic results in the θ-pinch experiments (see Sec. II-K).

A program of cryogenic energy storage and transfer has been initiated during the past year (see Sec. X-D). Such a storage system will probably be necessary for a scientific feasibility experiment of a high-β θ-pinch device. A parameter study for a proposed feasibility experiment has been completed (see Sec. X-B and -C).

A scaling law has been postulated to explain the behavior of the plasma sheath in $\theta$-pinch implosions. An experimental test of the law is proposed (see Sec. II-L).

## B. Construction and Testing of the Scyllac 5-Meter Toroidal Sector Experiment (C. F. Hammer, W. E. Quinn, A. S. Rawcliffe)

1. **Introduction.** In the last annual report[1] a description of the toroidal-sector installation and testing was given for the system as partially completed at that time. The present report summarizes the electrical and mechanical properties of the final installation and pertinent facts having to do with its completion.

2. **Initial Configuration of the Scyllac $\theta$ Pinch.** The initial configuration of Scyllac[2,3] consists of two separate $\theta$-pinch devices: 1) a 5-m toroidal sector device; and 2) a 5-m linear device. Figure II-1 is a plan view showing these devices located in the 100 by 100-ft experimental area of the Scyllac building.

The linear device is presently under construction with a scheduled completion date of January 1972. This device is a 5-m straight $\theta$ pinch with magnetic mirrors. The main objectives of this device will be to study: 1) diffusion rates in a collisionless plasma; 2) the effects of high-$\beta$ mirrors; and 3) thermal-conductivity along magnetic lines.

The construction of the toroidal sector device was completed in March 1971. This sector device has a major radius of 237.5 cm and subtends an angle of 120° or 1/3 of a complete torus. The toroidal coil has an arc length of 5 m with each meter being energized from a separate rack of energy storage capacitors.
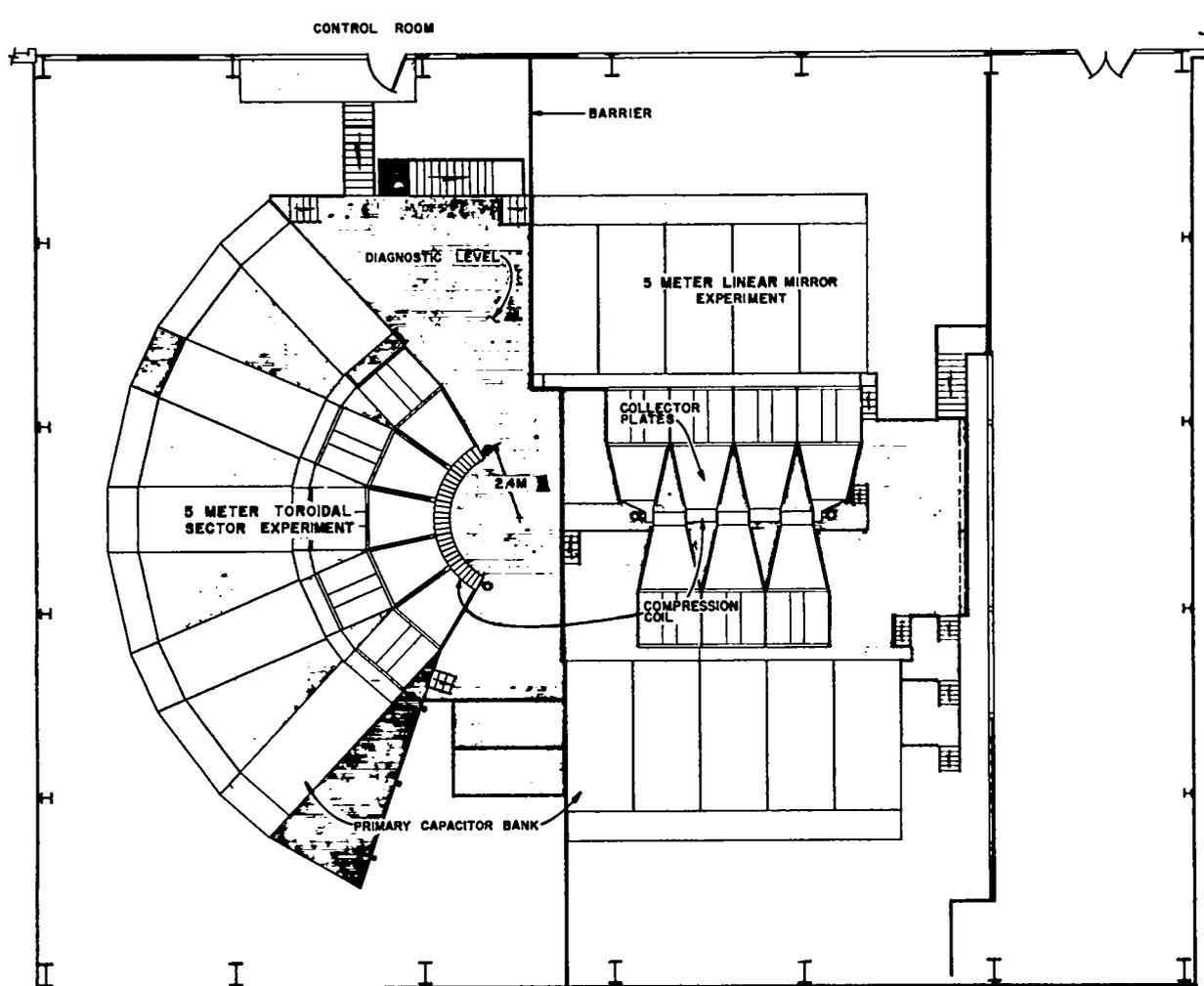


*Fig. II-1.*
*Plan view of the initial configuration of the Scyllac $\theta$ pinch.*

The conversion of the linear and sector devices to the full torus is presently planned to begin about January 1973.

3. Scyllac Design and Construction. The design and construction of the Scyllac device has been a cooperative effort. Table II-1 lists the staff personnel who have been involved in the design and construction of Scyllac. During the design and construction a Scyllac Steering Committee held regular weekly meetings. This committee made a significant contribution toward getting the device built.

Table II-2 lists the major, individual-component engineering designs.

The major component development is indicated in Table II-3. A large effort has been devoted to component development.

Major systems which have been developed for the Scyllac device are listed in Table II-4. This is the first time that a computer system and a scan-converter system have been incorporated into the operation of a CTR device.

Table II-5 lists the testing and assembly of various components. The pretesting of components has resulted in remarkably low failure rates in load cables, trigger source cables, spark gaps, and capacitors.

Table II-6 lists some of the significant dates during the construction of the Scyllac toroidal device.

4. Test and Checkout of the Toroidal Sector. Each meter of the toroidal sector was operated and tested electrically as its construction was completed. During these tests a few component faults developed in untested trigger cables, charge-lead connections in spark gaps, and capacitors. The major difficulty that developed during the checkout was that of prefires. This has been minimized and isolated to a single spark gap-capacitor unit through the addition of bias ballast capacitors and isolation resistors to the bank-bias systems.

## TABLE II-1

### RESPONSIBILITY FOR SCYLLAC DESIGN AND CONSTRUCTION BY GROUP

| P-16 | P-15 | ZIA-LACI | Eng. 7 | Eng. 4 |
|------|------|----------|--------|--------|
| Kemp | Ribe | Thompson | Bradley | Hazlett |
| Hanks | Quinn | | Banta | |
| Hammer | Sawyer | | Allen | |
| Boicourt | Gribble | | Haarman | |
| Borkenhagen | Rawcliffe | | Wing | |
| Harris | Thomas | | Meisner | |
| Bailey | Little | | | |
| | Ellis | | | |
| | Lillberg | | | |

## TABLE II-2

### MAJOR SCYLLAC DESIGN ENGINEERING

1. Spark Gaps (Hanks)
2. Collector Plates (Hanks)
3. Coil and Front End Assemblies (Hanks and Borkenhagen)
4. Trigger Systems (Hammer)
5. Charge Systems (Haarman)
6. Vacuum Systems (Borkenhagen)

7. Bank Layouts (Allen)
    a. Racks and Platforms - Structural
    b. Trigger Layouts
    c. Cable Routing
8. Bank Components (Banta)
    a. Liquid Resistors (Ref. 4)
    b. Shorting Balls
    c. Trigger Spark Gaps

## TABLE II-3

### COMPONENT DEVELOPMENT

1. Spark Gaps (Ref. 5)     (Gribble)
2. Capacitors     (Boicourt and Kemp)
3. Cable     (Boicourt and Kemp)
4. Prototype     (Hammer, Hanks, Harris, Bailey)

## TABLE II-5

### COMPONENT TESTING AND ASSEMBLY

1. Capacitors     (Wing and Meisner)
2. Cables     (Wing and Meisner)
3. Spark Gaps     (Sherwood)
4. Collector Plates     (Little)
5. $\ell = 1$ Coils (Ref. 6)     (Ellis and Zimmermann)
6. $\ell = 0$ Inserts     (Zimmermann)
7. Vacuum System     (McDowell)

## TABLE II-4

### SYSTEM DEVELOPMENT

1. Triggering System (Ref. 6)     (Gribble and Hammer)
2. Control System     (Rawcliffe)
3. Computer System     (Sawyer and Weldon)
4. Spark Gap Monitor System (Ref. 7)     (Brown and Sawyer)
5. Scan Converter System     (Gribble and Lillberg)
6. Time-Delay Pulser System     (Winston)
7. Plasma Diagnostics     (Burnett, Jahoda, Siemon)

## TABLE II-6

### SCYLLAC DATES

|  | Start | Complete |
|---|---|---|
| Building Construction | 11-21-68 | 3-15-70 |
| Erection of Capacitor and Machine Racks | 1-19-70 | 4-15-71 |
| Collector Plate Installation, Rack 13 |  | 6- 1-70 |
| Capacitor Installation and Cabling Rack 13 | 6-15-70 | 8-13-70 |
| Plumbers Strike Settled |  | 6-23-70 |
| Test and Checkout Rack 13 | 8- 4-70 | 10-13-70 |
| Construction of Rack 12 |  | 10- 1-70 |
| Toroidal Sector Installation (LACI) |  | 12-11-70 |
| Toroidal Sector Test and Checkout |  | 3-31-71 |
| Initial Plasma Experiments | 3- 8-71 | 4-12-71 |
| $\ell = 1, \ell = 0$ Installation | 4-12-71 | 4-30-71 |
| Plasma Experiments with $\ell = 1, \ell = 0$ | 5- 6-71 |  |

The installation of charge-lead isolation resistors has solved the charge-lead connection problem and has also helped to minimize the initiation of prefires through the added isolation between capacitors.

The installation of trigger cable clamps on every bank spark gap has resulted in improved triggering and in a reduction of prefires.

The prefire detection of the spark gap monitor has been improved.

**5. Parameters of the Toroidal Sector Device.** A plan view of the "front end" of the toroidal sector, including the 5-m toroidal coil and discharge tube, is shown in Fig. II-2. The diagnostic viewing slots and holes for the upper feeds of the $\ell = 1$ coils are also shown. The toroidal quartz discharge tube is pumped at each of its ends. Each meter of the toroidal coil is fed by an independent collector plate transmission line.

Figure II-3 shows the compression coil and discharge tube in cross section. In the initial control experiments reported below, the coil had a smooth bore of 14.4-cm diam and the discharge tube an inside diameter

of 8.8 cm. The helical $\ell = 1$ windings and the $\ell = 0$ grooves were not in place for these initial experiments.

A photograph of the front end of the toroidal sector is shown in Fig. II-4. The coaxial cables from the energy storage banks connect into the collector plates which feed the single-turn toroidal coil. The discharge tube is evacuated at each end by vacuum systems located below the floor.

A schematic circuit diagram of the 5-m toroidal device is given in Fig. II-5. In addition to the energy storage banks[2] indicated in the figure, an $\ell = 1$ bank for energizing the $\ell = 1$ helical windings and an $I_z$ bank for providing an axial toroidal current have been installed. Table II-7 lists the bank parameters of the toroidal sector.

The parameters of the preionization (PI) bank are listed in Table II-8 for each meter of the toroidal sector with one, three, and five capacitors per meter. These parameters are with a 14.4-cm-diam coil.

The main bank parameters for each meter of the toroidal sector are listed in Table II-9 for one-half and complete main bank at an operating voltage of 60 kV.

Oscillogram traces of the main toroidal compression
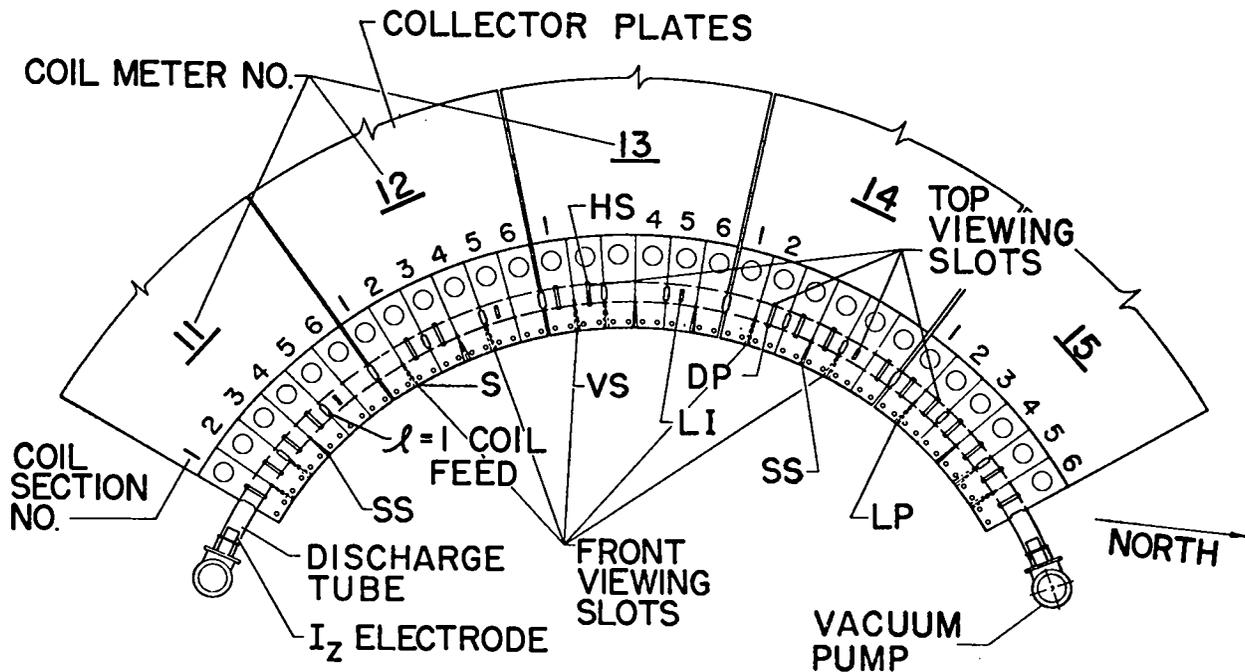


*Fig. II-2.*

*The 5-m Scyllac toroidal sector compression coil, with its various slots for viewing and for $\ell = 1$ coil feeds. The plasma measurements are identified as follows: HS, streak camera for horizontal motion; VS, vertical streak camera; SS, $\pm 45°$ stereoscopic streak camera; LI, coupled-cavity laser interferometer; DP, double magnetic probe; LP, plasma luminosity-profile measurement.*

## TABLE II-7

### SCYLLAC TOROIDAL-SECTOR BANK PARAMETERS

| Bank | No. of Capacitor Spark-Gap Units | No. of Cables | V (kV) | C ($\mu$F) | W (kJ) |
|------|------|------|------|------|------|
| Primary | 1,050 | 6,300 (42.8 km) | 60 | 1,942 | 3,500 |
| Primary Triggers | 11 (PC) 21 (SM) | 1,680 (17.5 km) | 60 120 | 7.7 | 21.6 |
| Primary Crowbar Triggers | 120 | 1,350 (10.8 km) | 75 | 84.0 | 236.2 |
| Preionization | 10 | 150 (1.3 km) | 75 | 7.0 | 19.7 |
| $1_z$ | 30 | 240 (2.1 km) | 75 | 21.0 | 59.1 |
| $\ell = 1$ | 60 | 450 (3.2 km) | 60 | 111.0 | 199.8 |
| Bias Field | 20 | 20 (0.6 km) | 10 | 3,630 | 181.5 |
| Miscellaneous Trigger Systems | 32 | 498 (1.6 km) | 20 to 120 | 12.8 | 31.6 |
| Totals | 1,354 | 10,268 (79.9 km) | | 5,816 | 4,254 |

## TABLE II-8

### PREIONIZATION BANK OPERATING PARAMETERS

| Parameters | No. of Capacitors | | |
|------|------|------|------|
| | 1 | 3 | 5 |
| V(kV) | 50 | 50 | 50 |
| C($\mu$F) | 0.7 | 2.1 | 3.5 |
| W(kJ) | 0.9 | 2.6 | 4.4 |
| $L_{source}$(nH) | 218 | 83.8 | 50.0 |
| $L_{coil}$ (nH) | 20.5 | 20.5 | 20.5 |
| $\alpha$ | 0.086 | 0.20 | 0.29 |
| $E_\theta$ (r = 4.3 cm)(V/cm) | 56 | 128 | 178 |
| f(kHz) | 390 | 340 | 320 |
| $1_{pk}$ (kA) | 60 | 150 | 327 |
| $B_{pk}$ (kG) | 0.8 | 1.9 | 4.1 |
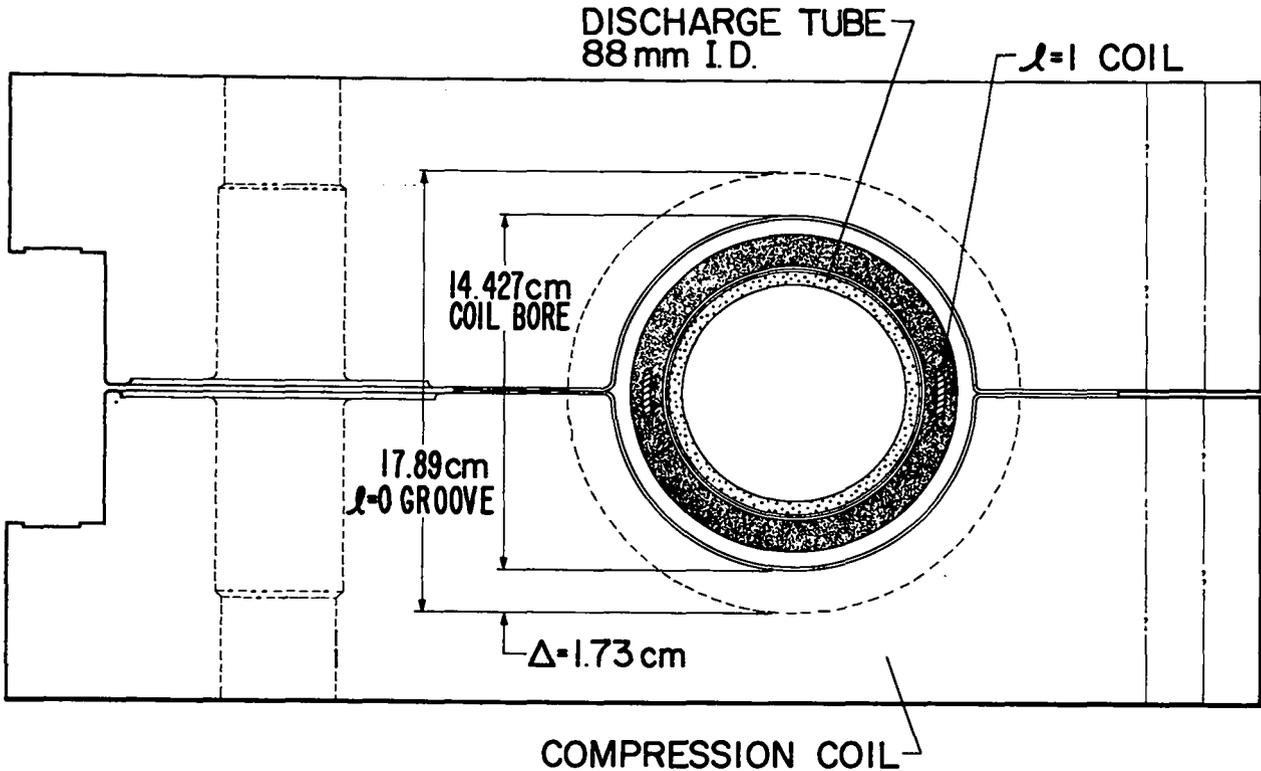
*Fig. II-3.*

*Cross section of compression coil and discharge tube with $\ell = 1$ coil and $\ell = 0$ groove.*

field, $B_z$, are shown in Fig. II-6 on time scales of 10 μsec and 50 μsec per division with the complete main bank. The crowbar L/R times are up to 280 μsec (see lower trace Fig. II-6). The crowbar peak-to-peak modulation is satisfactory at approximately 10%.

**References**

1. Los Alamos Scientific Laboratory report, LA-4585-MS, p. 18 (1970).

2. E. L. Kemp, G. P. Boicourt, R. F. Gribble, C. F. Hammer, K. W. Hanks, W. E. Quinn, and G. A. Sawyer, Proc. 6th Symp. Fusion Technology, Aachen, September 22-25, 1970. (Euratom, CID, Luxembourg, December, 1970). p. 227.

3. Proceedings of Symposium on Engineering Problems of Fusion Research, Los Alamos Scientific Laboratory report LA-4250 (1969).

4. R. A. Haarman, Ibid. p. DII-9-1.

5. R. F. Gribble, Ibid., p. DI-5-1.

6. C. F. Hammer and R. F. Gribble, Ibid., p. DI-4-1.

7. D. Brown, Rev. Sci. Instr. 42 1287 (1971).

C. Scyllac 5-Meter Toroidal Sector Experiment (S. C. Burnett, W. R. Ellis, C. F. Hammer, F. C. Jahoda, M. Kaufmann, W. E. Quinn, F. L. Ribe, G. A. Sawyer, R. E. Siemon, and E. L. Zimmermann).

1. Introduction. Since the last annual report[1] plasma experiments (beginning in April, 1971) have been carried out on the toroidal sector device. The effort during this report period has been devoted to: 1) control experiments to measure the plasma heating and toroidal drift in the presence of a pure toroidal field with no helical or bumpy fields; 2) initial measurements with $\ell = 1,0$ toroidal equilibrium field configuration (pre-Madison IAEA meeting); 3) measurements with $\ell = 1$ fields corrected for end effects; and 4) measurements with reduced $\ell = 0$ groove depths (0.9 cm). In this latter case the plasma column is confined for 6 to 8 μsec, after which an m = 1 motion carries the plasma to the wall.

2. Measurements with a Compression Coil of Constant Minor Diameter and No Helical Fields. Control experiments[2] were performed with a smooth-bore coil (14.4-cm diam) and with one-half the main bank to check the toroidal drift and plasma heating in the toroidal
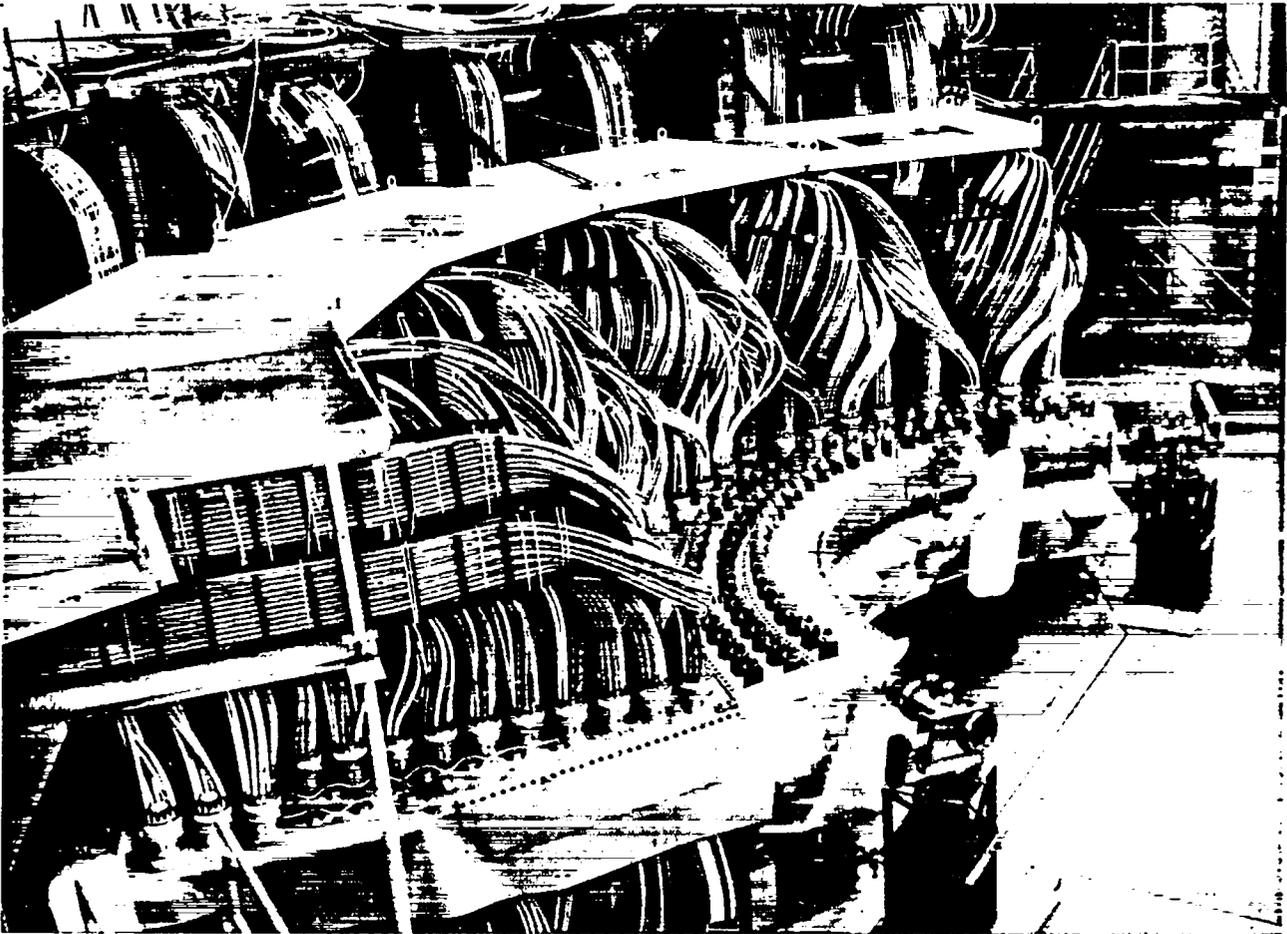
*Fig. II-4.*
*Photograph of the front end of the toroidal sector.*

geometry. These experiments were performed in the absence of equilibrium fields. The main bank was operated at 45 and 50 kV with initial deuterium filling pressures of 10, 15, and 20 mTorr. In addition, the temperature, density, and impurity level of the preionized plasma were investigated and the energy of the PI bank adjusted to a minimum compatible with approximately 100% ionization.

Figure II-7 is a photograph of the front end of the machine with different plasma diagnostic devices located in the sector area. The following plasma diagnostics were used:

- A spectrograph to determine the plasma electron temperature and impurities of the preionized plasma.

- A gas laser interferometer to measure the integrated plasma electron density along a vertical chord of the plasma cross section.

- Two streak cameras, viewing the plasma column side-on, to record the radial motions of the plasma column.

- A multichannel luminosity experiment to obtain optical intensity profiles of the plasma column.

- A magnetic loop and probe arrangement to measure the magnetic flux excluded by the plasma. The plasma $\beta$ can be obtained by combining this flux exclusion measurement with the radial density profile from the luminosity experiment.
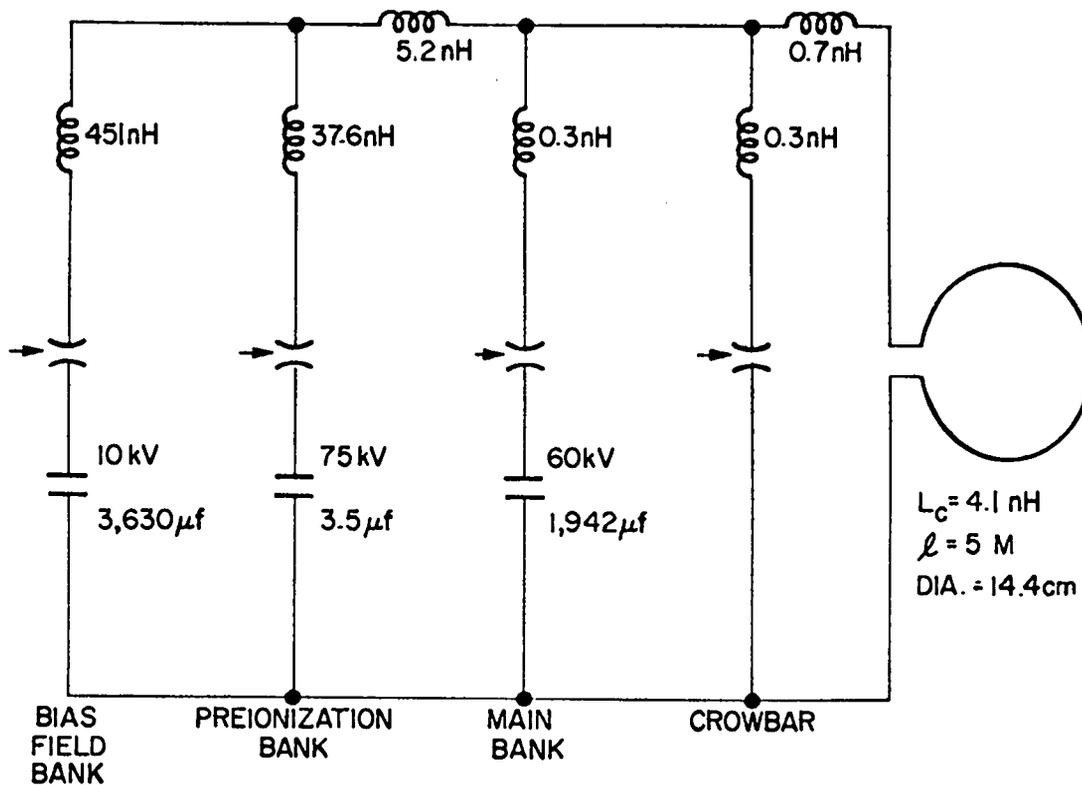
*Fig. II-5.*
*Schematic electrical circuit diagram of the 5-m toroidal sector device.*

• Time distributions of the neutron emissions were recorded by plastic-scintillation detectors located at five different positions. Absolute neutron yields were obtained by five silver activation counters located near the scintillation detectors.

Measurements of $n_e$, $T_e$, and impurities were made on the PI plasma with deuterium filling pressure of 10, 15, and 20 mTorr and with the PI bank operating at 50 kV with five, three, and one 0.7-$\mu$F capacitors per meter (see Table II-8). It was determined that with the present $\theta$-preionization arrangement, the optimum parameters of the PI plasma were obtained with one capacitor per meter.

The Scyllac preionized plasma was spectroscopically analyzed with a McPherson 1-m grating spectrometer to determine electron temperatures and impurities. Two $kT_e$ determinations were made at 15 $\mu$sec after firing the preionization bank: 1) a measurement of the intensity ratio of the $D_\delta$ line to a 16 Å interval of the Paschen continuum at 5400 Å; and 2) a measurement of the

relative intensities of $D_\delta$ and $D_\beta$. The results at filling pressures of 10 and 20 mTorr are presented in Table II-10. Time-integrated spectra showed a predominant Balmer spectrum with only weak impurity lines.

A coupled-cavity He-Ne laser interferometer, operating at a wavelength of 3.4 $\mu$m, measured the time history of the preionization electron density along the central line of sight across the quartz discharge tube. As the discharge cleaned up and the preionizer was reduced to one capacitor/meter, the interferometically measured density was found to agree with the filling density (see Table II-10).

3. Plasma Measurements with One-Half Main Bank and No Helical or Bumpy Fields. Side-on image-converter streak photographs were made at various positions indicated in Fig. II-2. Views of the horizontal and vertical plasma motion at the center of the compression coil are shown at the top of Fig. II-8 for a capacitor-bank voltage of 50 kV and a filling pressure of 20 mTorr. The initial plasma implosion is followed by compressive MHD oscillations. The plasma then drifts to the discharge-tube wall,

# TABLE II-9

## SCYLLAC TOROIDAL-SECTOR PARAMETERS

| Major Diameter | 4.75 m |
|---|---|
| Minor Diameter (coil bore) | 14.4 cm |
| Coil Length | 5 m |

| Fraction of Bank | One-Half | Full |
|---|---|---|
| V (kV) | 60 | 60 |
| C ($\mu$F) | 971 | 1,942 |
| W(MJ) | 1.75 | 3.5 |
| $L_{source}$ (nH)/m | 6.4 | 5.0 |
| $L_{coil}$(nH)/m | 20.5 | 20.5 |
| $\alpha$ | 0.76 | 0.80 |
| $E_\theta$ (r = 4.3 cm)(V/cm) | 600 | 630 |
| $(dB/dt)_{t=0}$ (Gauss/sec) | $2.46 \times 10^{10}$ | $2.74 \times 10^{10}$ |
| $\tau/4$ ($\mu$sec) | 3.6 | 4.9 |
| $I_{pk}$ (MA) | 24.0 | 34.5 |
| $B_{pk}$ (kG) | 59.9 | 86.2 |
| $(L/R)_{crowbar}$ ($\mu$sec) | 250 | 250 |



$B_z$ —— $10\,\mu$ SEC/ DIV

—— $50\,\mu$ SEC/ DIV
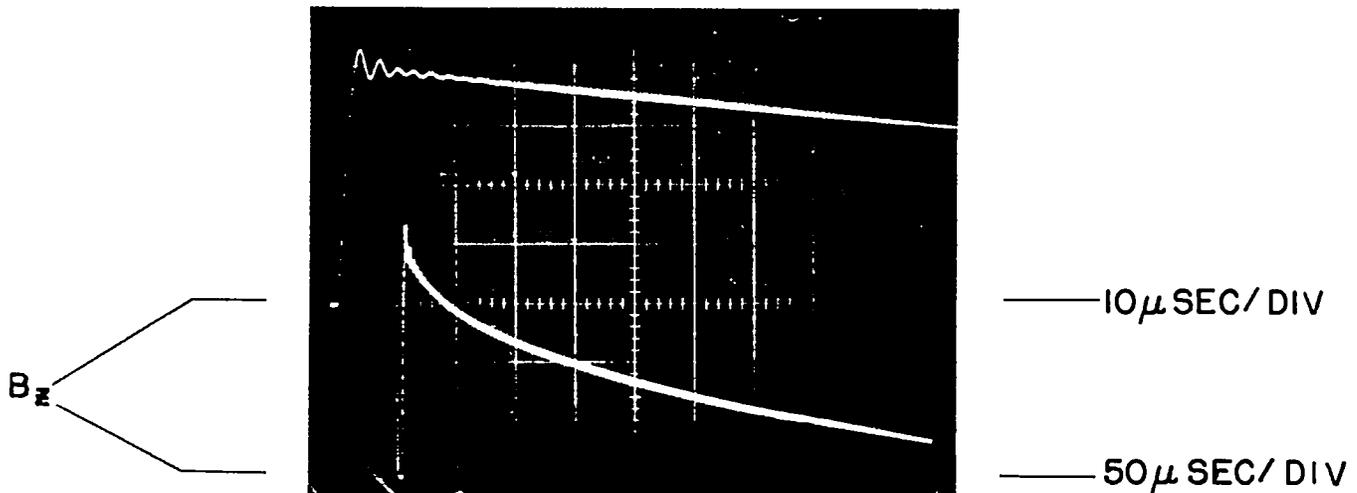
*Fig. II-6.*
*Oscillogram traces of the main toroidal compression field, $B_z$.*

remaining in the horizontal plane of the compression coil feed slot. Oscillograms of the main compression field and neutron emission for a 10 mTorr filling are shown at the bottom of Fig. II-8. The neutron signal is quenched when the plasma strikes the discharge tube. Streak photographs at various positions show that the plasma strikes the wall away from the center of curvature approximately simultaneously at various axial positions.

12
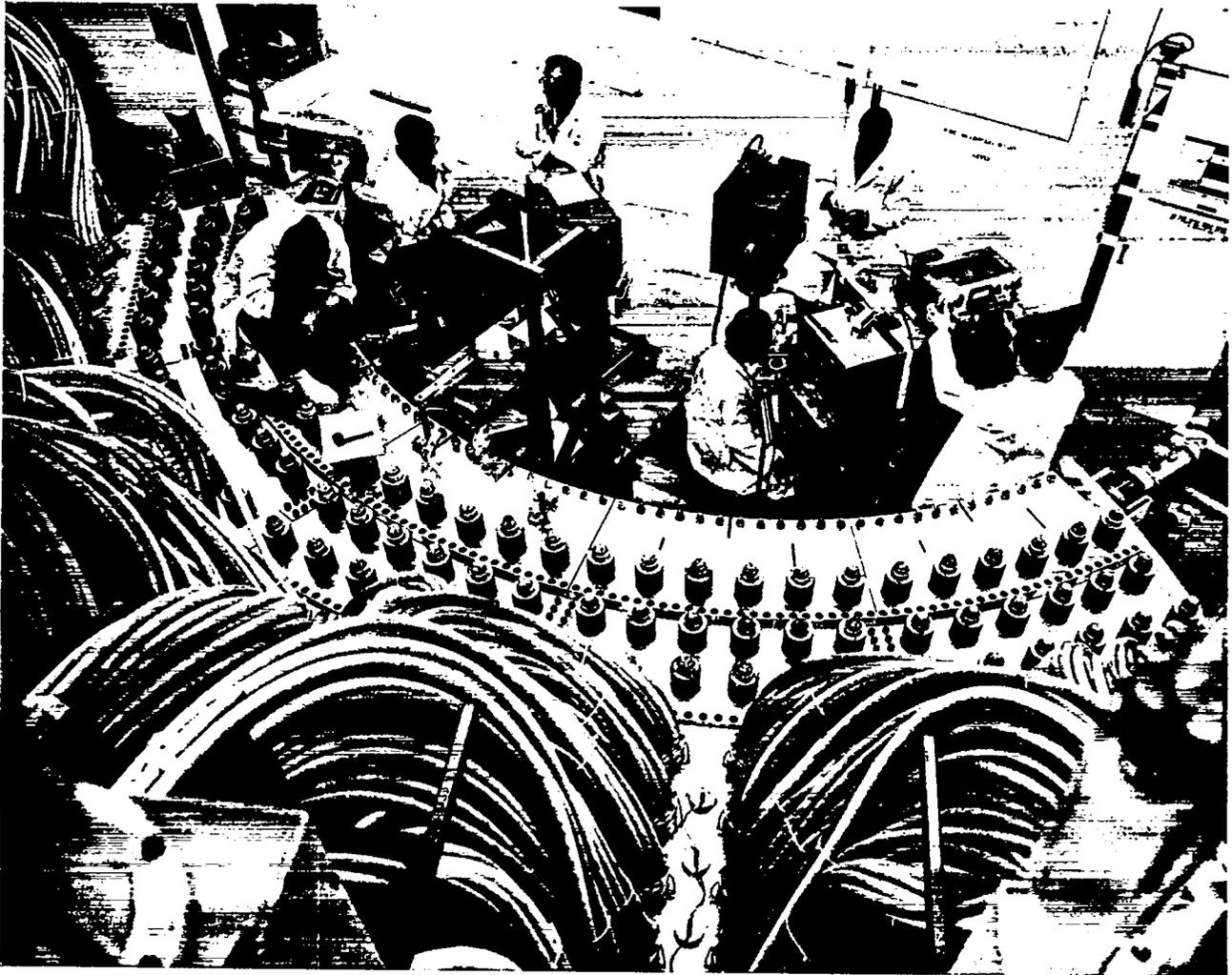
*Fig. II-7.*
*Photograph of sector front end with plasma diagnostic devices.*

TABLE II-10

PREIONIZED PLASMA PARAMETERS AT 15 $\mu$sec

|  | $P_{D_2} = 10$ mTorr | $P_{D_2} = 20$ mTorr |
|---|---|---|
| $T_e(D_\delta/C_P)$ | $1.8 \pm 0.4$ eV | $1.1 \pm 0.3$ eV |
| $T_e(D_\delta/D_\beta)$ | -- | $1.4 \pm 0.4$ eV |
| $n_{SAHA}$ | $7.0 \times 10^{14}/cm^3$ | $1.4 \times 10^{15}/cm^3$ |
| $n_{measured}$ | $6.4 \times 10^{14}/cm^3$ | $1.1 \times 10^{15}/cm^3$ |
| $n_0$ (filling) | $7.0 \times 10^{14}/cm^3$ | $1.4 \times 10^{15}/cm^3$ |

TOP

FRONT

|————————|————————|————————|————————|————————|
0                       1                       2                       3 $\mu$sec

B FIELD

NEUTRONS

←—2$\mu$sec
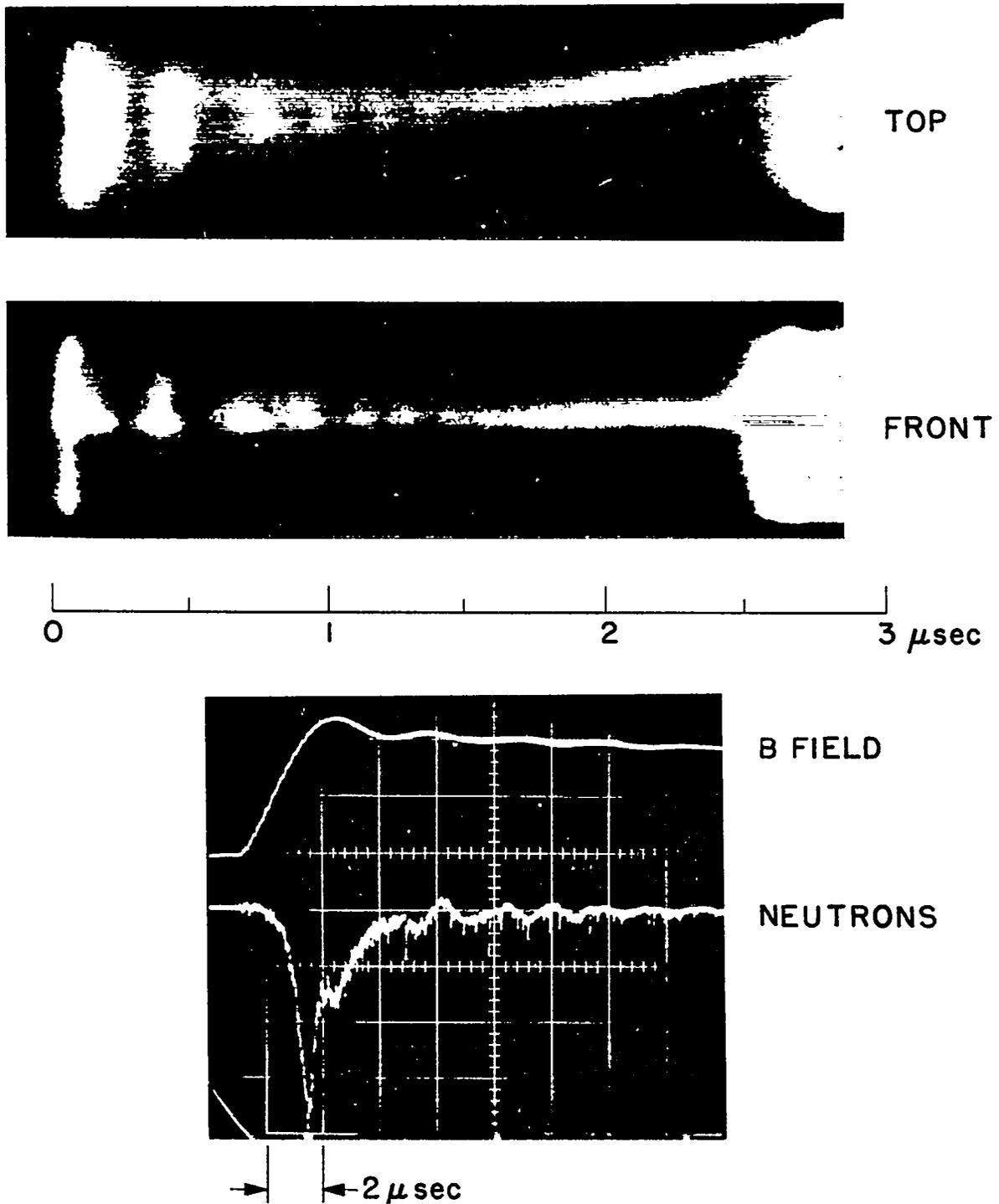
*Fig. II-8.*

Streak photographs of the plasma near the center of the Scyllac 5-m toroidal sector with $\ell = 0$ fields alone. "Top" view shows plasma motion in horizontal plane and "front" view in vertical plane. Oscillogram shows neutron emission.

The streak photographs show that the initial dynamic implosion phase of the discharge is unaffected by the toroidal curvature with the plasma imploding to the approximate center of the compression coil.

The observed radially outward toroidal drift of the plasma column is anticipated because of the toroidal force,

$$F_R = \beta B_0^2 a^2/4R , \qquad (1)$$

along the major radius R. $B_0$ is the main compression field outside the plasma column; $\beta$ is the ratio of plasma pressure to external magnetic field pressure; and a is the radius of the plasma column. This force is due simply to the radial decrease in the magnetic confining field $B_0$ in toroidal geometry. The corresponding time for the plasma column to drift a distance b under the force $F_R$ is given by

$$\tau_R = \left(\frac{8\pi b R\rho}{\beta B_0^2}\right)^{\frac{1}{2}} = \left[\frac{M_i Rb}{k(T_e + T_i)}\right]^{\frac{1}{2}} \qquad (2)$$

where $(T_e + T_i)$ is the time average of the electron and ion temperatures, and $\rho$ is the mass density.

Table II-11 presents the average times after the initiation of the main discharge at which the plasma column strikes the discharge tube wall for the various deuterium filling pressures and bank voltages. The time averages of the electron and ion temperatures are obtained from the drift times through Eq. (2) with b = 4.0 cm.

An estimate of ion temperature was obtained by normalizing the integrated scintillator signal to the absolute neutron yield given by the silver-activation counters. A plasma density of $2 \times 10^{16}$ cm$^{-3}$ was assumed at maximum neutron emission, and the plasma radius was taken to be $r_{1/2} = 0.72$ cm, estimated from the multichannel luminosity data. From the Maxwellian average d-d cross section times velocity, one derives $kT_i \approx 940$ eV. This

### TABLE II-11

### PLASMA DRIFT TIMES AND AVERAGE $(T_e + T_i)$

| $P_{D_2}$ (mTorr) | $V_B$ (kV) | $\tau_R$ ($\mu$sec) | $\overline{(T_e + T_i)}$ (eV) |
|---|---|---|---|
| 10 | 45 | 2.32 ± .06 | 396 |
| 10 | 50 | 2.23 ± .10 | 429 |
| 15 | 50 | 2.43 ± .06 | 361 |
| 20 | 50 | 2.72 ± .08 | 288 |

maximum ion temperature is reasonable in view of the 412-eV average of $k(T_e + T_i)$ derived from the drift and the fact that $kT_e$ is expected to be about 300 eV near maximum compression.

### 4. Scyllac Helical Equilibrium Field Arrangement.

In the Scyllac experiment the toroidal force along the major radius is balanced by an interference force produced by an $\ell = 1$ helical field with a smaller admixture of $\ell = 0$ axisymmetric field.[3,4] Figure II-9 demonstrates the magnetohydrodynamic principles used to create a toroidal plasma equilibrium. In the top left of Fig. II-9, a bumpy $\ell = 0$ field is applied to a pinch plasma to produce an axisymmetric column. In the middle left view, an $\ell = 1$ helical field is applied, causing the plasma column to become helical with a relative excursion $\delta_1$. In practice, $\delta_1 \sim 0.7$ and $\delta_0 \sim 0.2$. In the bottom view on the left, the effect of applying both $\ell = 1$ and $\ell = 0$ fields is shown. The plasma column becomes asymmetric and there is a uniform body force $F_{1,0}$ to the side of the asymmetry. The uniform toroidal force $F_R$, due to the gradient in the compression field, is balanced by the force $F_{1,0}$.

Figure II-10 shows the arrangement[5] for applying $\ell = 1$ and $\ell = 0$ fields to Scyllac to give the toroidal equilibrium depicted in Fig. II-9(B). The $\ell = 1$ fields were applied by means of bifilar helical coils[5] divided into one-period ($\lambda = 33$ cm) lengths as shown in the upper portion of the figure. The mean radius of the helical coils was 5.75 cm. The $\ell = 0$ fields were generated from annular grooves 1.80-cm deep and 16.6-cm long in the inner surfaces of the compression coil as shown in Fig. II-10. The onset of the $\ell = 0$ fields was delayed approximately 0.5 $\mu$sec by the annular sets of Inconel trapezoidal sections (lower portion of Fig. II-10) to maintain a homogeneous field during the time of the initial plasma implosion.

The $\ell = 1$ coils were driven by crowbarred capacitors so that the current rose to its maximum in approximately 3.2 $\mu$sec and decayed with an L/R time of 95 $\mu$sec and an initial 12% modulation. The $\ell = 1$ coils can be driven at various currents and with various time delays relative to the application of the main compression field. In the present experiments, the $\ell = 1$ capacitor bank was switched at time delays of 0 to 0.6 $\mu$sec.

Figure II-11 shows the Scyllac compression coil with $\ell = 1$ coils installed. The load cables from the $\ell = 1$ capacitor bank (top fore-ground) feed a common intermediate header which drives the 15 $\ell = 1$ coils in parallel through the cylindrical headers on top of the compression coil. The coaxial cables from the top headers to the boxes at the bottom of the compression coil provide the $\ell = 1$ coil interconnections. Figure II-12 shows a schematic diagram of the electrical connections and also establishes the convention on signs and phases of the transverse $\ell = 1$ field $B_1$.
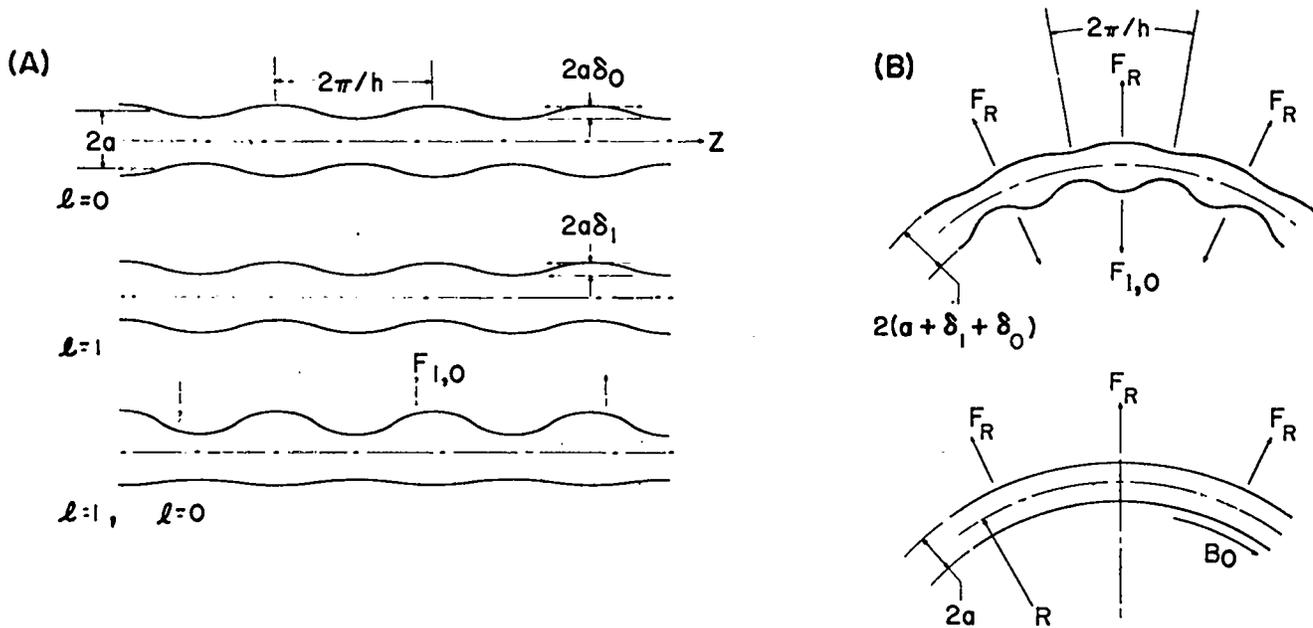
*Fig. II-9.*

*(A) Illustrating the parameters involved when $\ell = 1$ and $\ell = 0$ helical fields are applied to a plasma column to produce a body force $F_{1,0}$.*

*(B) Illustrating the use of the $\ell = 1,0$ body force to produce a high-$\beta$ toroidal equilibrium.*

## 5. Initial Measurements with $\ell = 1$ and $\ell = 0$ Fields

($\ell = 0$ groove depth = 1.8 cm). The streak photographs of Fig. II-13A show the vertical and horizontal plasma motions near the center of the sector compression coil with the $\ell = 1$ coils not excited. The two streak-camera viewing slits were 7.65-cm apart and the deuterium filling pressure was 20 mTorr. Even though the $\ell = 0$ fields were present because of the grooves, the plasma motion was a simple toroidal "drift" to the walls, essentially the same as previously observed in the smooth-bore coil and with no observable instability induced by the bumpy fields. The streak photographs of Figs. II-13B and C were taken with the $\ell = 1$ coils excited at maximum current values of 87 kA (0.5-$\mu$sec delay) and 75 kA (0.2-$\mu$sec delay), respectively. The horizontal plasma motion shows that the toroidal force is overcome by the $\ell = 1,0$ combination and the plasma returns toward the axis of the discharge tube while remaining close to the plane of the toroidal sector. In Fig. II-13C, with a $\ell = 1$ time delay of 0.2 $\mu$sec, the initial plasma motion is reversed more quickly; however, the wall light occurs sooner with the decreased $\ell = 1$ current of 75 kA. These streak photographs were taken with a 20-mTorr deuterium filling pressure and 45-kV primary-bank voltage. The times of observation in Figs. II-13B and C are limited by the sudden appearance of

light across the field of view. The bright luminosity illuminates the complete discharge tube even though the plasma does not touch the discharge tube wall in the vicinity of the viewing slits. The luminosity is caused by the plasma column striking the tube wall at some point or points. During these experiments there were viewing slits only in the center of the *lands* between the grooves of Fig. II-12, and between the lands and grooves, but not in the groove regions. At this time, a force imbalance existed between $F_R$ and $F_{1,0}$ in the end regions of the toroidal sector due to decreased currents in the end $\ell = 1$ coils as a result of the way the windings of the $\ell = 1$ coils were interconnected from top to bottom of the main compression coil (see Fig. II-12). These conditions suggested that the plasma might be striking the wall near the ends of the sector coil.

Figure II-14 shows the waveforms of the compression field and the $\ell = 1$ current (upper oscillogram), and the compression field and neutron-scintillator signal (lower oscillogram), for a 10-mTorr deuterium filling pressure and 50-kV main-bank voltage. The neutron signal, observed near the center of the sector, is quenched as the plasma strikes the discharge tube wall. The neutron emission quenches in approximately one $\mu$sec after the occurrence of the wall light. The rapid quenching of the

16
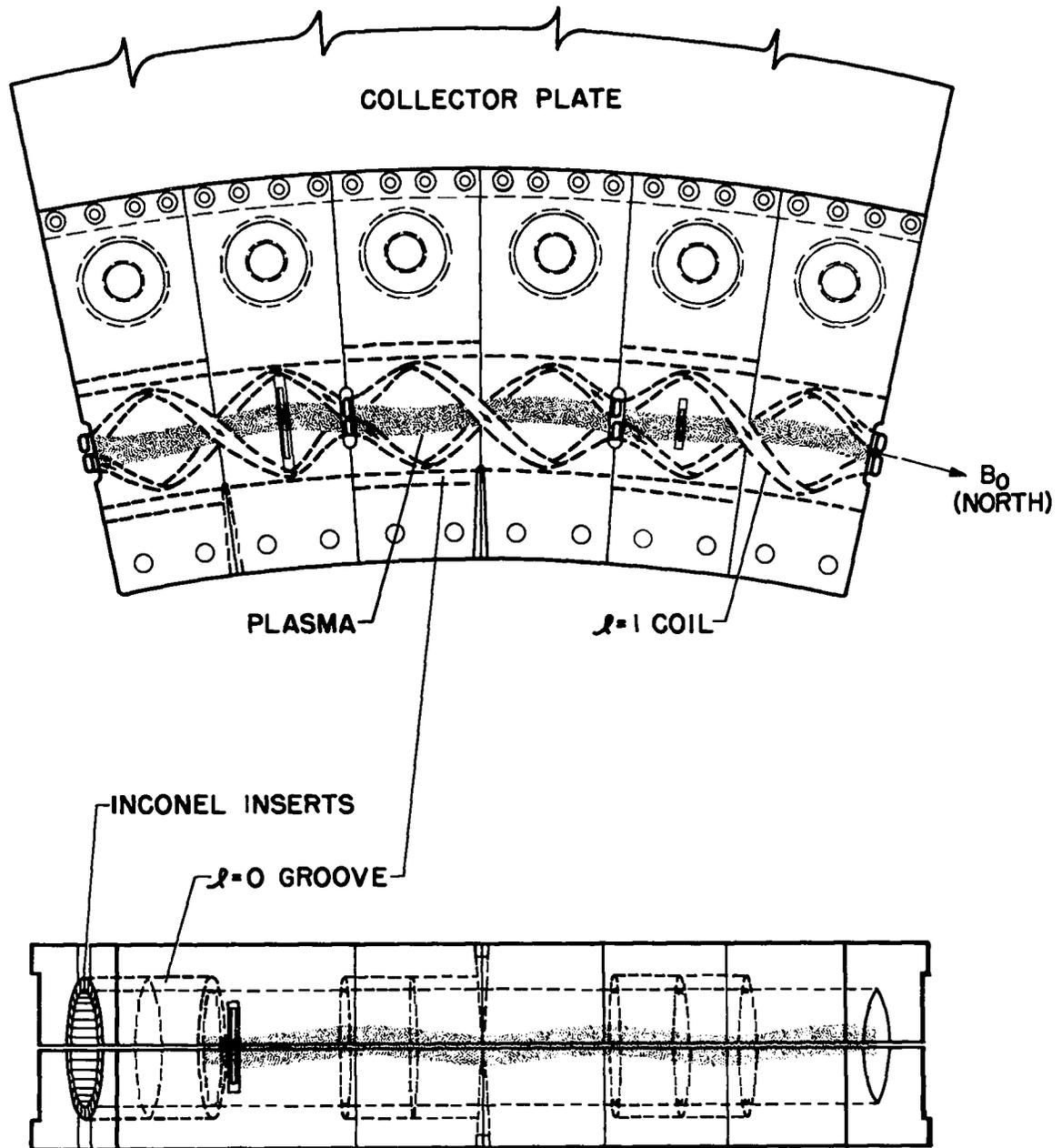
*Fig. II-10.*
*Arrangement of ℓ = 1 coils and ℓ = 0 grooves (with time-delay inserts) to give a toroidal equilibrium in the Scyllac 5-m toroidal sector.*

neutron emission suggested that the plasma column was striking the wall at other points than just at the ends.

**6. End Correction of ℓ = 1 Helical Fields.** In the initial sector experiments, the currents to the ℓ = 1 coils near the ends of the sector were less than those to the central coils due to the absence of coaxial currents on the interconnecting cables of the end ℓ = 1 coils (see Fig. II-12). "Dummy" end coils, which consist of simple half-turn coils, were fabricated and added to each end of the sector. The lengths of the cables connecting these dummy end coils to the ℓ = 1 intermediate header were adjusted to have appropriate inductances so that the dummy coil circuits receive the same currents as the central ℓ = 1 coils.

17
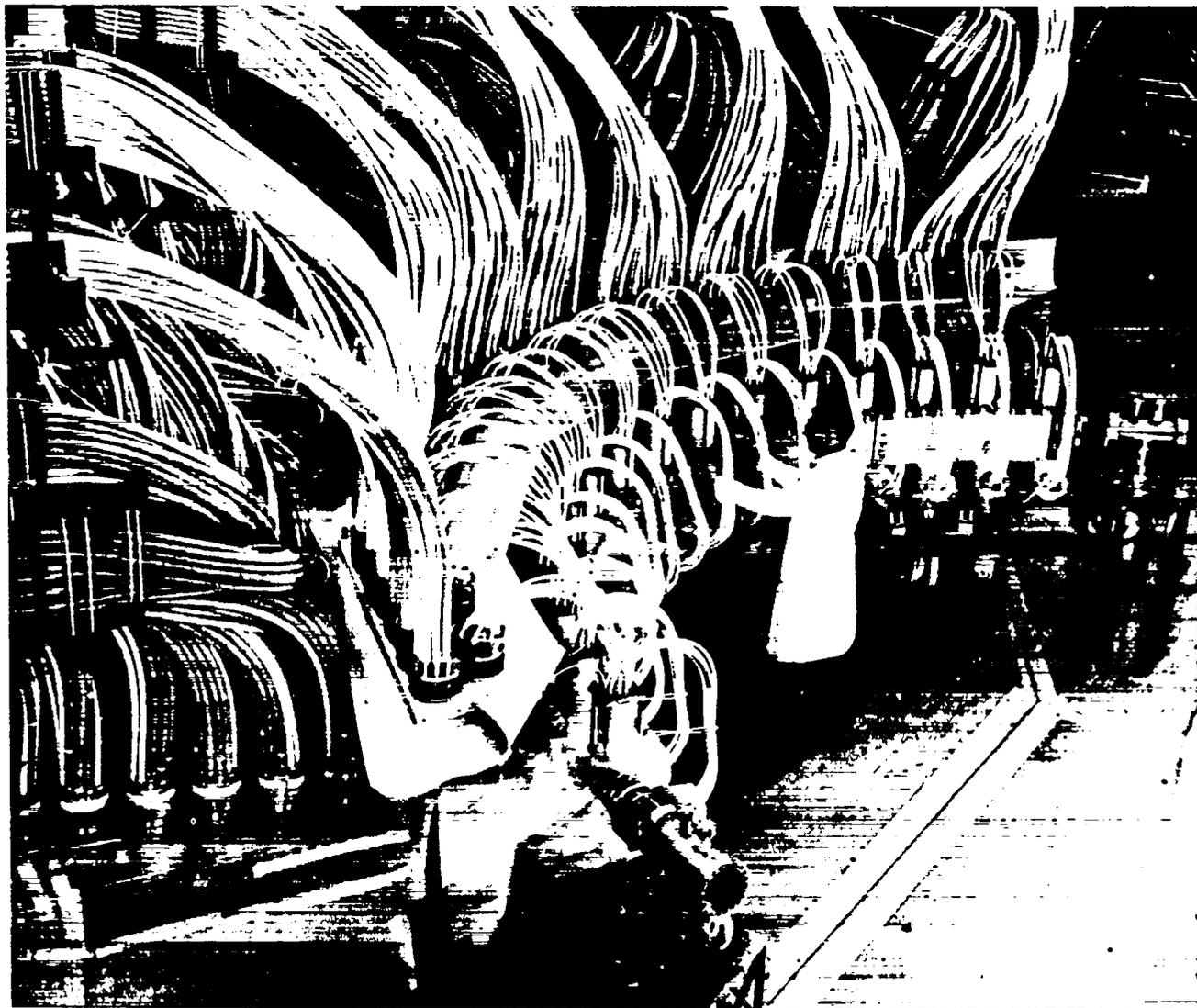
*Fig. II-11.*
*Photograph of the sector front end with the $\ell = 1$ coils installed.*

With this arrangement, the interconnecting cables on the end $\ell = 1$ coils carry currents on both of their coaxial conductors.

The $\ell = 1$ helical fields were probed in the toroidal sector geometry. The probing and field adjustments were done with an oscillator-current amplifier exciting the $\ell = 1$ coils at 20 kHz. The final $\ell = 1$ arrangement was probed with the $\ell = 1$ capacitor bank driving the helical windings. The radial component of the $\ell = 1$ field, $B_R$, was measured on the minor axis of the torus in both the horizontal and vertical planes.

Figure II-15 shows a plot of the maxima of the absolute value of $B_R$ ($r = 0$) in the regions of the lands and grooves of the compression coil in the vertical plane of the torus both before and after the end correction. The difference in amplitude of the $\ell = 1$ fields in the regions of the grooves and lands, Fig. II-15, is a result of the $\ell = 1$ coils having weaker image currents in the groove regions than in the land regions. Plots of the radial components of the $\ell = 1$ fields on the torus minor axis in both the horizontal ($B_{R-H}$) and vertical ($B_{R-V}$) planes are shown in Fig. II-16 for approximately two $\ell = 1$ wavelengths in

18
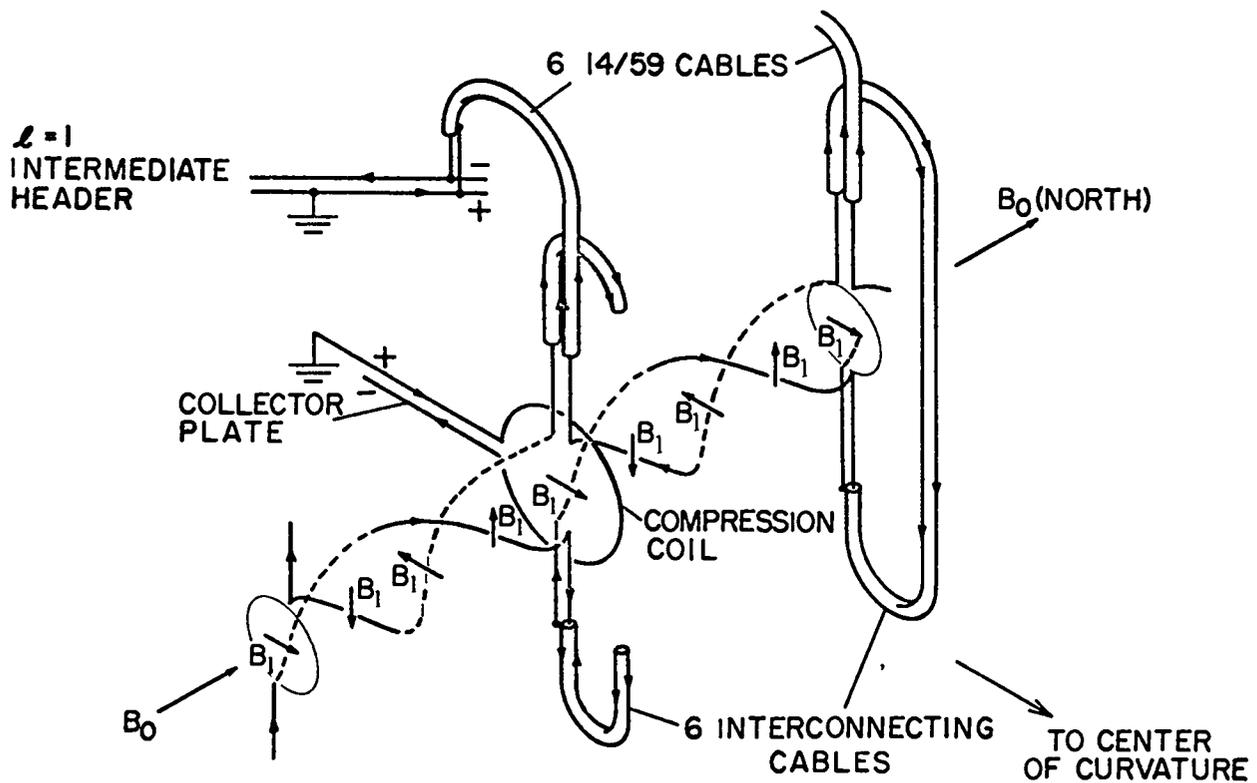
*Fig. II-12.*
*Schematic diagram of capacitor-driven ℓ = 1 coils in the Scyllac compression coil.*
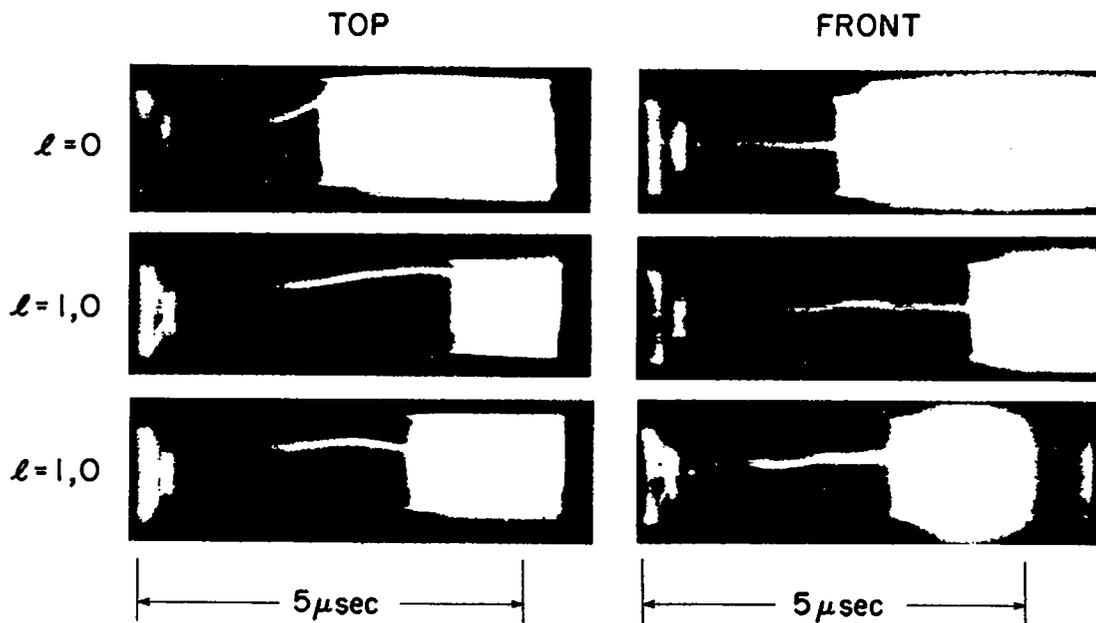


*Fig. II-13.*
*Streak photographs of the plasma at the center of the Scyllac 5-m toroidal sector with ℓ = 0 fields alone and with the ℓ = 1,0 combination.*
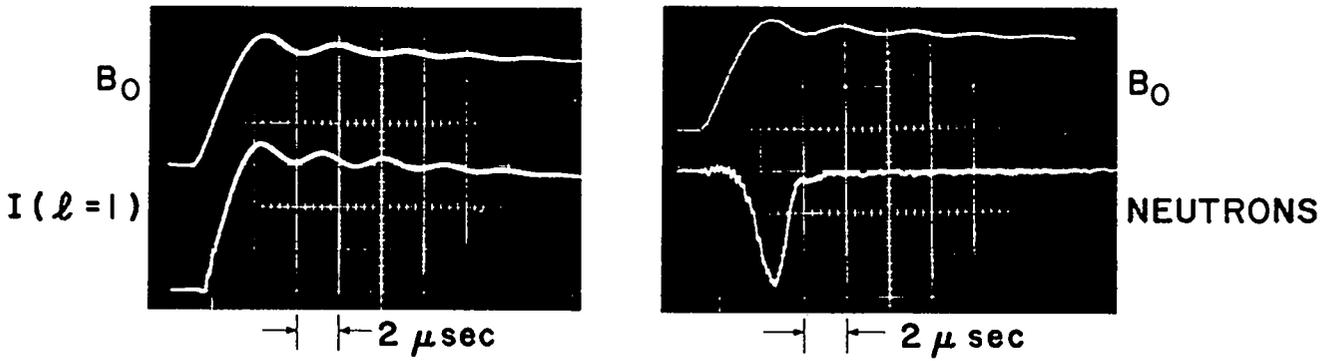
*Fig. II-14.*

*Oscillograms of compression field, current through the ℓ = 1 coils, and neutron emission when the ℓ = 1,0 combination was excited.*
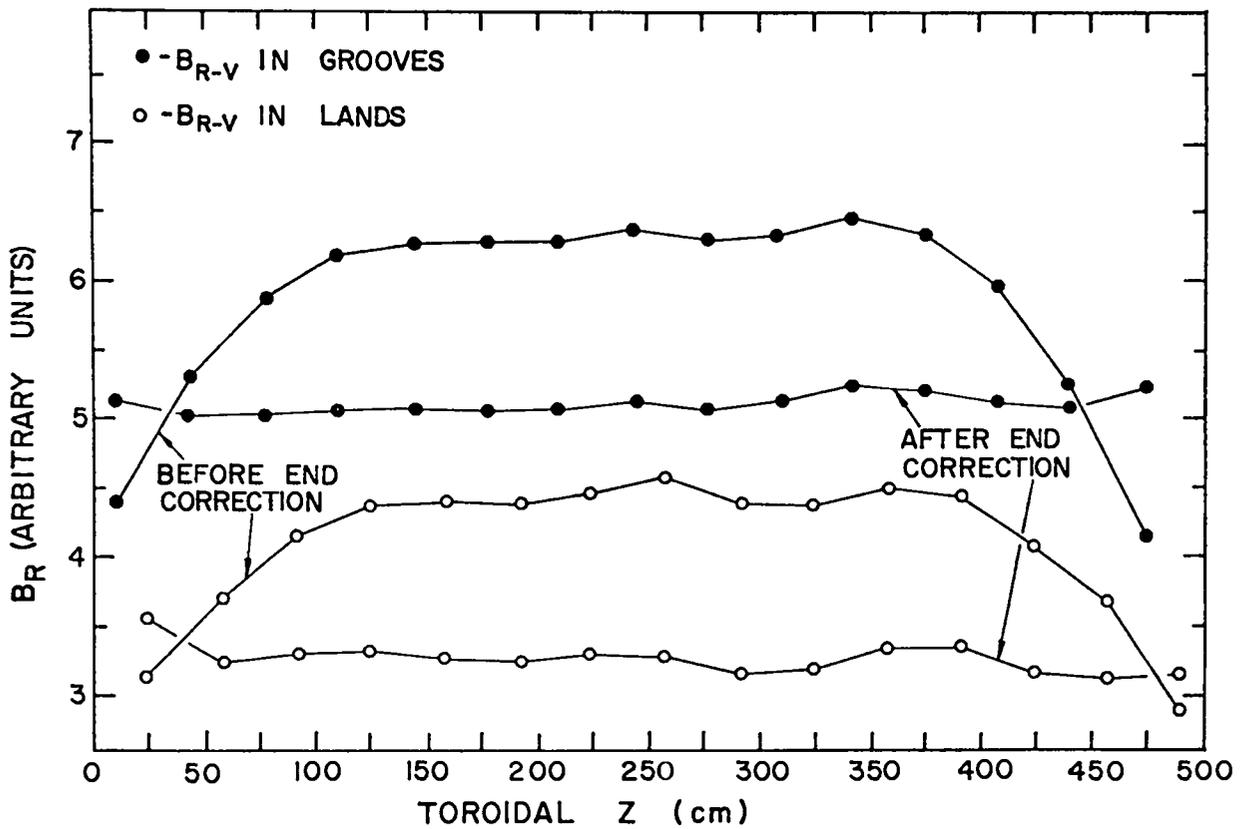


*Fig. II-15.*

*Graphs of the absolute maxima of $B_R$ on the torus minor axis in the land and groove regions of the compresison coil in the vertical plane.*

*Fig. II-16.*

*Graphs of the radial components of the $\ell = 1$ fields on the torus minor axis in both the horizontal ($B_{R-H}$) and vertical ($B_{R-V}$) planes in coil-meter 14.*

coil-meter 14 (see Fig. II-2). These show the $\ell = 1$ field in the horizontal plane to be approximately independent of the presence of lands and grooves on the minor axis. In the vertical plane the $\ell = 1$ field in the land regions is approximately 37% less than that in the groove regions, in reasonable agreement with the plots of Fig. II-15.

### 7. Plasma Measurements with End-Corrected $\ell = 1$ Fields (1.8-cm $\ell = 0$ groove depth).

*a. Transverse Motions of the Plasma Column.* The motions of the plasma column from its equilibrium position in the center of the tube are shown in Fig. II-17 for two discharges (1358 and 1360). The upper streak photographs, labeled A, show the motions in the horizontal plane in a groove region. The streaks labeled B show the vertical plane motion at a z position between the groove and land region (necessitated by the presence of the helical $\ell = 1$ coil). Horizontal plane motions in an adjacent land region are shown in the streaks labeled C. On discharge 1358 the plasma motions indicate that the plasma column strikes the discharge tube wall in the

upper, inward azimuthal quadrant at the time the bright luminosity occurs. The original of the streak photograph in the land region (1358C) shows the plasma column turning inward as the wall light occurs. These streak photographs (1358) indicate that the plasma column is moving to the wall in the $\ell = 0$ groove region. In the streak photographs of discharge 1360, Fig. II-17, the plasma motion is essentially the same on the south end of the groove region (1360B) as at the north end in 1358B. In the groove region the plasma column attains an equilibrium position after an outward drift (1360A). In the land region, the column drifts slowly outward after having attained an equilibrium position. On this discharge the plasma column appears to strike the wall in the upper outward quadrant near the vertical plane.

After the appropriate $\ell = 1$ end corrections (see Sec. II-C-6) and with the addition of viewing slits in the groove regions of the compression coil, the experiments showed that the plasma column was striking the tube wall periodically in each $\ell = 0$ groove. Furthermore, it appears that this may have resulted from a plasma instability rather

1358

1360

TOP
(13-1)

G

FRONT
(13-1,2)

FRONT
(12-6,13-1)

TOP
(13-2)

L

A

B

C

|←6 μ sec →|     |←6 μ sec →|
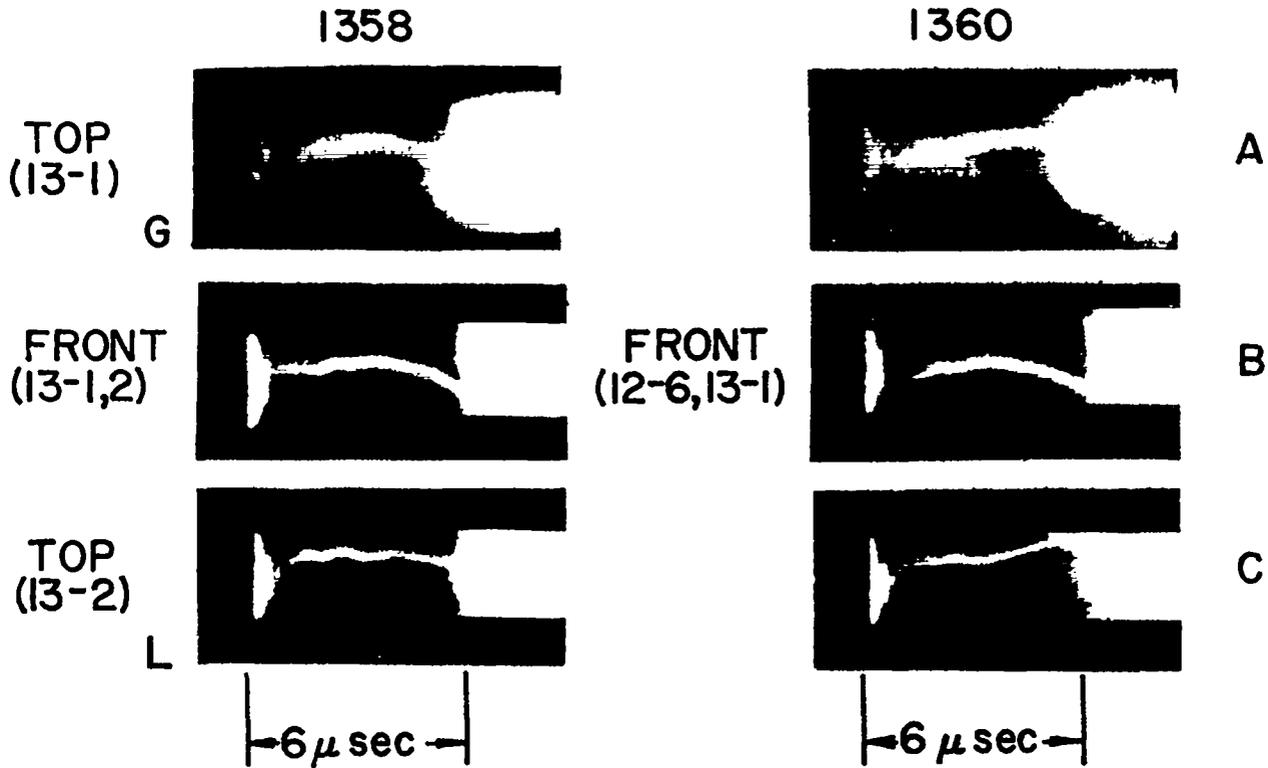
$P_{D_2} = 20$ mTorr;  $V_{PB} = 45$ kV;  $I_{\ell=1} = 67$ kA

Fig. II-17.
Streak photographs of the plasma near the center of the Scyllac 5-m toroidal sector. In the top views, A and C, an upward displacement is a radially outward motion of the plasma column in the horizontal plane of the torus. In the Front view B a downward displacement is an upward motion of the plasma column in the vertical plane of the torus.

than just an imbalance in the applied equilibrium force and the toroidal force. The onset time of the unstable motion was about 3 μsec, its effective growth rate about 1.3 MHz, and the time of wall light 5 to 6 μsec.

b. Neutron Emission. For a 15-mTorr deuterium filling pressure, the peak neutron emission rate occurs at 2.8 to 3.0 μsec after the initiation of the main discharge. A decrease in the emission rate follows before the plasma column strikes the wall with a more precipitous drop occurring as the column strikes the wall.

c. Laser Interferometer Density Measurement. The coupled-cavity interferometer was used to measure the time history of area denisty ($\int nd\ell$) through a diameter of the plasma in an $\ell = 0$ groove location in the central meter of the compression coil. Figure II-18 is the plot of $\int nd\ell$ vs. time as analyzed from a 15-mTorr discharge (shot 1140). The integral is started from zero at main-bank trigger time, although there is actually a small finite value $(0.5 \times 10^{16}$ cm$^{-2})$ due to the preionization at that time. As the plasma leaves the line of sight, there is a steep drop almost to zero before it rises again about the time the streak camera shows the plasma reaching the wall.
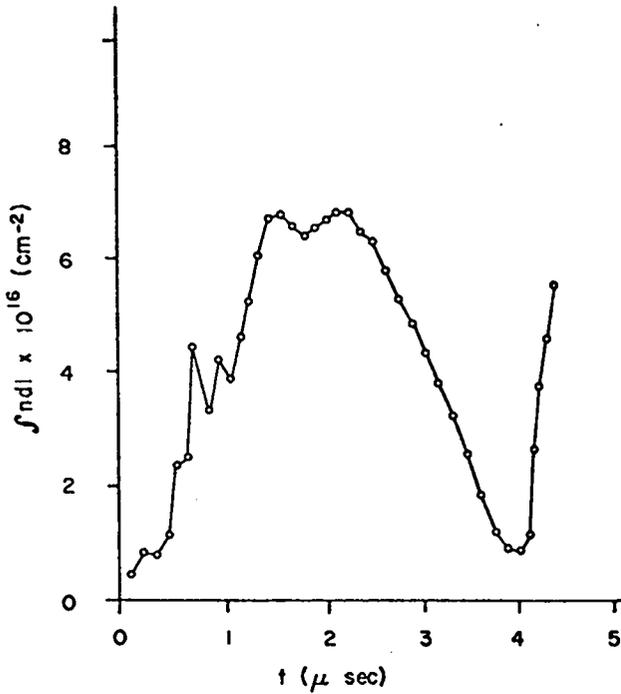
**Fig. II-18.**
*Graph of the area density ($\int nd\ell$) as a function of time from the laser interferometer.*

The peak density on axis occurs at 2.1 $\mu$sec and can be obtained by combining this result with the luminosity profile. Assuming a Gaussian profile yields

$$\int nd\ell = 2 \int_0^\infty n_o e^{-(r/a)^2} dr = n_o \sqrt{\pi}a \quad . \tag{3}$$

For a measured value of the plasma radius a = 1.3 cm (obtained for a different, but equivalent, shot when the luminosity was measured in a groove region)

$$n_o \sqrt{\pi}a = 7 \times 10^{16} cm^{-2}$$

and

$$n_o = 3.0 \times 10^{16} cm^{-3} \quad .$$

With the $\beta$ and B field values derived from the combined excluded flux and luminosity data, an estimate can be obtained for the sum of ion and electron temperature from pressure balance

$$n_o k (T_e + T_i) = \beta \frac{B_o^2}{8\pi} \quad , \tag{4}$$

or

$$(T_e + T_i) = 2.5 \frac{\beta B_o}{n_o} \quad , \tag{5}$$

with $T_e + T_i$ in eV, $B_o$ in kG, and $n_o$ in units of $10^{16} cm^{-3}$. For shot 1140 at 2.5 $\mu$sec, $\beta = 0.8$ and $B_o = 33$ kG; thus

$$(T_e + T_i) = 726 \text{ eV}.$$

The peak crowbarred field of 39 kG occurs at 3.2 $\mu$sec, after the column has moved out of the laser field of view. If one assumes $n_o$ remains constant ($\beta$ is measured to remain constant), the temperature is estimated to increase another 33% at peak field to approximately 960 eV.

*d. Excluded Flux and Luminosity Measurements.* The apparatus is described below in Section II-I, entitled "Applied Diagnostics on the Toroidal Sector." In the case of the luminosity measurement, the fiber optics and photomultipliers are calibrated with a strobe light, diffuser, and beam splitter 200 $\mu$sec before each plasma shot. The relative sensitivity of the ten channels is determined in this manner to better than 5%. By wrapping the discharge tube with black tape (fiber glass tape painted with flat black paint and heated to 200°C to remove volatiles), the relative plasma to background light ratio has been made better than 10:1.

Typical reduced data from the excluded flux and luminosity measurements are presented in Fig. II-19. This figure summarizes the data by giving the excluded flux (from the double probe), the plasma radius (from luminosity), and the plasma beta on axis as calculated from the above quantities, all as a function of time. Peak magnetic field on these shots occurred at about 3.0 $\mu$sec.

The excluded flux is characterized by an initial spike followed by several oscillations identified with mass oscillations, or bouncing, of the plasma column, associated with the initial implosion. The diamagnetism then decreases monotonically.

The actual plasma radius, as determined from luminosity profiles, is shown in the central plot. The plasma brightness profile is quite consistent with the assumption that the density is Gaussian

$$n_e(r) = n_o e^{-(r/a)^2} \quad ,$$

and that a uniform, and small ($\sim$ 10%), background comes from the walls. Therefore, a least-squares fit to determine the plasma radius is made for each time of interest for the nine channels of luminosity.

By combining the luminosity and excluded flux measurements, making the assumption that temperature is independent of radius, the plasma $\beta$ can be determined. The value of $\beta$ on axis is shown in the lower plot. On shots with applied $\ell = 1$ current and no initial bias field,

23
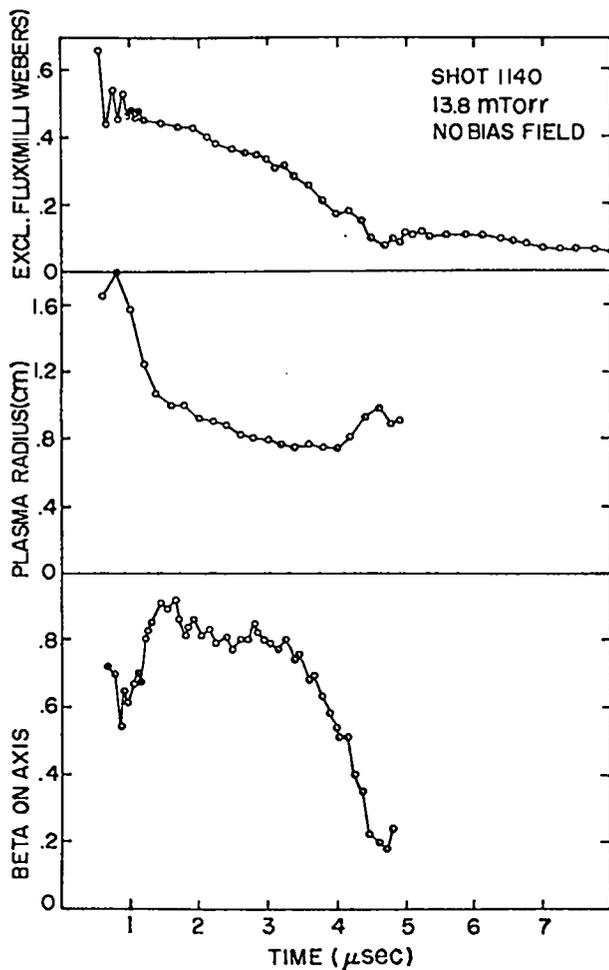
*Fig. II-19.*
*Graphs of the excluded flux (upper plot), the plasma radius (center graph) and the plasma β (lower plot) with a filling pressure of 13.8 mTorr.*

the plasma β is about 0.8 until three to four microseconds, when it drops rather quickly to smaller values. In the presence of a parallel bias field, the β values were found to be lower as one expects.

*e. Estimates of $\delta_0$ from Luminosity.* The luminosity apparatus was sometimes positioned to view a groove region rather than a land region as in the data reported above. Data were obtained with initial parallel bias of zero and 450 G.

With no initial bias, and at 15 mTorr filling pressure, groove and land-region measurements were compared to estimate $\delta_0$ ($\delta_0$ is defined in Fig. II-9):

| Shot | Measurement Location | Bias Field | Plasma Radius at 3.2 μsec |
|---|---|---|---|
| 1140 | land | 0 G | 0.78 ± .08 cm |
| 1157 | groove | 0 | 1.38 ± .14 |
| 1317 | land | 450 | 0.98 ± .10 |
| 1238 | groove | 450 | 1.12 ± .11 |

Sharp boundary calculations[5] provide an estimate of $\delta_0(\beta)$ which compare as follows:

| Beta | $\delta_0$ (sharp boundary) | $\delta_0$ (experimental) |
|---|---|---|
| 0.8 | 0.42 | 0.28 ± .09 |
| 0.3 | 0.14 | 0.07 ± .07 |

where $\delta_0$ (experimental) $\equiv \dfrac{a(\text{groove}) - a(\text{land})}{a(\text{groove}) + a(\text{land})}$ .

The experimental results are in reasonable agreement with sharp-boundary theory, although the plasma is not a sharp boundaried object. The expected scaling[5] of $\delta_0$ as $1/(1-\beta)$ seems to be valid within experimental error.

**8. Plasma Measurements with 0.9-cm ℓ = 0 Groove Depths.**

*a. Experimental Arrangement.* The results with the deep (1.8-cm) ℓ = 0 grooves showed that the plasma column was going to the discharge tube wall periodically in each ℓ = 0 groove region (a "ballooning" motion). The depth of the ℓ = 0 grooves was reduced from 1.8 cm to 0.9 cm. This was accomplished by boring out the land sections of the compression coil. In addition to halving the ℓ = 0 groove depth, this also affected the inequality of ℓ = 1 image currents in lands and grooves. The difference between the ℓ = 1 fields in the grooves and lands was reduced from 33% to 14%. In the experiments performed to date, the 0.9-cm ℓ = 0 grooves were not filled with the annular trapezoidal Inconel inserts because of procurement difficulties.

The results presented below were obtained under the following conditions: 1) the primary bank was operated with one-half its capacitance at a voltage of 45 kV; 2) the initial deuterium filling pressure was 15 mTorr; and 3) the ℓ = 1 current was in the range of 50 to 65 kA and was applied with an average delay of 0.3 μsec after the initiation of the main discharge.

*b. Results.* The streak photographs of Fig. II-20A show the horizontal plasma motions near the center of the compression coil with the ℓ = 1 coils not excited. Even though the ℓ = 0 fields were present because of the grooves, the motion was a simple toroidal "drift" to the

A (2033)
$I_{\ell=1} = 0$

B (1945)
$I_{\ell=1} = 56\ kA$

GROOVE
(13-1)

LAND
(13-2)

4 $\mu$ sec

10 $\mu$ sec

$P_{D2} = 15\ mTorr$;  $V_{PB} = 45\ kV$
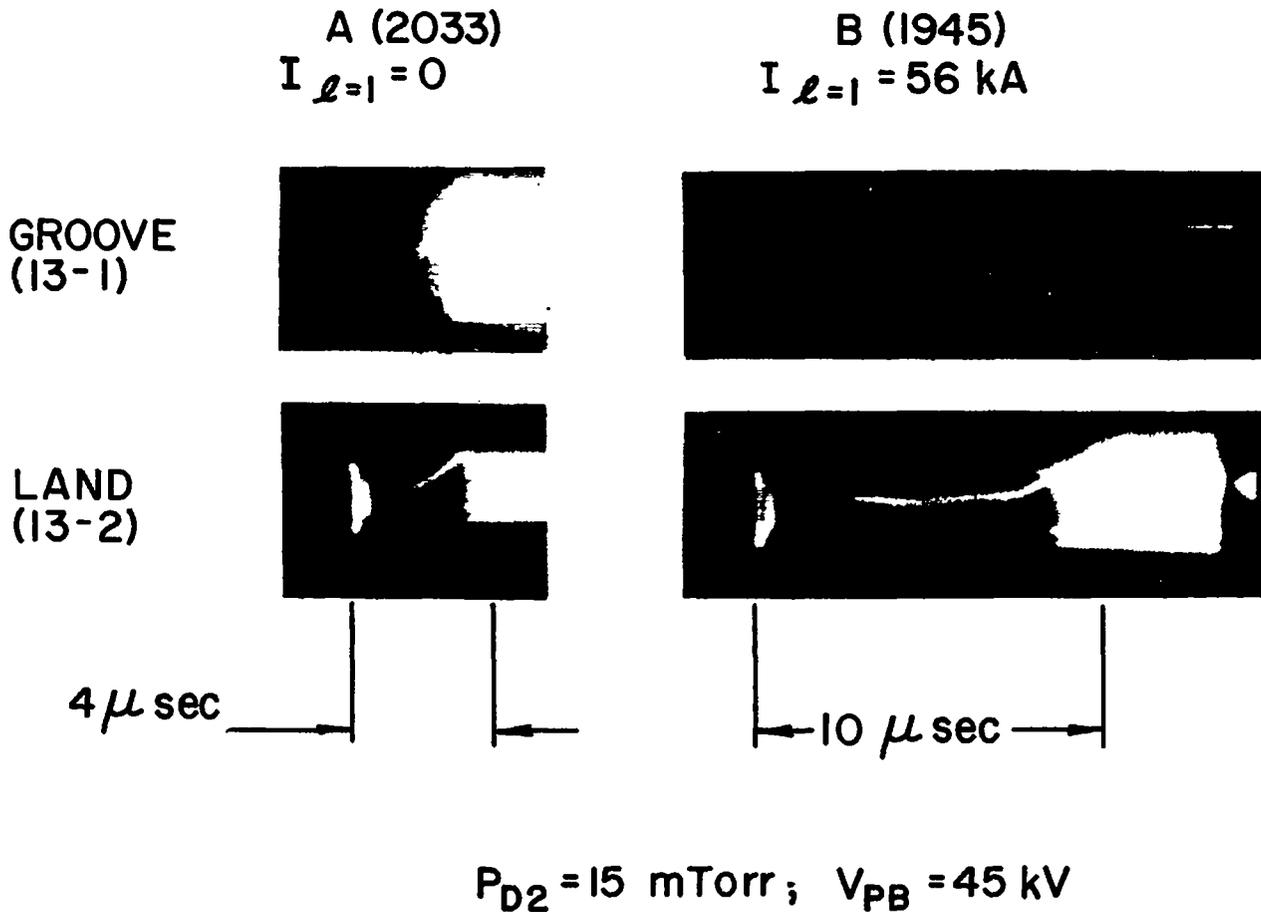
Fig. II-20.
Streak photographs of the plasma near the center of the 5-m sector with $\ell = 0$ fields alone (left column) and with the $\ell = 1,0$ combination (right column).

walls in both the groove and the land, with no observable instability induced by the bumpy $\ell = 0$ fields. The streak photographs of Fig. II-20B were taken with the $\ell = 1$ coils excited with 56 kA. Note that the toroidal force is overcome by the $\ell = 1,0$ field combination in both the groove and land regions. The plasma column takes up an equilibrium position, which is shifted slightly inward in the groove region and outward in the land region owing to the helical shift of the plasma column. The column remains in the equilibrium position to 6 $\mu$sec in the groove region and 7.4 $\mu$sec in the land region, at which times an outward motion of the plasma column develops. The column strikes the tube wall in the land region at 8.2 $\mu$sec. The streak photographs of Fig. II-21 show both vertical and horizontal plasma motions near the center of the compression coil.

The streak photographs of Fig. II-22 show the effect of a small variation in the amplitude of the $\ell = 1$ current on the plasma motion in the horizontal plane of

an adjacent land and groove near the center of the compression coil. In Fig. II-22A, with an $\ell = 1$ excitation current of 61 kA, an outward "drift" of the plasma column begins in both the groove region (at 2.5 $\mu$sec) and the land region (at 3.2 $\mu$sec). Figure II-22B, with a slightly increased $\ell = 1$ current of 63 kA, shows the plasma column developing an inward plasma motion in both the groove (at 3.1 $\mu$sec) and land (2.6 $\mu$sec) regions, striking the tube wall in the groove region.

c. Discussion of Streak-Photographic Observations. The similar plasma motions in the land and groove regions of Figs. II-20B, -21, and -22 suggest that the expected long-wavelength m = 1 plasma instability[6] may be developing. The motion of the plasma column develops in the horizontal plane of the torus rather than in random directions. This could occur because of a net driving force in this plane from a small imbalance of the $F_R$ and $F_{1,0}$ forces, as evidenced by the fact that small changes in the

25

## 2090



TOP (13-1)　　　　　　　　　GROOVE

FRONT (13-1,2)

TOP (13-2)　　　　　　　　　LAND

|←——— 6 $\mu$ sec ———→|
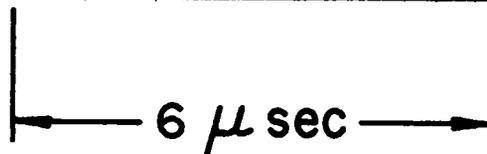
$$P_{D2} = 15 \text{ mTorr}; \quad V_{PB} = 45 \text{ kV}; \quad I_{\ell=1} = 59 \text{ kA}$$

*Fig. II-21.*
*Streak photographs of the plasma column near the center of the 5-m sector with $\ell = 1,0$ fields.*

$\ell = 1$ current have a large effect on the plasma motion (Fig. II-22).

With the assumption that an instability is developing, Table II-12 lists onset times ($\tau_{onset}$), growth rates $\gamma$, and the time the plasma column reaches the tube wall ($\tau_{wall}$) for the plasma in a groove region and in a land region.

It is intended to continue to optimize the operation of the toroidal sector by further reducing the $\ell = 0$ groove depth and improving the uniformity of the $\ell = 1$ field.

### References

1. Los Alamos Scientific Laboratory report, LA-4585-MS, p. 18 (1970).

$$A\ (1848)$$
$$I_{\ell=1} = 61\ kA$$

$$B\ (1856)$$
$$I_{\ell=1} = 63\ kA$$

GROOVE
(13-1)

LAND
(13-2)

|——6 $\mu$ sec——|

|——6 $\mu$ sec——|
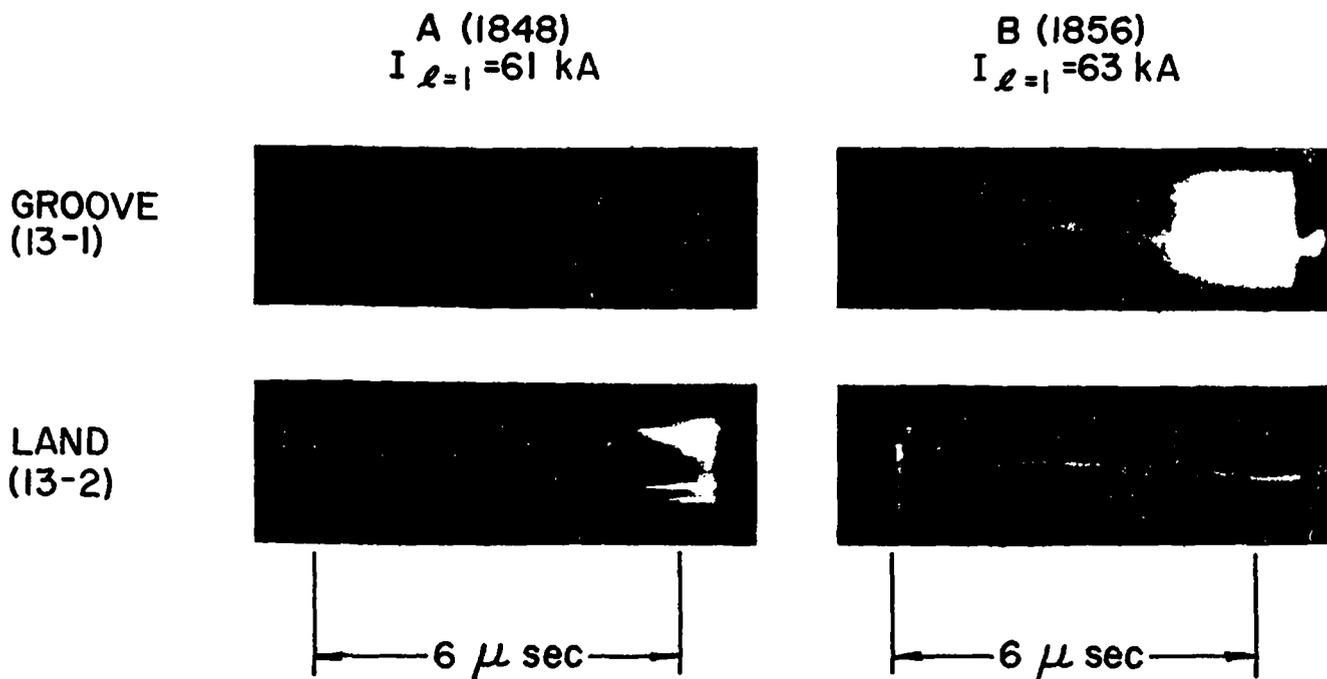
$$P_{D_2} = 15\ mTorr;\quad V_{PB} = 45\ kV$$

*Fig. II-22.*
*Streak photographs of the plasma in the horizontal plane showing the effect of a small change in the $\ell = 1$ current.*

TABLE II-12

TIMES AND GROWTH RATES FROM STREAK PHOTOGRAPHS

| No. of Shots | Location | $T_{onset}$ ($\mu$sec) | Plasma Motion | $\gamma$ (MHz) | $T_{Wall}$ ($\mu$sec) |
|---|---|---|---|---|---|
| 13 | Groove | 1.9 | Outward | 0.8 | 6.2 |
| 9 | Land | 3.6 | Outward | 0.9 | 6.5 |
| 12 | Groove | 2.4 | Inward | 1.0 | 4.3 |
| 13 | Land | 2.2 | Inward | 0.8 | - - |

2. S. C. Burnett, W. R. Ellis, C. F. Hammer, C. R. Harder, H. W. Harris, F. C. Jahoda, W. E. Quinn, A. S. Rawcliffe, F. L. Ribe, G. A. Sawyer, R. E. Siemon, K. S. Thomas, and E. L. Zimmermann, "Theta-Pinch Experiments with Helical Equilibrium Fields in a 5-Meter Toroidal Sector and in a 3-Meter Linear Device," Paper CN-28/J-4 presented at Fourth Conference on Plasma Physics and Controlled Nuclear Fusion Research, Madision, Wisconsin, June 17-23, 1971.

3. F. L. Ribe, Los Alamos Scientific Laboratory report LA-4098 (1969).

4. F. L. Ribe and M. N. Rosenbluth, Phys. of Fluids 13, 2572 (1970).

5. F. L. Ribe, W. H. Borkenhagen, W. R. Ellis, and K. S. Hanks, Los Alamos Scientific Laboratory report LA-4597-MS (1971).

6. J. P. Freidberg, "Survey of Scyllac Theory" Paper CN-28/J-4 Presented at Fourth Conference on Plasma Physics and Controlled Nuclear Fusion Research, Madison, Wisconsin, June 17-23, 1971.

**D. Experiments on Scylla IV-3 with $\ell = 1$ and $\ell = 0$ Helical Fields** (K. S. Thomas, W. R. Ellis, C. R. Harder, H. W. Harris, R. E. Siemon, and E. L. Zimmermann)

Experiments with capacitor-bank-driven $\ell = 1$ and $\ell = 0$ coils were conducted on Scylla IV-3. The purpose of these experiments was to conduct studies on a straight $\theta$ pinch of the effect of small helical fields on the equilibrium and stability of the plasma column and to measure the strength of the interference force caused by a combination of helical fields. These fields are used on the Scyllac toroidal sector to provide an equilibrium in the presence of the toroidal main compression field. The experiments reported here are an extension of the work reported in LA-4585-MS (p. 2) where $\ell = 1$ fields were generated by grooves machined in the main compression coil. The purpose of using a driven winding to generate the helical fields was to allow the plasma to be studied with and without the helical fields and to allow the generation of both $\ell = 1$ and $\ell = 0$ fields. In these experiments, the plasma $\beta$ (ratio of plasma pressure to external field pressure) was varied by applying a small bias magnetic field in the same direction as the main compression field. Plasma stability and equilibrium, and the $\ell = 1,0$ force term, were measured as a function of $\beta$. Preliminary results of these experiments have been published[1] and a complete report is being prepared for publication.

The helical fields[2] may be described by magnetic fields whose scalar potentials have the form

$$\chi_\ell = (B_0/h)[C_\ell I_\ell(hr) + D_\ell K_\ell(hr)] \sin(\ell\theta - hz) . \quad (1)$$

The equilibrium and stability of this system for a sharply bounded, straight, $\theta$-pinch plasma column has been treated extensively in the magnetohydrodynamic approximation.[3-5] Recently, Ribe and Rosenbluth[6] and Weitzner[7] showed that a combination of fields characterized by $\ell$ and $\ell \pm 1$ might be used to give a uniform transverse body force to counteract the toroidal pressure gradient and also to feedback-stabilize the the expected m = 1 instability.

For this experiment the main helical field has $\ell = 1$ symmetry with a longitudinal period of 30 cm ($h = 2\pi/30$ cm$^{-1}$). For a high-$\beta$ plasma, magnetohydrodynamic theory[3,4] predicts that this configuration should have a lower m = 1 instability growth rate than the fields with other $\ell$ values. To produce the body force, an additional, smaller $\ell = 0$ field was applied. The effect of these fields on a straight plasma column of radius a is to produce excursions $\delta_\ell$ of the plasma radius about r = a given by

$$r = a [1 + \delta_\ell \cos(\ell\theta - hz)] . \quad (2)$$

1. **Experimental Arrangement.** The experiments were performed on the Scylla IV-3 $\theta$ pinch[8] whose main capacitor bank has an energy storage of 700 kJ at 45 kV and produces a magnetic field $B_0$ inside the 3-m-long, 13.5-cm-diam, main compression coil which rises to 42.5 kG in 3.7 $\mu$sec. At maximum field, the bank is crowbarred (shorted), giving a peak-to-peak modulation of the nearly constant magnetic field of 20%.[8]

Figure II-23 shows the arrangement of the $\ell = 1$ and $\ell = 0$ coils inside the main compression coil. The currents in the $\ell = 1$ coils are in the direction shown and rise to 80 kA in 2.5 $\mu$sec. At this current a transverse helical field $B_r$ of 2.85 kG is produced on axis. The current to the $\ell = 1$ coils is fed in one-wavelength sections to keep the voltages induced by the main compression field to a manageable level. The $\ell = 0$ coils are driven by a capacitor bank, which in the present arrangement produces a maximum $|I_1| = |I_2| = 19$ kA with a rise time of 1.6 $\mu$sec. The coils are driven in pairs as shown in Fig. II-23 to cancel the induced voltage from the main bank. The system may be connected with $I_1$ and $I_2$ in either direction to vary the relative phases of the $\ell = 0$ and $\ell = 1$ fields, and hence the direction of the $\ell = 1,0$ force. The arrangement shown in Fig. II-23 gives an upward force. Since the present arrangement requires $I_1 = \pm I_2$, the direction of the force can only be applied in four directions, either horizontally or vertically. For a feedback system the amplitudes and phases of $I_1$ and $I_2$ would be varied independently, giving
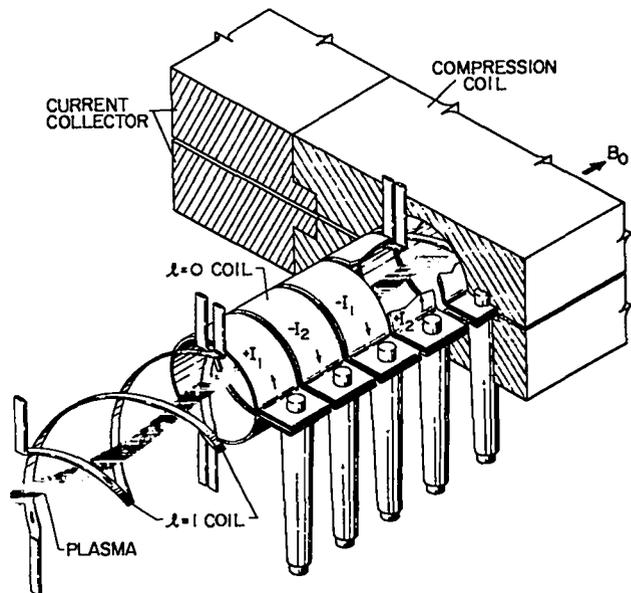


*Fig. II-23.*

*Arrangement of the $\ell = 1$ and $\ell = 0$ coils with relation to the main $\theta$-pinch compression coil.*

an arbitrary magnitude and direction to the $\ell = 1,0$ force. At 19-kA current, the present arrangement gives a first-harmonic amplitude of axisymmetric field $\delta B_0 = 0.65$ kG on axis. The construction of the $\ell = I$ coils is described in LA-4585-MS (p. 16). These coils are copper windings wrapped with a Mylar-based tape and then potted in epoxy. The $\ell = 0$ coils are brass, 6.5-cm wide, and are potted in epoxy.

**2. Diagnostics.** The plasma density profile was measured using a holographic ruby laser interferometer which makes interferograms at three times during the plasma lifetime. This interferometer was described in detail in LA-4585-MS (p. 18). The quanitity $\beta$ was measured both by means of Faraday rotation[9] at 6328 Å and by means of a double magnetic probe excluded-flux measurement.[10] The two measurements agree to within experimental error. Electron temperature measurements were made using a two-channel soft x-ray detector[11] which measures the energy transmitted through two different thicknesses of beryllium foil and determines the temperature from the ratio of the two signals. Ion temperatures are calculated from pressure balance and from d-d neutron production.

**3. Results.** The plasma parameters at the peak of the main compression field are given in Table II-13 for the three different $\beta$ values studied. When the $\ell = 1$ fields are applied with, or after, the main compression field, the plasma takes up a helical equilibrium configuration with $\delta_1$ proportional to $B_r/B_0$ regardless of whether the $\ell = 1$ field is applied simultaneously with $B_0$ or a few microseconds thereafter. The values of $\delta_1$ for peak $B_r$ and $B_0$ are given in Table II-13. This is measured by mathematically unfolding the interferograms[12] and (less accurately)

by comparing the position of the center of the fringe pattern on the interferogram with the location of the plasma at a given z position as measured by a streak camera. After the plasma becomes helical, a $k \approx 0$, m = 1 instability develops having the observed growth rates given in Table II-13. This is an exponentially growing sideward motion; no other m modes are observed. Owing to a small asymmetry in the $\ell = 1$ fields, this instability always develops in almost the same direction, downward and slightly away from the compression-coil feed slot. When the $\ell = 0$ coils, but not the $\ell = 1$ coils, are energized no detectable change in plasma behavior is observed.

The result of applying both fields is shown in Figs. II-24 and -25 for the case where $\beta = 0.88$. Figure II-24 shows streak photographs taken near the coil midplane at a point where the helical shift $\delta_1$ of the plasma due to the $\ell = 1$ fields would be downward. The streak pictures show stereoscopic views of the plasma 45° above and below the horizontal. In the upper half of each photograph, motion toward the center of the two views is plasma motion downward and away from the main-coil feed slot. In the lower half, motion toward the center of the two views is plasma motion upward and away from the feed slot. In all three cases, the helical fields were applied 1.2 $\mu$sec after the main compression field. The duration of the streak photograph is 9 $\mu$sec. The upper streak picture shows plasma behavior in absence of $\ell = 0$ fields. The plasma motion is that of the m = 1 instability induced by the $\ell = 1$ field. In the middle streak picture, $\ell = 1$ and $\ell = 0$ fields were applied simultaneously in the phase shown in Fig. II-23. As expected, this gives an $\ell = 1,0$ force $F_{1,0}$ in the upward direction. In the lower streak photograph, $I_1$ was reversed, and motion is observed in the direction toward the feed slot. Figure II-25 shows interferograms taken during the same plasma discharges. At 2 $\mu$sec after

TABLE II-13

**PLASMA PARAMETERS AT PEAK OF MAIN COMPRESSION FIELD**

| Plasma Parameters | Forward Bias (gauss) | | |
|---|---|---|---|
| | 0 | 320 | 750 |
| $B_z^{max}$ (gauss) | 42,500 | 42,500 | 42,500 |
| $\beta$ | 0.88 ± 0.03 | 0.70 ± 0.05 | 0.42 ± 0.06 |
| n (x $10^{16}$/cm$^3$) | 3.3 ± 0.3 | 3.2 ± 0.3 | 3.1 ± 0.3 |
| a (cm) | 0.70 ± 0.09 | 0.73 ± 0.05 | 0.77 ± 0.05 |
| $T_e$ (eV) | 390 ± 50 | 270 ± 50 | 250 ± 50 |
| $T_i$ (eV) | 800 ± 100 | 700 ± 100 | 350 ± 100 |
| $\delta_1$ | 0.70 ± 0.06 | 0.65 ± 0.06 | 0.54 ± 0.06 |
| $\gamma_1$ (x $10^6$/sec) | 0.53 ± 0.09 | 0.4 ± 0.1 | 0.2 ± 0.1 |

$9\ \mu\ sec$

$\mathcal{L} = 1$

$\mathcal{L} = 0, 1\ \uparrow$

$\mathcal{L} = 0, 1\ \leftarrow$

Fig. II-24.
*Streak pictures of three different experimental conditions. Upper, only $\mathcal{L} = 1$ coils energized; middle, both $\mathcal{L} = 1$ and $\mathcal{L} = 0$ coils energized with a phase which gives an upward body force; lower, both $\mathcal{L} = 1$ and $\mathcal{L} = 0$ coils energized with a phase which gives a body force toward the main-coil feed slot.*

the application of the main compression field, all three cases were indistinguishable, since no motion had yet occurred, and a typical interferogram is shown in the upper left of the figure. The other three interferograms show the plasma at $4\mu$sec. The main-coil feed slot is to the left. The small deviation of plasma motion from the

direction of the $\mathcal{L} = 1,0$ force is probably due to a component of horizontal instability motion, in the case where the $\mathcal{L} = 1,0$ force is vertical, and to vertical instability motion when the $\mathcal{L} = 1,0$ force is horizontal. In such a case, the direction of the deviation is in the direction of growth of the $m = 1$ instability in the absence of $\mathcal{L} = 0$ fields.

4. Analysis. The sharp-boundary model[6] gives for $\delta_1$

$$\delta_1 = \frac{B_r/B_0}{(1 - \beta/2)\ ha} \quad \text{(3)}$$

To compare the experimental values with the theoretical values, the quantity $\delta_1\ a/(B_r/B_0)$ vs $\beta$ is plotted in Fig. II-26. The data point with dashed error bars is from another experiment with $\mathcal{L} = 1$ grooves along the full length of the compression coil and no $l_z$ (LA-4585-MS, p.2). For this case, $\beta$ was not measured. The value $0.85 \pm 0.05$ is an estimate based on experience with other $\theta$-pinch configurations.

The instability growth rates $\gamma_1$, given in Table II-13, are for the cases when only the $\mathcal{L} = 1$ fields were applied, and were measured by fitting an exponential to the plasma displacements measured from side-on streak pictures. Figure II-27 gives a comparison of the experimental values with three theoretical values. All are sharp-boundary theories. Again, the dashed error bars indicate grooved-coil data.

The magnitude of the $\mathcal{L} = 1,0$ force was determined by studying the plasma's dynamical behavior on stereoscopic streak photographs. For the $\beta = 0.88$ case, in order to produce a motion which could be easily analyzed, plasma discharges were taken with the $\mathcal{L} = 1$ field applied first, allowing the $m = 1$ instability to develop. Then, 1 to 2 $\mu$sec later, the $\mathcal{L} = 0$ fields were applied to produce the force $F_{1,0}$ in a direction as nearly as possible opposite to that of the instability force. For the other values of $\beta$, the force term was smaller and could be better measured by applying the $\mathcal{L} = 1$ and $\mathcal{L} = 0$ fields simultaneously.

The observed transverse displacement $\xi$ was compared with that computed under the influence of the destabilizing force per unit length,

$$F_1 = \pi a^2 \rho \gamma_1^2\ \xi \quad \text{(4)}$$

($\rho$ is the maximum plasma density), and the constant force $F_{1,0}$. Initial conditions of the computation were chosen to reproduce the unstable motion alone, assuming that the instability term had the same growth rate as that measured when the $\mathcal{L} = 1$ fields were applied alone. In Fig. II-28, the data points represent typical measurements of plasma displacement perpendicular to the

30

$t = 2 \ \mu \sec$

$\ell = 1$
$t = 4 \ \mu \sec$

$\ell = 0, 1 \uparrow$
$t = 4 \ \mu \sec$

$\ell = 0, 1 \leftarrow$
$t = 4 \ \mu \sec$
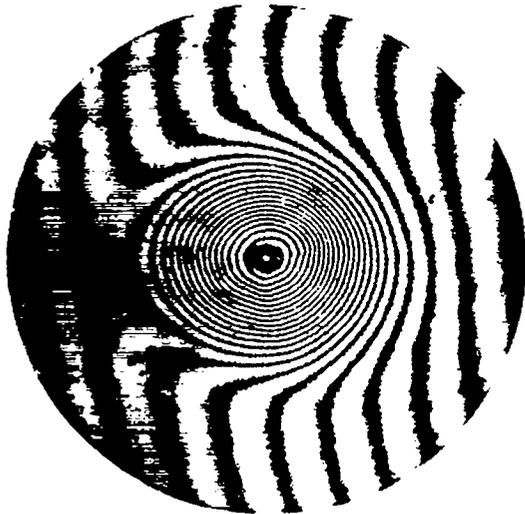
*Fig. II-25.*

*End-on interferograms of the cases shown in Fig. II-24. The upper-left interferogram shows the plasma position at early times in all three cases. The other three interferograms show the plasma position at a later time. Application of the main compression field is at time t = 0.*

compression-coil feed slot for the case where $\beta = 0.88$ and the applied $F_{1,0}$ was vertically upward. The computed motion represents the best fit under the assumption that $F_{1,0}$ is proportional to $(\delta B_0/B_0)B_r/B_0$. The result is

$$F_{1,0} = (1.01 \pm 0.15) \times 10^8 \ (\delta B_0/B_0)(B_r/B_0) \text{dyne/cm.} \quad (5)$$

The sensitivity of this computed trajectory to variations in turn-on time and magnitude of the $\ell = 0$ field was examined. For the case shown in Fig. II-28, an additional delay of 1 $\mu$sec in turn-on time of the $\ell = 0$ field resulted in failure to turn the plasma trajectory from the direction with the instability force alone. Variations in magnitude

31
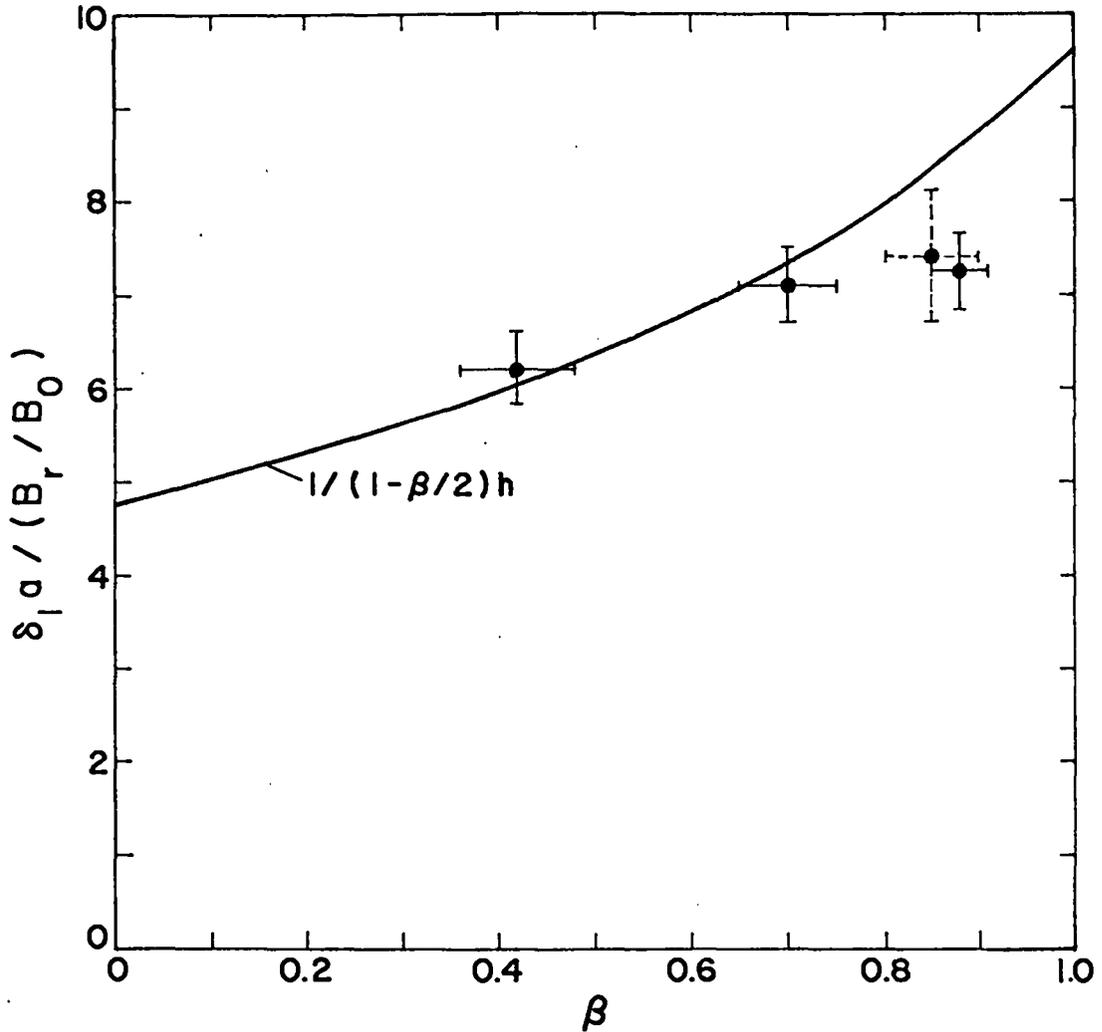
*Fig. II-26.*

*Comparison of the magnitude of the helical shift $\delta_1$ with sharp-boundry theory.*

of the $F_{1,0}$ force as small as 5% caused the trajectory to deviate observably from the experimental points.

Equation (5) is compared with the theoretical expression

$$F_{1,0} = [\beta(3 - 2\beta)/8] B_0^2 h^2 a^3 \delta_1 \delta_0 \text{, (ha} \ll 1) \tag{6}$$

using the measured maximum value of $\beta$ on axis and the value of plasma radius which, using the density on axis, reproduces the observed line density. When, in addition, the measured relation between $\delta_1$ and $B_r/B_z$ is used, Eqs. (6) and (5) give

$$\delta_0 = (4.2 \pm 0.6) \delta B_0/B_0 \text{ .} \tag{7}$$

Sharp-boundary theory[6] gives

$$\delta_0 = (ha)^{-2}(I_0 K_0)^{-1} [1 - (1 - \beta)I_0 K_0'/I_0^1 K_0]^{-1} \delta B_0/B_0$$

$$= 4.5 \, \delta B_0/B_0 \text{ ,} \tag{8}$$

where the argument of the modified Bessel functions is ha.

Similar analysis was performed for the other $\beta$ values. To a close approximation, for small ha, Eq. (8) may be written

$$\delta_0 = \frac{\delta B_0/B_0}{2(1 - \beta)} \text{ .}$$

32
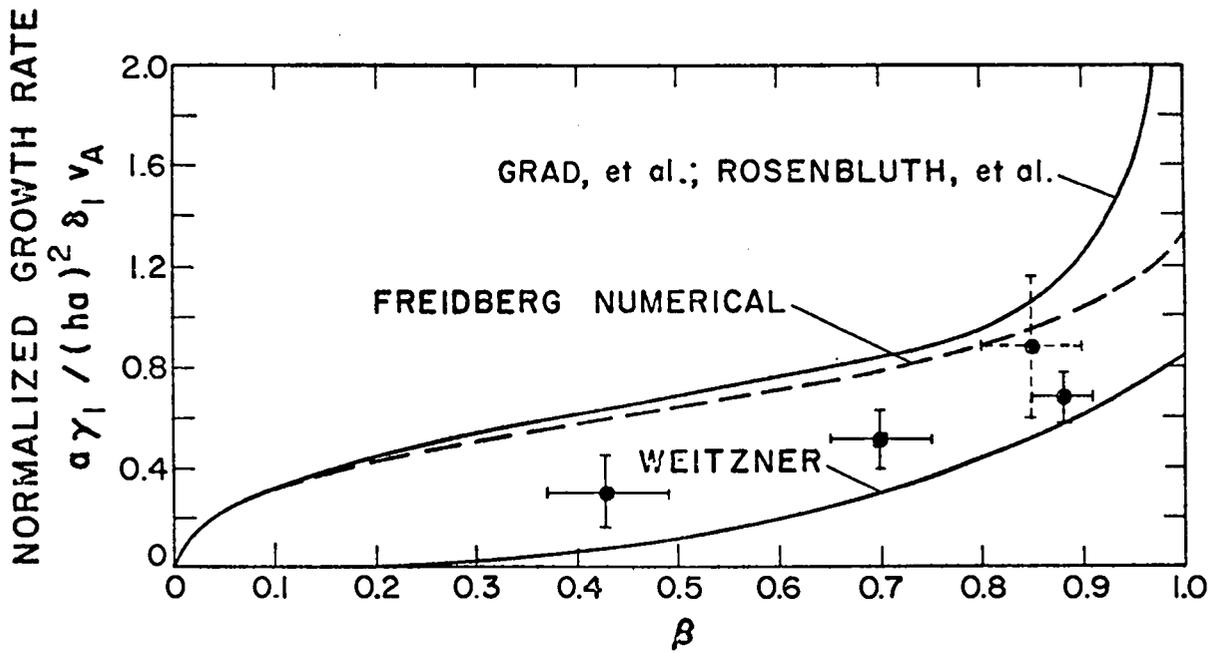
*Fig. II-27.*

*Comparison of observed m = 1 growth rate excited by ℓ = 1 coils with various ordering results of the MHD, sharp-boundary theory. In the Weitzner case $\epsilon = ha = 0.147$ and $\delta_1 = 0.7$.*
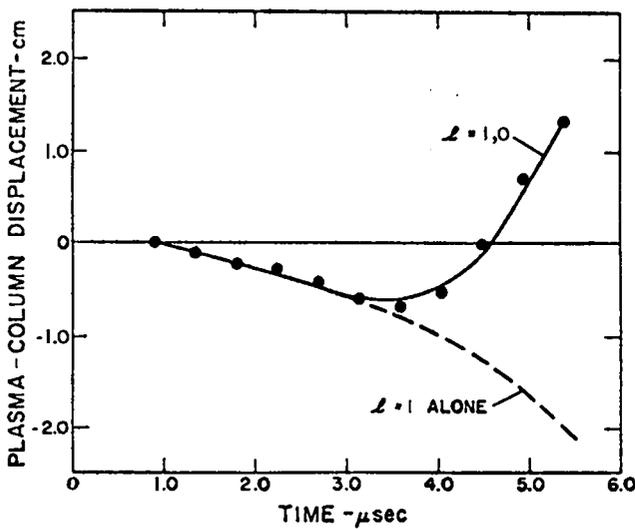


*Fig. II-28.*

*Computed plasma transverse motion under the influence of ℓ = 1 fields alone and for the ℓ = 1,0 field combination, compared with data points representing measured plasma displacement as a function of time.*

The measured force values are thus compared with sharp-boundary theory[6] in Fig. II-29 by plotting $\delta_0/(\delta B_0/B_0)$ vs $\beta$ and comparing the experimental values with the curve $1/[2(1-\beta)]$.
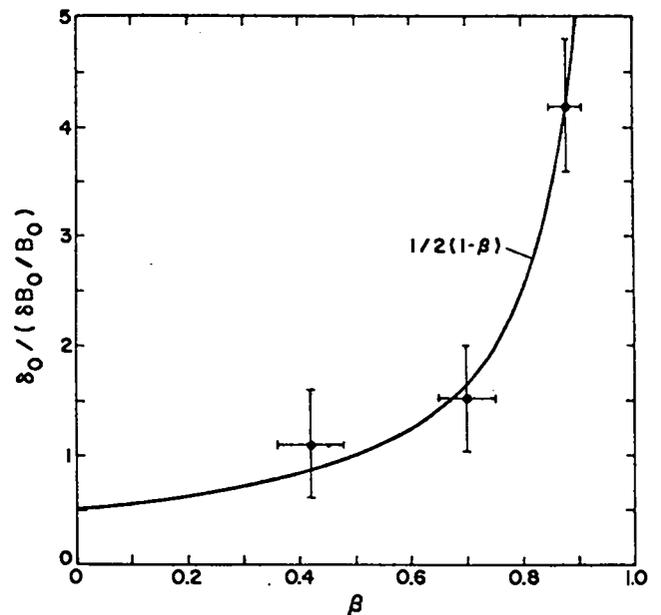


*Fig. II-29.*

*Comparison of $\delta_0$ with sharp-boundary theory.*

Recent theoretical results with a diffuse boundary profile[13] indicate that the sharp-boundary relationship is not accurate for large $\beta$ (a similar deviation is noted in the sharp-boundary theory for $\ell = 1$ in Fig. II-26). However, when the experimental value for $\delta_1$ is used, the sharp-boundary theory seems to predict the interference force accurately. Also in agreement with theory, the dominant instability generated by the $\ell = 1$ fields is $k \approx 0$, $m = 1$. The $\ell = 0$ field used here does not generate an observable instability. Sharp-boundary theory[6] is in agreement with this result since the field variation, $\delta B_0/B_0 = 0.015$, is too small to generate an instability that could be observed in the time interval ($\sim 5.5$ $\mu$sec) before end effects start to affect plasma motion.

## References

1. C. R. Harder, F. L. Ribe, R. E. Siemon, and K. S. Thomas, Phys, Rev. Letters 27, 386 (1971).

2. A. A. Blank, H. Grad, and H. Weitzner, in *Plasma Physics and Controlled Nuclear Fusion Research* (International Atomic Energy Agency, Vienna, 1969), Vol. II, p. 607.

3. M. N. Rosenbluth, J. L. Johnson, J. M. Greene, and K. E. Welmer, Phys, Fluids 12, 726 (1969).

4. H. Grad and H. Weitzner, Phys. Fluids 12, 1725 (1969).

5. J. P. Freidberg and B. M. Marder, Phys. Fluids 14, 174 (1971).

6. F. L. Ribe and M. N. Rosenbluth, Phys. Fluids 13, 2572 (1970).

7. H. Weitzner, Phys. Fluids 14, 658 (1971).

8. R. F. Gribble, W. E. Quinn, and R. E. Siemon, Phys. Fluids 14, 2042 (1971).

9. R. F. Gribble, E. M. Little, R. L. Morse, and W. E. Quinn, Phys. Fluids 11, 1221 (1968).

10. G. A. Sawyer, V. A. Finlayson, F. C. Jahoda, and K. S. Thomas, Phys. Fluids 10, 1564 (1967).

11. E. M. Little, W. E. Quinn, F. L. Ribe, and G. A. Sawyer, Nucl. Fusion Suppl. Pt. 2, 497, (1962).

12. R. E. Siemon and H. Weitzner, Bull. Amer. Phys. Soc. 15, 1479 (1970).

13. H. Weitzner, Bull. Amer. Phys. Soc. 16, 1255 (1971).

## E. The $\ell_{1,0}$ Coil System for Scyllac and Scylla IV (W. H. Borkenhagen, W. K. Ellis, H. W. Harris, and E. L. Zimmermann)

Scyllac equilibrium is established by the addition of small ($\leq 10\%$) $\ell = 1$ and $\ell = 0$ fields to the main $\theta$-pinch field $B_0$. The $\ell = 1$ field in the 5-m toroidal sector is provided by 15 $\ell = 1$ coils of length 33-1/3 cm, energized by an external capacitor bank and fed individually by $SF_6$-pressurized junction boxes. Similar coils of 30-cm length are used on the Scylla IV-experiment. Figure II-30 shows a cross-sectional view of the Scylla-IV installation, including $\ell = 0$ coils.

Each $\ell = 1$ coil consists of a pair of helical bifilar windings which are electrically insulated from their surroundings with thermal bonding Mylar tape and encased in a fiberglass and epoxy support structure (which also helps the insulation problem). Figure II-31 shows a pair of toroidal coils used in Scyllac.

The $\ell = 0$ field for toroidal equilibrium is provided in the Scyllac experiment by annular grooves in the compression coil wall, which acts as an axial flux conserver. The grooves are filled with fabricated Inconel
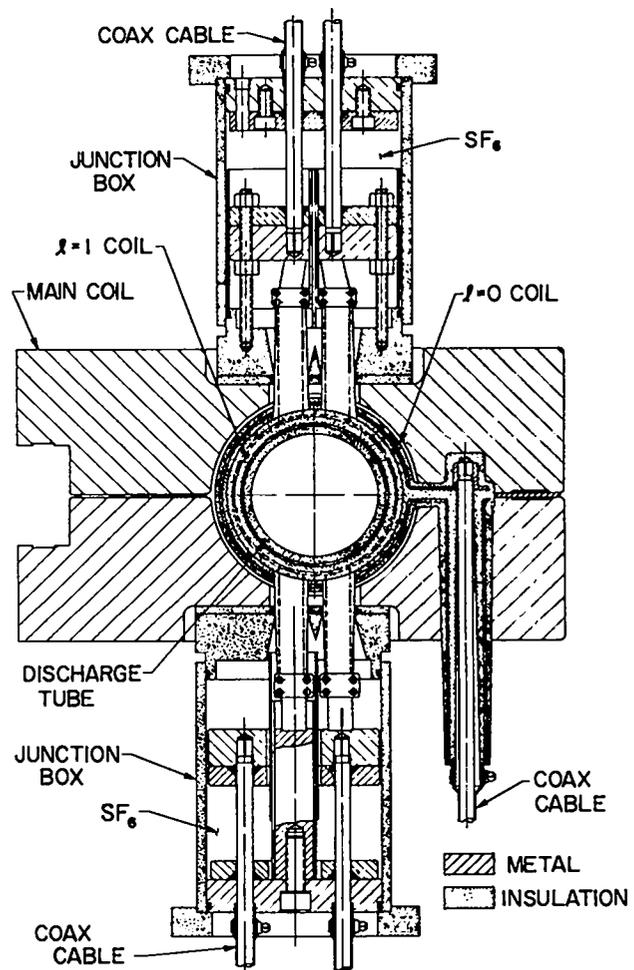


*Fig. II-30.*

*The $\ell_{1,0}$ coil system installed on Scylla IV.*

*Fig. II-31.*
*Scyllac $\ell = 1$ coils.*

inserts, shown in Fig. II-32, which serve to delay penetration of $B_0$ for $\sim 1/2 \, \mu sec$, permitting a smooth implosion.

The $\ell = 0$ field in Scylla IV is produced by driven $\ell = 0$ coils, four per $\ell = 1$ wavelength, which provide an additional degree of control for feedback experiments. Special $\ell_{1,0}$ modules, shown in Fig. II-33, have been developed for this application. Future feedback

experiments on Scyllac are expected to require similar units.

An extensive electrical testing program was needed to arrive at a final design for the various coils described above. All are now operating satisfactorily on the Scyllac and Scylla IV experiments, having survived several hundred shots without a failure on either machine. Pulsed voltage and hold-off in excess of 120 kV has been measured in the case of the Scyllac coils.

A detailed description of the $\ell = 1$ and $\ell = 0$ coil systems, including theory of operation, methods of fabrication and testing, and external electrical circuits has been published (November 1971) as Los Alamos Scientific Laboratory report LA-4815-MS.

## F. Modeling Experiments (W. R. Ellis and E. L. Zimmermann)

A detailed program of modeling measurements has been carried out during this report period to investigate the field structure and scaling laws for the $\ell = 1$ and $\ell = 0$ fields. In the Scyllac and Scylla IV experiments, these fields are generated by helical conductors, annular coils, and flux shapers, and differ in their spatial distributions and harmonic content from ideal (i.e., purely sinusoidal) $\ell = 1$ and $\ell = 0$ fields. The relevant vacuum fields have been measured *in situ* on Scyllac and Scylla IV, and in more detail in a linear, radially full-scale Scyllac model of 1-m length.

Figure II-34 shows one period of the theoretically predicted "flat-topped" $\ell = 0$ bumpy field generated on-axis by the annular grooves used in Scyllac. Also shown is its decomposition into Fourier components. Only $\cos(2n-1)hz$ terms appear, and in the "ideal" case only the $a_1 \cos hz$ term would occur.

Figure II-35 shows a similar analysis of the $B_z$ waveform measured experimentally on the Scyllac model. We see there is a richer Fourier spectrum than predicted by theory, although some of the harmonic content, in particular the $\sin nhz$ terms, are probably due to end effects.

Figure II-36 shows a typical sample of the vertical $B_r$ field generated on-axis by the bifilar $\ell = 1$ coil as measured in the Scyllac model. Measurements made on Scyllac itself are very similar. In the case of $B_r$, end effects are negligible; the obvious asymmetry is due to an axial variation in the $\ell = 1$ image currents caused by the presence of the $\ell = 0$ grooves in the compresison coil wall. Recent modeling measurements indicate that this undesirable z dependence in the $\ell = 1$ field (and hence in the $F_{1,0}$ restoring force) can be greatly reduced or eliminated by the use of specially designed inserts, which, in effect, act
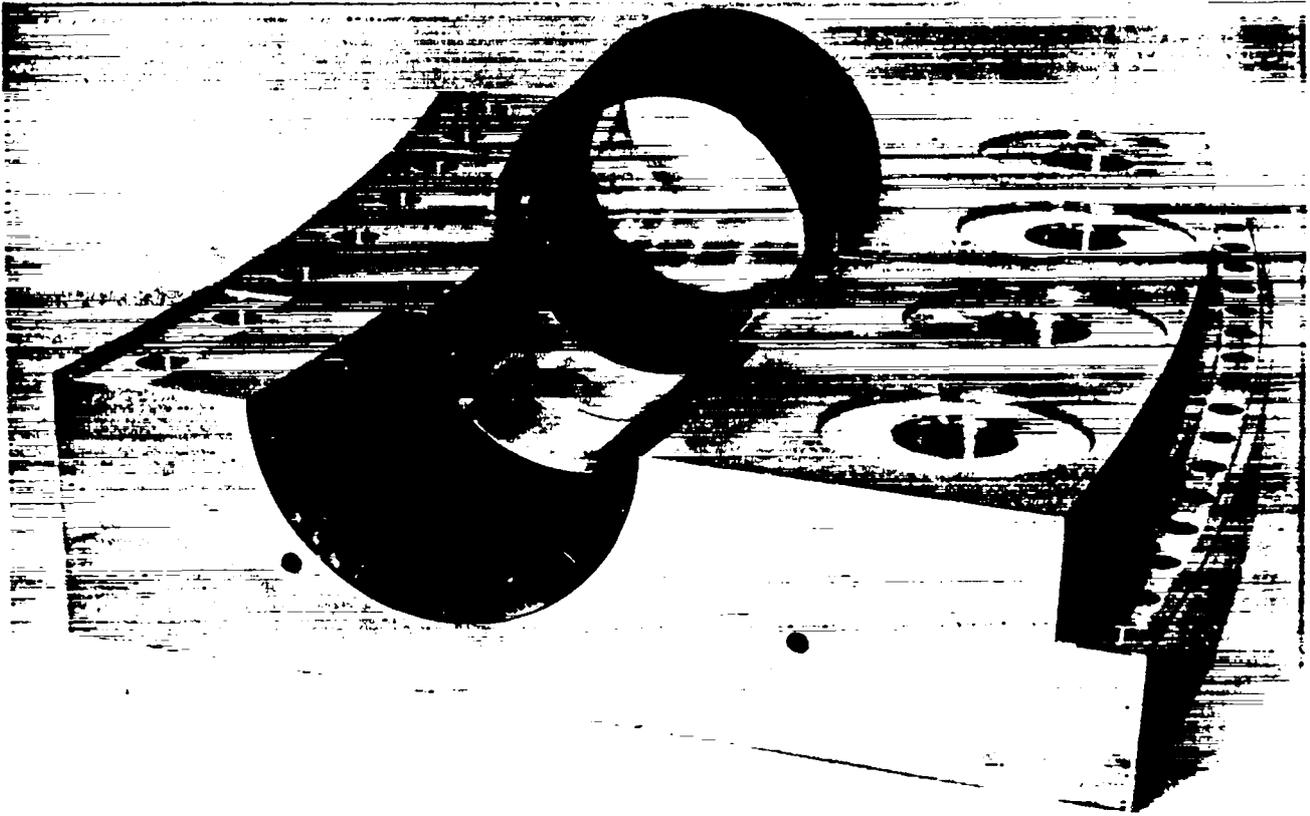
*Fig. II-32.*
*Scyllac ℓ = 0 Inconel inserts in compression coil.*

as a "pseudo wall" for the image currents. An "ideal" ℓ = 1 field would contain only the $b_1$ sin hz term.

An LA report on these modeling measurements in detail is being prepared.

### G. ℓ = 0 Feedback System for Scylla IV-3 and Scyllac (R. F. Gribble S. C. Burnett, D. L. Call, A. S. Rawcliffe, and K. Thomas)

An ℓ = 0 MHD feedback experiment to control the m = 1 mode on a plasma column subject to ℓ = 1 helical fields is nearly implemented. Feedback stabilization will first be tried on a linear θ pinch (Scylla IV-3) and then on the toroidal Scyllac sector.

The feedback system has three basic components: a position detector, a signal processor, and a power amplifier. All components are designed and the first units have been built. The system is being installed on Scylla IV-3 for testing under actual plasma conditions.

The installation of filament power and deionized water is proceeding on schedule and the first

power-amplifier module is assembled and ready for initial checkout at Scylla IV-3. The experiment will initially use 10 power modules to drive the ℓ = 0 coils and is designed for extension to 20 modules if necessary.

**1. Position Detector.** The detection system used to sense plasma position for feedback stabilization must meet 2 requirements: 1) accurate tracking of plasma column displacements; and 2) fast response of the position sensing system with respect to the risetime of the feedback amplifiers. In addition, it is desirable for the position-sensitive signal to be linear over a wide range of plasma displacements.

Early system designs were capable of a linear response in detecting a wide range of plasma displacements, but the high, intrinsic resistance of the detector used restricted the detection system to risetimes greater than 0.5 $\mu$sec. Current designs incorporate 10-nsec-risetime, bi-cell silicon detectors that can accurately detect plasma motions ranging from < 1mm to approximately 1 cm off axis.

36
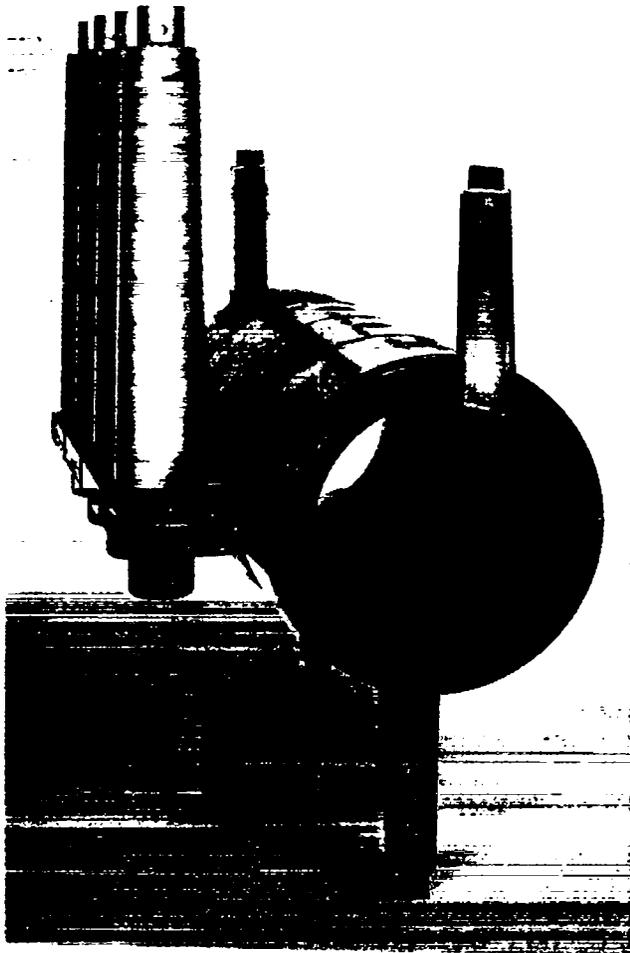
*Fig. II-33.*
*Scylla IV $\ell_{1,0}$ feedback module.*

A United Detector Technology pin-spot two-dimensional detector and a Solid State Radiations bicell detector have been used with a fast amplifier to sense the position of the Scyllac and the Scylla IV-3 plasma columns. The optics of the detection system are arranged to focus the image of the plasma column (diameter ~ 2.5 cm) to ~ 75% of the size of one element of the bi-element detector (for the UDT-2D, image diameter ~ 1 mm). The position is then determined by observing the difference in the currents ($\Delta$ signal) in the two elements of the detector. The sum of the detector currents ($\Sigma$ signal) is also monitored for the purpose of normalization. If the luminosity of the plasma column were rectangular in profile, then the position response of the bi-cell detector would be linear until the column moved one

plasma radius off center, after which a constant difference signal would be observed. However, the profile of the plasma luminosity is Gaussian and the response of the bicell detector is thus only approximately linear for motions less than 0.7 times the plasma radius. For the feedback problem, this degree of linearity is sufficient.

On recent Scyllac experiments, a pellicle mirror was placed in front of one of the streak cameras, and the position detector, along with its associated electronics and optics, was positioned to observe the 10% of plasma light reflected from the mirror. The detector signals are compatible with the simultaneous streak photographs.

It should be emphasized that the purpose of the position detector in the feedback system is to detect small shifts from the equilibrium plasma position, a task that the present system does quite well.

Figure II-37 is a drawing of the optical setup at Scylla IV-3. The geometry was necessitated by space limitations and has been a slight disadvantage in optical alignment; the entire optical system can be moved to look at the equilibrium position the plasma assumes due to the $\ell = 1$ helical shift.

2. Signal Processing Unit. The intermediate amplifiers connected between the position sensors and the power modules may more properly be called signal processors since they normalize the sensor output, add damping and filtering to the signal with remote control of gain and damping, and provide a clamp for setting the equilibrium value of the plasma position. Figure II-38 shows a block diagram of this unit which is mounted in a double shielded enclosure with its own power supply.

The remote control of gain and damping is obtained from an integrated circuit multiplier with modified external circuitry to provide a 15-nsec risetime. Output amplitude and scale factor were sacrificed to improve the risetime.

The normalization circuit employs an integrated circuit in the feedback path of a fast amplifier to achieve analog division. Here division accuracy was sacrificed to obtain sufficient speed of response. Where $\Delta$ is the difference between the sensors outputs and $\Sigma$ is the sum, the circuit output is given by $0.6\Delta/(\Sigma - 0.08)$V. The range of $\Sigma$ signals will be between $-0.05$ and $-1.0$ V with an obvious error of 50% for $\Sigma = -0.08$ V. For $\Sigma = -0.05$ V the output risetime is 50 nsec, decreasing to 15 nsec for $\Sigma = -1.0$ V. The circuit is unstable for negative $\Sigma$ signals (the detectors are negatively biased so that the $\Sigma$ signal is positive) and for $\Sigma > 1.1$ V.

The equilibrium selector performs two functions: 1) it gates off the signal from the position detector during the first 2 $\mu$sec of the discharge while the plasma column is being established; and 2) it electronically selects the actual plasma position at the time the gate is opened as the null position for feedback.

(AMP. = 100%)

$a_1 \cos hz$
(106%)

$a_3 \cos 3hz$
(6.3%)

$a_5 \cos 5hz$
(0.35%)
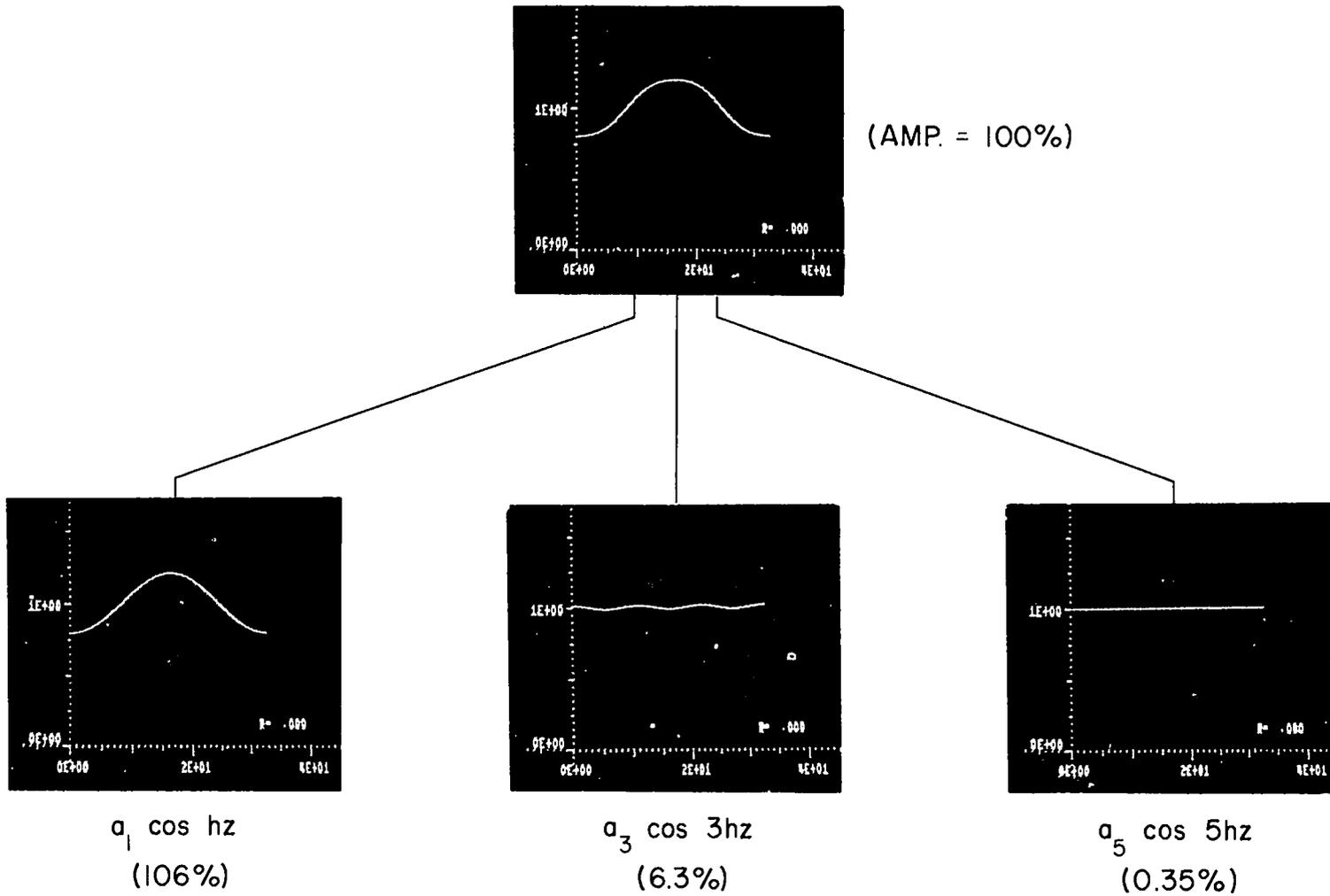
$B_z$—FOURIER COMPONENTS OF THEORETICAL
SCYLLAC $\ell = 0$ WAVEFORM, r = 0 cm

Fig. II-34.
Scyllac $\ell = 0$ waveform, theoretical.
(Fourier components of the axial field $B_z(z)$ on axis).

$B_r = B_x$
(EXP. AMP. = 100%)

| $a_0/2$ | $a_1 \cos hz$ | $a_2 \cos 2hz$ | $b_1 \sin hz$ | $b_2 \sin 2hz$ | $b_3 \sin 3hz$ |
| (1.5%) | (99%) | (0.94%) | (3%) | (4.7%) | (0.02%) |
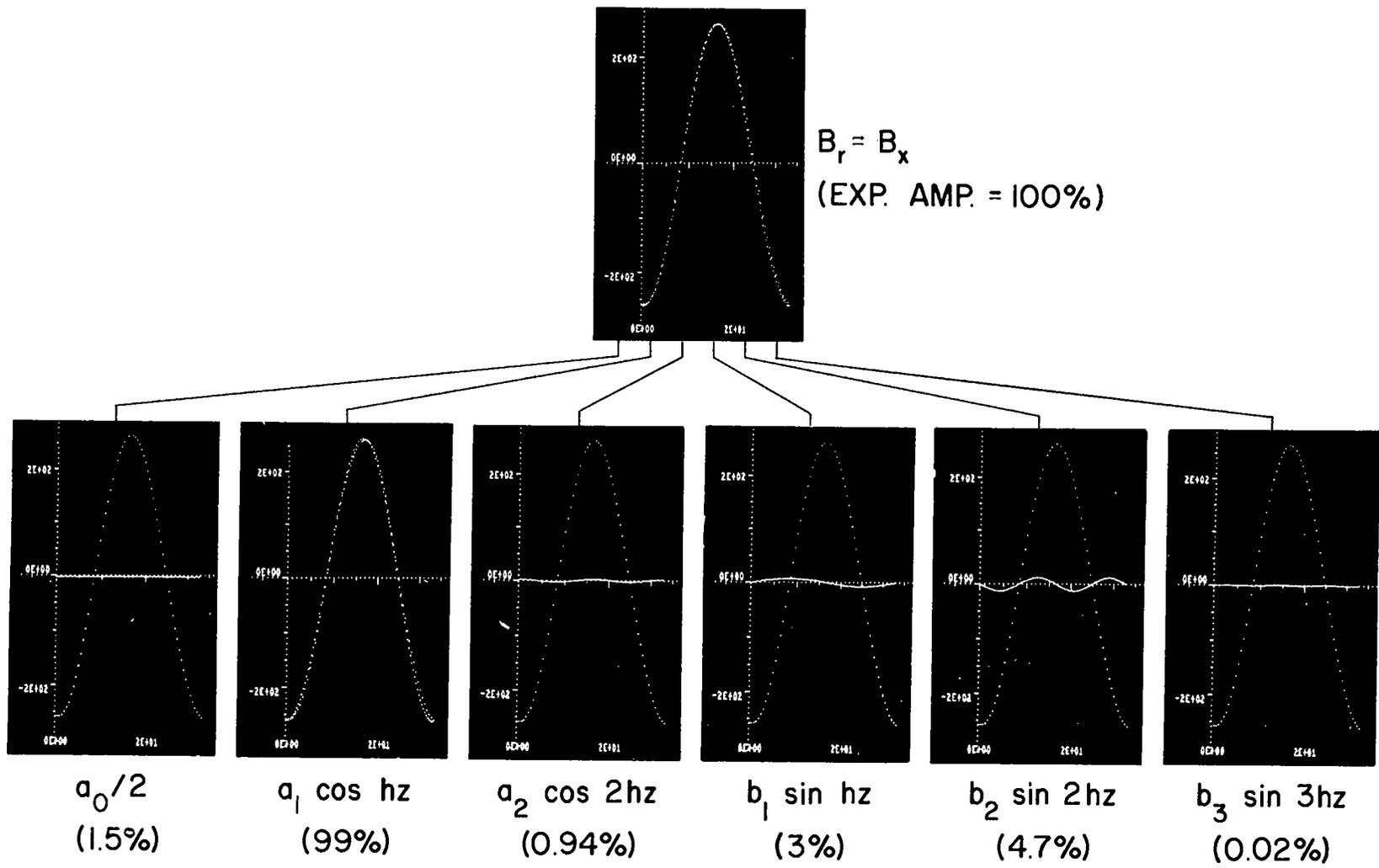
$B_x$—FOURIER COMPONENTS OF $\ell = 1$ PROBE DATA (SCYLLAC MODEL)

$\theta = 0°, \quad r = 0$ cm

Fig. II-35.
*Scyllac $\ell = 0$ waveform, experimental.*
*(Fourier components of the axial field $B_z(z)$ on axis)*

$B_r = B_y$
(EXP. AMP. = 100%)

$a_0/2$ (8.2%)

$b_4 \sin 4hz$
(0.61%)

$a_1 \cos hz$
(3.7%)

$a_2 \cos 2hz$
(6.1%)

$a_3 \cos 3hz$
(0.41%)

$b_1 \sin hz$
(84%)

$b_2 \sin 2hz$
(1.4%)

$b_3 \sin 3hz$
(1.6%)
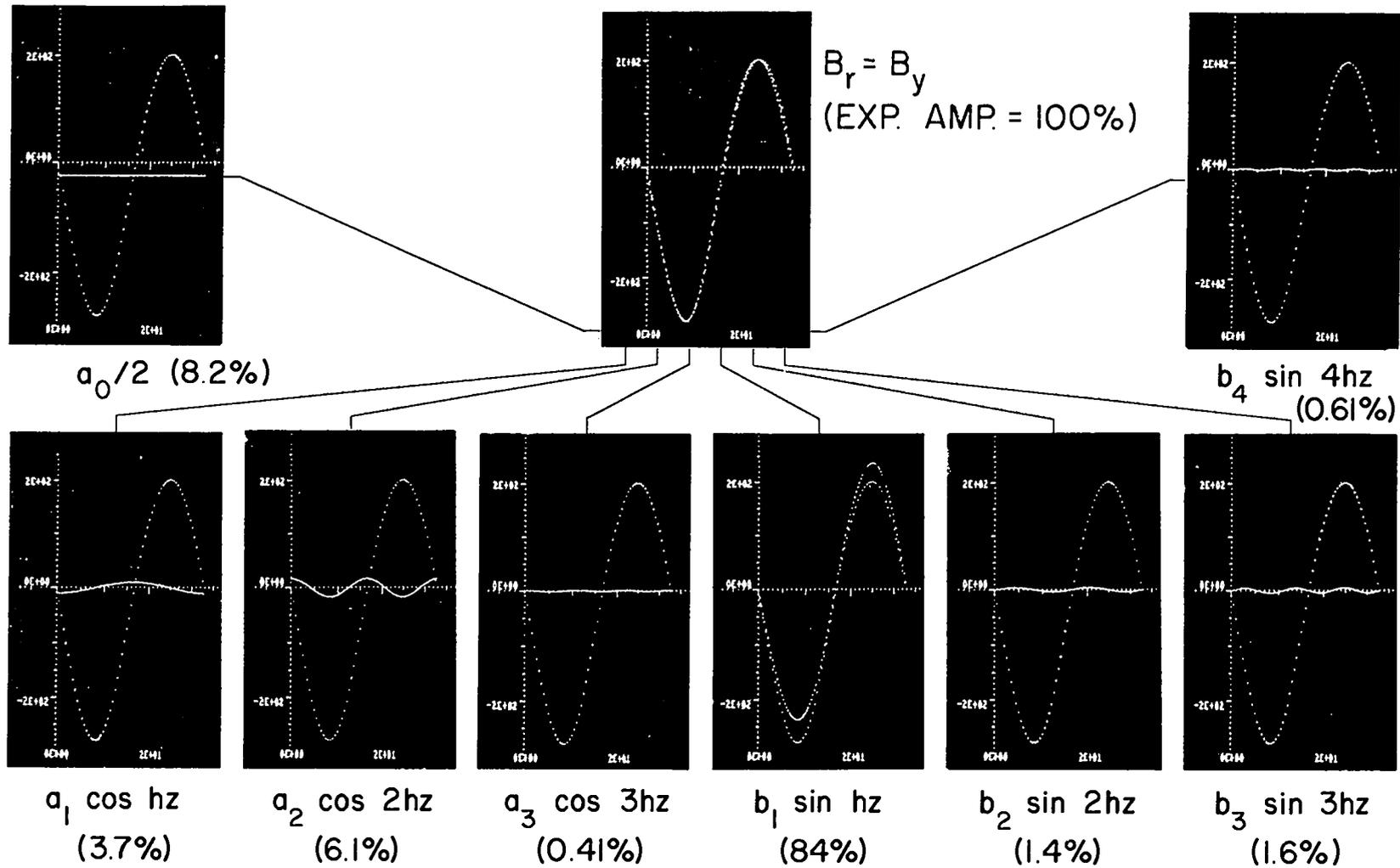
$B_y$—FOURIER COMPONENTS OF $\ell = 1$ PROBE DATA (SCYLLAC MODEL)

$\theta = 0°$, r = 0 cm

Fig. II-36.
Scyllac $\ell = 1$ waveform, experimental.
(Fourier components of the vertical field $B_y(z)$ on axis)
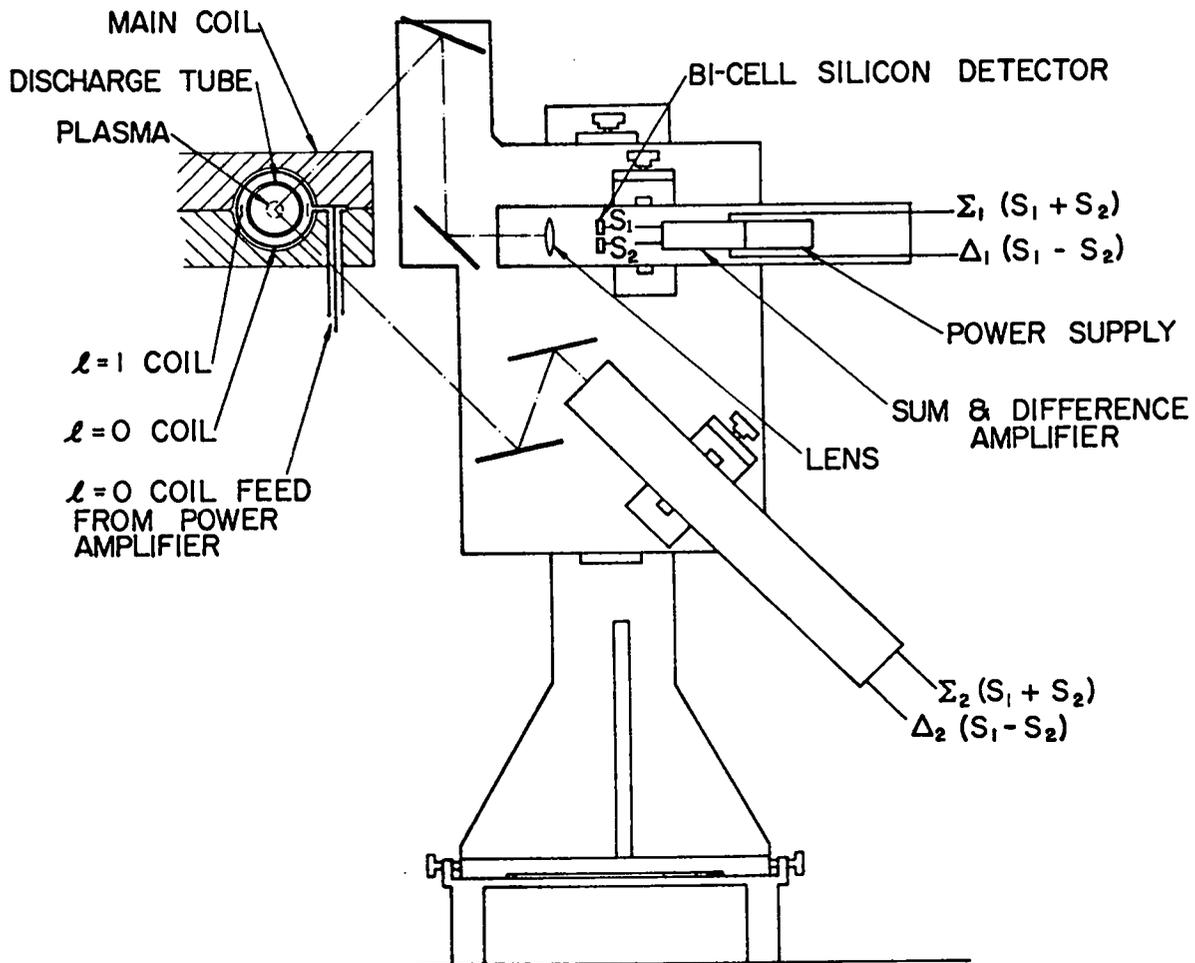
*Fig. II-37.*
*Schematic of position-sensing system for feedback stabilization.*

### 3. Power Amplifier.

*a. The ML 8618 Power Tubes.* The 70 ML-8618 power vacuum tubes that were ordered for the system have all been purchased and tested. Three were rejected because of mechanical shorts from grid to cathode. Each of the power tubes must have ten to fifty hours of aging under high-current pulsing to satisfy our requirements. These are: that each tube must operate for at least 15 min without arcing at 35-kV plate voltage and 9.0 VAC filament voltage (7.5 VAC is the rated value), while being pulsed to 600 A for 10 $\mu$sec at 5 pulses per second with a 10-ohm load.

*b. Power Supply System.* Power supply controllers which utilize saturable reactors driven by simple, solid-state amplifiers were designed. The controller provides feedback current limiting, accurate voltage regulation, power supply crowbarring following a tube arc, and programmed rate of voltage rise following an arc. The arc detector that triggers the crowbar initiates the automatic power supply shut-down and restart sequence.

*c. The ML-8618 Driver Amplifier.* The ML-8618 grid drive amplifier, (Fig. II-39), has an output of 7.5 kV at 30 A for an input of 10 V. There is also a delay of 0.15 $\mu$sec from input to the output start. The 0.1-$\mu$sec risetime for the ML-8618 grid-drive amplifier is satisfactory since for a step input the load-current risetime with the $\ell = 0$ coils would be greater than 0.1 $\mu$sec, determined by the minimum practical load inductance and the maximum usable ML-8618 plate voltage. A major problem in the design was the output coupling transformers.

DC CONTROL

| SUM ($\Sigma$) | DIFFERENCE ($\Delta$) → NORMALIZATION UNIT $\Delta/\Sigma$ |

Figure labels: $\xi$ → REMOTE GAIN ADJUST → $\alpha_1\xi$ → X 3 GAIN AMPLIFIER → $\alpha_2\xi$ → X 3 GAIN SUMMING AMPLIFIER → $\alpha\xi + \beta\xi$

$\xi$ → REMOTE GAIN ADJUST (DAMPING) → $\beta_1\xi$ → DIFFERENTIATOR X 3 GAIN → $\beta_2\xi$

DC CONTROL

$\alpha\xi + \beta\xi$ → EQUILIBRIUM SELECTOR → $\alpha\xi + \beta\xi \pm$ CONST. → 50 OHM LINE DRIVERS → 1 TO 15 OUTPUTS TO POWER AMPLIFIERS

TRIGGER

SIGNAL PROCESSING UNIT
FEEDBACK SYSTEM
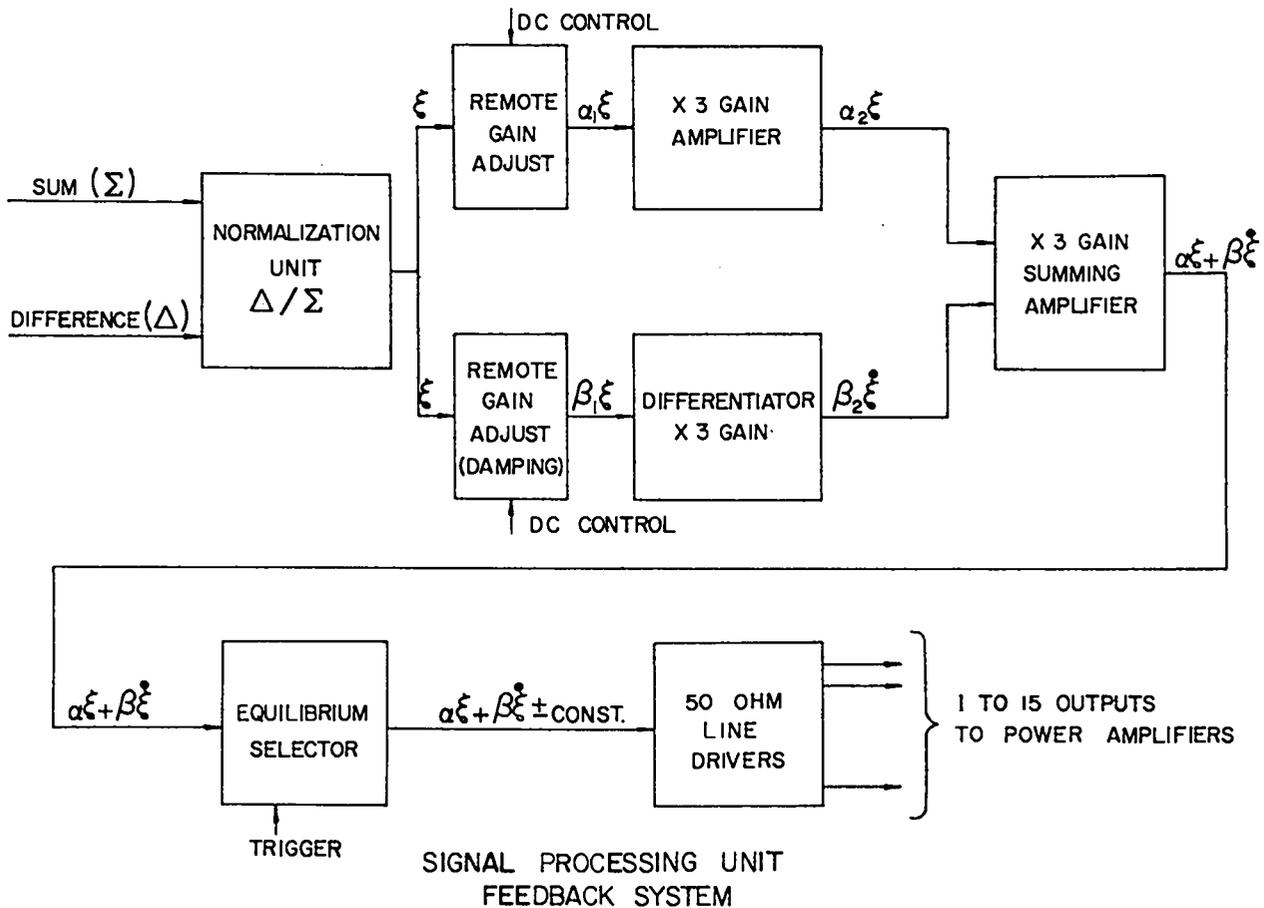
*Fig. II-38.*
*Block diagram of the signal-processing unit for feedback stabilization system.*

Fourteen transformers were wound before the optimum compromise between winding-to-winding capacitance and leakage inductance was obtained.

The amplifier consists of two independent vacuum-tube sections. The coupling transformers are biased so that smaller cores can be used for a given saturation time. A unity gain-phase splitter channels positive input signals to one amplifier and negative going input signals to the other. Each of the two-stage, transistor amplifiers provides 280 V at 1/4 A, 30-nsec risetime to the 4CX600J vacuum tubes stage. The transformer coupled 4CX600J output is 2.5 kV at 20 A. This drives the 3-100Z grid, which in turn drives an ML-8618 to 7.5 kV at 30 A. About 6 dB of negative voltage feedback is employed on each of the driver vacuum-tube stages and 3 dB of negative current feedback is used on the ML-8618 power-tube

stage. All of the vacuum tubes are pulse biased to a low conduction state 70 $\mu$sec before signal application. In addition, the ML-8618 tube grids are pulsed off after 100 $\mu$sec to reduce drain on the plate capacitor bank.

*d. The Power Module.* The power module contains prewired subassemblies for ease of module wiring and replacement. The transistor stages and their associated dc power supplies are mounted in separate, shielded plug-in boxes so that they can be replaced and repaired without removing the power module from the system. All components of the power module have been located in a 2 by 3 by 3 ft frame in such a manner that the dc voltage breakdown from the ML-8618 anode to the frame and components is greater than 60 kV. The oil-insulated, push-pull output transformer has also been

**SIGNAL PROCESSING UNIT**

SUM

∿ .1V

DIFFERENCE

10 V

LOW LEVEL AMPLIFIER

2 STAGE TRANSISTOR AMPLIFIER AND PHASE SPLITTER

VACUUM TUBE DRIVER

I ST STAGE
2
4CX600J

2 ND STAGE
2
3-1000Z

ML8618

ML8618

POWER AMPLIFIER

+35 kV

ℓ = 0 COILS

FEEDBACK AMPLIFIER AND LOGIC SYSTEM
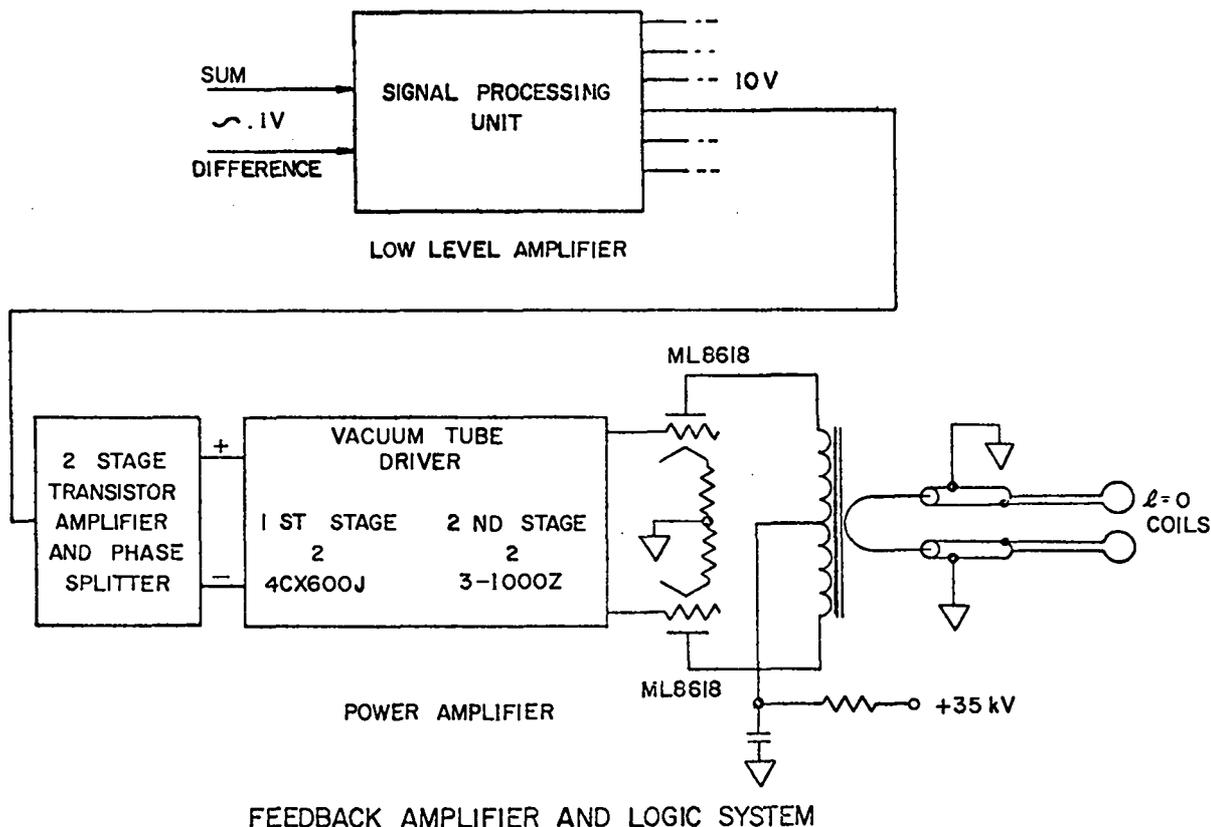
*Fig. II-39.*
*Block diagram of the power amplifier and logic system for the feedback stabilization system.*

breakdown-tested to 100-kV dc. With a one turn strap secondary, the output transformer primary turns can be selected to trade-off output current for rise time from 35 kA at 0.3-$\mu$sec risetime to 7 kA at 1.2 $\mu$sec.

Figure II-40 shows the response of the module for 9.0 V on the 8618 filaments and 30 kV plate voltage. The top trace of each exposure is the input to the module at 5 V per cm. At 2000 A per cm, the lower traces show the module output with two sets of 12, 14-59 cables of 21-ft length. Subsequent models will use 32 cables rather than 24. Each set is terminated in a dummy load of about 0.1 nH. The turns ratio of the output transformer is 5:1. Obviously, the 8618 tubes are not matched and are highly nonlinear. We may add diode compensation circuits for each tube to improve linearity. The oscilloscope beams were aligned to show approximately the time relation between input and output. The actual delay from input to the start of output current is about 0.2 $\mu$sec. A more accurate value is yet to be determined.

*e. The Control System.* Wiring of the module power supply control system has begun. A temporary control system will be used on Scylla IV until the large control system is completed. In the large system, variable 8618 power tube filament voltage will be obtained from motor-driven variable transformers. A newly designed integrated circuit operational amplifier meter relay circuit will control the operating filament level. The 40 kV, 8618 plate power supply will be voltage-regulated with variable current limiting by a saturable reactor driven from a recently designed 100-W transistor-integrated circuit operation amplifier controller.

**H. Linear Scyllac Installation and Testing (C. R. Harder, H. W. Harris, and A. S. Rawcliffe)**

Construction work on the seven-rack linear experiment will be completed in December.
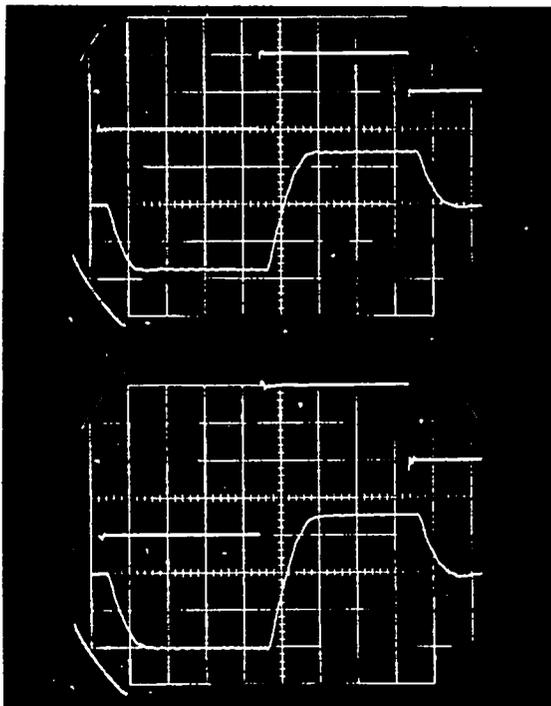
*Fig. II-40.*
*Response of power module for ML 8618 filament*
*voltage of 9.0 V. Time scale is 1 μsec/cm. Upper*
*trace of each exposure is the input, 5 V/cm. Lower*
*trace is the output, 2000 A/cm. The time relation*
*between two beams is approximately correct.*

| | |
|---|---|
| No. P. I. bank capacitors | 5 |
| No. C/B bank capacitors | 24 |
| No. primary bank capacitors | 210 |
| Rack capacitance (primary) | 390 $\mu$F |
| Energy stored (primary) at 55 kV | .59 MJ |
| Inductance (P.I. system) | 46.1 nH |
| Test coil inductance | 10.9 nH |
| Inductance (primary system) | 5.1 nH |
| $\tau/4$ (primary) | 3.9 $\mu$sec |
| C/B e-folding time | 120 $\mu$sec |
| Peak $B_z$ field at 55 kV | 85 kG |
| $B_z$ crowbar modulation | 8 % |

Plasma experiments will start in late January 1972 as soon as checkout of the first five racks is finished. Checkout of the two mirror racks will continue during evenings while these first experiments are going on.

Checkout of the linear system has been proceeding rack-by-rack since August on four-hour evening shifts to avoid interference with the construction crews' working days. Checkout of the first four of seven racks has proceeded faster than expected and component failures have been very low. This favorable experience is attributed in part to improvements made in the system based on experience with the toroidal sector. Some of the improvements made and the general method of checkout are described in the last annual report (LA-4585-MS).

A summary of component failures during checkout of the first four racks is as follows: 10 capacitors, 11 spark gaps, 13 source cables, 10 trigger cables, 2 pulse charge cables, 3 pulse transformers, and 1 load cable.

Cable lengths and coil diameters differ slightly from those in the toroidal sector. The parameters for each rack of the linear Scyllac experiment are:

I. Applied Diagnostics on the Toroidal Sector (S. C. Burnett, W. R. Ellis, F. C. Jahoda, and R. E. Siemon)

The diagnostics used in the initial operation of Scyllac are well-established $\theta$-pinch techniques chosen to provide measurements of the most needed parameters. Desirable techniques requiring time-consuming innovations such as side-on interferometry at 10.6 $\mu$ or side-on Thomson scattering are at various stages of development.

1. Coupled-Cavity Interferometry for Density. A coupled-cavity He-Ne laser interferometer operating at a wavelength of 3.4 $\mu$ was used to measure the time history of electron density integrated along a given line of sight across the quartz discharge tube. Its design, shown schematically in Fig. II-41, is such that this line can be through the axis or along a chord as much as 2-cm off axis. The standard mode of operation was to use a moving corner mirror in the external cavity and to measure the time distortions in the regular mirror modulation periodicity of the laser output to determine the line-integrated plasma density.

2. Double Loop for Excluded Flux Measurements. Double loops arranged as shown in Fig. II-42 provided measurements of flux excluded by the plasma column. Combined with density profiles from luminosity and the assumption of a uniform temperature, the excluded flux could be expressed in terms of the plasma $\beta$.

The loop and probe were arranged so that their difference without plasma was nearly zero. In the presence of plasma the additional difference was proportional to the excluded flux. Typical data are given in Fig. II-43 where the vacuum and plasma results are compared.

3. Luminosity for Determining Density Profiles. Using the optical arrangement shown in Fig. II-44, it was possible to measure the plasma luminosity along ten parallel chords as a function of time. After Abel inversion of

COUPLED-CAVITY INTERFEROMETER

ROTATING WHEEL

THETA PINCH COIL

QUARTZ TUBE

HeNe LASER OPERATING AT 3.39μ AND .6328μ

MIRRORS FOR SCANNING TUBE

3.39μ FILTER

In As DETECTOR

TO PRE-AMP + SCREEN ROOM
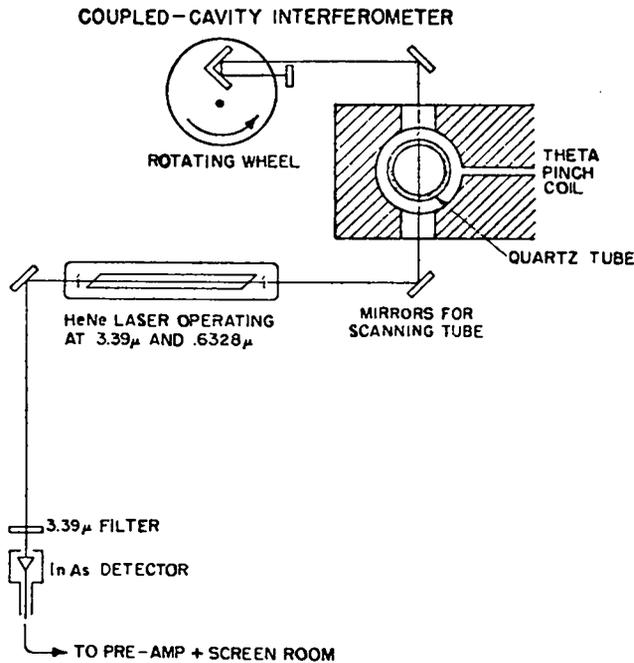
*Fig. II-41.*
*Schematic of coupled-cavity interferometer.*

the data, a relative plasma density profile was determined. The profiles were used in conjunction with the coupled-cavity interferometer to determine absolute density and with the excluded flux to determine plasma $\beta$. The absolute density and $\beta$ measurements were then used to determine plasma temperature through pressure balance with the external field.

Figure II-45 indicates the voluminous data that could be obtained on a single discharge. At various instants of time, the ten channels were digitized and fed to the Scyllac computer for Abel inversion and curve fitting. Additional pulses, which are light signals recorded 250 $\mu$sec before each discharge from an auxilary optical system can be seen on the oscilloscope traces. These calibrate the relative channel sensitivities.

## J. Two-Dimensional Interferometry with a Pulsed 10.6-$\mu$m Laser (P. R. Forman, F. C. Jahoda, and R. W. Peterson)

A simply constructed $CO_2$ TEA (Transverse Excitation Atmospheric) laser has been used for making space-resolved, end-on interferograms of the refractivity due to the free electron density of a short $\theta$-pinch plasma at late times during the discharge. For 10.6-$\mu$m radiation, a phase shift of $2\pi$ requires only $2 \times 10^{16}$ electrons/cm$^2$, a factor of 15 increase in sensitivity over interferograms made with a ruby laser as the light source.

The laser was designed to have a spatially uniform output with pulse energies in excess of one joule. An electrode configuration employing resistor-limited discharges was chosen because of its simplicity and consistent operation. The laser power supply is a 0.1-$\mu$F capacitor with a triggered spark gap. The optical cavity is formed by two 10-m radius mirrors. One of these is gold-coated beryllium copper and the other is a 65% reflecting germanium output mirror. With the capacitor charged to 40 kV, and a mixture of 90% He: 7% $CO_2$: 3% $N_2$ at local atmospheric pressure (650 Torr), the output energy is $2.4 \pm 0.1$ J. For a 92% He: 8% $CO_2$ mixture, the output is $0.9 \pm 0.05$ J. The removal of nitrogen has the previously observed effect of both reducing the amplitude of the gain-switched giant pulse and removing the slower (1 to 2 $\mu$sec) low-power secondary pulse. Since interferometry of $\theta$-pinch plasmas requires a submicrosecond pulse to prevent smearing out of the fringes, the work reported here required the use of the 0.9-J pulses without $N_2$ in the gas mixture. These have a 0.2-$\mu$sec half width.

The Mach-Zehnder interferometer shown in Fig. II-46 has been used in conjunction with the above laser to measure the electron density distribution in the Scylla 1A $\theta$ pinch. For these experiments, the quartz end windows were replaced with polished sodium chloride windows to allow the 10.6-$\mu$m radiation to traverse the plasma. Mirror $M_3$ approximately collimates the laser radiation. The beam splitters are germanium flats, anti-reflection coated on one surface. A NaCl lens images the central plane of the plasma onto the detector. Scylla IA produces a cylindrical plasma 20-cm in length with a peak electron density in the range of $2 \times 10^{16}$ cm$^{-3}$. Therefore the high sensitivity $CO_2$ interferometer is useful only after peak density, when not too many fringes need to be resolved.

The first detector used consisted of a layer of encapsulated cholesteric liquid crystals, sprayed to a thickness of 0.0025 cm onto a 0.0008-cm-thick Mylar film. A 0.005-cm thickness of flat black paint was sprayed over the crystals to enhance absorption of the laser radiation. The liquid crystals change from nonreflecting to a spectrally selective strong reflection ranging from red through blue and back to nonreflecting over a one degree temperature change at 33°C ambient. This detector was photographed with a flash exposure through a blue filter 40 msec after the laser-plasma event. Figure II-47 shows an interferogram of a 2.5-cm-diam circular section near the center of the plasma tube. The oscilloscope trace in the upper part of Fig. II-47 shows the timing of the laser pulse with respect to the magnetic field of the $\theta$ pinch.

Figure II-48 shows an interferogram taken very late in the discharge using Thermofax paper as the detector.

45

# DIFFERENCING CIRCUIT



THETA PINCH COIL
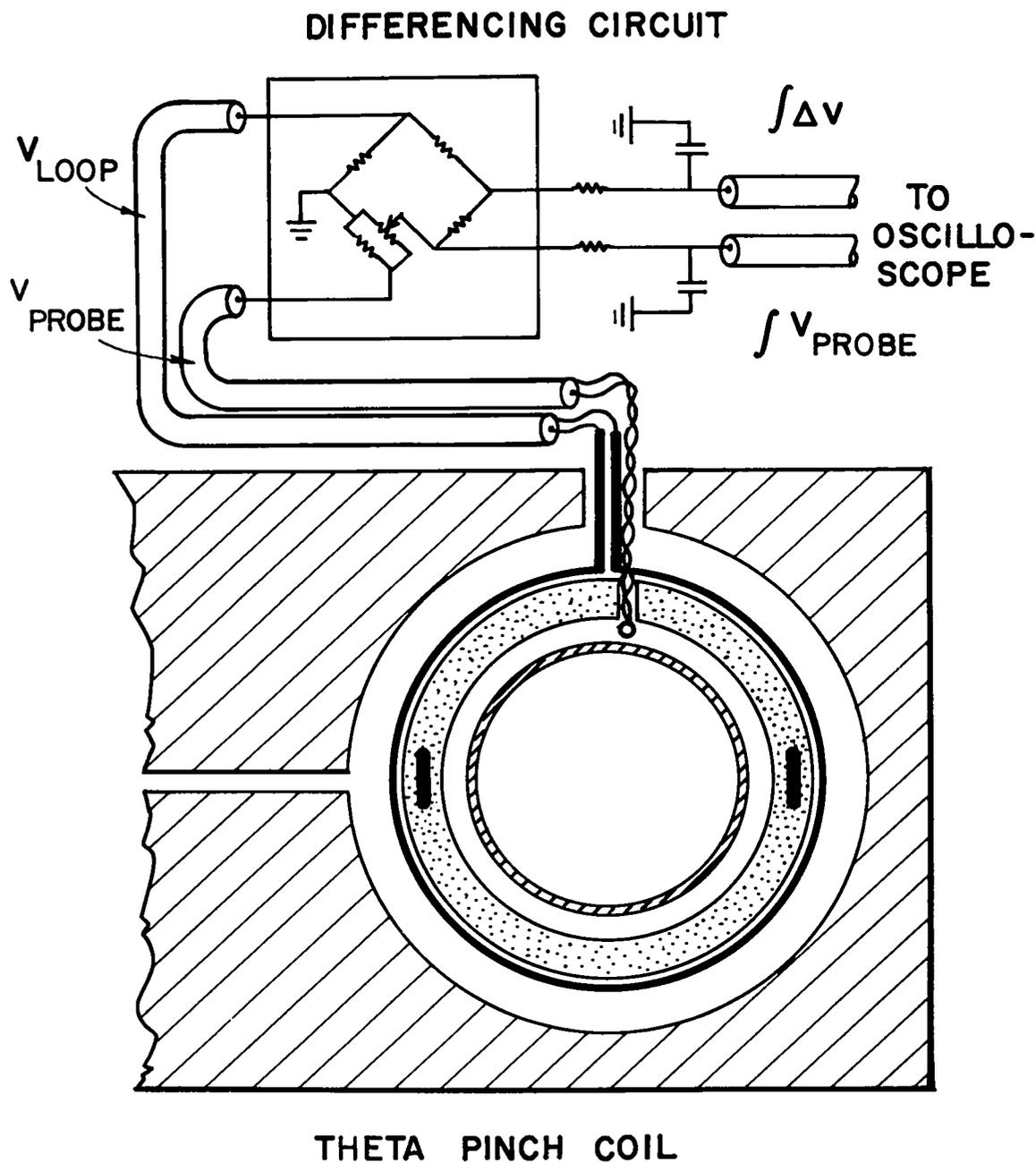
*Fig. II-42.*

*Positions for the loop surrounding the plasma and the probe beside the plasma are shown with the differencing circuit used to determine excluded flux.*

We have found that Thermofax paper requires approximately $2 J/cm^2$ to make it turn blue. An advantage of Thermofax is that a permanent record is obtained directly, without requiring any further processing. To aid in detecting a small fringe shift, Fig. II-48 is a composite of two interferograms. The left-hand side is a background exposure, i.e. one taken without plasma, while the right

side has plasma, but of much lower density than the plasma of Fig. II-47.

While our prime motivation has been the development of the $CO_2$ interferometry technique, the results of Figs. II-47 and -48, combined with data for intermediate times, can be analyzed for the radial density distribution and end-loss after peak field for Scylla IA, as shown in

# VACUUM (1291)



ΔV

B$_Z$
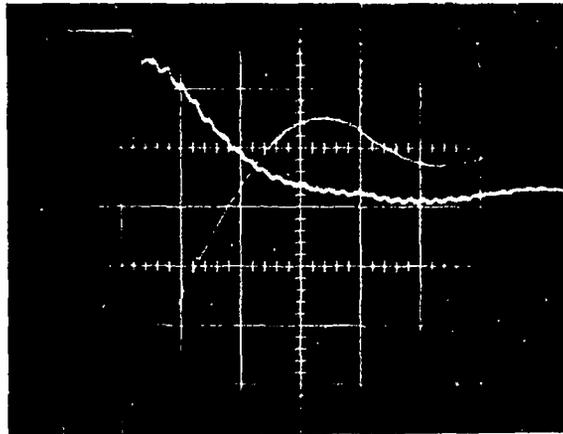
# PLASMA (1316)
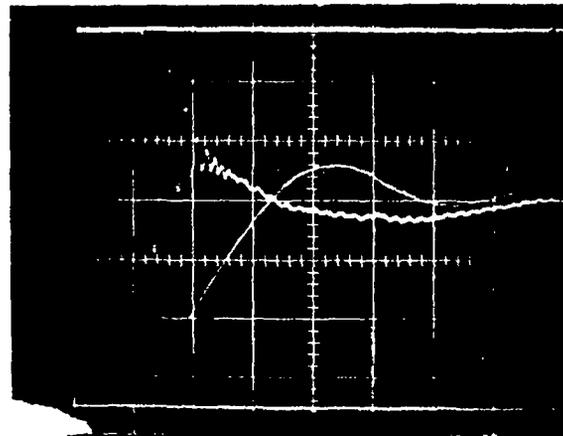


ΔV

B$_Z$

# EXCLUDED FLUX DATA

*Fig. II-43.*

*Typical data are shown for the balanced probe (1 μsec/cm). Excluded flux is proportional to the difference between the plasma and vacuum ΔV signals.*

Fig. II-49. The time history indicates an e-folding time of about 0.6 μsec between 1 and 2 μsec after peak field, with an apparent slowing down after 2 μsec, presumably due to the accumulation of an increasingly significant percentage of plasma outside the θ-pinch coil ends.

It would be very desirable to extend the $CO_2$ Mach-Zehnder interferometry illustrated here to $CO_2$ laser holographic interferometry, primarily to have holography's ability to utilize curved windows. This extension requires a detector with a high spatial-resolution capability, of the order of 25 lines/mm.

For this purpose, subsidiary experiments were made to approximately determine the resolution of the different detectors. Thermofax paper has a resolution of at least 40 lines/mm. With the liquid crystal detector, however, we achieved a resolution of only approximately 4 lines/mm after transfer to Polaroid film.

Another detector of interest is Transperex, a dispersed polymer made by Agfa-Gevaert for overhead projectors, which changes from water soluble to insoluble when raised to a certain transition temperature.

47

## PHOTOMULTIPLIERS

## BAND PASS FILTER
## ( λ = 5000 Å )

**LENS**

**MIRROR**

**IO CHANNEL FIBER OPTICS ARRAY**

**TO SCREEN ROOM**

**QUARTZ TUBE**

## LUMINOSITY APPARATUS

**THETA PINCH COIL**
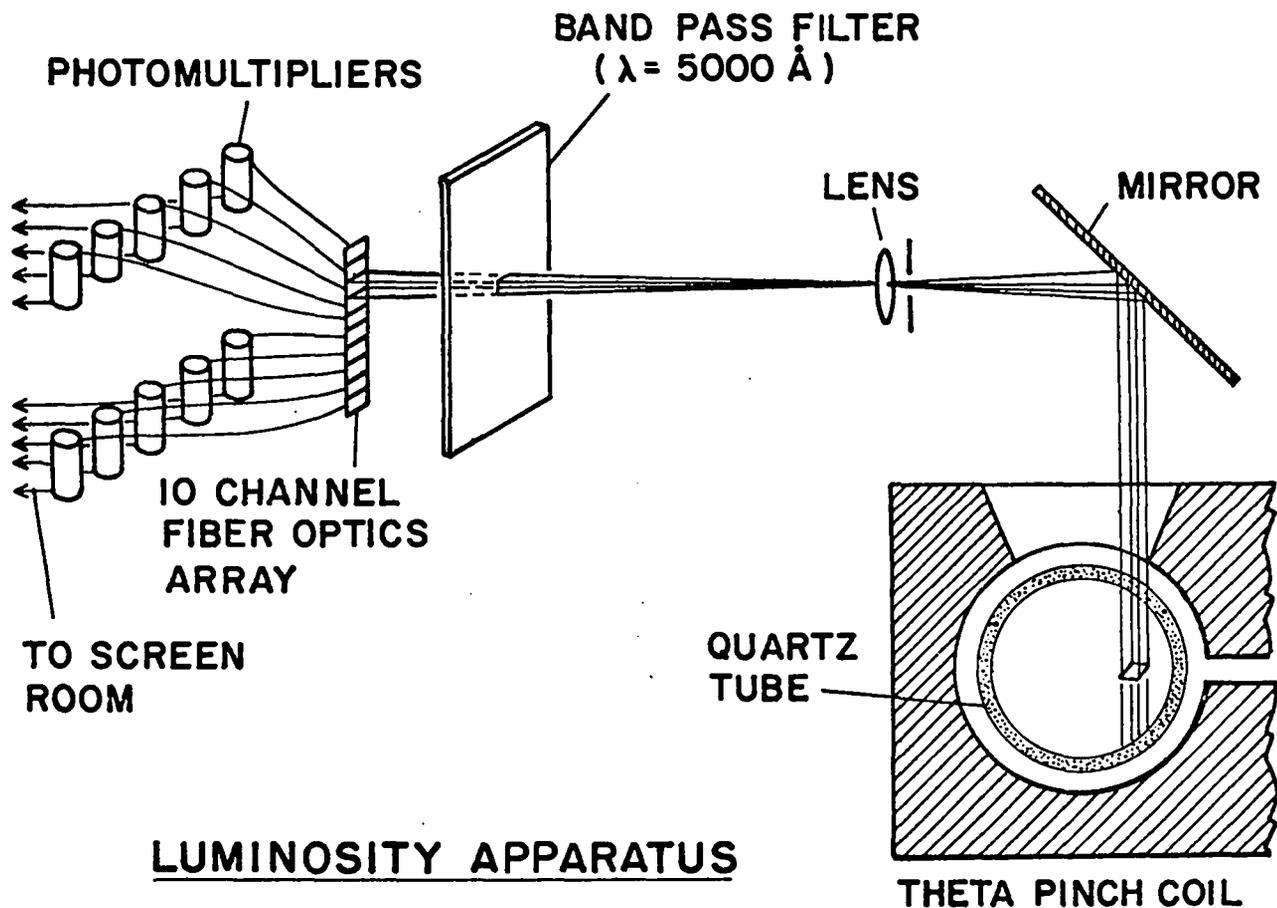
*Fig. II-44.*
*Ten simultaneous measurements of plasma brightness along parallel chords were determined with the apparatus shown here schematically.*

Consequently, when Transperex is immersed in water, previously heated areas remain opaque while unheated areas wash off and become transparent. We have found that approximately 1 $J/cm^2$ is required to expose this material in the case of fast pulses at 10.6 μm. We have made small gratings on Transperex with our $CO_2$ laser with a 100 lines/mm grating spacing. However, Transperex is characterized by a very limited exposure range, and thus any nonuniformities in the laser beam result in overexposed or underexposed regions that do not record the fine grating structure. Nevertheless, this constitutes a promising material if higher-energy, more uniform laser radiation can be obtained.

### K. Scyllac Computer and Data Acquisition (J. W. Lillberg, G. A. Sawyer, and D. M. Weldon)

As Scyllac has come into operation, so has the full Scyllac monitor program. Considerable time has been spent in refining and debugging the program. It now performs the functions of charge monitoring, logging shot information, reading gap monitor times, and reading scan-converter data, in addition to sorting, reducing, and displaying results.

We are still making refinements in the gap monitor system, although it has been in operation for some time. The gap monitor is now in use on Scylla IV, the Scyllac toroidal sector, and on the 5-m linear Scyllac, routinely detecting and locating gaps that prefire, in addition to the numerous gaps that fire slightly early or late. Load-gap prefire is a fairly common occurrence but we rarely get a repeat prefire on the same gap.

Eight channels of scan converter (storage oscilloscope with waveform digitizing) are in use on the Scyllac toroidal sector experiment. Various signals, such as magnetic field, luminosity signal, and position detector have been recorded and displayed by the computer display system. Direct processing of magnetic probe data, combined with luminosity data to yield plasma β on each shot of Scyllac, is under development.

LUMINOSITY
(1140)

CHANNEL

1
2

3
4

5
6

7
8

9
10

INTENSITY   VS.
TIME

0.4   0.6   0.8   1.0   1.2   1.4

1.6   1.8   2.0   2.2   2.4   2.6

2.8   3.0   3.2   3.4   3.6   3.8

4.0   4.2   4.4   4.6   4.8   4.9

INTENSITY VS. POSITION AT VARIOUS TIMES
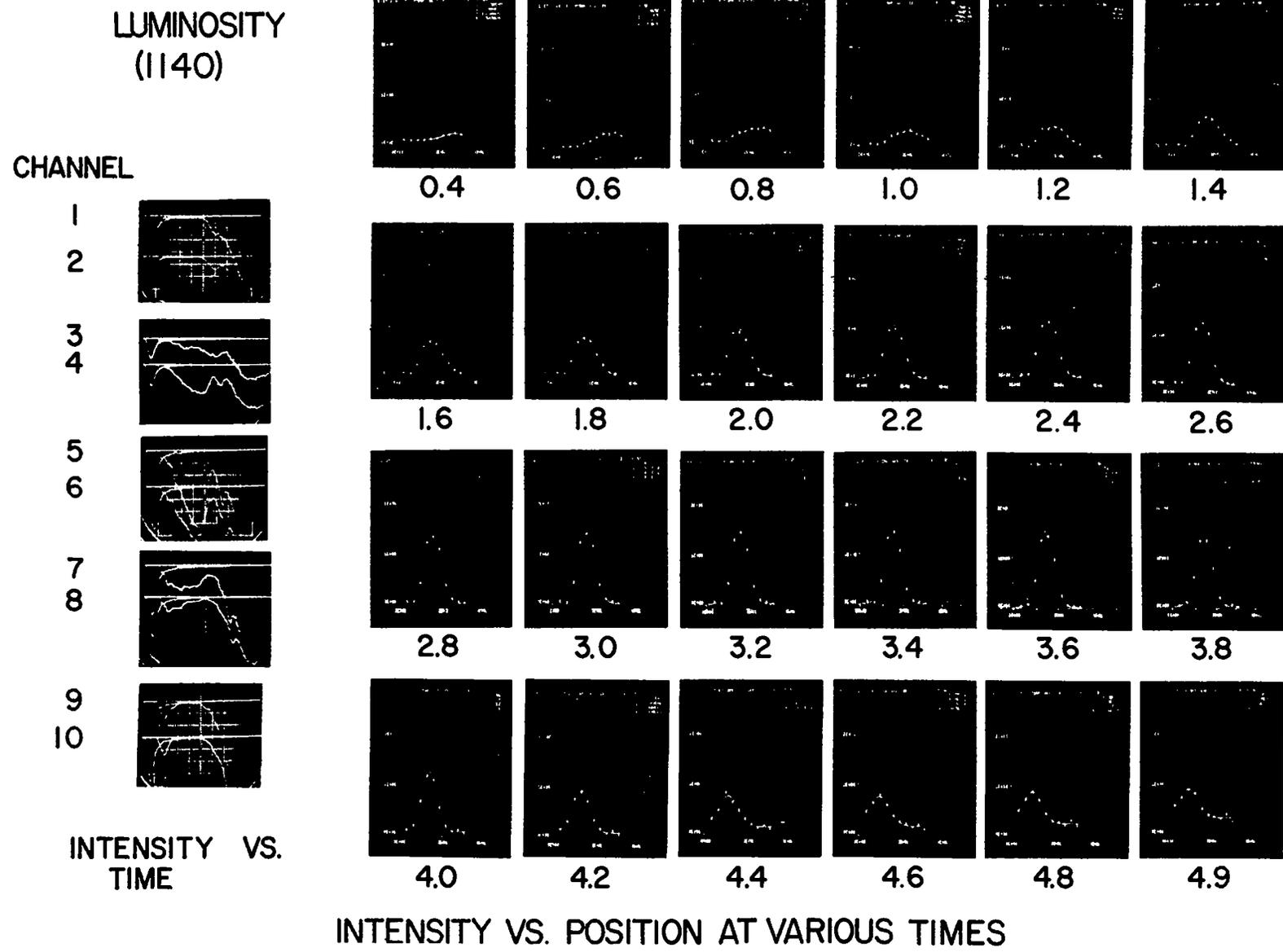
Fig. II-45.
Photomultiplier signals on the left (1 µsec/cm) are shown on the right as intensity vs position at various
times (µsec) along with computer fitted curves.
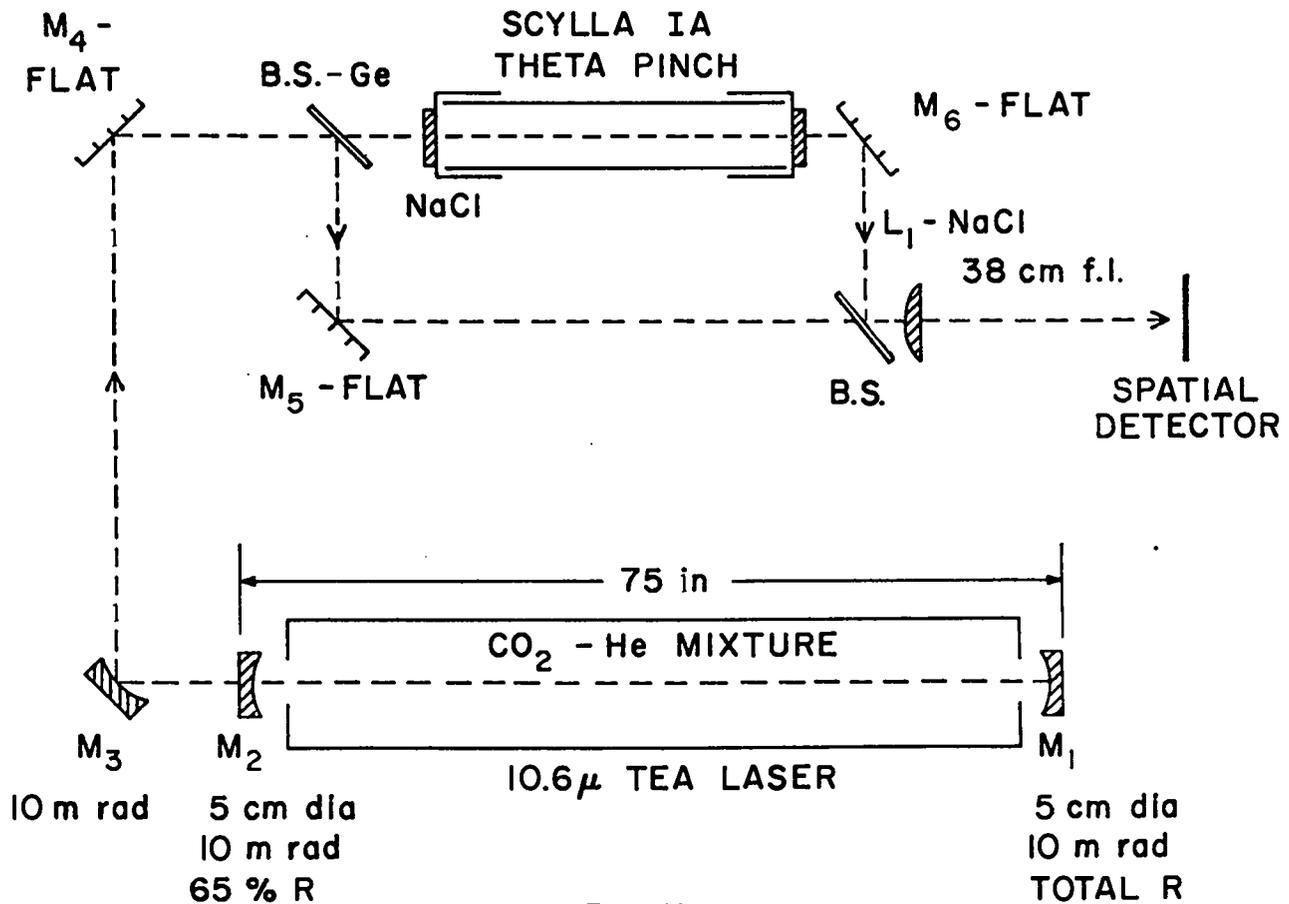
*Fig. II-46.*
*Schematic of $CO_2$ laser Mach-Zehnder interferometer.*

The analog-to-digital converter system for reading the Scyllac panel meters has been interfaced to the computer and tested.

In addition, the Sigma-2 computer has been used extensively in off-line data reduction and analysis, such as Scylla IV hologram data, gas laser interferometer results from Scyllac, and many others. It is convenient to use the Sigma-2 for this work because of instant turn-around and the possibility of operator interaction to make changes in the analysis.

**L. Microinstabilities and Sheath Broadening (M. Kaufmann, F. L. Ribe, and R. E. Siemon)**

For a number of years it has been known that $\theta$-pinch plasmas are highly diffusive during their early, dynamic phase and become less so, approaching classical diffusion, during the quiescent phase. This has been explained qualitatively by turbulence generated when the electron diamagnetic drift velocity $v_D$ exceeds the threshold for some microinstability. The resulting diffusion broadens the plasma-magnetic-field interface (sheath), lowering the drift velocity and cutting off the instability.

The microinstability responsible for this turbulent diffusion has commonly been taken to be unstable ion sound. This, however, requires that $T_e/T_i > 1$ for the instability to occur, a condition which does not occur in $\theta$ pinches. Recently Forslund, Morse, and Nielson[1,2] have postulated the electron-cyclotron-drift, or Bernstein, instability, as the cause of this turbulence, since in this case instability occurs for $v_D < v_{th}$ and $T_e \cong T_i$.

In the following, we derive the scaling of the onset of sheath broadening in $\theta$-pinch implosions on the assumption that the instability threshold is that of the electron-cyclotron-drift instability and that the electrons are heated by resistive or diffusive field mixing during the implosion. We use this scaling to order various existing high-voltage $\theta$-pinch experiments and to predict the conditions for excessive broadening of the sheath in future $\theta$ pinches and other shock-heating experiments. A more
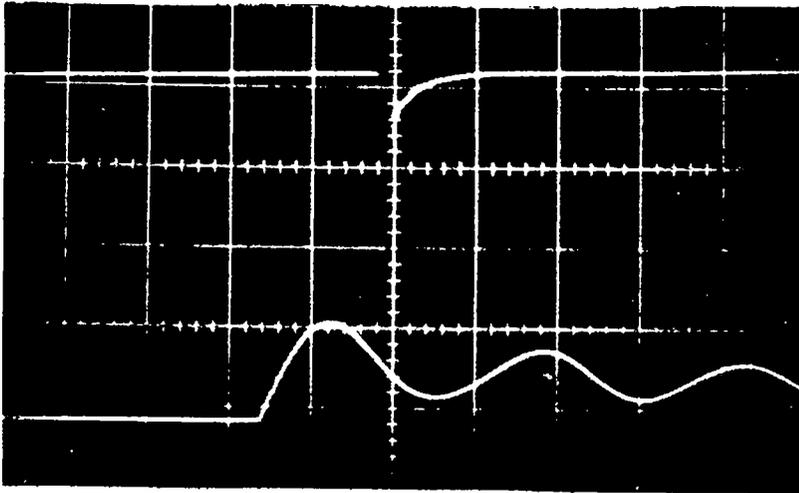
Laser Pulse Signal
1 V/div;   2 μsec/div
$CO_2$:   He Mixture

Field Trace
10 V/div;   2 μsec/div

Resultant Fringe Shifts

Background Fringes

Tube
Diameter

Fig. II-47.

*Interferogram obtained with liquid-crystal detector of θ-pinch plasma. Oscilloscope traces show laser pulse (upper beam) and magnetic field of the plasma (lower beam).*
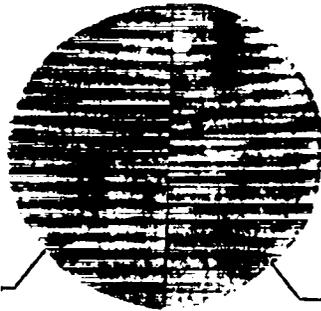
INTERFEROGRAMS MADE

ON THERMOFAX (3/16" CIRCLES)

BACKGROUND FRINGES ⌐                              ⌐ SHIFTED FRINGES

*Fig. II-48.*
*Interferogram obtained with Thermofax paper as detector. Left half with no plasma, right half with plasma at late time during the discharge, as shown by oscilloscope traces.*

complete treatment is being prepared by M. Kaufman as an LA report.

We also consider a 20-cm diam, 120-kV shock-heating experiment as one phase of the linear Scyllac work, showing that it could test this scaling law and provide important knowledge of the heating limits in future separated-shock, $\theta$-pinch experiments.

**1. Scaling of the Sheath-Broadening Onset Condition.** Consider the situation illustrated in Fig. I'-50. An imploding sheath of thickness $\Delta r$ is driven by a magnetic field $B_s$. The quantity $\omega_{pe}$ is the electron plasma frequency, $\omega_{ce}$ the electron gyro frequency, $v_s$ the sheath velocity, $v_D$ the electron drift velocity, and $v_{th}$ the electron thermal velocity. The onset condition for the electron-cyclotron-drift instability is

$$v_D = (\omega_{ce}/\omega_{pe})v_{th} \quad . \tag{1}$$

Maxwell's $\Delta XH$ equation can be written

$$n_o e v_D = (c/4\pi)B_s/\Delta r \quad . \tag{2}$$

Diffusive field mixing in the sheath is described by

$$1/2\, n_o m_e v_{th}^2 = f\, B_s^2/8\pi \quad , \tag{3}$$

where f is a dimensionless constant of order unity. Combining Eqs. (1), (2), and (3) gives for the sheath thickness

$$\Delta r = f^{\frac{1}{2}}\,(c/\omega_{ce}) = m_e c^2/f^{\frac{1}{2}} e B_s = m_e\, c^2/f^{\frac{1}{2}} e \dot{B} t \quad , \tag{4}$$

where t is the transit time of the sheath in a linearly rising field of constant $\dot{B}$. Faraday's law of induction relates $\dot{B}$ and the voltage $V_c$ around the shock-heating coil of radius R

$$B_s/t = \dot{B} = 10^8\, V_c/\pi R^2 \quad . \tag{5}$$
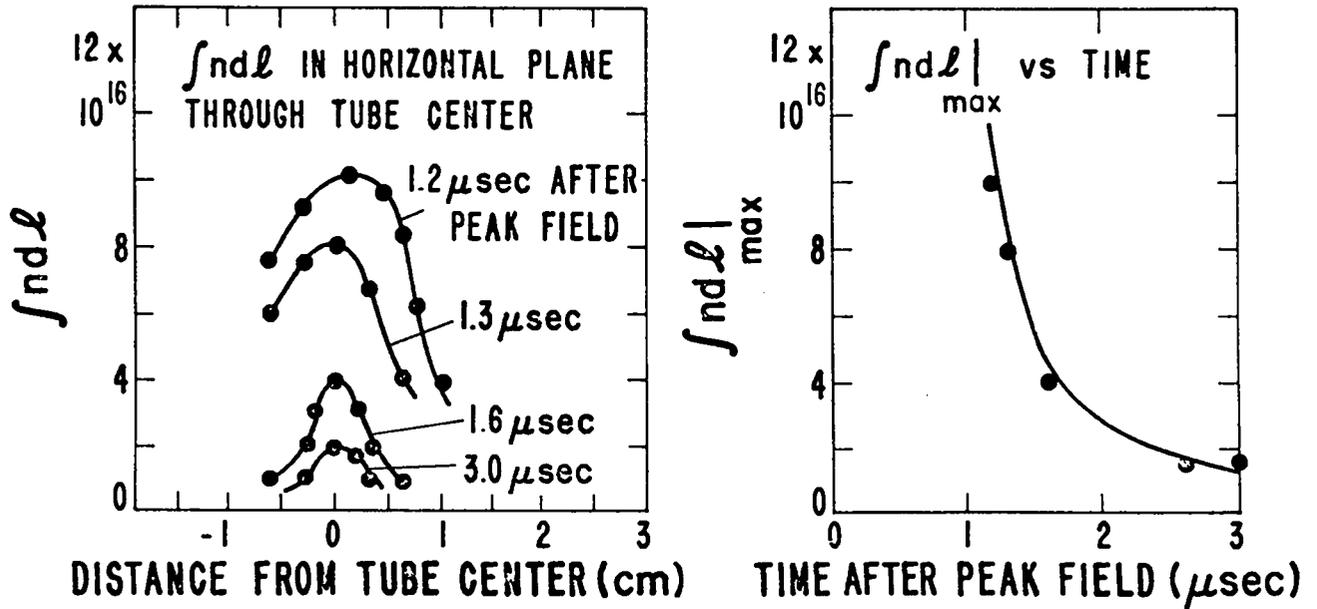
Fig. II-49.
Measured decay of Scylla IA line density.
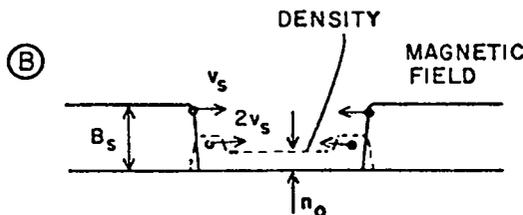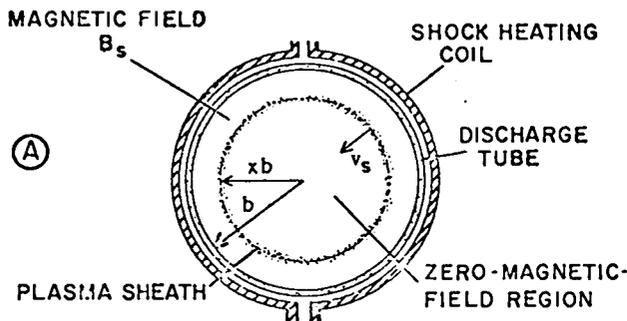


Fig. II-50.
Schematic diagram of piston-heated plasma with magnetically driven sheath.

Substituting into Eq. (4) gives

$$\Delta r = c_1 \ R^2/V_c t \ . \ \ (c_1 = \pi m_e \ c^2/10^8 e f^{1/2}) \tag{6}$$

In order to eliminate the time in this expression we use the equation of momentum for the sheath

$$B_s^2/8\pi = 2n_0 m_1 v_s^2 \ . \tag{7}$$

The distance traveled in one transit time t is thus

$$R = \int_0^t v_s dt = \dot{B} t^2/32\pi^{1/2} n^{1/2} m_i^{1/2}$$

$$= V_c R^{-2} t^2 n_0^{-1/2}/C_2 \ , \tag{8}$$

where $C_2 = 32\pi^{3/2} m_i^{1/2} \times 10^{-8}$, and we have used Eq. (5). As a criterion for criticality, where the sheath loses its effectiveness in accelerating ions, we take $\Delta r \approx R$. We set $\Delta r = R$ in Eq. (6) and substitute the resulting expression into Eq. (8). The result for the critical lower limit of density for sheath broadening is

$$n_0 = (C_1^4/C_2^2)/R^2 V_c^2 \ . \tag{9}$$

Figure II-51 shows a graph of minimum filling density vs the product $RV_c$ for various $\theta$-pinch experiments. In practice $n_0$ is usually the optimizing density for ion temperature. The points labeled 7 and 8 represent recent low-density, collisonless shock experiments.[3,4]

53
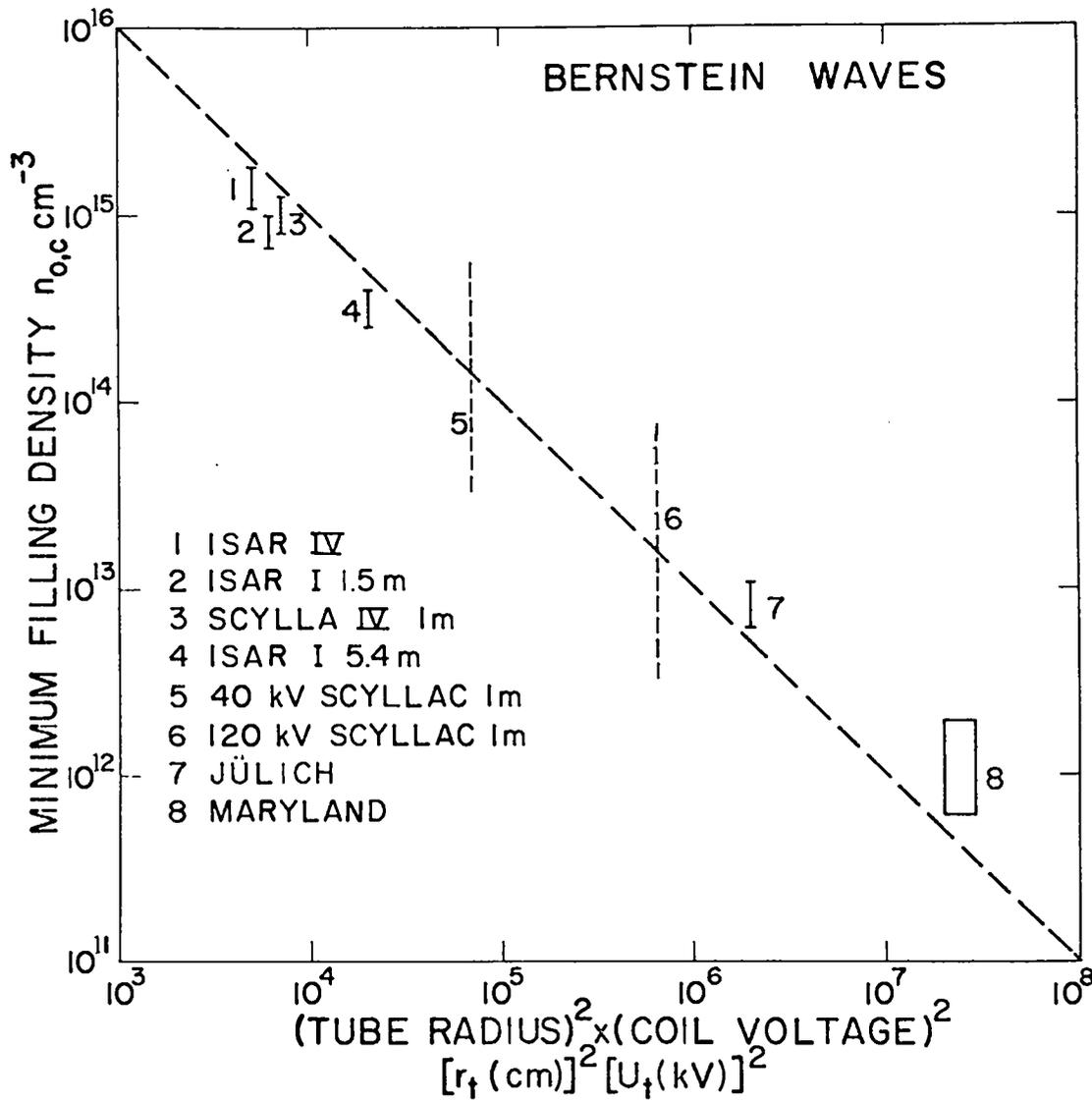
*Fig. II-51.*
*Critical minimum density for sheath broadening as a function of the product of shock-heating coil radius and voltage.*

**2. Projected Linear Scyllac Sheath-Scaling Experiment.** A heretofore unexplored range of $RV_c$ (or $r_t U_t$) is available if we make use of a portion of the linear Scyllac device to drive a 20-cm coil of 1-m length. A voltage doubling arrangement can be used with one capacitor rack on the south driving the upper half of the compression coil and one half each of two racks on the north driving the lower half of the coil. Such a

"clamshell" arrangement would develop a nominal voltage of 120 kV and is identified in Fig. II-51 by the abscissa labeled 6. A single-sided drive from only the south rack would develop 60 kV and is labeled 5 in Fig. II-51.

A configuration in which this experiment could be carried out with minimum interference with the 7-m linear Scyllac experiment or the toroidal Scyllac experiment is illustrated in Fig. II-52. It is proposed to initiate

# CONTROL ROOM
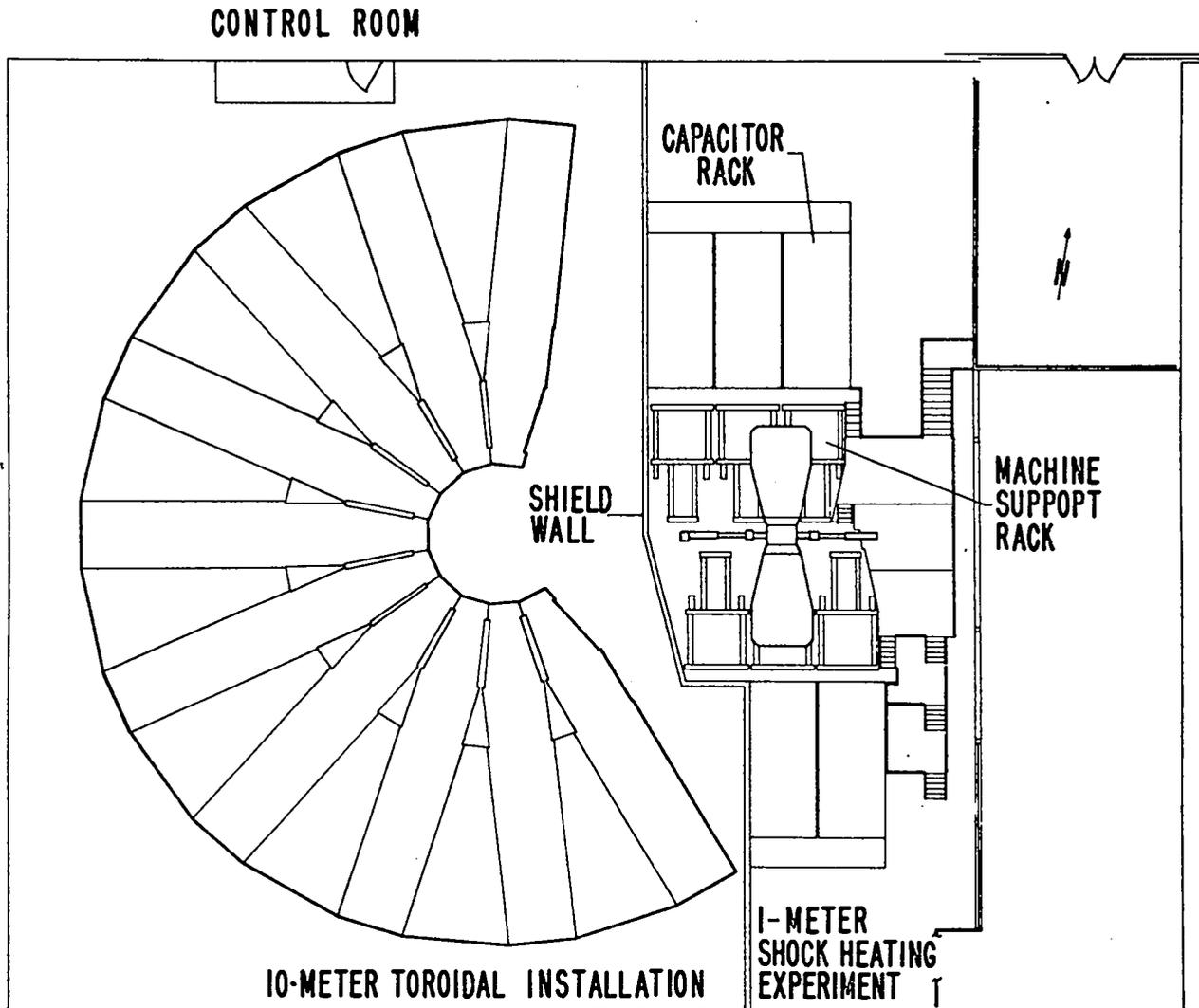


*Fig. II-52.*

*Transition phase of the toroidal Scyllac conversion, showing the 1-m clamshell piston-heating experiment.*

this experiment after completion of the 7-m linear experiment during the time (beginning about December 1972 or January 1973) when the conversion of capacitor racks to the 15-m torus is being carried out. This conversion will occupy approximately a year. During the first 4 to 6 months it is proposed to leave five linear racks in place which include the clamshell sheath-scaling experiment, while carrying out the first phase conversion to 10-m of torus. Note that in the clamshell experiment the piston-heated plasma will be compressed, giving a measure of ion temperature. In the final compressed state it should reach 10 kV or more.

## References

1. D. W. Forslund, R. L. Morse, and C. W. Nielson, Phys. Rev. Letters 25, 1266 (1970).

2. D. W. Forslund, R. L. Morse and C. W. Nielson in Fourth IAEA Conference on Plasma Physics and Controlled Nuclear Fusion Research, Madison, Wisconsin 17-23 June, 1971. Paper CN-28/1E-18.

3. W. D. Davis, A. W. DeSilva, W. F. Dove, H. R. Griem, N. A. Krall, and P. C. Liewer, Op. Cit. Paper CN-28/J-12.

4. P. Bogen, K. J. Dietz, K. H. Dippel, E. Hintz, K. Hothker, F. Siemsen, and G. Zeyer, Op. Cit. Paper CN-28/J-11.

## III. THE Z-PINCH PROGRAM

### A. Summary (J. A. Phillips)

In our Z-pinch program we are examining pinches which are shock heated by the $B_\theta$ magnetic field of the fast rising Z current.[1,2] At the high temperatures achievable by this method, the limitations found in our earlier ohmic-heated Z-pinch (Perhapsatron and Columbus) experiments[3] may be avoided.

During the past year, the toroidal experiment, ZT-1, has been assembled and run both in the slow (ohmic heating) and fast (shock) modes of operation. In the slow mode, the Z pinch reproduces earlier Z-pinch results and exhibits stability against the m = 1 mode for $\lesssim 6$ to 8 $\mu$sec. In the fast mode, at one-half the maximum voltage, the experiment operates as expected, proving out the basic design. In these first experiments, the discharge current rings out with a quarter period of 10 to 15 $\mu$sec determined by the LC of the electrical circuit. This stage of operation is known as ZT-1A. The reproducibility of the Z pinch in the fast mode is not yet satisfactory. In most discharges, the pinch column goes m = 1 unstable in $\lesssim 3$ $\mu$sec. On two discharges, however, pinches have been produced which are stable for the full quarter-cycle of the Z-current. Apparently the conditions of the plasma after the preionization current pulse is important. When the necessary conditions are understood and stable pinches are reproducible, the $B_z$ field outside the pinch column will be reversed as is required by MHD stability theory. (See Section III-C.)

With these encouraging results the components required for the second stage, ZT-1B, of the toroidal program are being designed and tested. Here the feedplates of the torus will be crowbarred with the Z-current falling with an L/R time constant of $\sim 1$ msec. A metal-to-metal crowbar switch is undergoing test. (See Sec. III-D.)

While measuring the $B_z$ bias magnetic field across a minor diameter of the torus, perturbations in the field have been found due to holes in the primary for the pump-out ports. Using numerical codes and simplified models (see Section III-E), it was found that $B_z$ and $B_\theta$ field lines $\lesssim 2$ mm inside the discharge tube are displaced outward to intersect the surface of the ceramic wall at these holes. This is not considered serious.

Magnetic energy storage systems using fuses are presently energizing our fast Z-pinch experiments. Replacement of fuses after each discharge is not completely satisfactory and is not considered practical for a larger experiment. A peaking capacitor circuit has been suggested which does not require fuses. (See Section III-F.)

The Z-pinch program has been supported in part by the following: 1) the MHD stability of the Z-pinch in toroidal geometry is being examined (see Section III-G); 2) the effect of the $B_z$ bias field, required for stability, on plasma heating by a strong shock has been considered (see Section III-H); and 3) the question of anomalous diffusion where there is an abrupt change in the electrical resistivity has been examined for two numerical schemes (see Section III-I).

### References

1. Los Alamos Scientific Laboratory report LA-4585-MS (1970).

2. D. Baker et al., paper CN-28/B-2 presented at IAEA Conference on Plasma Physics and Controlled Fusion, Madison, Wisconsin, 1971.

3. J. A. Phillips, Los Alamos Scientific Laboratory report LA-4664, (1971).

### B. The Shock-Heated Toroidal Z-Pinch Experiment (J. Phillips, A. Schofield, L. Burkhardt, J. DiMarco, P. Forman, A. Haberstich, and H. Karr)

This experiment is being performed to attain a high-temperature toroidal pinch with field configurations predicted to be stable by the energy principle.[1]

The experiment which is shown on Figs. III-1, -2, and -3 became operational in June of this year. The design parameters are presented in Table III-I.

Current in the storage inductor is diverted into the Z-pinch by the voltage developed across the four fuses when they evaporate. The lower part of the 244-cm-diam coaxial conductor is designed to be the 40 nH storage inductance, while the top part connects the four fuses with low inductance to force the voltages developed across the fuses to be identical. The four transfer switches are pressurized low-inductance gaps, preset to a breakdown voltage by adjusting the gap pressure.

The machine can be operated in two modes, a capacitively driven slow mode and an inductively driven fast mode.

The slow mode is achieved by shorting the transfer switches, removing the fuses, and driving the plasma current directly from the capacitor bank. Initial $\dot{I}$'s of $\sim 2 \times 10^{11}$A/sec makes shock heating negligible. Ohmic heating results in low plasma temperatures of $\sim 25$ eV.

Streak photographs taken through a quartz window are shown in Fig. III-4. Two examples are shown at three

TORUS PRIMARY (11.6 cm bore)

$B_z$ WINDING

IRON CORE

TRANSFER SWITCH

LOAD CABLES

MAGNETIC STORAGE INDUCTOR

Z - PINCH

PORCELAIN VACUUM CHAMBER

FUSE

*SHOCK HEATED TOROIDAL Z -PINCH*
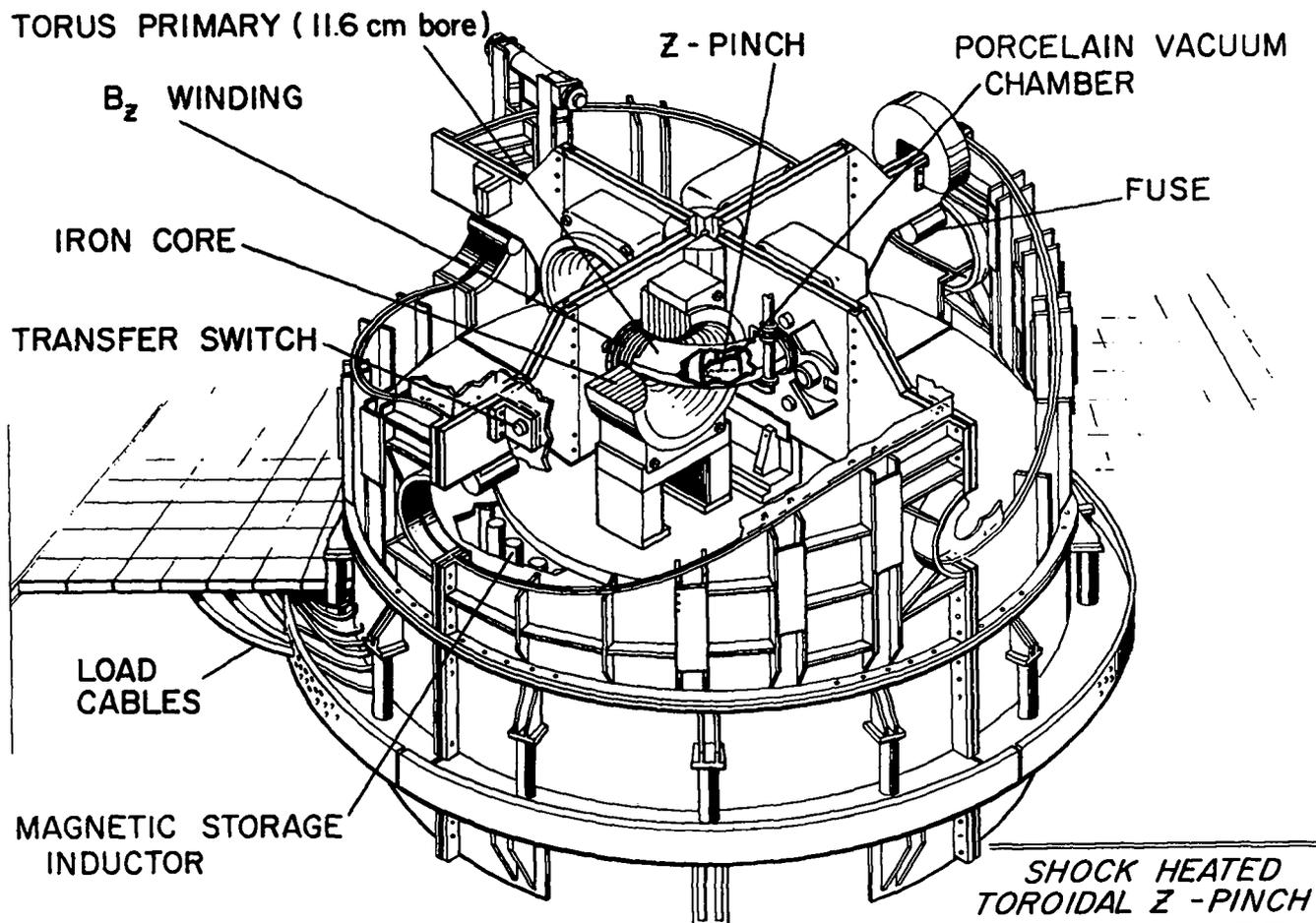
*Fig. III-1.*
*Schematic of shock-heated toroidal Z-pinch experiment.*

values of $B_z$ bias field with deuterium gas at 50 mTorr. They show the formation of a pinch which lasts 3 to 6 $\mu$sec, depending on the magnitude $B_z$ bias field. The plasma then moves toward the wall. A typical measurement of the $B_z$ field outside the ceramic tube is shown in Fig. III-5. Initially $B_z$ drops by 80 to 90%, as it should from flux conservation, and at the onset of instability reverses direction, reaching values of the order of the initially applied field. This reversal is observed in every case when the pinch goes unstable, and is presumably due to the onset of an m = 1 instability.

The fast mode is obtained by using the current diversion technique with fuses. During these preliminary runs the experiment has been run at half its design voltage giving I's ~ 1.4 x $10^{12}$A/sec which should give moderate shock heating with $T_i + T_e$ ~ 100 to 200 eV.

In Fig. III-6 are shown the discharge current and voltage across a fuse as functions of time. The data were obtained at a deuterium gas pressure of 50 mTorr and a

$B_z$ bias field of 1.9 kG. In Fig. III-7 are shown the corresponding streak photograph, the voltage around an iron core, the discharge current, and the $B_z$ magnetic field outside the ceramic torus on an expanded time scale. The luminous front implodes towards the axis with a velocity ~ 1.4 x $10^7$cm/sec. At 2.2 $\mu$sec the pinch has moved off axis and apparently strikes the wall. The $B_z$ field at the wall again initially drops close to zero, and at ~ 2.2 $\mu$sec reverses. In the streak photograph it is encouraging to see that the discharge moved away from the wall with no evidence of a secondary breakdown at the wall.

These results are to be compared with those in Fig. III-8. The streak photograph shows a plasma column existing for 6.2 $\mu$sec, which is the duration of the streak. After the initial implosion and bouncing, the plasma relaxes to a hollow diffuse structure. The central region has a rather sharply defined boundary while the outside region is diffuse. This diffuse appearance may be due to small grain turbulence since programming of the magnetic

57
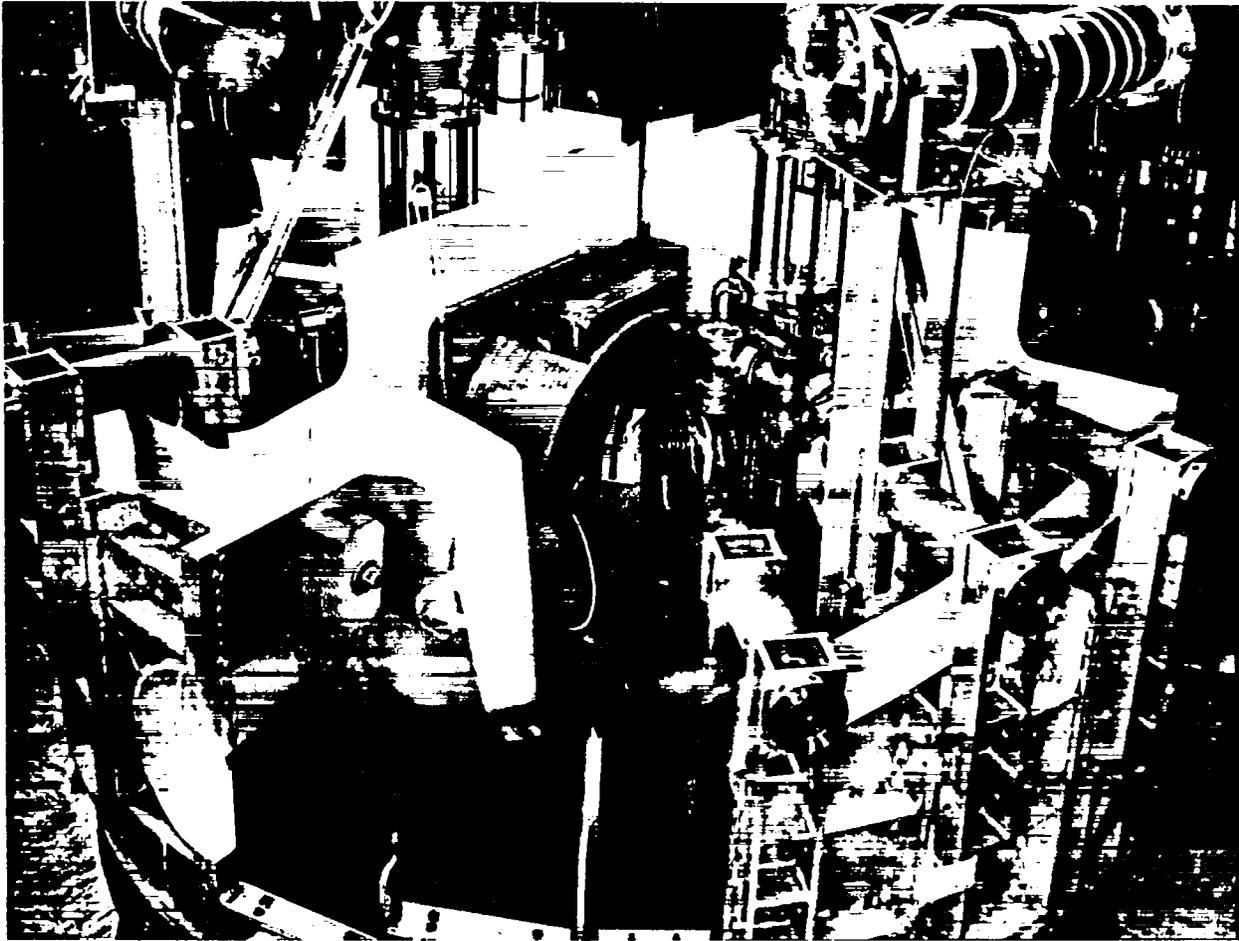
*Fig. III-2.*
*Photograph of the toroidal Z-pinch experiment, ZT-1.*

field is not yet available and unstable local modes would be expected in this region. The $B_z$ field at the wall again falls close to zero, but no reversal is observed. It returns to almost its original value when the z-current goes to zero at about 11 $\mu$sec. The calculated $B_z$ field indicated on the graph results from a simple thin-sheath model which assumes no plasma pressure.

This different behavior is borne out by a measurement with a flux loop around the alumina discharge tube. At the onset time of the pinch, part of the small amount of flux outside the discharge tube is seen to move inside the loop. Then there is a slow rise due to the addition of flux from the aluminum primary and a partially charged $B_z$ capacitor bank, but no sudden increase in flux is seen as has been characteristic of all other discharges in ZT-1. These results are entirely different from earlier observations of the Z-pinch.

This behavior has been observed twice, and presently is not reproducible. A number of approaches are being applied to improve the repeatability of our results.

These results are encouraging since the data, while limited, are indicative that the initial requirement of achieving a grossly stable plasma in ZT-1 experiment may be satisfied. When this behavior is made reproducible, the experiment will then advance to $B_z$ field programming to attempt to eliminate the small grain turbulence on the outside boundary of the pinch.

Reference

1. D. C. Robinson, High-$\beta$ Diffuse Pinch Configurations, Plasma Physics, 13 439 (1971).

C. **Programmed** $B_z$ **Field for ZT-1 (A. E. Schofield and R. Holm)**

The radial profile of $B_z$ and $B_\theta$ magnetic fields is to be changed from the existing situation in which the $B_z$
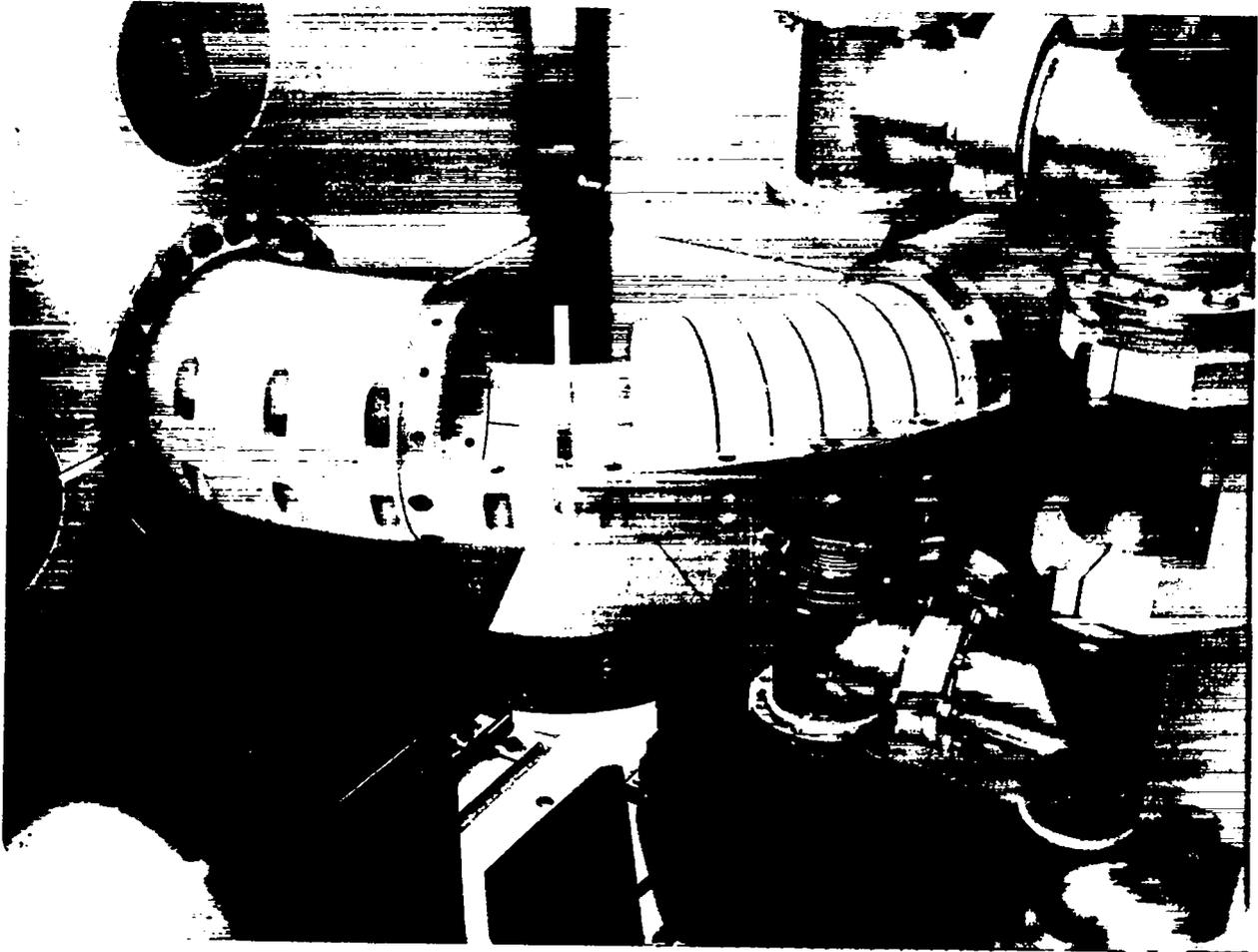
*Fig. III-3.*
*One quadrant of ZT-1 showing the assembly of the porcelain discharge tube, aluminum primary, and one diagnostic loop.*

## TABLE III-1

### DESIGN PARAMETERS

| | |
|---|---|
| Major diameter | 76.5 cm |
| Minor diameter | 11.6 cm |
| Rate of rise of plasma current | $\sim 3 \times 10^{12}$ A/sec |
| Peak plasma current | $\sim 300$ kA |
| Maximum voltage per quadrant | $\sim 80$ kV |
| Primary energy source | 0.5 MJ at 40 kV |
| Longitudinal bias $B_z$ field | $\lesssim 6$ kG |

field is unidirectional inside and outside the pinch to one in which the $B_z$ field external to the pinch is reversed shortly after the pinch is formed. MHD theory predicts that stability outside the pinch would be improved by this change.[1]

In the existing system, the $B_z$ winding on the torus consists of 4 coils of $\sim 75$ turns each. The four coils, one wound around the aluminum primary in each quadrant, are fed in parallel with an inductance of $\sim 40\,\mu$H for the system. Of this inductance, approximately 90% is accounted for by the volume inside the ceramic discharge tube, with $\sim 10\%$ representing the volume of the discharge tube wall and clearance space plus the inductance external to the primary.

The desired parameters for the programmed $B_z$ are as follows:

Forward $B_z$

1) 0 to 5 kG, flat within 2.5% for 10 $\mu$sec.

2) $B_z$ max at $\sim 90$ to 100 $\mu$sec.

WALL

$B_{z_0} = 0.6 kG$

$B_{z_0} = 1.9 kG$

$B_{z_0} = 4.4 kG$

TIME ($\mu$sec)

TIME ($\mu$sec)

$B_{z_0} = 4.4 kG$

$B_{z_0} = 1.9 kG$
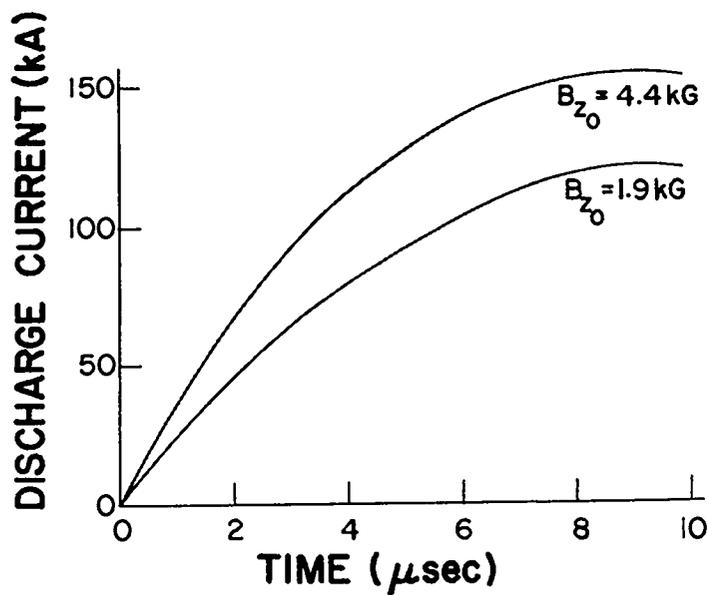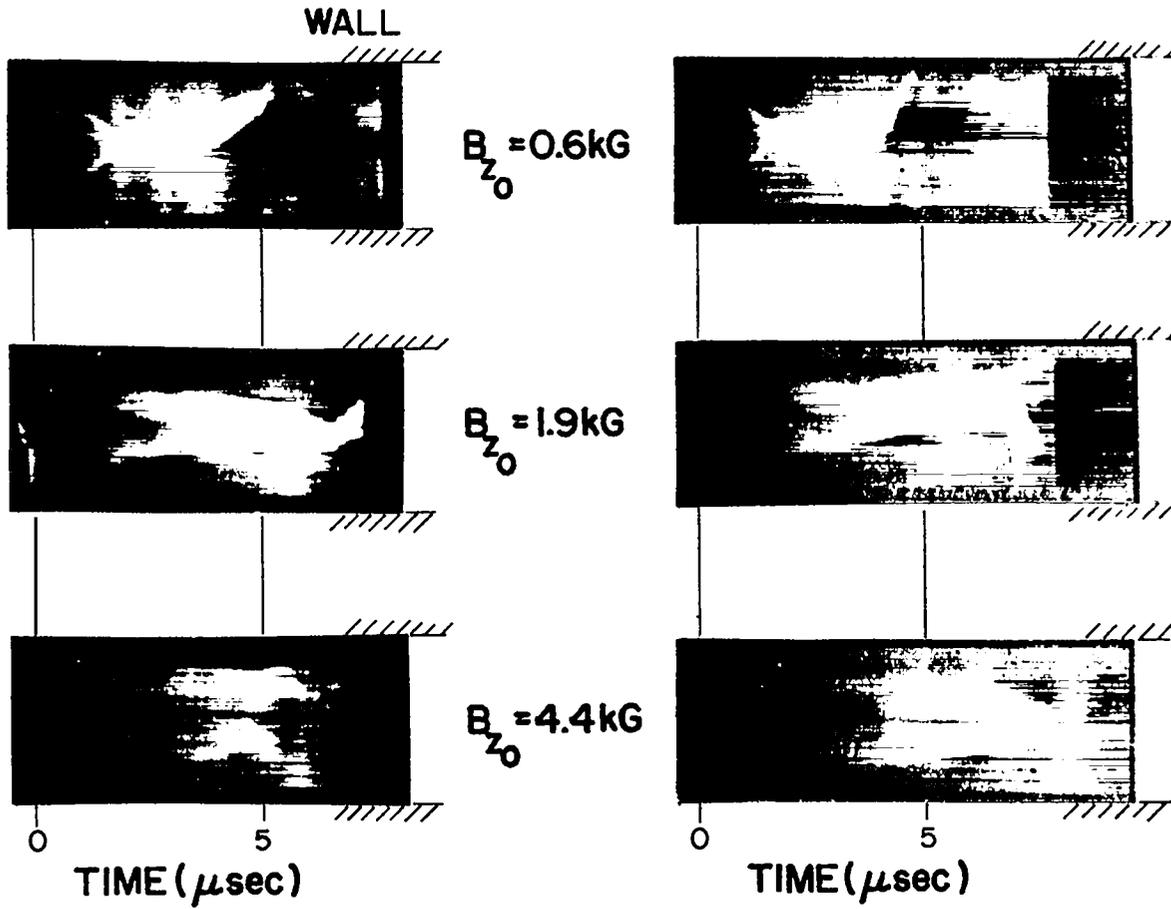
*Fig. III-4.*

*Two examples of streak photographs for three values of $B_z$ bias field, and time behavior of the discharge currents from ZT-1 run in the slow mode.*
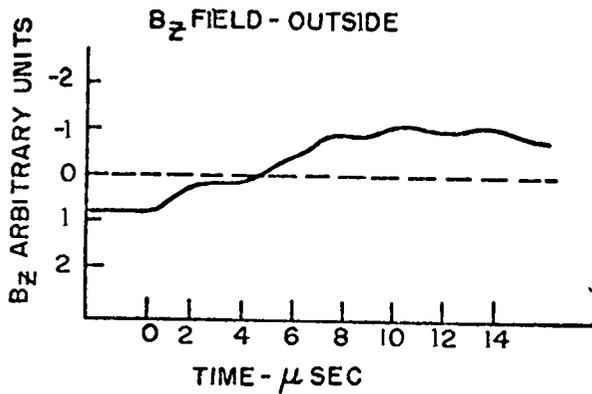
*Fig. III-5.*

*The $B_z$ magnetic field as measured outside the porcelain wall showing the reversal associated with an instability.*
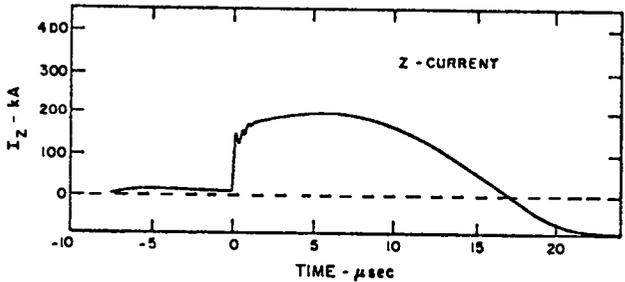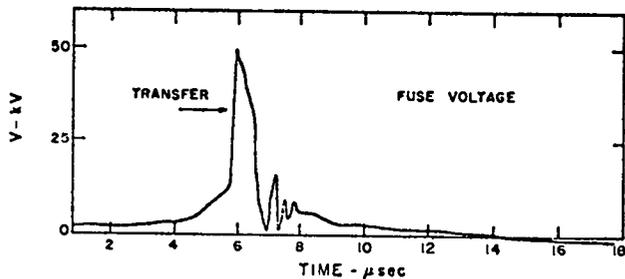


*Fig. III-6.*

*The current and voltage as function of time for a discharge run in the fast mode.*



*Fig. III-7.*

*Time correlation between the streak photograph, pinch voltage, discharge current,and $B_z$ at the wall for a discharge run in the fast mode.*

Reverse $B_z$

1) $B_z$ max $\sim$ 0 to 5 kG
2) $\dot{B}_z$ max $\sim 10^9$ G/sec
3) $B_z$ max at $\sim$ 40 $\mu$sec
4) Reverse $B_z$ to be fired from 0 to 5 $\mu$sec after start of Z-pinch.
5) Modulation of the reverse field by effects of the forward field should be minimized.

In order to meet these requirements, several factors must be considered. The external inductance should be kept low. The inductance not associated with the volume to be filled with plasma should be no more than 10% of the total system inductance at the time the pinch is formed. This is necessary because flux conservation will cause the flux associated with the external inductance to enter the discharge tube and fill the region between plasma and the conducting wall when the plasma pinch takes place. This makes reversing the $B_z$ field more
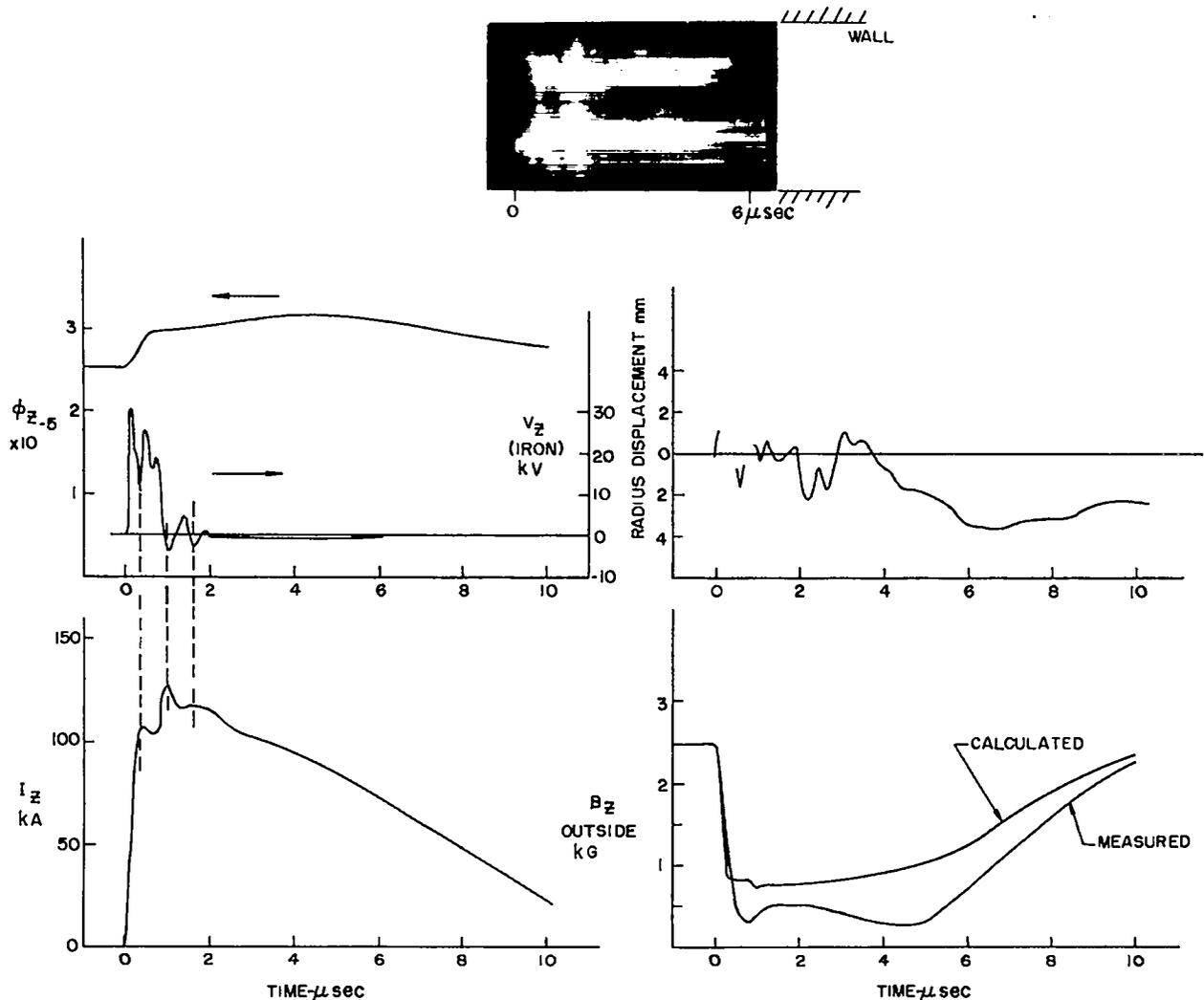
*Fig. III-8.*
*Observations obtained on a discharge run in the fast mode which does not show $B_z$ field reversal.*

difficult since this flux has to be driven out by the reverse $B_z$ source; and also reduces the voltage around the primary in the $\theta$ direction which is generated by the $\dot{L}I$ voltage, (where $L$ is the inductance outside the pinch which is increasing with the pinch velocity). After the pinch is formed, the $B_z$ compressed, the external circuit should not drive fast oscillations in flux until the reverse $B_z$ is fired (up to 5 $\mu$sec after the pinch is formed).

The circuit Fig. III-9 allows the current $I_{Bz}$ to build up in the heavily damped circuit $C_1$, $SW_1$, $L_1$, $R_1$, $R_2$, $L_4$, and $L_5$. At peak field, $I_{Bz}$ max, $SW_2$ is closed, dropping $I_{Bz}$ with an $L/R$ time constant of 40 $\mu$sec, also $C_1$ is clamped with $L_2$ being the only common impedance in the $I_{Bz}$ and $I_2$ circuits. Since $L_2$ is the inductance of $SW_2$

and is kept very small compared to $L_1$, $L_4$, and $L_5$, there is little modulation of $I_{Bz}$ by $I_2$. The $L/R$ decay of $I_{Bz}$ is less than 2½% if the pinch is formed within 0.5 $\mu$sec after closing $SW_2$. When the sheath compresses, the flux inside the sheath is isolated from the $B_z$ windings and the only flux outside the sheath is that driven by the external inductance $\sim$ 10% of the original. $C_2$ is charged opposite in polarity to $C_1$ such that, when $SW_3$ is closed, $I_{Bz}$ is reversed.

The initial installation will use 40 kV on $C_2$ and provide a reverse $\dot{B}_z$ of $\sim$ 5 x $10^8$ G/sec. The machine will be operated in this mode to evaluate the effect of reversing $B_z$. If necessary, $C_2$ can probably be charged to 80 kV with no major modifications to the machine, producing the specified $\dot{B}_z$ of $10^9$ G/sec.

62
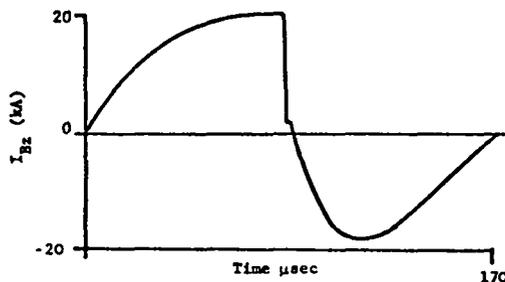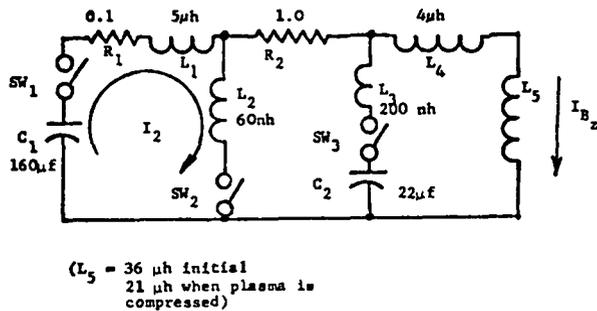
*Fig. III-9.*

*Circuit diagram and predicted time behavior of the current in the $B_z$ winding for the programmed $B_z$ field.*

### Reference

1. J. Phillips, Los Alamos Scientific Laboratory report LA-4352, p. 5.

### D. Detonator Crowbar Switch (R. Dike and R. Kewish)

The development of the detonator crowbar switch for use on ZT-1 has reached a stage where it is ready for actual test in a typical switching environment. Before using it on ZT-1, the switch will be proof-tested on the linear Z-pinch device where its reliability of operation with a system will be assured.

The basic design of the switching section as shown in Fig. III-10, uses the expanding gases of a detonator discharge to achieve a metal to metal contact between the *driven plate* and the *die plate* as shown.

The housing of the switch has been designed in such a manner that its incorporation within the ZT-1 experiment simply involves the removal of one through assembly and replacing it with the detonator switch assembly.

In its present design this switch has the following characteristics. With a peak voltage requirement of 40 to

50 kV and using a 0.030 inch thick polyethylene insulator to hold off this pulsed voltage spike, the switch will carry about 400 kA. This is assuming a current density of less than 100 kA/cm. The total closure time, that is, the time between the igniting pulse and when contact is made, is $\sim 12\,\mu\text{sec}$. This results in a metal motion time of about 5 to 5.5 $\mu$sec. The resistance in the switch contacts is about $< 10\,\mu\Omega$ and the total inductance including housing hardware is calculated to be about 20 nH.

### E. Pump-Out Port Perturbations (D. Baker, H. Karr, J. Di Marco, L. Mann, and J. Phillips)

While probing the magnetic fields in ZT-1, a 17% drop-off of the $B_z$ field at the pump-out ports was measured, Fig. III-11. A perturbation in this field had been anticipated and the holes in the primary had been kept small, $\sim 1.9$-cm diam. We have examined with computer codes the perturbations on both the $B_z$ and $B_\theta$ magnetic fields produced by the pump-outs.

1. $B_z$ Field Perturbations. Since round holes in the primary are beyond the present state of the computational art, an azimuthal symmetric slot, 1.9-cm width, is taken in the primary, inside radius 5.7 cm, (Fig. III-12). A coaxial center conductor with a 1.85 cm diam constrains the $B_z$ lines at this radial position to be parallel to the axis as seen in the experiment. The code calculates the position of flux lines and the strength of the magnetic fields. In Fig. III-11, the $B_z$ field is plotted along a radius leading out through the center of the slot. The field drops as expected with a 21% reduction at the inside surface of the porcelain wall. In Fig. III-13 is shown the radial displacement of flux lines as a function of radius. From this figure, flux lines $\sim 2.5$ mm from the wall intersect the ceramic wall at the slot. Since a round hole has a smaller effect than a slot, a probable displacement of flux lines of $\lesssim 2$ mm is expected.

2. $B_\theta$ Field Perturbations. The pump-out ports also distort the $B_\theta$ magnetic field lines of the Z current. The toroidal geometry shown in Fig. III-14 was considered. The dimensions again match those of ZT-1 with an inside conductor, which carries the Z current, of radius either one-half or three-quarters that of the primary, inside radius 5.7 cm. The perturbations are two slots, one above and the other (not shown) below the median plane. The slots are continuous around the major circumference. Figure III-14a shows the conductors and Fig. III-14b the shape of typical flux lines.

The displacements of flux lines from geometric circles which are tangent to flux lines at the maximum perturbation are shown in Fig. III-15. In case A there is
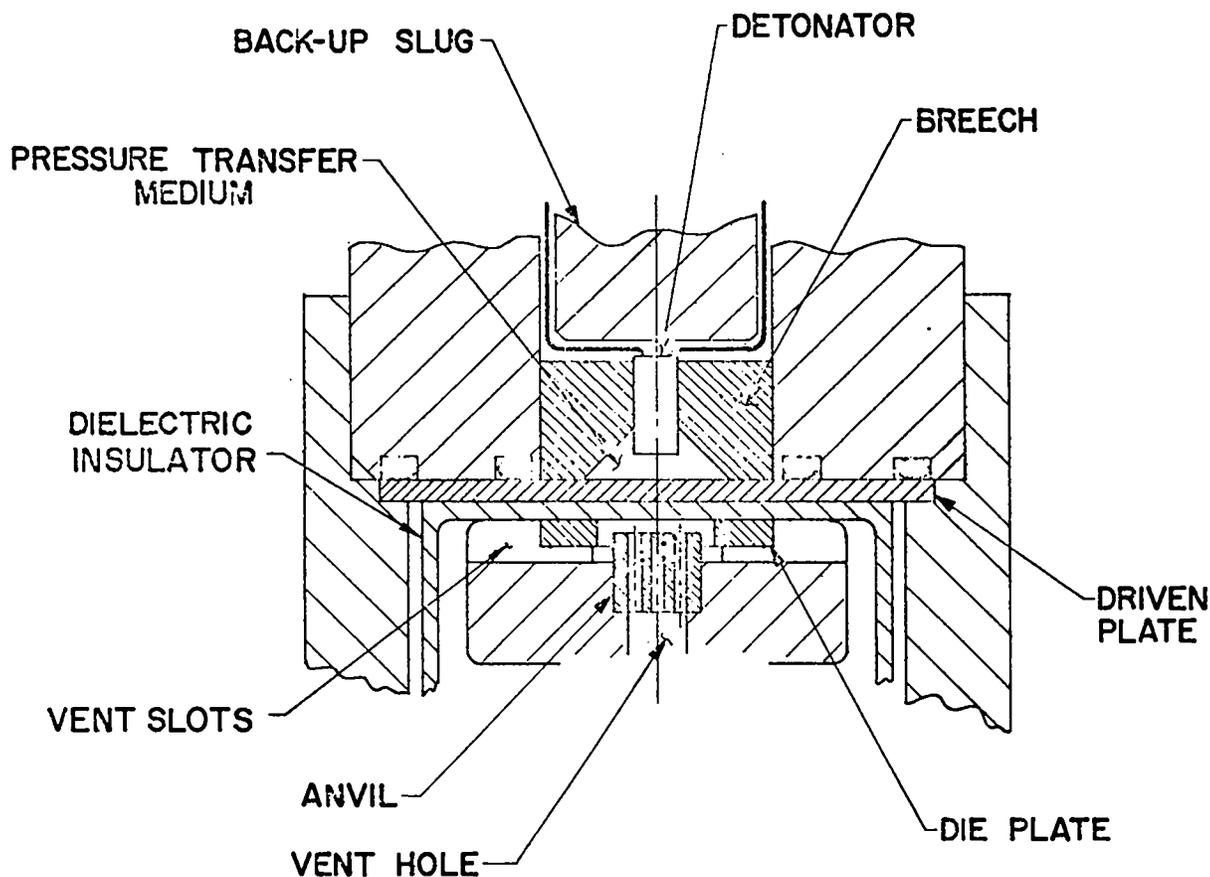
*Fig. III-10.*
*Cross section of the crowbar switch using an explosive detonator.*

no slot and the displacements $\Delta R_1$ and $\Delta R_2$ show the effect of the toroidal geometry: flux lines are compressed on the inside surface and expand at the outer surface where $\Delta R_2$ is negative. Case B is for a center conductor with one, half the primary diameter and case C the three-quarter diameter. Note that again the displacement of the $B_\theta$ lines at the position of the ceramic discharge tube is $\sim 2$ mm.

Since tolerances in the assembly of the discharge tube (76.4-cm major diam) are estimated to be $\sim 1$ mm the above estimated perturbations of $\lesssim 2$ mm, they are not considered serious.

### F. Capacitive Transfer Circuit (J. Di Marco and P. Forman)

Interruption of the current in an inductive circuit with a fuse has resulted in current transfer rates as high as $2 \times 10^{12}$ A/sec in the fast linear Z pinch. The toroidal Z

pinch has, to date, achieved $1.4 \times 10^{12}$A/sec using the same technique. One drawback is the requirement to change the fuse after every transfer. Accordingly, circuits or techniques that avoid this are being sought.

The requirements are that a rapid transfer of current be possible and, in addition, the energy source should act as a constant current system. One possible circuit is shown in Fig. III-16.

The operation of the circuit is as follows: $S_1$ is closed, establishing a current in loop 1. If $C_1 > C_2$, $C_2$ will be charged to $V_0$ at the time of peak current. $S_2$ is then closed. If the transfer condition is satisfied, namely, the current in loop 1 before transfer is equal to the current in loop 2 after transfer, the current in the resistance load will have an initial $\dot{I}$ determined by $V_0/L_2$ and a rise time of $L_2/R_L$. The important fact is that the current transfer rate is independent of $L_1$.

Assuming $C_1 > C_2$, the transfer conditions can be written

$$R_L^2 = \left(\frac{V_0}{V_0 + V_1}\right)^2 \frac{L_1}{C_2} \qquad .$$
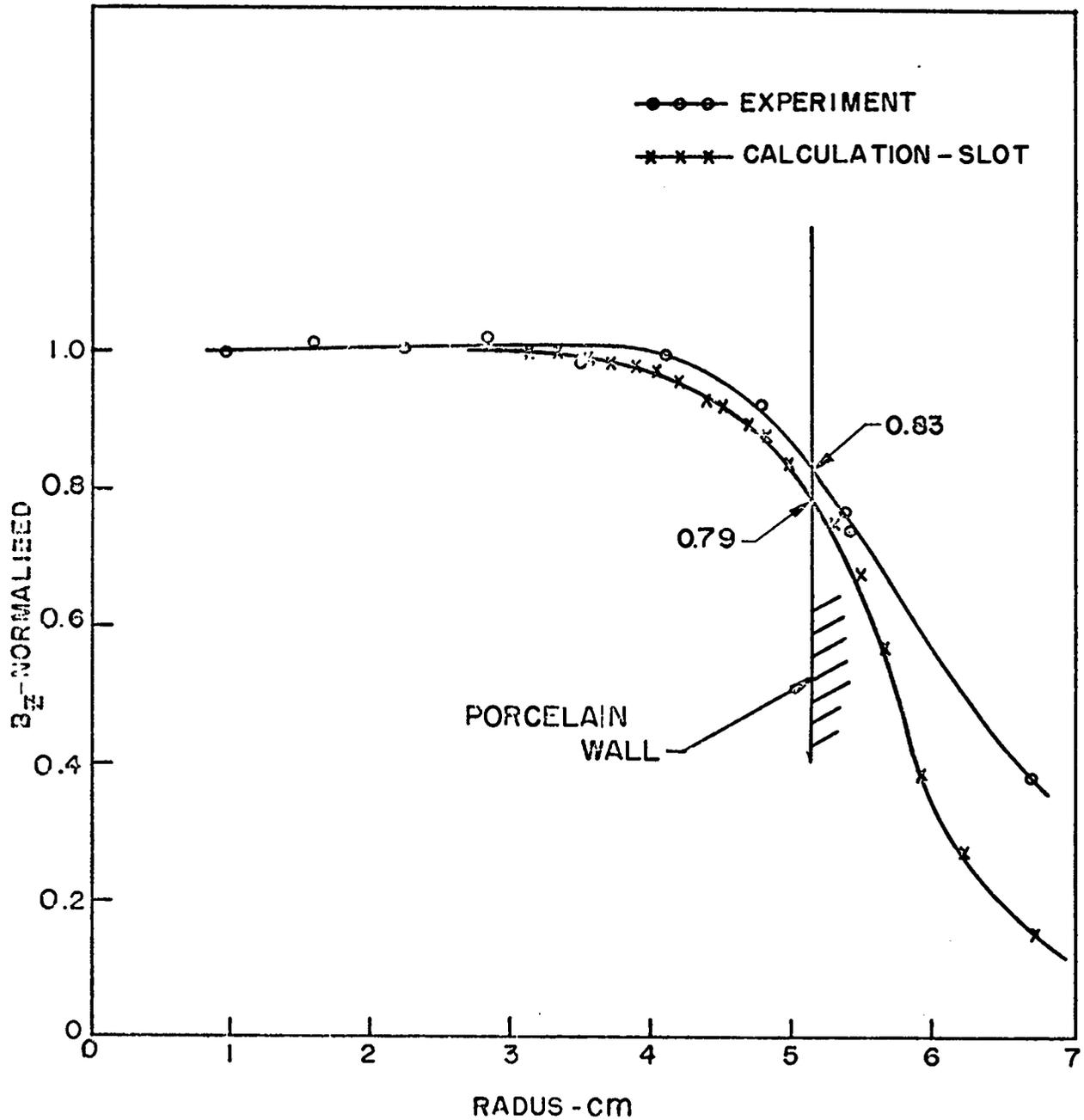
*Fig. III-11.*
*The measured radial distribution of the bias $B_z$ field compared with a numerical calculation.*

Also, the ratio of the stored energy in $L_1$ to that in $C_2$ at the time of peak current is

$$\frac{W_{L_1}}{W_{C_2}} = \frac{(V_o + V_1)^2}{V_o^2} \quad .$$

Therefore, by back-biasing $C_2$ the circuit will act inductively and should have constant current characteristics when working into a load inductance that varies in time. The current in loop 2 will oscillate with the amplitude and period determined by the pinch inductance and $C_2$. For a specified load resistance, back-biasing allows the
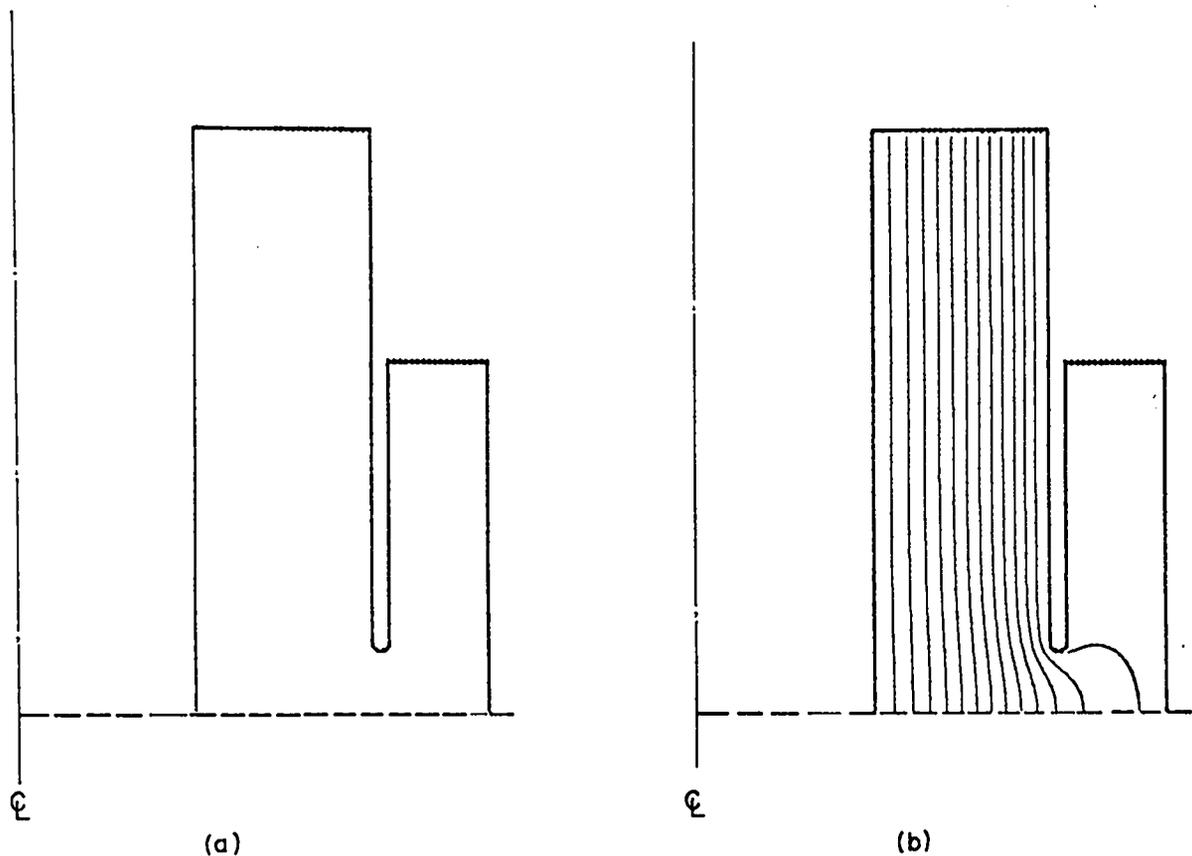
AXIAL SYMMETRY WITH 1.9 cm GAP, OUTER
CONDUCTOR 7.6 cm RADIUS AND INNER CONDUCTOR
2.8 cm RADIUS.

*Fig. III-12.*

*The geometry used in the calculation of the perturbation of $B_z$ flux lines. In (a) the azimuthal slot is shown and in (b) the distortion of the $B_z$ flux lines.*

value of $C_2$ to be reduced, thereby reducing the amplitude of the current oscillations in loop 2.

To determine the operation of this circuit with a time varying inductive load, T. Oliphant obtained a self-consistent solution with this circuit and an MHD modeling of the plasma. Some of the results are shown in Figs. III-17 and III-18. The conditions employed an $C_1 = 37\,\mu F$, $C_2 = 0.25\,\mu F$, $L_1 = 62\,nH$, $R_L = 0.25\,\Omega$, $L_2 = 12\,nH$, $V_o = 90\,kV$, and $V_1 = -90\,kV$. The small-scale oscillations of the current (0.1 $\mu$sec period) are magnetohydrodynamic in origin. The next longest scale (0.6 $\mu$sec) of oscillation is the ringing of the transfer capacitor $C_2$ with the pinch inductance. The longest scale ~10 $\mu$sec results from the series combination of $C_1$, $R_L$, and the total inductance in the circuit. The back EMF

shown in Fig. III-18 illustrates the constant current character of the circuit, for at the time of maximum constriction (~ 0.35 $\mu$sec), the voltage across the pinch has dropped. This is to be compared to a capacitive energy storage system that would develop maximum voltage across the pinch at this time. The fact that the voltage is not zero is due to the effect of the transfer capacitor.

The circuit has some of the characteristics that are required to produce large I's and an inductance match into the Z pinch. Whether its limitations are detrimental to the operation of the Z pinch can be determined only by an experiment.

66
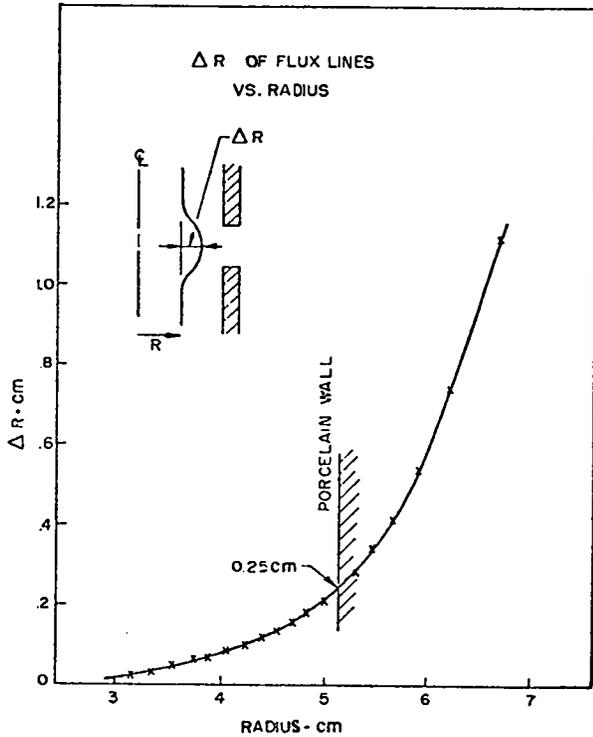
Fig. III-13.
*The radial displacement of $B_z$ flux lines at the perturbation.*

## G. MHD Stability Calculations of Axisymmetric Mixed Field Toroidal Equilibria (D. A. Baker and L. W. Mann)

Our previous work (LA-4351-MS, p. 25) allowed a complete MHD stability analysis of an axisymmetric equilibrium having poloidal fields only. For that case the problem was reduced to integrating ordinary differential equations along the equilibrium field lines. This method proved very successful in predicting stability properties of the Los Alamos quadrupole experiment, but it is not general enough to analyze toroidal Z-pinch equilibria. When toroidal field is added, the Euler-Lagrange equations, corresponding to a minimization of $\delta W$, become partial differential equations which may contain troublesome singularities. To avoid the singularity problem we decided to study $\delta W$ directly by reducing it to discrete form and studying its minimization numerically. Fortunately, a considerable amount of thought about such an approach had been done by B. R. Suydam. Exploratory testing of the approach on one-dimensional equilibria was also done by Suydam and A. Sykes. Considerable effort has been required to extend the numerical approach to apply to our numerically obtained two-dimensional equilibria. The steps involved can be sketched briefly as follows:

- Numerically compute the toroidal equilibrium in cylindrical coordinates.



(a)

(b)
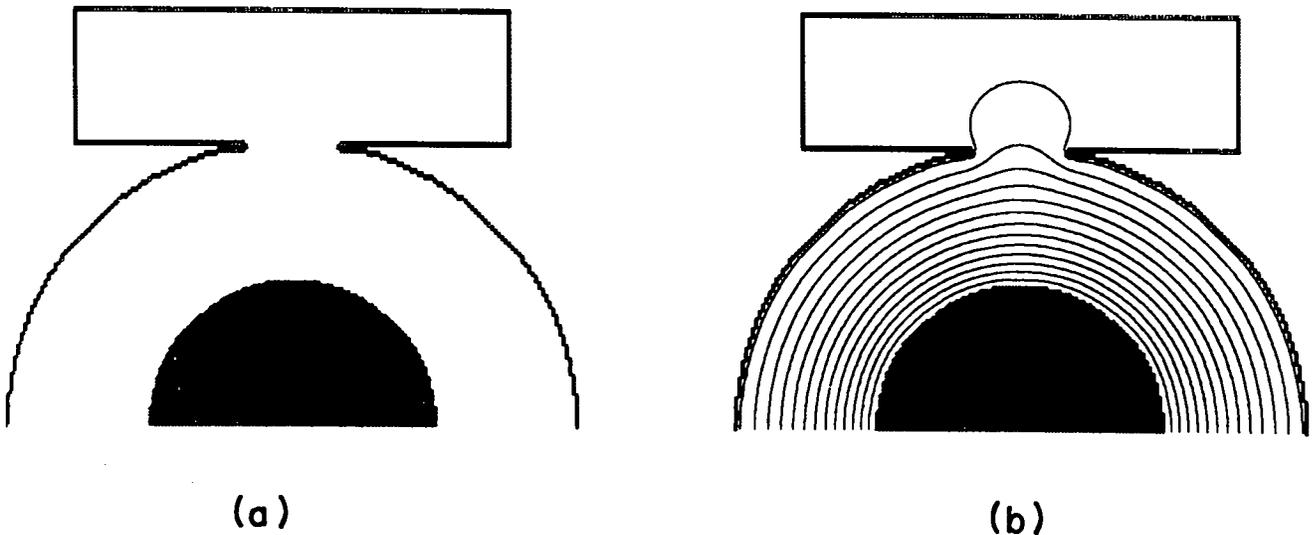
## MAJOR AXIS ON THE LEFT IN BOTH CASES.

Fig. III-14.
*The distortion of $B_\theta$ flux lines due to a slot in the primary. In (a) the slot is shown and in (b) the $B_\theta$ flux lines.*
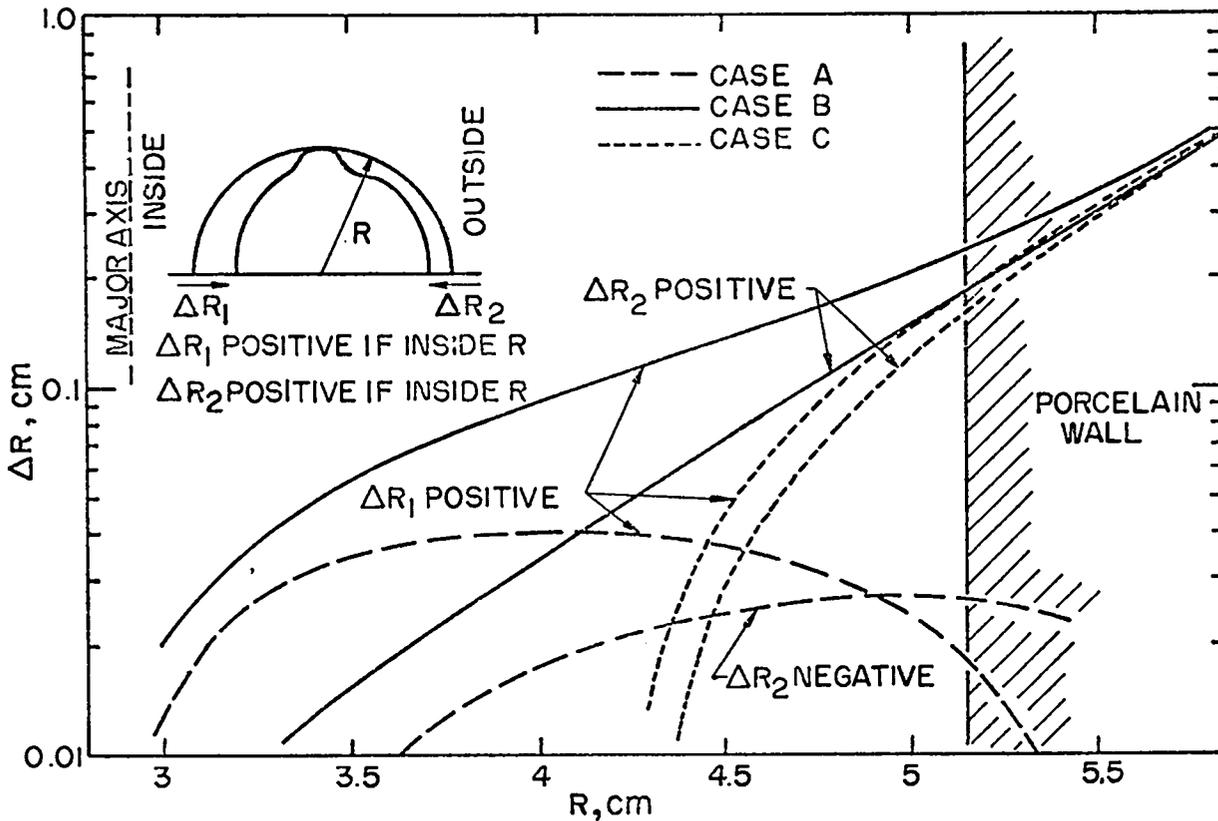
Fig. III-15.
The radial displacement of $B_\theta$ flux lines as a function of radius due to the perturbation.
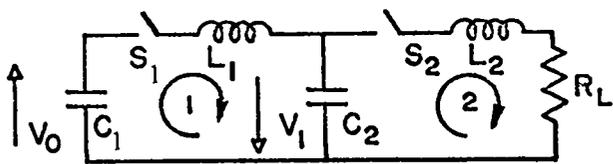


Fig. III-16.
The circuit diagram for current diversion using a capacitor.

- Introduce a new orthogonal coordinate system $(x_1, x_2, x_3)$ where $x_1$ measures position normal to the poloidal flux surfaces, $x_2$ is the toroidal angle variable, and $x_3$ measures position along the poloidal field lines.

- Fourier expand and integrate $\delta W$ with respect to $x_2$. Since the equilibrium is independent of the toroidal variable $x_2$, these modes uncouple and can be studied independently.
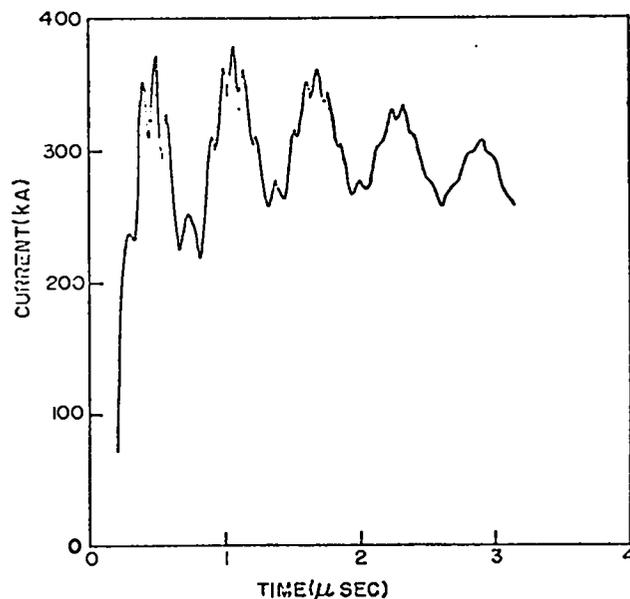


Fig. III-17.
The transferred Z-pinch current obtained by numerical calculation.
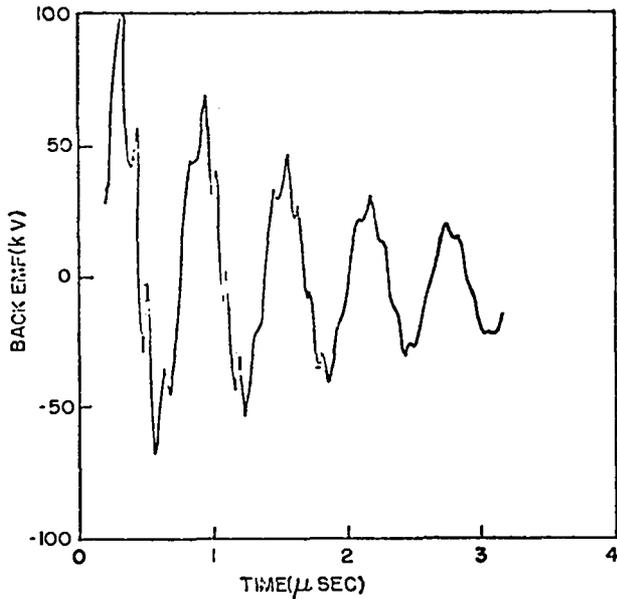
*Fig. III-18.*
*The Z-pinch voltage obtained by numerical calculation.*

- Fourier expand and integrate over the poloidal variable $x_3$. These modes are coupled, but the series can be truncated and minimized.

- The final integration over $x_1$ is written in finite difference form; the result is a large quadratic form.

- Test this quadratic form to see if it is positive definite. The system is stable, i.e., $\delta W > 0$ (within the resolution of the numerical calculation) if, and only if, this quadratic form is positive definite.

The major share of the computer time is taken up in the equilibrium calculation and diagonalizing the matrix (see last step above).

Extensive testing of the program is currently being done using the pressureless Bessel function model and the hard-core pinch. Further comparison checks are planned for Tokomak stability calculations in coorperation with the University of Texas.

Once confidence in the numerical procedures is established, the program will be used to find stable Z-pinch toroidal equilibria. The stability of noncircular cross section Z pinches will also be investigated.

## H. Shock Heating of a Z Pinch (T. Oliphant and P. Forman)

A study has been made of the shock heating that can be produced in a Z pinch with stabilizing $B_z$ bias field relative to the amount that can be produced in the absence of this biasing field if stability were not a consideration. This study has been divided into two parts, 1) plane wave, steady-state shock theory, and 2) cylindrically symmetric converging shock driven by a constant magnetic piston pressure, calculated by numerical differencing in Lagrangian coordinates.

In the plane wave, steady-state shock theory, the upstream quantities $(p_1, \rho_1, v_1, B_1)$ are related to the downstream (shocked) quantities $(p_2, \rho_2, v_2, B_2)$ by the Rankine-Hugoniot relations and a total pressure $P$ is defined by

$$P = p + \frac{B^2}{8\pi} . \tag{1}$$

The following normalized pressures are defined,

$$\tilde{P} = \frac{P_2}{P_1} , \quad P_B = \frac{B_1^2}{8\pi p_1} . \tag{2}$$

The change in temperature of the plasma as a result of the passage of the shock wave is given by

$$\Delta T = T_2 - T_1 . \tag{3}$$

This quantity is parameterized in terms of the quantities defined in Eq. (2). The quantity of interest is the ratio of this $\Delta T$ with bias field present to that without bias field present. This is given by

$$R(\tilde{P}, P_B) = \frac{\Delta T(\tilde{P}, P_B)}{\Delta T(\tilde{P}, 0)} , \tag{4}$$

For steady-state, plane shock this quantity is easily obtained from the Rankine-Hugoniot relations. The lower curve in Fig. III-19 is a plot of R vs $\tilde{P}$ for $P_B = 21.4$. For comparison, the upper curve was plotted from the results of the numerical, cylindrical case. The data represent the actual example calculations. For the numerical case we ran each problem with $T_1 = 5$ eV, $n_1 = 10^{15}$ cm$^{-3}$, tube length = 30 cm, initial plasma diameter = 5 cm, $\sqrt{8\pi p_1} = 448$ gauss, $B_1 = 2.07$ kG. These conditions correspond to the $P_B = 21.4$ of the plane wave theory and the piston pressures $P_2$ varied between 3.17 kG and 10.0 kG corresponding to the values of $\tilde{P}$ plotted in Fig. III-19.
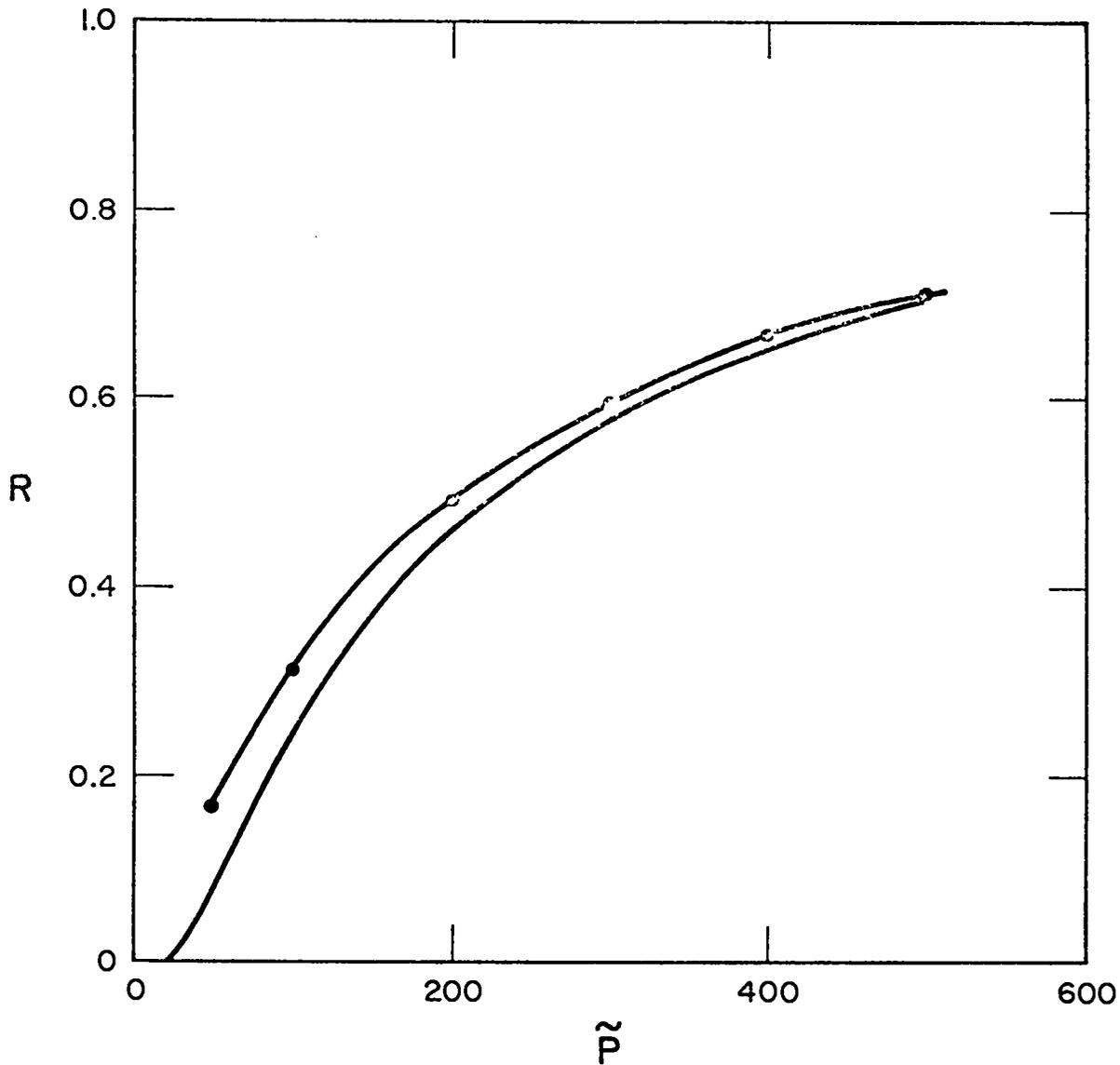
*Fig. III-19.*

*The ratio R of the temperature increase with and without a bias field as a function of the parameter $\tilde{P}$. The lower curve is for the case $P_B = 2.14$. The upper curve is the result of MHD numerical calculations in cylindrical geometry.*

Actually, both curves approach 1.0 asymptotically as $\tilde{P} \to \infty$. However, stability considerations limit the usable portion of the curve roughly to that plotted in Fig. III-19. The interesting point is that R rises above 50% for the projected, stable experimental conditions.

**I. Nonlinear Diffusion Problem** (Albert Haberstich and Bergen Suydam)

One way of simulating anomalous diffusion in numerical MHD calculations is to replace the classical

resistivity $\mu_c$ locally by a larger anomalous value $\mu_a$ whenever the current density j exceeds a critical value $j_c$.[1,2] Since the electric field in the plasma must be continuous, the transition is usually carried out over a current density interval $\Delta j$.

To study the properties of such numerical solutions we have considered the following one-component, one-dimensional problem:

$$\frac{\partial B}{\partial t} = \frac{\partial}{\partial x}\left(\mu\,\frac{\partial B}{\partial x}\right) \quad ,$$

where $\mu$ is of the form

$$\mu = \begin{cases} \mu_c & ,\ j \leqslant j_2 \\[2mm] \mu_c + (j - j_2)\dfrac{\mu_a - \mu_c}{j_1 - j_2} & ,\ j_2 < j < j_1 \\[2mm] \mu_a & ,\ j \geqslant j_1 \end{cases}$$

with

$$j = \left|\frac{\partial B}{\partial x}\right|,\ j_1 = j_c + \Delta j/2\ \text{and}\ j_2 = j_c - \Delta j/2 \ .$$

The problem has a traveling wave solution, that is, a solution traveling undistorted at constant velocity v, of the type shown in Fig. III-20. B(x,t) then consists of a leading edge where $j < j_2$, a trailing edge where $j > j_1$, and a transition region where $j_1 \geqslant j \geqslant j_2$. Letting $j(x_1) = j_1$ and $j(x_2) = j_2$, we find:

$$x_2 - x_1 = \frac{1}{v}\left[2(\mu_a - \mu_c) + b \ln\frac{\mu_c + b}{\mu_a + b}\right] \quad ,$$

where

$$b = \frac{\mu_a j_2 - \mu_c j_1}{j_1 - j_2} \quad .$$

Thus, the width of the transition region remains finite and the electric field remains continuous as $\Delta j$ goes to zero.

The same problem has been solved numerically with implicit and explicit flux-conserving, finite-difference schemes,[3] and the results compared against the analytic solution. The explicit RMS error averaged over the transition region, for example, is found to be of the order of $3 \times 10^{-5}$ at time $t = 1$, for $\Delta x = 0.05$ and $\Delta t = 10^{-4}$, under the conditions of Fig. III-20. The implicit solution converges in the sense that the error is approximately proportional to $(\Delta x)^2$ and that it decreases with $\Delta t$ for small values of $\Delta x$.

In Fig. III-21a are plotted explicit values of $x_1$ and $x_2$ as functions of time, for $\Delta j = 0.1$. The result agrees within a mesh size with the analytic prediction. Figure III-21b shows the corresponding result for $\Delta j = 0$. The
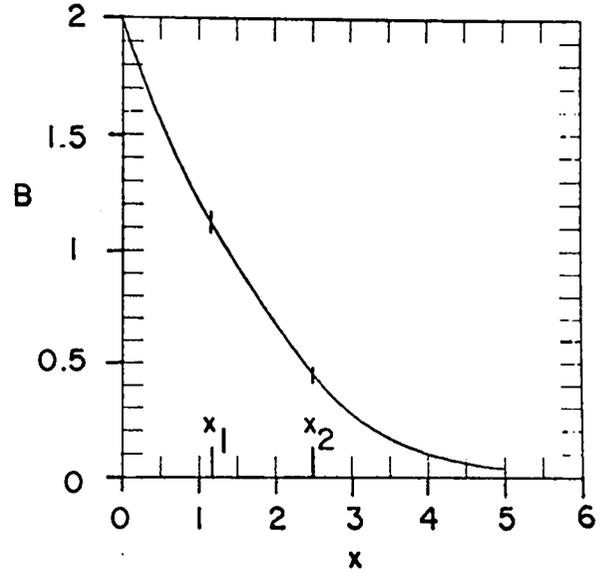


Fig. III-20.
Traveling wave solution B(x,t) with $v = 1$, $\mu_c = 1$, $\mu_a = 2$, $j_c = 0.5$, and $\Delta j = 0.1$, at $t = 0$.

transition region in this case is oscillatory. The oscillation appears for values of $\Delta j$ smaller than a certain threshold, which is of the order of 0.045 in the present situation.

Figures III-22a and -22b show explicit solutions of the diffusion equation with the initial and boundary conditions

$$B = \begin{cases} 0 & ;\ x \geqslant 0,\ t \leqslant 0, \\[2mm] 1.9; & x = 0,\ t > 0, \end{cases}$$

for $\Delta j = 0.1$ and 0, respectively. A transition region develops in both cases and travels away from the origin at nearly the same speed. The transition region is somewhat narrower for $\Delta j = 0$, as one would expect from the traveling wave solution. A comparison of B(x,t) at $t = 1$ shows a difference of less than 1% between the two cases. Similar calculations have been carried out for ratios $\mu_a/\mu_c$ of 10 and 100. The magnitude of the leading edge is then greatly reduced, the transition region becomes somewhat wider, and the overall rate of diffusion is essentially governed by $\mu_a$.
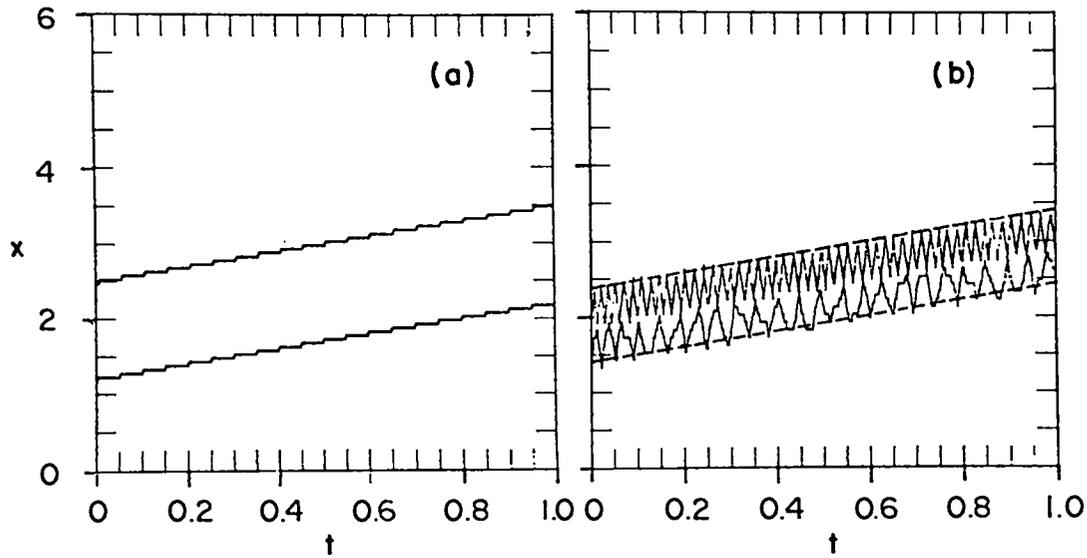
*Fig. III-21.*

*Position of the transition region of the traveling wave solution as function of time. (a) $\Delta j = 0.1$, (b) $\Delta j = 0$.*
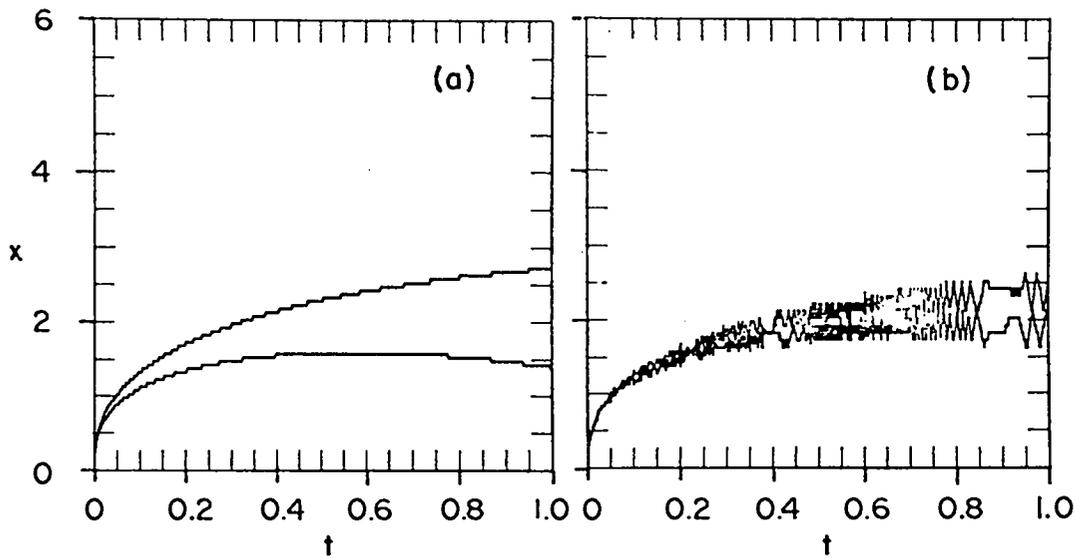


*Fig. III-22.*

*Position of the transition region of the fixed boundary solution as function of time. (a) $\Delta j = 0.1$, (b) $\Delta j = 0$.*

### References

1. H. A. B. Bodin, J. McCartan, and G. H. Wolf, Third European Conference on Controlled Fusion and Plasma Physics, Utrecht, June 23-27, 1969.

2. A. Haberstich, Los Alamos Scientific Laboratory report LA-4585-MS, p. 37.

3. R. D. Richtmyer, *Difference Methods for Initial-Value Problems*, New York, 1957, p. 93, Cases 1 and 3.

# IV. EXPERIMENTAL PLASMA PHYSICS GROUP PROGRAM

## A. Summary (H. Dreicer)

During the past year we concentrated our experiments on the very fundamental process of microwave absorption near the electron plasma frequency. We find that parametric instabilities involving the simultaneous excitation of high- and low-frequency plasma oscillations appear to control the absorption, provided that threshold electric fields are exceeded. This parametric process is closely related to a wide range of plasma phenomena in which decay into several waves limits the amplitude of an unstable wave in its nonlinear regime. This mechanism may play an important role in determining the dc electrical resistivity of a nearly collisionless plasma. Our experimental determination of the threshold conditions for the onset of anomalously large ac absorption and anomalous electron heating is, therefore, a matter of great importance, the more so because our measurements are carried out in simple geometry devoid of sheath effects, end effects, and toroidal geometry effects.

I expect our work to clarify not only the problem of the ac electrical resistivity, but to elucidate many features of the dc problem as well. Potential benefits also exist for the program devoted to laser heating of very dense plasmas,[1] for the understanding of powerful radar propagation through the ionosphere,[2] and for the utilization of intense RF fields to heat, confine, and stabilize CTR plasmas.

The rate at which this work can progress is presently limited by the shortage of available scientific manpower. In an indirect attempt to alleviate this situation we have improved the speed and accuracy of data acquisition by interfacing our measuring instruments with fast computer storage. This system is nearly operational now, and was primarily D. G. Henderson's responsibility.

An electron injector was successfully developed, with the collaboration of D. Ignat, for synchrotron radiation studies. This device routinely produces a $\sim$ 1 kV, $\sim$ 200 $\mu$A electron beam in a magnetic field with a perpendicular-to-longitudinal energy ratio of 20 to 100. A study of its synchrotron emission during traversal of a long waveguide shows it to be a profuse source of synchrotron radiation due to the relativistic maser effect.[3] The possibility of simultaneous intense coherent synchrotron emission due to prebunching of the beam electrons by the injector remains to be investigated. Eventual injection of this electron beam into plasma for the purpose of studying CTR cynchrotron radiation-loss problems depends upon the availability of manpower.

Theoretical work is under way on several fronts to support the experimental program. However, our requirements in this area far surpass our ability to fill these needs, again, because of severe manpower limitations.

Earlier this past year, two members of the group became interested in the need to initiate fundamental studies of the neutron damage problem which faces every conceivable controlled fusion reactor. The result is an assessment of existing intense neutron sources and the conclusion that the expected D-T fusion reactor neutron fluxes could be simulated by an ion accelerator bombarding a dense supersonic gas target, a development which would utilize existing technology. An appraisal of this proposal will be carried out at LASL.

Several years ago, in anticipation of our future magnetic field requirements, we began to improve the quality and flexibility of the dc power supplies available for this purpose. Although manpower limitations forced this project to move very slowly, it is now essentially completed. As a result we have available up to 3 MW of steady-state power in combinations of 500 kW, 1.25 MW, and 1.25 MW (or 2.5 MW), with a current stability of one part in $10^4$ against fast transients and slow drifts. Only minor, but nevertheless important, engineering improvements related to ensuring operations reliability remain to be carried out. The main responsibility for this job was carried by J. Rand and J. McLeod. Its completion makes possible the installation of the existing large, 5-ft-diam pancake coils with which we hope to extend our research possibilities during the coming years. N. Gardner and A. Mondragon have provided expert assistance in all phases of the group's experimental activities.

## References

1. J. P. Freidberg and B. M. Marder, Phys. Rev. A, 4, 1549 (1971).

2. W. F. Utlaut, J. Geophys. Res. 75, 6402 (1970).

3. R. Q. Twiss, Australian J. Phys. 11, 564 (1958).

## B. Anomalous Microwave Absorption Near the Plasma Frequency (H. Dreicer, D. B. Henderson, J. C. Ingraham, and F. E. Wittman)

We have observed[1] the absorption of intense electromagnetic waves near the critical density on a plasma profile, where the electron plasma frequency $\omega_p$

approximately equals the wave frequency $\omega$. Theory indicates the possibility of enhanced absorption[2] when the intense fields excite high-frequency instabilities.[3-5] Our measurements were made on the highly ionized plasma column of our single-ended Q-machine. By operating over a large range of electric fields and plasma densities, our measurements yield: 1) a quantitative value for the classical resistivity; 2) the threshold electric field for the onset of instability and anomalous dissipation; 3) an experimental estimate for the anomalous dissipation under conditions shown to be free of electron inelastic effects; and 4) evidence for the production of energetic electrons. The experiment determines the absorption by plasma of microwave energy stored in a 11.7-cm-diam $TM_{010}$ microwave cavity. The cavity resonates near 2 GHz with a Q of 21,700 without plasma, and is coaxial with the plasma column for 8.6 cm. The microwave electric field is primarily axial and parallel to $B_0$. The distribution of vacuum electric-field components in the cavity, known for the actual geometry from numerical computations,[8] is used to relate $\Delta f$ to $\omega_p^2$. The measured increase in inverse Q, $\Delta(1/Q)$, is equal to the additional energy absorption per radian caused by the plasma, divided by stored cavity energy. In analyzing our data we use the perturbation-theory results[9] for $\Delta f$ and $\Delta(1/Q)$, which are based on the assumption that the vacuum fields are not disturbed by the plasma. In the stable regime this assumption is valid[10] because the collisionless plasma skin depth, $(c/\omega)[(\omega_p/\omega)^2 - 1]^{-1/2}$, is never smaller than the plasma diameter in our experiment. At each plasma density we measure Q and the peak microwave field $E_0$ for a range of incident microwave powers. We also monitor the power $P_T$ transmitted through the resonator. The measurements of $\Delta(1/Q)$, which are summarized in Fig. IV-1 for four densities, show enhanced absorption provided the density

is large enough. The assumed profile (identified on Figs. IV-1 and -2) is in good agreement with measured profiles.

At these high densities, $\Delta(1/Q)$ increases sharply at the threshold described in Fig. IV-2, in terms of the ac drift speed $V_E = eE_0/(m\omega)$ and the electron thermal speed $V_T = \sqrt{2kT/m}$.

Figure IV-2 also compares our measured values to the theoretical threshold predicted by the ac two-stream instability theory[5-7] for two values of the growth rate $\gamma$. Although this theory describes a uniform infinite plasma, we apply it locally to the density profile. In this we assume that the threshold for the finite plasma is the minimum threshold for the density range encountered on the profile. For large $\omega_p^2$, $\Delta f > 85$ MHz, the theoretical minimum threshold is due to those electrons on the wings of the density profile for which $1.0 > (\omega_p/\omega)^2 > 0.90$, rather than due to those near the center of the plasma column where $\omega_p = \omega_{po}$ and $(\omega_{po}/\omega)^2 > 1$. The electron collision rate used in the calculation includes both electron-ion collisions and an effective collision rate due to Landau damping. The profile radius is adjusted so that experiment and theory agree at $\Delta f = 80$ MHz. The theoretical curves for the decay parametric instability[3,4] would be quite similar to the theoretical curves on Fig. IV-2.

Figure IV-3 shows $\Delta(1/Q)$ as a function of $(\Delta f/f)^2$ at low power. We believe that this is the first report of an observation that can be compared quantitatively with the weak-field theory for the high-frequency resistivity.[11] This comparison, carried out for three different density profiles, takes into account the radial variation of density in the volume integration of the resistive part of the plasma dielectric coefficient.



Fig. IV-1.
$\Delta(1/Q)$ vs $P_T$ (in MW) for four densities.
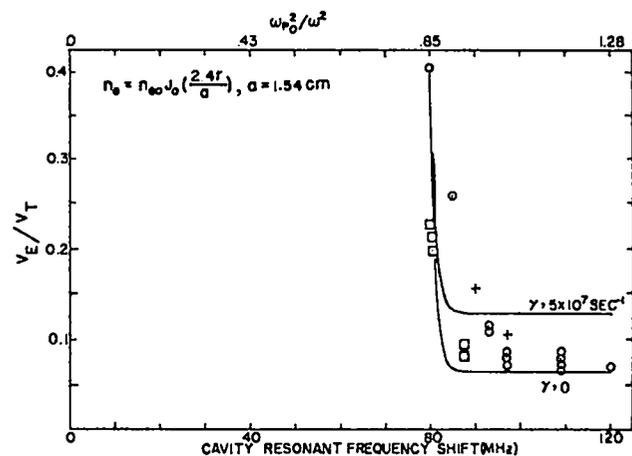


Fig. IV-2.
Threshold $v_E/v_T$ values vs $\Delta f$ or $\omega_{po}/\omega^2$. Points are measured data. Solid lines are from theory.
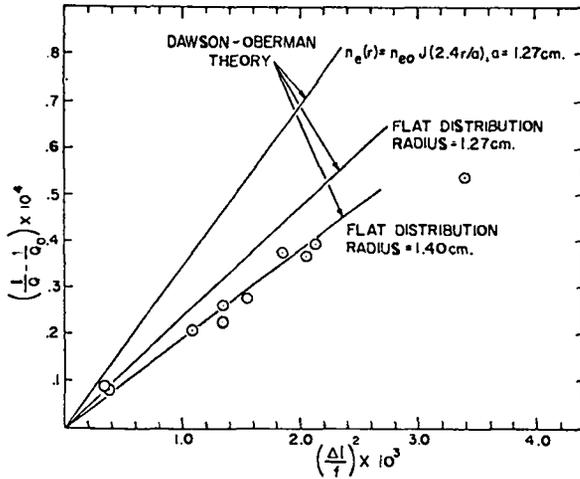
*Fig. IV-3.*
*Low-power $\Delta(1/Q)$ vs $(\Delta f/f)^2$. Points are measured data. Solid lines are from theory for three different assumed profiles.*

Examination of the current $I_{ce}$ drawn by a cold plane collector plate, outside of the resonator (see Fig. IV-5), discloses the appearance of a pulse (see insert in Fig. IV-4)

whenever unstable conditions exist. This pulse is believed to be due to electrons because its peak amplitude $I_{ceo}$ decreases as the collector voltage $V_c$ is biased more negatively. The onset of $I_{ceo}$, as shown in Fig. IV-4, agrees with the threshold found from the resonator's response curves. Further observations are described in the Section IV-C.

We have found no influence upon the threshold due to electron inelastic collisions with $K^+$ ions or background K atoms. By varying the hot plate temperature, with potassium flux F to the hot plate held constant, it is possible to vary $\omega_p^2$, although the K-atom density $n_g$ remains constant. In this case, the threshold results near $\Delta f = 75\text{-}85$ MHz (Fig. IV-2) were found to be identical with those observed when $\omega_p^2$ is varied by changing F. The sudden increase in $\Delta(1/Q)$ observed with increasing $v_E/v_T$ is found to be strictly a function of $\omega_p^2$ rather than $n_g$. Another technique used[1] also rules out ionization as a sudden microwave dissipation source.

## REFERENCES

1. H. Dreicer, D. B. Henderson, and J. C. Ingraham, Phys. Rev. Letters 26, 1616 (1971).
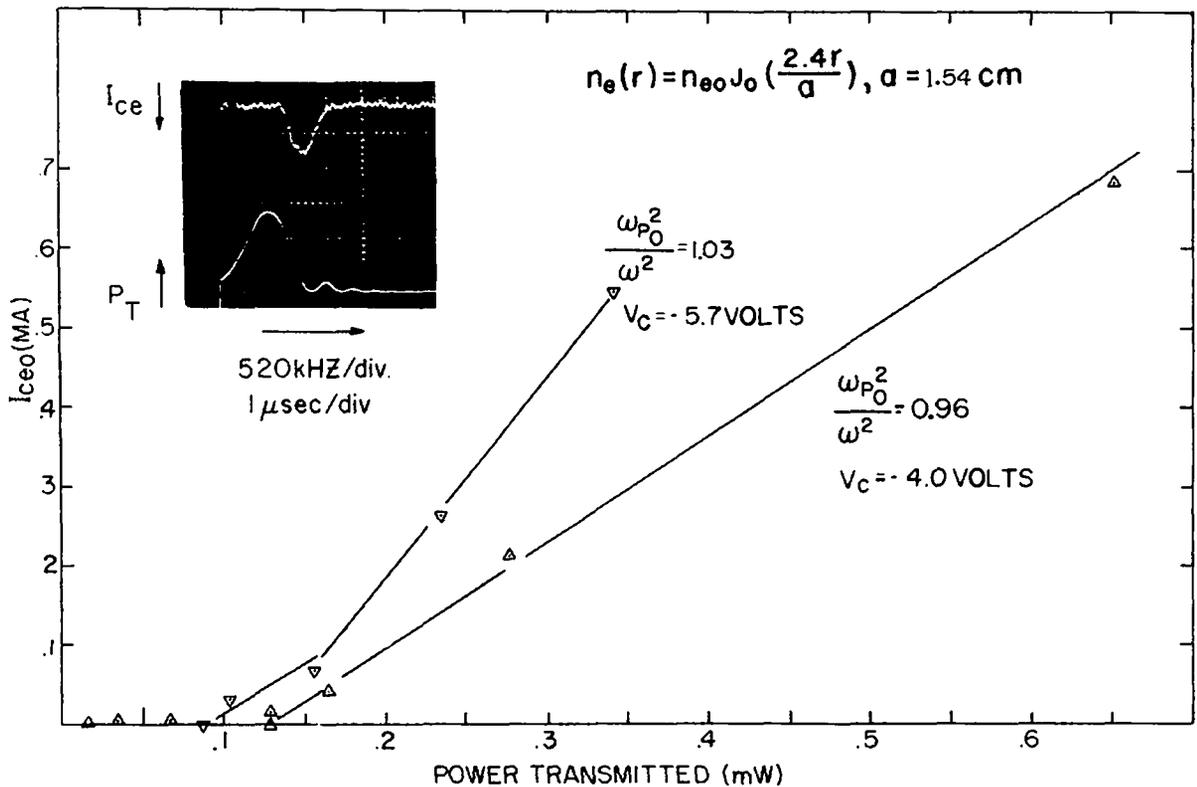
*Fig. IV-4.*
*$I_{ceo}$ vs $P_T$ (in mW) for two plasma densities. Insert shows electron current collected and $P_T$ vs t.*

2. W. L. Kruer, P. K. Kaw, J. M. Dawson, and C. Oberman, Phys. Rev. Lett. 24, 987 (1970).

3. D. F. Dubois and M. V. Goldman, Phys. Rev. Lett. 14, 544 (1965).

4. V. P. Silin, Zh. Eksp. Teor. Fiz. 48, 1679 (1965) [Sov. Phys. JETP 21, 1127 (1965)].

5. K. Nishikawa, J. Phys. Soc. Jap. 24, 916, 1152 (1968).

6. P. K. Kaw and J. M. Dawson, Phys. Fluids 12, 2586 (1969).

7. J. R. Sanmartin, Phys. Fluids 13, 1533 (1970).

8. H. Dreicer and W. F. Rich, in Proceedings of the International Conference on Physics of Quiescent Plasmas, Paris, 1968 (Ecole Polytechnique, Paris, France, 1969), Part III, p. 135.

9. V. E. Golant, Zh. Tekh. Fiz. 30, 1265 (1960) [Sov. Phys. Tech. Phys. 5, 1197 (1961)].

10. S. J. Buchsbaum, L. Mower, and S. C. Brown, Phys. Fluids 3, 806 (1960).

11. J. M. Dawson and C. R. Oberman, Phys. Fluids 5, 517 (1962), and 6, 394 (1963).

## C. Excitation of Plasma Oscillations and Anomalous Heating of Electrons (J. C. Ingraham, H. Dreicer, and F. E. Wittman)

Our microwave-absorption experiment has provided clear evidence that the absorption becomes anomalously large when the electric field strength exceeds the threshold value documented in Fig. IV-2. This result raises the question: Where is the anomalously absorbed energy deposited? While our studies on this subject are incomplete, we do have experimental evidence that some of the energy is channeled into plasma waves and ultimately into electron kinetic energy.

Our observations are carried out with the several probes shown in Fig. IV-5. The cold end collector probe C is biased negatively at $V_c$ to collect all positive ions and reflect all electrons whose axial energy is less than $U = e (\Phi - V_c)$, where $\Phi$ is the plasma potential. The probe marked RF consists of a 0.05-in.-o.d., 50 $\Omega$ microwave coaxial probe detector which can be moved axially and transversely through the plasma column and, like collector C, can also be used as an ion saturation current detector. In FM operation (transient filling of the resonator), both of these probes record time-delayed current pulses provided that the resonator's fields exceed the threshold given in Fig. IV-2. An example of the transit time delay between the current pulse and the application of microwave power is shown in Fig. IV-4. This current pulse, seen on both probes, is believed to be due to electrons, because its peak amplitude $I_c$ decreases as the collector voltage $V_c$ is biased more negatively. Figure IV-6
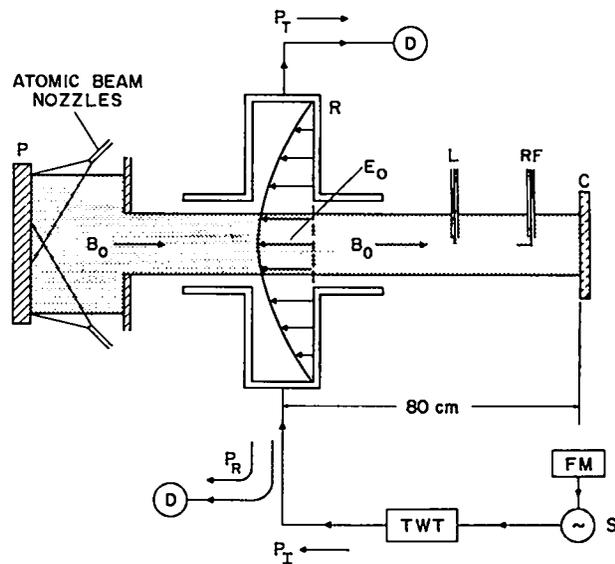


*Fig. IV-5.*

*Experimental layout showing: Q-machine hot plate (P), plasma column, and collector (C); microwave resonator (R) and microwave circuitry; Langmuir (L) and RF probes.*
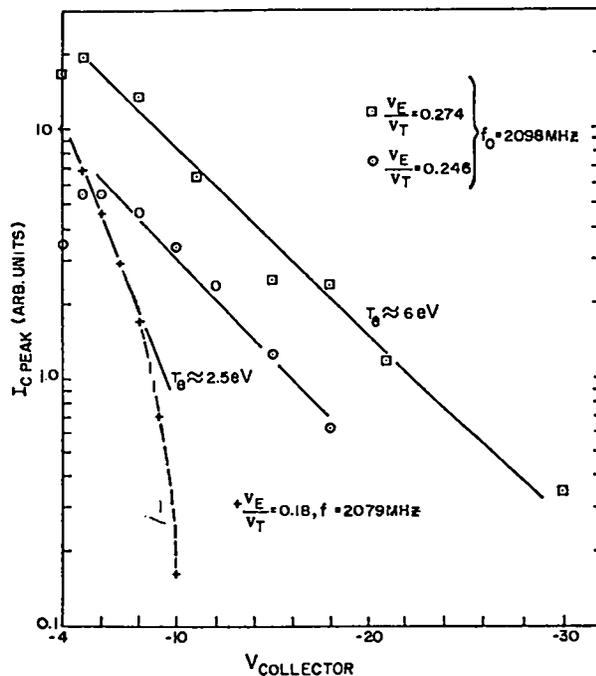


*Fig. IV-6.*

*Semilog plot of peak of electron pulse measured by collector vs. retarding voltage (for electrons) on the collector ($f_o$ = 2098 MHz and $f_o$ = 2079 MHz correspond, respectively, to cavity resonant-frequency shifts of 107 and 88 MHz on Fig. IV-2).*

shows the result of such retarding potential measurements carried out at two different densities. Well into the unstable density regime, defined in Fig. IV-2, we find hot electrons whose energy $kT_e/e = 6$ eV is about 20 times larger than their original energy ($kT_e/e \approx 0.25$ eV). This measurement is in reasonable agreement with the energy deduced from the transit time delay seen on the two probes.

A study of the radial distribution of this current pulse at low densities ($\omega_{po}^2/\omega^2 \approx 0.85$) shows it to be more highly peaked and concentrated near the axis of the plasma column than the radial density profile. When the density is just high enough, such that a high-frequency plasma wave is detected with the RF probe, then the wave amplitude is also concentrated in radius. For the range of plasma densities studied, these observations are consistent with the excitation of parametric instabilities near $\omega_p$.[1-3]

## REFERENCES

1. D. F. Dubois and M. V. Goldman, Phys. Rev. Letters 14, 544 (1965).

2. V. P. Silin, Zh. Eksp. Teor. Fiz. 48, 1679 (1965) [Sov. Phys. JETP 21, 1127 (1965)].

3. K. Nishikawa, J. Phys. Soc. Jap. 24, 916, 1152 (1968).

4. P. K. Kaw and J. M. Dawson, Phys. Fluids 12, 2586 (1969).

5. J. R. Sanmartin, Phys. Fluids 13, 1533 (1970).

## D. New Techniques for Rapid Q Measurements (J. C. Ingraham and H. Dreicer)

Our experimental determination of the microwave absorption near the electron plasma frequency is based upon a Q measurement made on a plasma-filled resonator. An important limitation on this measurement is due to the inherent low-frequency electron-density fluctuations in the plasma. These occur at frequencies below 10 kHz and have an amplitude that causes the cavity resonant frequency to fluctuate over a frequency range as large as several MHz. Although this corresponds to only a few percent change in electron density for typical operating conditions, this excursion is much greater than the 100 to 500 kHz natural width of the cavity resonance. Thus, it is impractical to measure the cavity Q using the usual technique of slowly sweeping the oscillator frequency over the region of the cavity resonance while monitoring the power transmitted through the cavity. It is necessary in this case either 1) to sweep the oscillator frequency sufficiently rapidly across resonance so that the electron density does not change appreciably in this time (rapid

FM method), or 2) to apply a resonant exciting signal to the cavity and observe the rapid decay of the power transmitted by the cavity following the even more rapid termination of the signal incident on the cavity (AM method).

The performance and application of the FM method (Fig. IV-7) has been described by us elsewhere.[1,2] The AM method operates as follows. We employ the self-oscillating microwave circuit shown in Fig. IV-7 to keep the resonator fully excited[3] despite the changes in resonant frequency $\omega_0(t)$ produced by ambient density fluctuations. This requires that the gain of the amplifier (a traveling wave tube type) is sufficient to overcome the absorpiton of the remainder of the circuit, and that the total signal phase shift around the circuit is an integral multiple of $2\pi$. The resonator Q is then measured by suddenly switching the incident power to the resonator to zero and observing the time rate-of-change of the transmitted power $P_T$. The instantaneous Q can then be deduced from the relation

$$\frac{1}{P_T} \frac{dP_T}{dt} = - \frac{\omega_0(t)}{Q(t)} \quad,$$

provided

$$\left| \frac{d}{dt}(\log \omega_0) \right| \ll \omega_0/Q$$

and

$$\left| \frac{d}{dt}(\log Q) \right| \ll \omega_0 \quad.$$

Figure IV-8 illustrates the operation of this system with a comparison of the decay of the powers incident on, and transmitted by, the empty resonator in the switched AM mode. Preliminary measurements indicate that the anomalous absorption properties determined with the AM method agree with our earlier results obtained with the FM method. The AM technique is, however, easier to interpret since nearly instantaneous Q and electric field measurements can be made in the initial decay period immediately following steady-state excitation, while the FM technique tends to provide values that are averaged over the entire sweep through resonance.

## REFERENCES

1. H. Dreicer, D. B. Henderson, and J. C. Ingraham, Phys. Rev. Letters 26, 1616 (1971).

2. J. C. Ingraham and H. Dreicer, Los Alamos Scientific Laboratory report LA-4585-MS, p. 69, (1970).

3. H. Dreicer and J. McLeod, Los Alamos Scientific Laboratory report LA-4351-MS, p. 89 (1969).

## FM METHOD

```
┌──────────┐   ┌──────────┐   ┌──────────┐   ┌──────────┐
│    FM    │→  │OSCILLATOR│→ │ AMPLIFIER│→ │ VARIABLE │→  ◯
│ MODULATOR│   │          │   │          │   │ATTENUATOR│
└──────────┘   └──────────┘   └──────────┘   └──────────┘   RESONATOR
```

```
┌──────────┐
│ DETECTOR │ ←──────────────────────────────
└──────────┘
```

## AM METHOD

```
              ┌──────────┐   ┌──────────┐   ┌──────────┐
           ┌→ │   LINE   │→ │ AMPLIFIER│→ │ VARIABLE │→  ◯
           │  │ STRETCHER│   │          │   │ATTENUATOR│
           │  └──────────┘   └──────────┘   └──────────┘  RESONATOR
┌──────────┐  ┌──────────┐
│    AM    │→ │   FAST   │
│ MODULATOR│  │  SWITCH  │
└──────────┘  └──────────┘
              ↑
         ┌────┘ 10dB
┌──────────┐ │  DIRECTIONAL
│ DETECTOR │←┘  COUPLER
└──────────┘
```
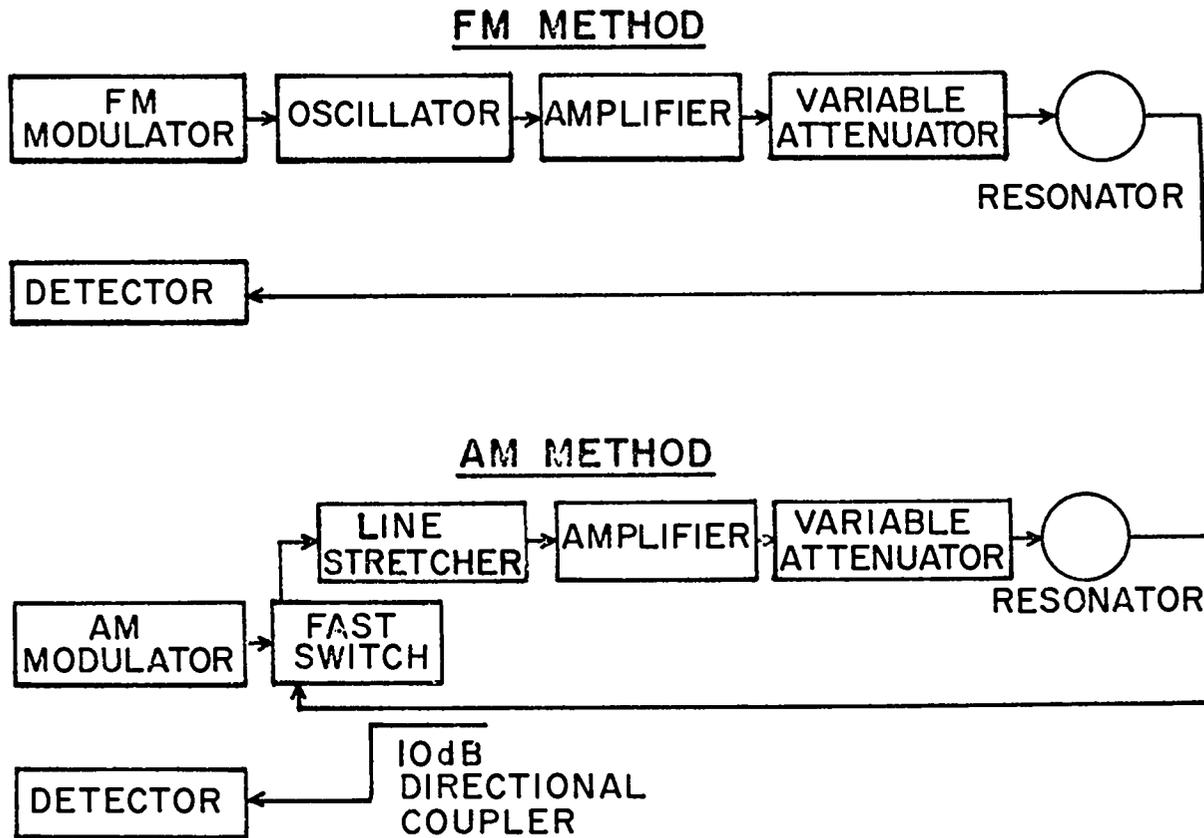
*Fig. IV-7.*
*Block diagrams of microwave components for FM and AM methods.*

### AM METHOD
### POWER DECAY



$P_{TRANS}$

$P_{INC}$

I $\mu$sec / DIV →
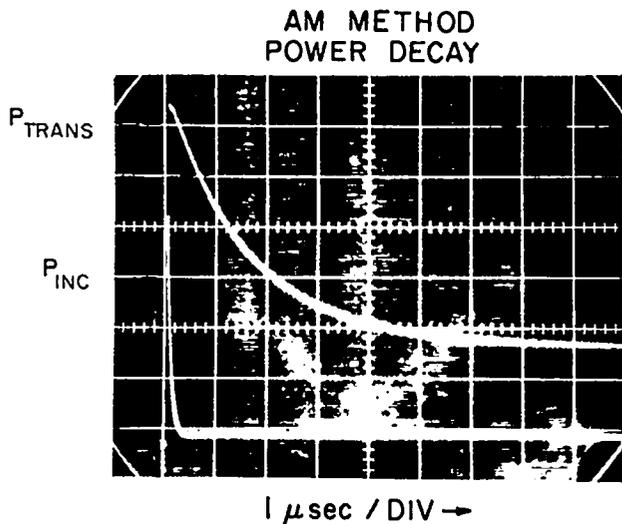
*Fig. IV-8.*
*Comparison of incident and transmitted power decays in the AM method.*

**E. Influence of Charge Exchange on Plasma Ion Drift Speed** (H. Dreicer, D. B. Henderson, and J. D. Thomas, Visiting Staff Member, New Mexico State University)

We have previously reported on the important influence charge exchange may have upon diffusion of ions across magnetic fields[1] and upon the drift speed with which ions move in a plasma.[2] Based upon observations made in our Q machine with radioactive $^{42}$K tracer ions[2], we concluded that the slowing down of ions, due to charge exchange with colder atoms, might account for the surprisingly low ion drift speeds (or ion current densities) measured. During the past year this conjecture has been put to the theoretical test with a kinetic-theory computation of the ion velocity distribution (and thus drift speed) in the presence of charge exchange.

The computation proceeds from the time-independent, space-dependent Boltzmann equation for positive ions, which includes the self-consistent space charge electric field and utilizes the Sena[3] "relay" model for the charge exchange encounters. According to this model, electrons are passed from nucleus to nucleus, but

the momentum exchange between nuclei is neglected. This is a very good assumption for the interesting case of resonant charge exchange, in which ions move in their parent gas and electrons are transferred in relatively distant encounters. Our calculation assumes that the neutral atoms are at rest, but they may be spatially distributed in any arbitrary prescribed way. We consider the case of the Debye length being much shorter than the mean free path for charge exchange, and thus approximate the Poisson equation by the quasi-neutral condition, found to be valid for the interior of the plasma. The electrons are assumed to be distributed according to the Maxwell-Boltzmann distribution.

Solution of these two equations has been effected for the case of a space charge potential decreasing monotonically with distance s from the position where the ion velocity distribution is prescribed. Figure IV-9 depicts the ion velocity distribution $f(w,s)$ of those ions which have resulted from charge exchange. Here $w$, normalized to $\sqrt{2kT/M}$, is the component of the velocity along the space charge electric field. This distribution is the result of a monoenergetic ion beam entering the plasma at $s = 0$ with the normalized beam speed $\sqrt{MU^2/(2kT)} = 1.92$, and an electron temperature of $2500°K$. The neutral gas density corresponds to our experimental conditions near the Q-machine hot plate

$$n_g(s) = n_{go}\exp(-s/7.5) \quad,$$

and the mean free path for charge exchange $\lambda$ is computed to be 35 cm from an estimate of $n_{go}$ and our

measurement[4] of the cross section for this process. Ion-ion encounters are ignored in this computation since this greatly simplifies the problem without affecting the drift speed.[5] Such encounters do not alter the net momentum carried by the ions.

This technique permits us to specify the electron density at $s = 0$, $f(w,0)$, and the current density $n(s)\, v_d(s)$ carried by the ions. In turn, the solution yields the electrostatic potential $V(s)$ and the electron density $n(s)$ for $s \geqslant 0$. For the $n_g(s)$ described above, Fig. IV-10 shows that the computed value $n(s)$ and the measured value $n_p$ can be made to agree for an expected range of $\lambda$'s without introducing experimentally significant variations of $n(s)$ and $V(s)$ with s. We regard this result as a reasonable explanation of the low ion drift speeds observed.[2,6]

## REFERENCES

1. H. Dreicer and D. B. Henderson, Phys. Rev. Letters 20,374 (1968).

2. H. Dreicer, D. B. Henderson, and D. Mosher, Phys. Fluids 14, 1289 (1971).

3. L. A. Sena, Zh. Eksperim. i Teor. Fiz. 16, 734 (1946).

4. H. Dreicer, D. B. Henderson, D. Mosher, F. E. Wittman, K. Wolfsberg, Proc. of the International Conf. on Physics of Quiescent Plasmas, Part III, p. 11,Paris,September 1969.

5. D. B. Henderson and H. Dreicer, Status Report of the LASL CTR Program for 12-month period ending October 1970, Los Alamos Scientific Laboratory report LA-4585-MS, p. 73, (1970).

6. S. A. Anderson, V. O. Jensen, P. Michelsen, and P. Nielsen, Phys. Fluids 14, 728 (1971).

Fig. IV-9.

Ion velocity distribution as a function of normalized speed with position as a parameter.
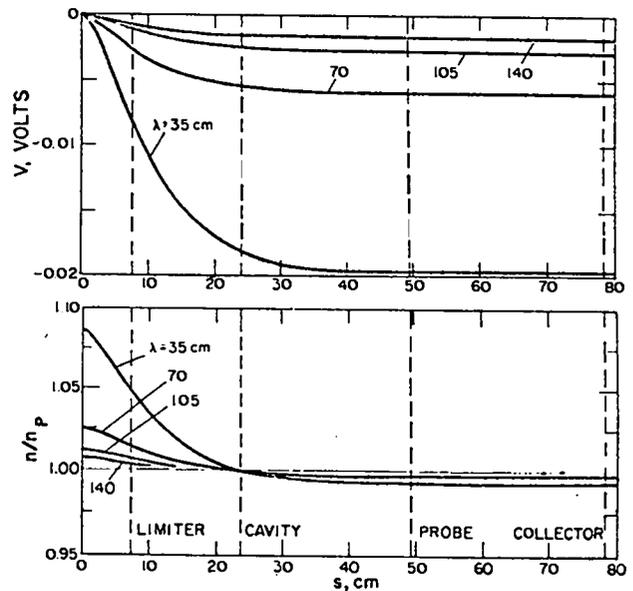


Fig. IV-10.

Electrostatic potential and normalized electron density as a function of s with charge exchange mean free path as parameter.

# V. QUADRUPOLE INJECTION EXPERIMENT

(J. E. Hammel, J. Marshall, A. R. Sherwood)

## A. Introduction

This experiment is the latest of a series directed toward the study of the interaction of a coaxial gun plasma stream with a stationary magnetic field. In this case the trapping and containment of the gun plasma was investigated in a quadrupole device designed to contain a peak density of $5 \times 10^{13}$ cm$^{-3}$ protons having an energy of 2.5 keV within the MHD stable region. Thus, the experiment differs markedly from other multipole experiments because of the higher density and temperature of the plasma. Also, a unique scheme of magnetically guarded current feeds is used to connect the interior conductors to the outside world. Measurements have been made to determine the size of the leak introduced into the containment volume by this dipole guard. The experiment was terminated during the period covered by this report.

In this final progress report, the objectives are here restated and the following sections give a brief summary of the experimental results relating to each objective. The original objectives of the experiment were:

- To investigate the injection and trapping properties of the quadrupole geometry,

- To investigate the nature and the magnitude of the leak introduced by a dipole-guarded coil support,

- To investigate the containment properties of the device,

- To check on the theoretically predicted MHD stability for the case of a hot, finite-$\beta$ plasma.

## B. Injection and Trapping

A schematic diagram of the apparatus is shown in Fig. V-1. Each coil is supported by a single pair of dipole-guarded current feeds which are not shown. The plasma is injected parallel to the axis of the coils and directly at the null of the quadrupole field. The four flux-shaping rings increase the height of the magnetic barrier that must be crossed by the injected plasma and provide a continuous injection slot so that the quadrupole field is not perturbed by an injection port at one azimuthal position. Figure V-1b shows the magnetic field shape. The maximum design value for the field is 40 kG

between the small coil and its cylindrical flux-shaping surface. Further details can be found in References 1 through 3.

From previous experiments it is known that the plasma coming from our coaxial gun has a fast component in which most of its energy is in streaming motion and very little in thermal motion. It has been shown that such a plasma can be injected into a transverse magnetic field with practically no loss of directed energy. Although the entry process of the plasma into the field is not understood, it is known that the plasma becomes mixed with field, then streams through it by means of $\vec{v} \times \vec{B}$ polarization electric fields. In the present experiment, these electric fields have been measured by means of double electric probes. They were found to vary linearly with B as expected and to be equal to $-\vec{v} \times \vec{B}$ within experimental error.

After injection, trapping occurs by means of depolarization currents that flow along magnetic field lines when the plasma stream crosses the quadrupole null. These depolarization currents have been measured by means of Rogowski loops; they are found to be about right to provide the proper impulse to cancel the momentum of the incoming plasma stream.

On the basis of the plasma density measurements in the containment region, it appears that the overall trapping efficiency of the device is very high (greater than 50%). That is, the measured plasma density multiplied by the containment volume about equals the expected average output of the plasma gun. Any more precise measurement of trapping efficiency would have been dependent on careful measurement of the output of the gun in order to take into account the ever present shot-to-shot variations in gun behavior, but we never had time to make such measurements. Supporting evidence for high trapping efficiency is the fact that no plasma was detected with a laser interferometer on the far side of the quadrupole field from the plasma gun if the quadrupole field was energized.

Thus, the evidence is that the plasma is stopped and trapped by the depolarization currents with very high efficiency.

## C. Losses Introduced by Dipole-Guarded Current Feeds

The dipole-guarded feed to the interior coils was included as a part of the experiment because it allows the quadrupole to operate with a high-energy plasma without
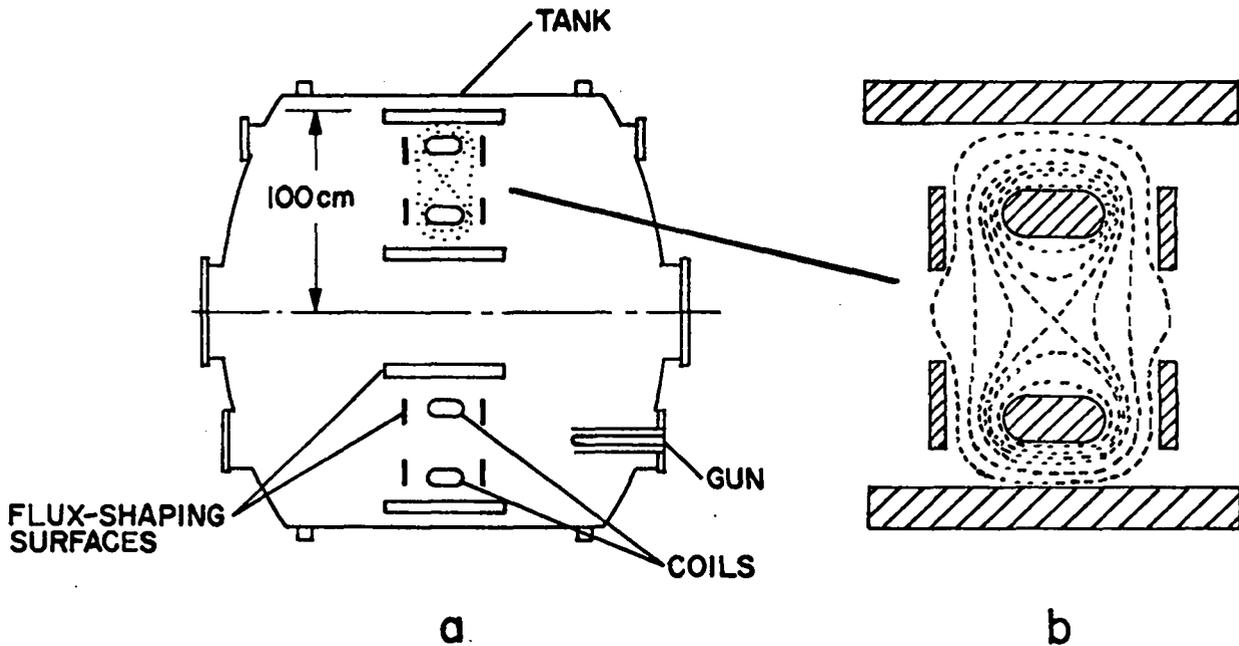
*Fig. V-1.*
*(a) Schematic diagram of the experimental apparatus. (b) Typical magnetic field lines.*

the difficulty and cost of a levitated system, and because it would provide experimental evidence of the practicality of direct access to an interior conductor through magnetic guarding. That is, although the dipole guard produces an inevitable leak from the containment volume, such a leak could be acceptable if it were small enough. At present this leak rate is not known and is a matter of controversy in the literature.

Simplified theoretical models, such as Meade's,[4] or our very similar one,[3] have been applied to the question of the leak introduced by dipole guarding. In our opinion these models are not realistic enough to apply convincingly to the actual case. For example, no account is taken of density gradients or the plasma flow, and for our geometry the two-dimensional nature of the model is insufficient. Thus experimental measurements of the actual leak rate due to dipole guarding are necessary.

One pair of magnetic-dipole-guarded current feeds is used to support each coil. The dipoles are force-free and are placed in the high-field region of each coil. The dipole is on the symmetry plane of the quadrupole field, an important feature not achieved in experiments at other laboratories where dipoles were introduced into multipoles. The nulls created by the combination of the dipole field and the main quadrupole field are closed by a suitable cross-current before they can reach the coils.

They extend out of the containment region through holes in the flux-shaping surfaces, and thus conduct plasma captured in the null out of the containment volume. This prevents the plasma from hitting the interior conductor.

For our first set of interior coils (the "old" coils), time-integrated photographs of the dipole guards were obtained. These photographs showed that the current feeds themselves were not being bombarded by plasma, so the dipole guarding scheme works. Furthermore, thin lines of light were seen at the positions of the dipole nulls. These lines did not intersect the surface of the coil and, indeed, the coil was not being bombarded. Thus the scheme of closing off the nulls appears to have worked also. On the old coils, however, there was an unguarded metal piece which protruded above the surface of the coil and was present for producing the cross-current for closing the nulls. This protruding piece was observed to be bombarded as soon as the injected plasma reached it. Therefore, another set of coils (the "new" coils) were designed, fabricated, and installed for which this cross-current conductor was recessed below the surface of the coil. Very few data were obtained with these new coils before the termination of the experiment; but because the plasma containment with these new coils was very much improved (see next section), it is quite likely that the recessed design either solved or alleviated the problem.

81

A direct measurement of the leak associated with the dipole was not obtained. We had intended to make energy-loss measurements in the dipole region for the new coils, but there was not enough time. However, with the old coils an indirect measurement of the leak rate was obtained from electric field measurements obtained in the vicinity of the dipole. Potential differences between magnetic field lines which pass near the dipole were measured by means of a set of five double probes. The maximum electric fields were less than 50 V/cm and were generally observed by the probe spanning the dipole separatrix (the line going through the dipole null). The signals were found to be very small, or negative, about 2 cm on either side of the dipole separatrix. After an initial transitory period of 5 to 10 $\mu$sec, the larger signals dropped in value to 10 to 20 V/cm or less. For the electric field at the separatrix, the $\vec{E} \times \vec{B}$ drift velocity was such as to transport the plasma out of the machine. The equivalent area of the leak can be defined by

$$A = \frac{4 \int \oint \frac{E}{B} \, d\ell \, d\eta}{v_{therm}} \quad ,$$

where $\ell$ is the coordinate along $\vec{B}$ and $\eta$ is the coordinate normal to $\vec{B}$ and to the dipole axis. Since experimentally it was observed that the electric field remained essentially unchanged along the magnetic field lines in the vicinity of the dipole guard, E can be taken out of the integral over $\ell$. Thus the area can be obtained from the calculated value of $\oint (d\ell/B)$ around the quadrupole and the electric field as measured by the probes. For the worst case, the resultant equivalent leak area is just under 4 cm$^2$. The corresponding area predicted by the model of Meade is 90 cm$^2$.

So the dipole guarding was found to be effective and satisfactory for the old coils except for the bombardment of the protruding conductor. This latter problem was apparently corrected with the new coils. The indirect measurement for the leak rate produced a value much smaller than might have been expected. It is unfortunate that we were unable to repeat these measurements with the new coils or to make a direct measurement of the energy loss.

## D. Containment

A combination of two types of diagnostics has been employed to study the plasma containment of the device. First, area density measurements of the plasma in the region of the quadrupole null have been made as a function of time by means of a $CO_2$ laser interferometer. These measurements were made at an azimuthal position 75° from the injection region and 90° from the

dipole-guarded coil supports. Two examples of the results obtained for the density as a function of time can be found in Fig. V-2. Although most of the density measurements were taken along a line passing through the quadrupole null, some measurements were taken along other parallel lines displaced towards either coil. The observed profile for the area density was essentially flat.

In addition, plasma diamagnetism has been measured by magnetic pickup loops placed at various azimuthal and axial positions. They must, however, be kept outside of $\psi_{crit}$ because if they are placed inside of this surface they are found to be bombarded by the plasma. Plasma energies have been inferred from the flux change in these magnetic pickup loops. To do so, a model for the plasma distribution is employed and the perturbed magnetic field calculated, as is explained in more detail elsewhere.[2,3] (The model for the plasma distribution is in agreement with the observed flat profile for the area density.) The plasma energies inferred in this way can be combined with the area densities given by the interferometer to yield a value for the plasma temperature. Examples of the results so obtained for the plasma temperature as a function of time are shown in Figs. V-2 and -3.

The total amount of high-energy plasma deduced in the above manner to be in the containment region at early times is very close to the expected average total output of energetic plasma from the gun.

The earliest data were obtained with the old coils at low magnetic-field strengths. These data showed a drop in plasma temperature and a large rise in density, as is shown by the dotted curves in Fig. V-2. This behavior is believed to be due to a large influx of cold plasma. One source was secondary plasma from the bombardment of the protruding cross-over conductor. Another was caused by bombardment of the coils and flux-shaping surfaces by energetic particles escaping because the containment field was not nearly high enough. The gun produces plasma in the 5- to 10-keV range whereas, even at full design field, the containment region has only 5 gyroradii (null to $\psi_{crit}$) for 2.5-keV protons. The results obtained at higher magnetic field were much improved, as is shown in Fig. V-3. This figure shows the observed plasma temperature as a function of time for cases of the magnetic field strenght being 40% and 75% of the full design value. Although the density measurements are not shown in the figure, at higher magnetic fields the density rise at later times became less and less severe. In fact, the diamagnetic pickup loop signals showed directly that the plasma energy containment time was a monotonic function of the quadrupole field strength over the range investigated.

Unfortunately, our attempts to achieve fields approaching the full design value were thwarted by engineering difficulties. On the two occasions that we achieved 75% of design field, only a few shots were
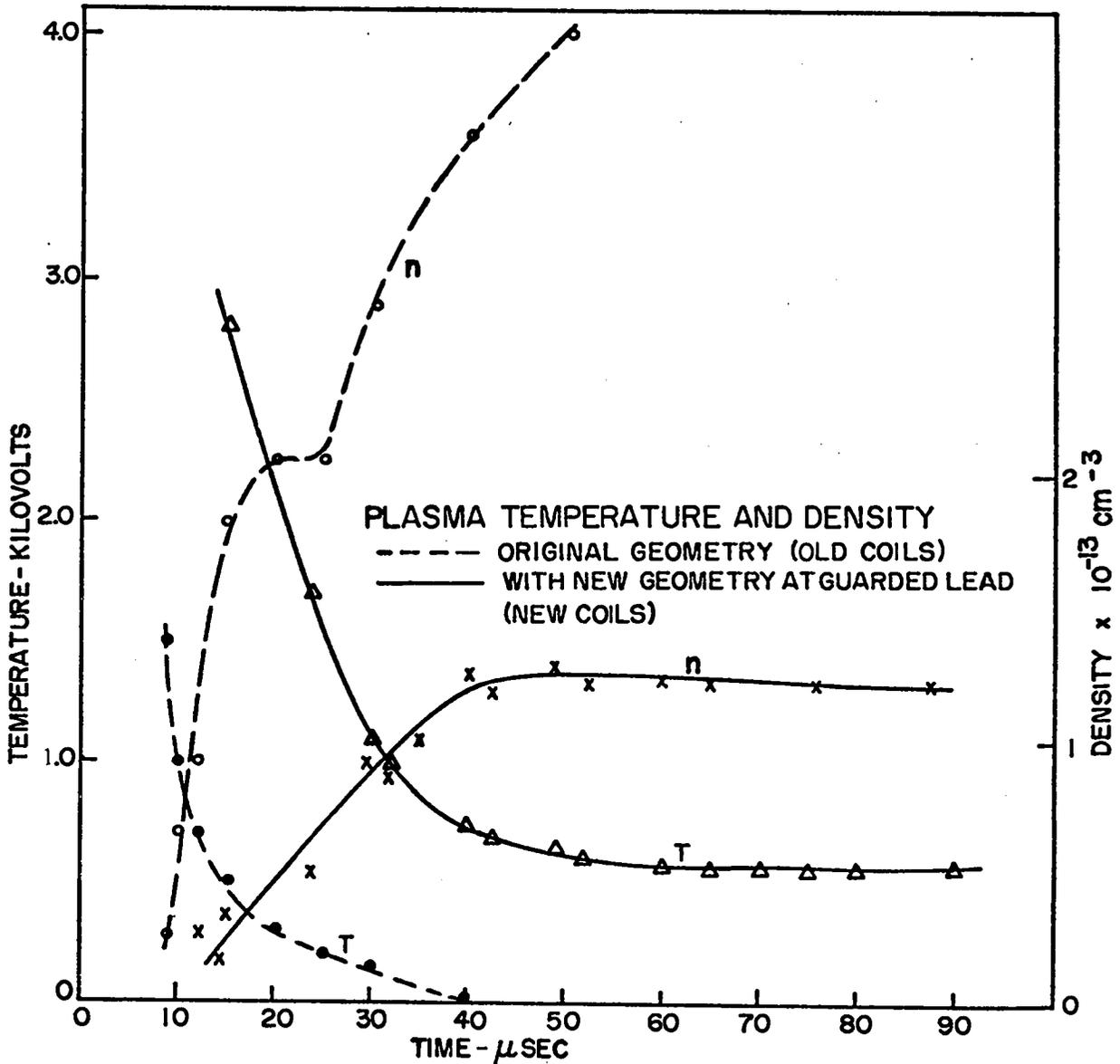
*Fig. V-2.*

*Comparison of temperature and density observations for the two sets of coils under similar conditions. The magnetic field was 40% of full design field.*

obtained before an electrical failure occurred. The failures occurred in the two most highly stressed (in terms of current per unit length) current joints in the inner coil feed system. In each case, a redesigning of the joint and somewhat extensive repairs were required. After the second failure, insufficient time remained before the termination date for the experiment to allow for any more high-field shots with the old coils, so the old coils were removed and the new coils were installed. After a brief period of operation, during which the only data-taking shots were a few at 40% of full design field, the experiment was terminated a little prematurely by a failure in one dipole lead. The failure apparently occurred at what seems to be a most unlikely place. At any rate, somewhat extensive damage resulted in the region where the guarded current feeds join the coil.

As was previously mentioned, an essential feature of the new coils is the recessing below the coil surface of the conductor for the cross current. The limited data obtained with these new coils showed improvements beyond our expectations. Even at low fields and without adjustments in gun energy and gas load, the diamagnetic loop
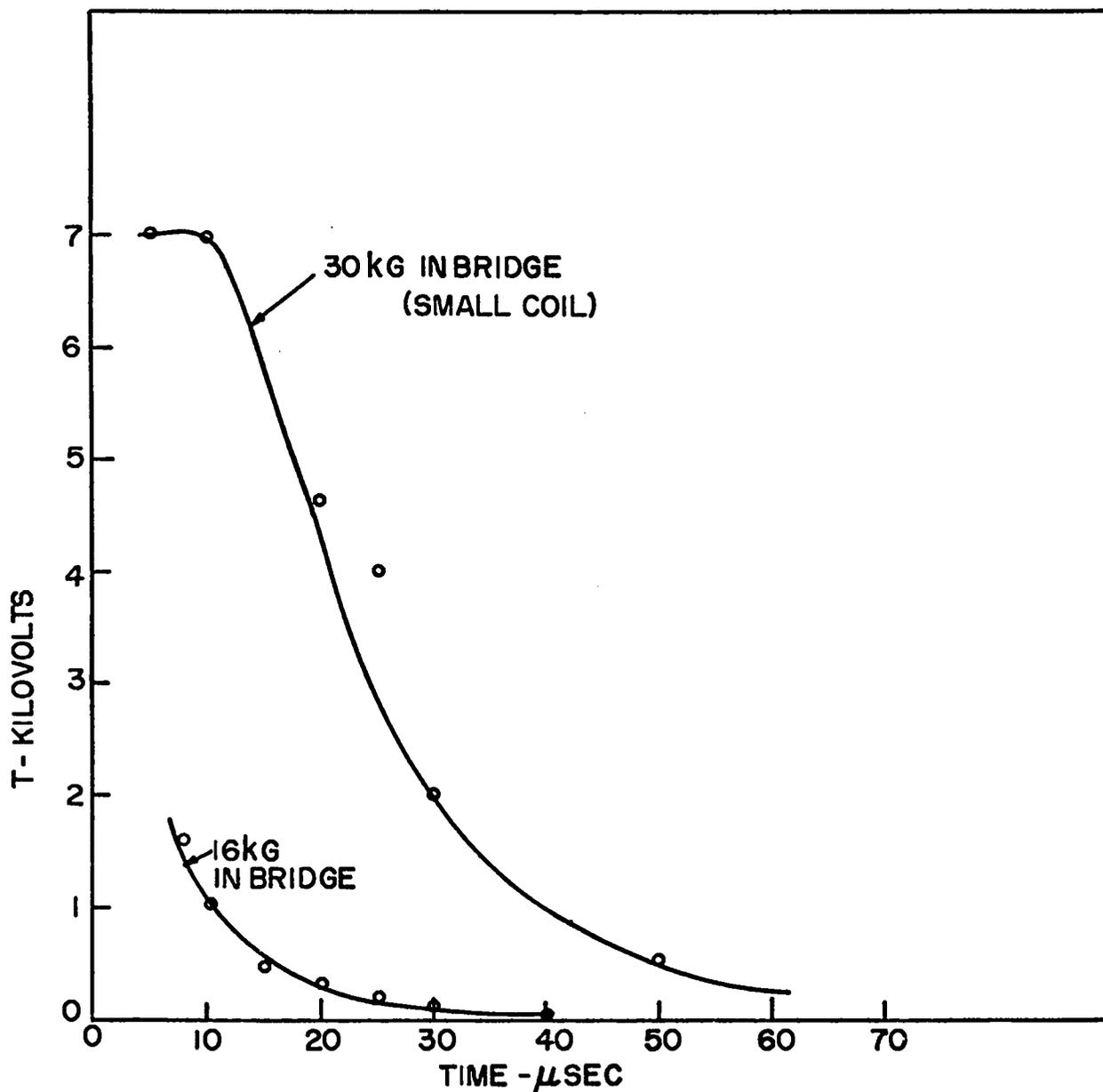
*Fig. V-3.*

*Comparison of temperature observations for two magnetic field strengths with the old coils. The curve labeled "16 kG in bridge" corresponds to 40% of full design field, whereas the curve labeled "30 kG in bridge" corresponds to 75%.*

signals rose, then remained essentially flat for the full 100-μsec duration of the scope traces. Both probes gave essentially the same signal and were quiet after the first 10 μsec following injection. The density rose for 25 μsec after injection, then remained constant. The density and temperature are shown in Fig. V-2, along with results from the old coils obtained at the same low value for the magnetic field. It is clear that recessing the cross-current conductor resulted in a great improvement in the containment.

For the limited data that we did obtain, after settling down, the temperature and density remained essentially constant for the duration of the scope sweep. Thus the decay time for the new coils cannot be determined.

However, assuming that the new coils would have shown the same improvement in the containment with increasing magnetic field as the old coils did, one can expect that, at fields well within the design value, the device would contain a plasma of temperature higher than 1 keV for at least several hundred microseconds. It is unfortunate that the experiment had to be terminated at this interesting point.

### E. MHD Stability

The finite-$\beta$ toroidal MHD stability has been studied by Baker and Mann using the $\delta W$ formulation. A model for the plasma distribution is required for the calculation; however, the plasma pressure at the stability limit is somewhat insensitive to the distribution chosen. In the experiment with the new coil configuration, the plasma temperature and density leveled off with a pressure equivalent to 60% of the predicted maximum. In addition to the fact that the density and temperature became essentially constant with time at 60% of the predicted stable limit, the form of the magnetic and density signals further supports the view that the plasma is MHD stable. As described previously, the magnetic loops are placed just outside $\psi_{crit}$ at the radius of the null.

Also, the two probes are on opposite sides of the plane of the plasma and at different azimuthal positions. For the first 15 $\mu$sec after injection the magnetic probe signals show hash; however, after this period the signal becomes smooth with both probes giving the same amplitude. This indicates that after injection the plasma becomes quiet and centered on the null and is evidently uniform in azimuth. The density measurement is likewise a smooth function of time.

### F. Conclusion

It is obvious that the experiment is far from complete; however, with the qualification that the experiments were conducted below 75% of design field and without hard crowbar, all the objectives of the experiment have been met or exceeded. The system, as finally operated with some suitable engineering changes in the current connections, would be ideal for comparing finite-$\beta$ effects with the numerous zero-$\beta$ multipole results obtained in other laboratories. Of most interest would be the study of the quadrupole operating at full field with a hard crowbar. Such a study could answer questions about long-term finite-$\beta$ stability in a quadrupole, make a precise measure of the magnetic guarding effects, and perhaps answer some scientific questions on the role of quadrupoles in CTR.

### References

1. "Status Report of the LASL Controlled Thermonuclear Research Program for 12-month Period Ending October, 1969", Los Alamos Scientific Laboratory report, LA-4351-MS, p. 77 (1969).

2. "Status Report of the LASL Controlled Thermonuclear Research Program for 12-month Period Ending October, 1970", Los Alamos Scientific Laboratory report, LA-4585-MS, p. 54 (1970).

3. Proceedings of IAEA Conference on Plasma Physics and Controlled Nuclear Fusion Research, Madison, Wisconsin, June 1971; paper CN-28/A-7.

4. D. M. Meade, Phys. Fluids 11, 2497 (1968).

# VI. THEORETICAL PLASMA PHYSICS

## A. Summary (W. B. Riesenfeld)

The past year's activities of the mathematical physics and numerical simulation group have been focused on support of major programmatic efforts such as the Scyllac $\theta$ pinch, the shock-heated toroidal Z pinch, and absorption of laser radiation by dense plasmas. The demands of these and other programs have imposed on us the necessity of gaining better understanding of such basic processes as collisionless shocks in plasmas, nonlinear development of microinstabilities, saturation mechanisms for these instabilities, and the structure of turbulent plasma states. In pursuing these goals we have found that the technique of numerical computer simulation of plasma-field systems has assumed an ever greater role in furnishing us with information on the behavior of Vlasov systems. This information, in fact, is now on a par with traditional experimental input in its importance in directing theory and suggesting physical interpretations of observations. The trend is for numerical simulation to emerge as a full-fledged third partner to laboratory experiment and mathematical analysis in making scientific progress; the term *computer experimentation* is being increasingly used to describe this third approach, which indeed has many features of traditional experiment and yet is capable of idealization and isolation of specific phenomena without suffering the consequences of experimental contamination, impurities, and interference. Idealization and simplification have obvious disadvantages as well as advantages, and the same caution in interpretation is required for computer experimentation as for laboratory experimentation. The rapidly growing sophistication of computers, software, and programs leads us to expect, however, that in the foreseeable future the idealization may become less of a necessity than an investigative virtue, and that numerical simulation may approach impressively close to "real" physical conditions.

During the year, an improved theory of high-$\beta$ plasma stability has been devised, in which ion motion is assumed to be governed by the Vlasov equations, while the electrons comprise a charge-neutralizing magnetohydrodynamic fluid. The new theory has important implications for the behavior of $\theta$-pinch plasmas because it predicts, for reasonable values of the relevant physical parameters, growth rates for $m \geqslant 2$ instabilities which are drastically reduced from the ideal MHD values, while the $m = 1$ mode retains its MHD value. The relative suppression of $m \geqslant 2$ modes has long been an experimental fact of life and the theory, while it still contains numerous analytical approximations, seems to provide a needed reconciliation. In essence it is a high-$\beta$ generalization of the Rosenbluth, Krall, and Rostoker finite ion gyration radius stabilization effect. More exact numerical evaluations of its consequences are planned.

An improved version of the general toroidal, diffuse profile MHD equilibrium code was written and tested, along with an accompanying stability code which exploits the high-$\beta$ energy principle and considers all possible perturbations within numerical resolution. These codes are applicable to a wide range of axisymmetric toroidal geometries, including multipoles, Z pinches, and Tokamaks, and consequently have generated interest and collaboration with other laboratories such as Culham, Garching, and the University of Texas, some of which have analogous or complementary numerical programs. These codes, of course, have provided design input for the LASL shock-heated toroidal Z-pinch device, and will be used to analyze its performance. In addition, the effectiveness of the shock heating mechanism in this machine has been evaluated both analytically and numerically, including the effects of a bias magnetic field and the characteristics of the external driving circuit. The results indicate that large amounts of plasma heating are possible even with trapped bias fields, provided that certain input requirements are met.

A theory has been developed which provides a simple physical picture of collisionless electrostatic and magnetic shocks in plasmas and which reproduces many of their features as seen in numerical simulation. Either system is described by two critical Mach numbers, between which a steady-state shock is able to propagate. An effective dissipative mechanism (ion viscosity) is provided by ions reflected from, and trapped behind, the shock front. This work has been complemented by a numerical simulation code for high-Mach-number shocks, which follows self-consistent ion and electron motion in a three-component electromagnetic field. The code has been used to study detailed shock structure, and results have been obtained on the critical Mach number for total ion reflection as a function of propagation direction relative to the magnetic field, the structure and processes which occur ahead of the magnetic piston, and the existence of laminary shock waves in hydrogen with Mach numbers up to 30.

As already mentioned, a major program is under way to study the various microinstabilities which arise as a consequence of particle velocity anisotropies and beam structures in the distribution functions. Results have been

obtained and compared, using analysis, numerical solution of dispersion relations, and numerical simulation. The expected importance of general electromagnetic modes (as opposed to the purely electrostatic modes of low-$\beta$ theory) has been confirmed explicitly with respect to several processes, including electron current driven electromagnetic ion cyclotron waves. Special interest has been attracted by the electron cyclotron drift instability (Bernstein modes driven unstable by relative ion-electron drift across the magnetic field) and the resulting turbulence. The threshold, growth rates, and nonlinear turbulence properties of this complex phenomenon are such as to cause us to suspect that it may be responsible for anomalous transport and shock structures in high-density fusion plasmas.

The plasma microstructure work has found application in understanding the mechanism of laser energy absorption in plasmas via collisionless and turbulence processes. Several numerical simulation codes were successfully used to study the absorption mechanism in the extreme nonlinear regime, and a mechanism for efficient absorption of radiation by the surface of a target has been proposed.

Development of improved two-dimensional MHD codes of the PIC type has proceeded through the year. Of special note in this area is a new technique of computing magnetohydrodynamic flows, which is able to deal with shocks without inclusion of artificial viscosity and which is numerically stable. Finally, several smaller investigations have dealt with such diverse topics as the role of anomalous viscosity in the structure of sheared current layers, the effect of alignment and field errors on very long $\theta$ pinches, and the adaptation of an algebraic computer language to meet local requirements.

B. Heating and Diffusion of Pinch Plasmas (R. Morse, C. Nielson, J. Freidberg, R. Forslund, and R. Mitchell)

For years the theoretical study of high-temperature pinch plasmas, especially in $\theta$ pinches, was hung up on the observation that in about the first microsecond of plasma life, and concurrent with the initial shock heating, there is an extremely rapid diffusion of plasma across the confining magnetic field. This diffusion determines not only the details of the shock heating but also the density profile and hence the gross stability of the plasma for the remainder of its confinement.

Until the discovery of the electron cyclotron drift instability at this laboratory a year and a half ago, there was no explanation of this rapid diffusion. The threshold conditions for this instability were then found to be consistent with the onset of diffusion and hence the

instability was seen as the desired explanation. Further work during the last year has borne this out by showing in detail, through computer simulation, how strong plasma turbulence develops from a nonlinear extension of the instability and how this turbulence causes diffusion of the plasma across the magnetic field and heating of the plasma electrons. This nonlinear heating and diffusion mechanism, which was reported at the IAEA meeting by D. W. Forslund, R. L. Morse, and C. W. Nielson, is qualitatively different from all previous models of anomalous resistance and diffusion and constitutes a new concept in plasma turbulence theory.

An important immediate consequence of this new understanding of anomalous diffusion has been that we now expect to be able to produce a thin sheath in $\theta$-pinch plasmas by increasing the diameter of the plasma column. If realized, this means that a considerable improvement in fast compression heating from bounce model behavior of the ions in a magnetic field free plasma column can be achieved. (In this model ions are reflected, i.e., "bounce," and hence move ahead of an imploding magnetic piston; no separated shock-like behavior develops.) Consequently, numerical simulation studies of fast-compression heating have been conducted assuming that the plasma-vacuum sheath remains reasonably thin. These studies, which are being done to provide support for future machine design, have shown that the efficiency of filling the pinch tube volume with plasma--which will be important in reactors-- as well as the heating itself can be significantly improved by tailoring the magnetic compression pulse. A report on this work by J. P. Freidberg and R. L. Morse is being prepared.

D. W. Forslund, J. P. Freidberg, and R. W. Mitchell have conducted a more general study of laminar collisionless shock waves in plasmas with initial magnetic bias fields of various strengths. Some of the results are reported in a recent Physical Review Letter.[1] In addition to improving our understanding of basic plasma processes through comparison of our numerical simulation models with some recent collisionless shock experiments, this work also applies directly to understanding shock heating of toroidal pinch plasmas such as the LASL toroidal Z pinch and possible modifications of Scyllac. There the magnetic compression heating is complicated and made more difficult by a magnetic bias field which is built into the plasma to stabilize the toroidal confinement. Two critical Mach numbers are obtained which separate three regimes of shock behavior. In the first regime below the lower critical Mach number, i.e., with the strongest bias fields, a strong oscillatory wave train develops with no reflected ions ahead of the wave front and hence no direct heating of ions. Between the two critical Mach numbers a fraction of the ions is reflected and the wave train is

strongly damped. In the third regime, with the weakest bias fields, there is total reflection from the wave front and in fact no shock structure separates from the magnetic piston. In this limit then the shock results go over to the bounce model. This study also considered propagation of collisionless shocks oblique to the background or bias magnetic field, a situation which can occur in more complex field geometries as well as at the ends of conventional $\theta$ pinches. In this situation a large amplitude standing whistler wave propagates in front of the shock front and has the effect of increasing the upper critical Mach number.

### Reference

1. D. W. Forslund and C. R. Shonk, Phys. Rev. Lett. 25, 1699 (1970).

### C. Development of Numerical Simulation Methods and Codes (R. Morse, B. Marder, R. Mitchell, G. Cudahy, H. R. Lewis, L. Rudzinski, and C. Nielson)

By the beginning of this year we had developed PIC (particle-in-cell) numerical methods for simulating just about any collisionless, or slightly collisional, plasma phenomenon, given adequate computer capacity. The emphasis in method and code development in the last year has, therefore, been a bit different from before. Substantial progress has been accomplished in three areas: the systematic analysis and comparison of the basic numerical difference schemes in use, development of fluid MHD methods and codes for treating plasma flow and containment on the full experimental time scale, and improvement of the coding of inner loops and systems routines to increase the running speed of major codes. In addition, a versatile one-dimensional code has been prepared for distribution under our cooperative program.

Previous Hamiltonian derivations of PIC schemes from first principles have been extended to include full electromagnetic interactions and general curvilinear coordinates. In addition to giving some mathematical respectibility to numerical methods which were originally arrived at intuitively, this work indicates which schemes can be expected to conserve energy well in the limit of small time steps and how to modify Cartesian difference equations and their boundary conditions to cylindrical geometry. This work by H. R. Lewis will also be published in the Journal of Computational Physics.

Surprising as it seems, there are no really satisfactory multidimensional MHD (magnetohydrodynamic) numerical schemes suitable for simulating magnetically confined high-$\beta$ pinch plasmas. One would think that this area would be more advanced than collisionless microturbulence simulation, but it is not. A major modification of conventional fluid PIC methods has been undertaken for this purpose by B. M. Marder and has resulted in a method called GAP which is more Lagrangian in spirit than conventional PIC. A code employing this method has been applied quite successfully to plasma focus problems. A slightly different approach to the problem has been pursued by Major G. Cudahy and R. L. Morse in an effort to reduce numerical dissipation to a minimum, but this method is still in the one-dimensional test-problem stage. It is not yet clear what method will be used in production simulations of pinch plasmas.

The inner computing loops of our major two-dimensional electrostatic and electromagnetic simulation codes have been recoded in assembly language by C. W. Nielson and L. Rudsinski for a gain of a factor of three in inner loop speed and two in overall code speed. This then made these codes distinctly disk-transfer-rate limited (most applications of two-dimensional simulation codes require disk storage of particle quantities), i.e., the full benefit of the computing speed improvement was not seen. Disk system routines were then rewritten by R. Mitchell to gain a factor of around two in transfer rate, which is now about 90% of the mechanical disk limit. The codes are now just slightly computer-limited and a little over twice as fast as before. This is a significant saving.

In practice, the benefits of our cooperative simulation program to those with no substantial simulation experience has been mostly restricted to those with the time and inclination to spend several weeks or more at LASL learning the trade. To further broaden the use and understanding of numerical simulation, a one-dimensional electromagnetic EMI (electromagnetic inductive) code, has been rewritten and documented by D. Forslund and R. Mitchell, specifically for distribution to inexperienced users with limited local computing and graphics capability. We believe that this code, which allows all particle velocity components and field components to depend on time and one space coordinate, is optimum for this purpose. Quite a bit of physics can be done with it, and it has the structure of multidimensional codes but is not nearly so expensive to run.

### D. Laser Fusion Theory (R. Morse, J. Friedberg, R. Mitchell, C. Nielsen, and B. Marder)

During the last year there have been theoretical studies of several aspects of the laser initiation approach to controlled fusion, with support from the LASL laser project as well as from the division of CTR.

The earliest and still major area of activity is the

study of microscopic mechanisms by which laser energy is absorbed in target plasmas with initially solid densities. Three mechanisms have been considered. The first is the alternating current two-stream instability which is expected to occur in the skin layer when oscillating laser-light fields impinge on a target surface. This instability, which is surprisingly different from the standard steady two-stream instability, has been known to exist for a long time, but only rather limited analytic estimates of the growth rates were available. To fill the need for accurate values of the growth rates over ranges of physical parameters, a numerical method was developed for computing these exactly using a version of Flouquet theory. The rates have now been computed for the interesting ranges of frequency and target temperature. A selection of these calculations by J. Freidberg and B. Marder is published in Physical Review,[1] Simulations of the nonlinear development of this instability in one and two dimensions by C. Nielson and L. Rudsinski have shown qualitatively predictable behavior and have not thus far been published. Electrons are heated far more than ions, and in other respects the turbulence develops about as one would expect from the linear theory and past experience with beam plasma instabilities. Incorporation of this work into the full inhomogeneous problem is, however, far from complete.

The second mechanism is a resonance mechanism which does not involve an instability. It has been shown by linear analysis with collisonal resistivity and by complementary collisionless simulations to be capable of absorbing of the order of 50% of light energy incident on a target surface at optimum angles of the order of $10°$ to the normal. The energy is deposited in a small fraction of the target electrons and therefore produces a high temperature tail on the electron velocity distribution.[2]

The third mechanism is a pumping of electrons in the target surface by the radiation pressure. This mechanism, which is of course more effective when the incident power density is higher, has been simulated by a relativistic electromagnetic code. Results are only preliminary, but the absorption does appear to be significant for incident power values within reason.

Our understanding of the propagation of intense laser beams through materials such as lenses, solid state laser rods, and even target materials has been considerably improved through nonlinear optics studies by B. Suydam. The main concern has been with the stability of intense beams with respect to self-focusing, a phenomenon which reduces beam uniformity and causes material damage. The nonlinear development of self-focusing has now been successfully simulated by a two-dimensional wave packet propagation code written by D. Dickman with B. Suydam. As it develops this code is expected to be useful in designing laser systems.

References

1. J. Freidberg and B. Marder, Phys. Rev. A4, 15401 (1971).

2. J. Freidberg, R. Mitchell, R. Morse, and L. Rudsinski, "Resonant Absorbtion of Laser Light by Plasma Targets," Los Alamos Scientific Laboratory Report LA-4852-MS, 1971.

## E. Scyllac Theory (J. Freidberg)

1. **Stability of the m = 1 mode.** A theory has been formulated relaxing several of the constraints resulting from earlier expansion calculations. The theory involves a numerical calculation which includes each of the two early expansions as special limits as well as significantly extending the range of parameters over which the theory applies. The basic results are that $\ell = 1$ equilibria exist only if $\beta\delta < \pi^2/16$ where $\beta = 2\mu_0 p/B_0^2$ and $\delta$ is the normalized helical displacement. Surprisingly, the m = 1 stability of this system is very accurately described by the earliest theory despite the fact that the corresponding expansion ordering is strongly violated. The growth rate of the m = 1 mode normalized to the Alfven transit time across the radius is approximately given by

$$\frac{\gamma^2}{V_a^2/a^2} = \epsilon^2\delta^2\left[-\beta^2\left(\frac{a}{b}\right)^4 + \frac{\beta(4-3\beta)(2-\beta)}{8(1-\beta)}\right]\epsilon^2 \quad ,$$

where a/b is the plasma to wall ratio, $\epsilon = ha$, a is the plasma radius, and h is the pitch number of the helix.

2. **Stability of higher m modes.** A theory has been developed to explain the absence of higher m modes in Scyllac experiments despite the fact that the ideal MHD predicts sufficiently higher growth rates for these modes. The theory includes the effect of finite ion trajectories which can have a significant stabilizing effect. The results of the theory applied to Scyllac indicate that higher m modes are essentially completely surpressed if

$$\frac{r_L}{a} > \frac{8(1-\beta)\beta^2}{2-\beta}\epsilon^2\delta^2 \quad ,$$

where $r_L$ is the average ion Larmor radius.

3. **$\ell = 0$ ballooning modes.** Initial experimental measurements on the Scyllac sector have led to the speculation that the m = 1 mode of the $\ell = 0$ bumpy pinch may have the form of a ballooning mode rather than a pure sideways shift because of the relatively large $\ell = 0$ field. Numerical calculations on the sharp boundary, pure $\ell = 0$ system show that this is not the case. That is, for $\beta \approx .8$ and an $\ell = 0$ bumpiness of $\delta_0 = .05$ the ratio of the peak value to minimum value of the eigenfunction was about 1.3, which can hardly be construed as ballooning.

**F. Comparison of Numerical Simulation Methods (H. R. Lewis, LASL, and A. Sykes and J. A. Wesson, Culham Laboratory)**

Comparison between four particle-in-cell methods for plasma simulation in one dimension were made with the KDF-9 computer at the Culham Laboratory.[1] The objectives of the comparisons were to investigate a) the utility of using a higher-order representation of the scalar potential than piecewise linear, and b) the effects of smoothing the electric field as opposed to simply calculating it from the gradient of the scalar potential at every point. The potential was represented either as a continuous piecewise linear function of position or as a smooth piecewise quadratic function. Numerical comparisons were made using a simple test problem in which a Maxwellian distribution of positrons streams stably through a Maxwellian distribution of electrons. With various numbers of simulation particles per Debye length, time steps, and grid spacings, the time variation of the relative stream velocity of the positrons and electrons was used to determine a collision time, and fluctuations in total energy and momentum were monitored. The investigations with this test problem indicate that the four methods are similar to one another with regard to collisional effects, although the collisional effects are usually somewhat less pronounced with the smoothed electric field and the piecewise linear representation of the potential. All of the methods exhibit a strong dependence on initial conditions and time step with this test problem. With regard to fluctuations of total energy and momentum, the comparison of the methods depends very much on the grid spacing and time step.

It was hoped that the introduction of a higher-order representation for the potential would lead to a significant reduction in collisional effects. That our numerical results do not indicate such a reduction for the quadratic representation is disappointing. Nevertheless, it still may be advantageous to use a higher-order representation in applications to highly nonlinear problems or in two- and three-dimensional problems. Langdon[2] has recently suggested using a quadratic representation of the potential to improve the accuracy of numerical simulations. Two of the methods compared are Hamiltonian, those in which the electric field is calculated from the gradient of the scalar potential without any smoothing. For applications in which it is desirable to use a large grid spacing compared to the Debye length, as may be the case in two- and three-dimensional simulations, a Hamiltonian method is preferable in order to avoid a numerical instability described by Langdon[3]. Okuda[4] has observed such an instability to be absent from our Hamiltonian method which uses a piecewise linear potential but present with

some other, non-Hamiltonian, methods in accordance with Langdon's theory.

Further comparisons of numerical simulation methods will be carried out at Los Alamos.

**References**

1. H. Ralph Lewis, A. Sykes, and J. A. Wesson, "A Comparison of Some Particle-in-Cell Plasma Simulation Methods," to be published in J. Computational Physics.

2. A. Bruce Langdon, to be published in J. Computational Physics.

3. A. Bruce Langdon, J. Computational Physics 6, 247 (1970).

4. Hideo Okuda, to be published in J. Computational Physics.

**G. Numerical Simulation of the Ion-Sound Instability (H. R. Lewis, LASL; J. A. Wesson and A. Sykes, Culham Laboratory)**

A two-dimensional numerical simulation has been made at the Culham Laboratory of the growth and nonlinear development of the ion-sound instability arising from the presence of a current.[1] Exponential linear growth is observed when separate modes are isolated. When all modes are present the growth is more complicated. The predominant macroscopic feature is a fall in the current due to the resistive effect of the enhanced spectrum of ion-sound modes. On the microscopic level the instability leads to a stabilizing modification of the electron distribution function and this in turn to a reduction of the growth of the total fluctuation energy. Ultimately, the distribution function becomes essentially stable and the fluctuation energy decays.

The initial resistance is remarkably constant and can be used to derive an effective collision frequency. A correction is made for binary collisions by means of a control run in which ion-sound modes are stabilized by ion Landau damping. The resulting collision frequency was determined as a function of the drift velocity v and was found to be proportional to $(v - c_s)$, where $c_s$ is the sound speed.

**Reference**

1. J. A. Wesson, H. R. Lewis, and A. Sykes, to be published.

## H. Variational Algorithms for Fully Electromagnetic Numerical Simulation (H. R. Lewis)

Energy- and charge-conserving algorithms for numerical simulation of collisionless plasma with point particles, including electromagnetic interactions, have been derived from Hamilton's variational principle.[1] The formulation is suitable for advancing the electromagnetic potentials with a time-centered leapfrog difference scheme, and has been derived for curvilinear coordinates. These algorithms can be viewed as natural generalizations of electrostatic particle-in-cell methods. An example of the formulation has been given for the two-dimensional Weibel instability treated by Morse and Nielson.[2]

### References

1. H. Ralph Lewis, to be published in J. Computational Physics.

2. R. L. Morse and C. W. Nielson, Phys. Fluids 14, 830 (1971).

## I. Linearized Stability Analysis of Collisionless Plasma (H. R. Lewis)

Further study of the linearized variational analysis of collisionless plasmas[1,2] has been undertaken to extend the application to include external fields and electromagnetic interactions. This has included a search for an exact particular solution of the equations in analogy to the solution for the electrostatic case. An application to the exponential stability of high-$\beta$ pinch plasmas has been begun in collaboration with J. Freidberg.

### Reference

1. H. Ralph Lewis, to be published in Phys. Fluids.2

2. Status Report of the LASL Controlled Thermonuclear Research Program for 12-Month Period Ending October 1970, Los Alamos Scientific Laboratory report LA-4585-MS, p. 77.

# VII. TECHNOLOGICAL DEVELOPMENT FOR SHOCK-HEATING EXPERIMENTS

(J. Hammel, J. Marshall, A. Sherwood)

## A. Introduction

Plans are being made for an experimental program aimed at the study of shock heating or, more exactly perhaps, fast implosion heating. The purpose of this program is to provide support for the $\theta$-pinch program, particularly for the ideas of using separate shock heating and compression. In a scientific sense the results should be applicable to Z pinches as well as $\theta$ pinches, and technological developments should apply to both programs. A major purpose is to provide an in-house experimental program in association with the LASL theoretical work already in progress in this field. The program would differ from studies that have already been made or might be made in the future under the $\theta$-pinch program in that attention would be focused on the implosion heating phenomena alone, with no specific requirement for the subsequent compression or containment after heating.

Related work is being done at other laboratories. In particular Garching, Julich, Maryland, and N.R.L. Present plans are to use a system similar to theirs in general size (~ 40-cm $\theta$-pinch coil diam, 1-m long), but to attempt to go to higher electric fields actually on the plasma. The diameter is larger than would ordinarily be used in the $\theta$-pinch program at LASL because it facilitates investigation of the implosion phenomena. The higher electric fields would be in keeping with $\theta$-pinch requirements for a feasibility demonstration.

Great attention will have to be applied to the problems of preionization, both as to methods used to produce it and accurate measurements of the degree of preionization achieved. It is expected that deviations from 100% preionization may be quite important in achieving definite boundaries between plasma and magnetic field as required in some of the present ideas for extrapolation to feasibility demonstrations and reactors.

## B. High-Voltage System Studies

Initial intentions were to follow general practice in collisionless shock experiments at other laboratories and use a Blumlein generator system for applying high voltage to the $\theta$-pinch coil. Early in the studies it became apparent that the Blumlein arrangement of transmission lines suffers from having an unnecessarily large impedance, and that this limits the voltage, current, and magnetic field that can actually be applied to the plasma.

This can be seen by considering the Blumlein generator circuit as shown in Figs. VII-1 and -2. The total impedance of the circuit is $2 Z_0 + Z$. Consideration of the system in terms of line reflection theory shows load voltage to be

$$I_{\varrho} = \frac{2V}{2 Z_0 + Z} \quad .$$

The current persists for twice the electrical length of the line, then returns to zero for an equal length of time. One effect of driving the load with a transmission line is to double the effective emf in the circuit; another is to place the line impedance in series with that of the load. In the case of the Blumlein arrangement, another length of line is also connected in series, so that the total source impedance is $2 Z_0$. However, this is not the only method of using a line to drive a load. A lower impedance arrangement is achieved by replacing the output section of line in the Blumlein generator by a capacitor as in Fig. VII-3. Another possibility is shown in Fig. VII-4 where the capacitor is connected in series with the switch at the input end of the transmission line. In both of these the emf in the circuit is twice the charging voltage, but appears only for a time corresponding to twice the electrical length of the line and is in series with line impedance.

The capacitor in Figs. VII-3 and -4 is assumed to have negligible inductance. This may seem to be a radical and unwarranted assumption, but is not unreasonable when other circuit inductances are considered. First of all there is an irreducible inductance in the machine we expect to drive with the generator, i.e., the inductance associated with the volume inside of the load coil containing both insulation and the discharge tube. If 1 cm of radius is used up by these materials in a 40-cm-diam coil, the inductance amounts to about 15 nH. There is also the inductance of the switch. This can probably be made to be less than 1 nH by using solid dielectric multichannel switches, following Martin at AWRE and Dokopoulos at Julich. A capacitor inductance of 1 nH would make them completely negligible in this context.

It may be possible to develop a high-pressure spark gap with only a few nH of inductance, thus increasing convenience with a relatively unimportant inductance increase.

Adequately low capacitor inductance may be achievable by connecting a number of commercial capacitors in series-parallel. This would lead to an undesirably large
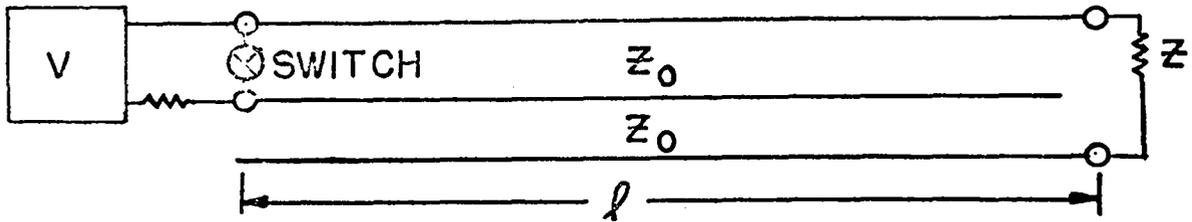
*Fig. VII-1.*

Blumlein generator as usually assembled with parallel plate lines. Each half of the system has characteristic impedance $Z_0$. Center conductor is initially charged to potential $V$ and shorted to one of the outer plates by low-inductance switch. Lines are of length $\ell$
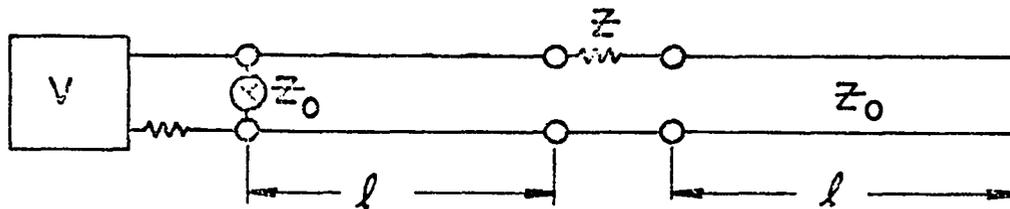


*Fig. VII-2.*

Alternate circuit diagram for Blumlein generator, equivalent to that of Fig. VII-1. Center conductor of Fig. VII-1 has been split down the middle and unfolded. Total impedance of circuit is that of input line $(Z_0)$ plus that of the load $(Z)$ plus that of the output line $(Z_0)$, and so is $2 Z_0 + Z$.
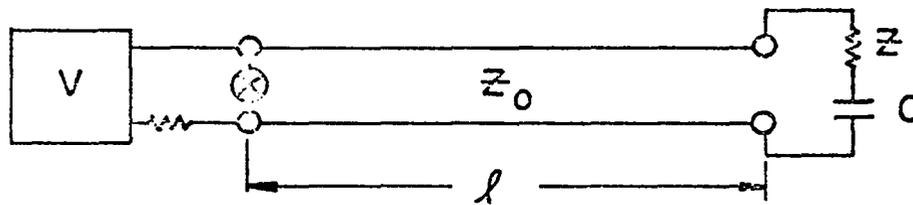


*Fig. VII-3.*

Line and capacitor arrangement to replace Blumlein generator. Capacitor replaces output line. If capacitor has large capacity and negligible inductance the total circuit impedance is $Z_0 + Z$.
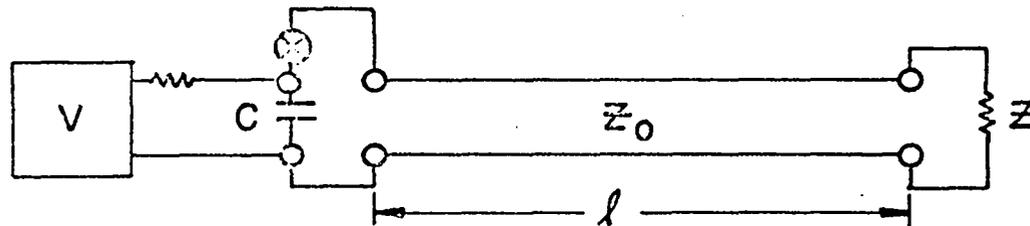


*Fig. VII-4.*

Line and capacitor arrangement nearly equivalent to that of Fig. VII-3. Total circuit impedance is still $Z_0 + Z$, but energy is stored initially only in capacitor, and this reduces performance slightly.

93

amount of stored energy with the capacitances usually available, but it should be possible to specify lower capacity with the same terminals. Alternatively, it appears feasible to construct capacitors with completely negligible inductance for these purposes. A parallel plate arrangement would be used with Mylar insulation folded around each plate of one set. Each plate would be connected directly to one side of a parallel-plate line or to the $\theta$-pinch coil. In Fig. VII-5 an attempt is made to show how this is done in a working model capacitor. The capacitor will be immersed in slightly conducting water to grade potential along the insulation extending beyond the
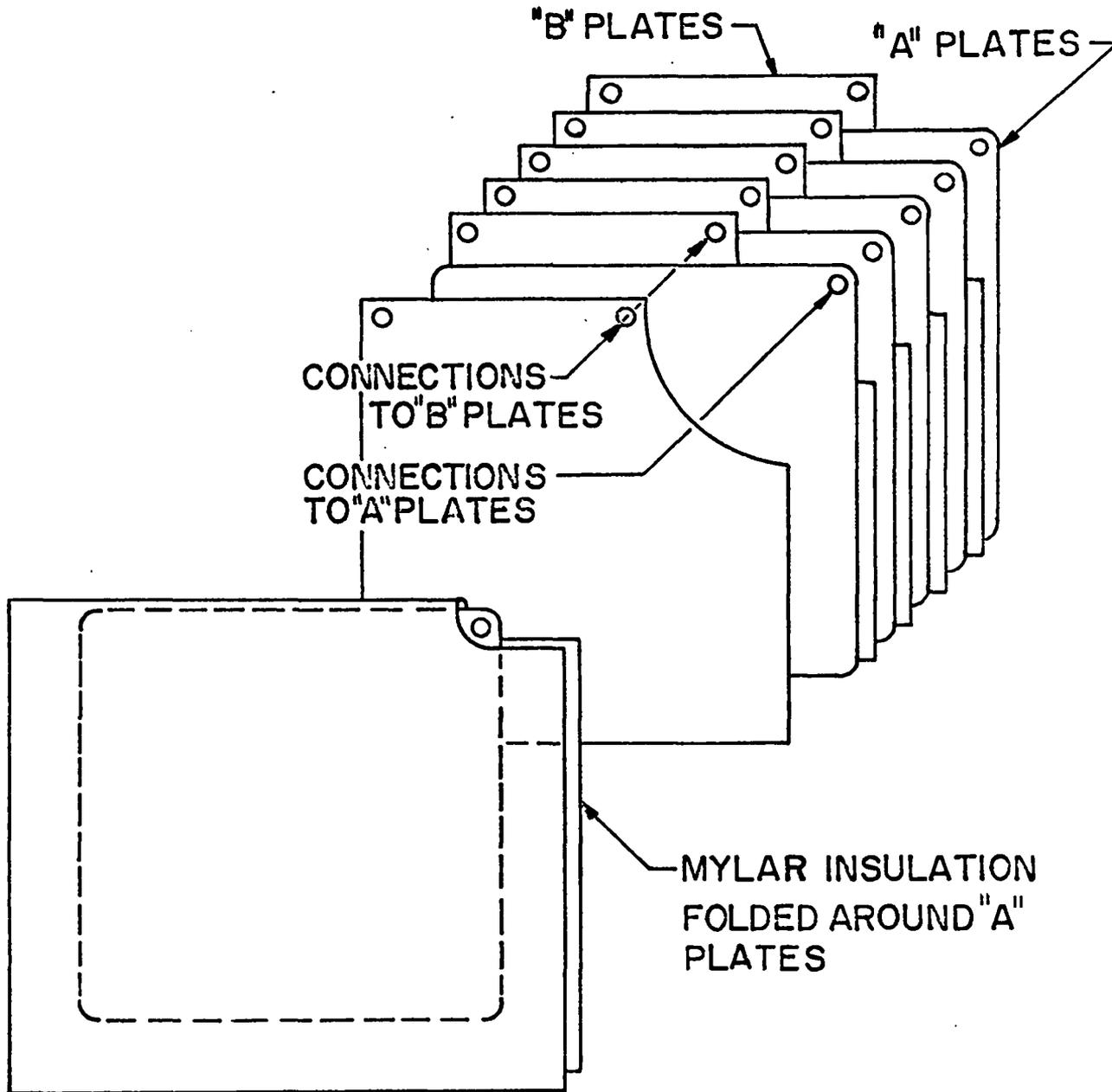


Fig. VII-5.

*Working model of low-inductance, high-voltage capacitor. Connections to the two sets of plates emerge to the right as a parallel plate line. Electric fields are graded on the Mylar insulation by immersion in water.*

edges of the plates. This is the usual solution to the problem of insulating high-voltage transmission lines and appears to introduce no insuperable difficulties. It necessitates pulse charging, but this is probably desirable in any case.

A full-scale capacitor could be assembled out of 150 1/4-in. plates, for example, each one with an area of 1.5 $m^2$. These would be insulated with 2 mm of Mylar on each side and interleaved with 1/32-in. plates of equal area. The assembly of 149 plates would have a total stacked thickness of $\sim 66$ in., a capacity of $\sim 5.6\,\mu F$, could be charged to 200 kV, and would be housed in a water tank about 6-ft square by 4-ft deep. It would store a little more than 100 kJ of energy.

A simple Marx generator for pulse charging capacitors and lines has been designed, using ignitron switching and 20-kV capacitors which are on hand. With 10 shelves, it could provide 150 to 200 kV. It is hoped to assemble this generator in the near future and use it for component testing.

If transmission lines are used, they will have to be of considerable length ($\sim 44$ m for 0.5-$\mu$sec pulse length). They will have to be immersed in water and, because of space limitations, will have to be folded several times. They will have to be of quite low impedance in order not to limit load current unduly and thus will have to be of considerable width. A 0.2-$\Omega$ line for 200-kV, 1/2-$\mu$sec pulse length would be 4.46-m wide, 44-m long, and insulated with 4 mm of Mylar. This is the line considered in one of the alternatives of Fig. VII-6. The reason for what may appear to be an excessive thickness of insulation will be discussed below.

In order to evaluate these various possibilities for voltage generators realistically, the behavior of the system has been calculated, taking into account the effect of plasma-sheath motion on voltage and current in the system. This has been done for Blumlein generators, line and capacitor systems, and simple capacitor systems, all connected to the coil through what appears to be a realistic inductance. The plasma sheath is assumed to obey the "bounce" model, i.e., each ion is driven ahead of a thin current sheath with twice the sheath velocity. The velocity of the sheath then is given by the relation

$$2\rho v^2 = \frac{B^2}{8\pi} \quad .$$

The inward motion of the sheath appears as a varying inductance in the circuit producing a back emf given by

$$E = \frac{d}{dt}\,(LI) = I\dot{L} + L\dot{I} \quad .$$

The resulting circuit equations are solved numerically. The results show that if transmission lines are to be used
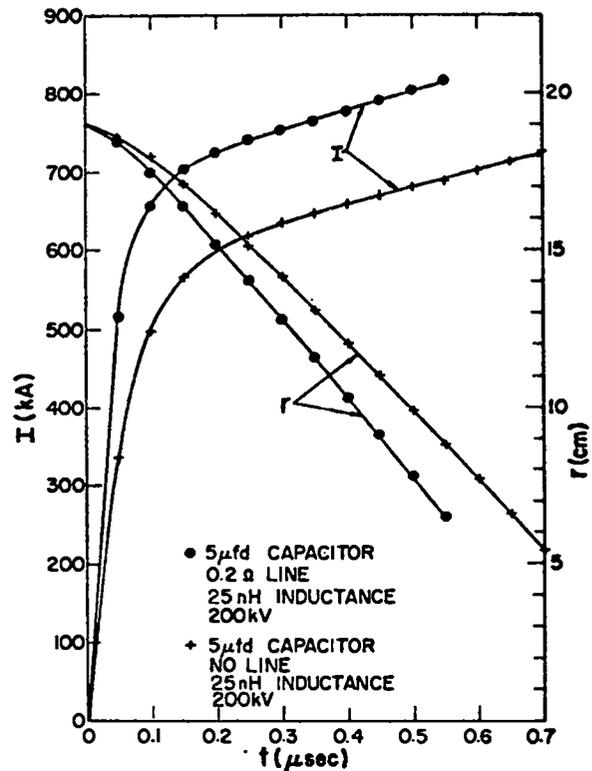


*Fig. VII-6.*
*Current and plasma piston radius as a function of time for θ-pinch coil driven by line, capacitor, and switch system compared with a capacitor and switch with no line. Both systems use a 40-cm-diam coil, 1-m long, and a filling of $10^{15}$ deuterons/$cm^3$. A 15-nH inductance is allowed for the discharge tube and 10 nH for switch and connections. The line would be 4.4-m wide, 44-m long, and insulated by 4 mm of Mylar.*

at all, they must be of extremely low impedance and/or operated at high voltage. This puts a premium on the line and capacitor system, as compared with the Blumlein generator, since equivalent results can be obtained with twice the line impedance. The awkwardness and difficulty of constructing long, extremely low-impedance, high-voltage lines impels us to seek other solutions. We have looked at the problem of using capacitors and switches directly with no transmission lines. The results indicate that performance is somewhat better when a line is used in addition to a capacitor, but it appears not to be enough better to make the extra difficulty worthwhile. A

comparison of the two systems is given in Fig. VII-6. In both cases we include the same parasitic inductance; both systems use 200-kV charging voltage; both systems include a 5-$\mu$F, 200-kV capacitor. It should be pointed out that a credible accident in the case of a line-driven coil is failure of preionization or gas filling pressure in the discharge tube. This would have the effect of terminating the line in a comparatively high impedance, and would produce voltage doubling. In any case there will always be voltage enhancement caused by the irreducible parasitic inductance of the coil, which looks like a high impedance to the high-frequency components of the wave front. The transmission line therefore requires insulation for up to twice its charging voltage. This is not the case with the capacitor and switch system.

## VIII. SCALING OF COAXIAL GUNS TO LARGER ENERGIES
### (I. Henins and J. Marshall)

After the success of the Birdseed-I and -II operations (injection of high-energy plasma into the ionosphere by a rocket-borne coaxial gun), there appears to be interest in further experiments of this kind. It would be desirable, however, to scale up the amount of plasma and its total energy by an order of magnitude or more. This problem has been investigated and a tentative design made for the larger gun. Work is being done elsewhere in the Laboratory to develop an explosive generator system with a superconducting solenoid flux source to drive the gun. The following considerations about gun scaling indicate that the scaling-up process can be done.

Calorimetric measurements on previous coaxial guns have shown that they are remarkably efficient devices. Nearly all of the energy delivered to the gun terminals ($> 90\%$) emerges from the muzzle. In the case of relatively high atomic number gas, such as neon in the Birdseed program, perhaps 40% of the terminal energy is emitted as radiation, mostly in the far ultraviolet. This still leaves about half of the energy as kinetic energy of plasma. It appears then that a good first approximation to producing a more energetic plasma stream from the gun is simply to get the energy into the gun terminals as $\int IE \, dt$.

Estimates have been made to calculate the characteristics of a scaled-up gun. A simplified model is used in which uniform gas density in the space between the electrodes and a velocity of the current front agreeing with that observed experimentally in previous "Snowplow" experiments is assumed. Magnetic field is assumed to fill the space behind the current front as though there were no plasma pressure or acceleration in that region. While this is not strictly true experimentally, it is nearly enough true not to affect the results by very much. It is also assumed that the voltage is held constant across the gun terminals and that the discharge starts at the terminals, as indeed it would if the gas filling were uniform. Under these conditions the current would be constant until the discharge reached the muzzle. The electrical energy delivered through the terminals until the time at which the discharge reaches the muzzle is calculated assuming the generator voltage is cut off at that time and the terminals are crowbarred.

Thus the magnetic pressure at the surface of the inner electrode is assumed to be equal to the influx of momentum of the ambient gas as it is swept up, so

$$\rho v^2 = \frac{B^2}{8\pi} \quad .$$

This gives the velocity of the current sheath

$$v = \frac{I}{r_1 \sqrt{200\pi\rho}} \quad ,$$

where I is in amperes, v in cm/sec, $\rho$ in g/cm$^3$. This has been confirmed experimentally over a wide range of parameters for $r_2 \gg r_1$, $r_1$ and $r_2$ being the radii of the inner and outer electrodes.

The energy delivered to the gun terminals is given by

$$U = EIt = EI \, \frac{\ell}{v} = E\ell r_1 \, \rho^{\frac{1}{2}} \sqrt{200 \, \pi} \quad ,$$

where E is the number of volts applied to the gun terminals, $\ell$ and r are the length and radius of the inner electrode in cm, and $\rho$ is the filling density in g/cm$^3$. The current in the energy formula has been canceled out by the current in the velocity formula, so that it does not appear explicitly. This simplifies the expression considerably, since the current is given by

$$I = \frac{E^{\frac{1}{2}} r_1^{\frac{1}{2}} \rho^{\frac{1}{4}}}{\left[\ln \frac{r_2}{r_1}\right]^{\frac{1}{2}}} \, (\frac{\pi}{4})^{\frac{1}{4}} \times 10^5 \text{ A} \quad .$$

The tentative design for the Birdseed III gun is $r_1 = 21.6$ cm, $r_2 = 35.6$ cm, $\ell = 150$ cm, gas load 1.24 g of Ne to give an average filling pressure of 2.8 Torr and a filling density of $3.29 \times 10^{-6}$ g/cm$^3$. If this gun were driven by 30 kV on its terminals, the above analysis would give

I = $6.98 \times 10^6$ A,

v = $7.1 \times 10^6$ cm/sec,

t = 21.1 $\mu$sec (time for discharge to reach the muzzle), and

U = $4.41 \times 10^6$ joules energy into the terminals.

The analysis is unrealistic in that the gas filling will actually be far from uniform (the gun would not perform properly if it were). The effect of this is to start the discharge part way along the barrel and, on the average, to raise the velocity of the sheath. Both effects reduce the energy transferred to the gun. In order to achieve the above energy input, it will probably be necessary to raise the voltage somewhat, and perhaps raise the gas density. The energy in practice may be raised to some extent by another effect, namely that the voltage will not be cut off when the sheath reaches the muzzle, but will continue for some time thereafter. Thus, energy will continue to be fed in while plasma is emerging from the muzzle.

# IX. SHERWOOD ENGINEERING
## (E. L. Kemp)

## A. Scyllac Support (C. Hammer, H. Harris, W. Borkenhagen, K. Hanks)

The design of the Scyllac system was completed early in the year and the design team was reduced to a 2.5-man effort. The installation and checkout of the 5-m toroidal sector was completed and a preionization plasma was produced on March 8, 1971. This was followed by a complete system shot on April 1. The toroidal sector operated satisfactorily and produced plasma data preceding the June IAEA at Madison, Wisconsin.

The only significant operational problem with the toroidal system was prefiring. When a spark gap prefired it would remove the common bias to 53 other spark gaps and cause them to fire at random. The random firing would usually destroy one or more capacitors by overcharging them. It would also cause large currents to flow in the charging circuit which would burn the charge connections to the capacitors. This problem was corrected with two modifications. A 5-$\mu$F, 25-kV capacitor was connected by a 25-ft insulating coaxial cable to each common bias bus. This capacitor sustained the common bias to the gaps in the event of a prefire. A 300-$\Omega$ electrolytic resistor was also installed in each capacitor charging lead to limit the charging current following a prefire or a misfire. These modifications were incorporated in the linear system.

The installation of the linear experiment began in April 1971. A blast wall was installed in front of the 5-m experiment so it could be operated without endangering the linear installation personnel. The installation work proceeded smoothly until July 1 when the installing union craftsmen went out on strike for about 8 weeks. During this period the installation was continued with supervisory personnel. The crafts returned on August 23 and the installation proceeded on the original schedule.

The schedule was maintained by working two shifts. The craftsmen worked during the 8-h day shift, installed all components, and made most of the connections. Each rack required a crew of about 15 craftsmen for four weeks. This was followed by a two-week period during which a technician crew made the final terminations and prepared the rack for electrical checkout. This checkout was done by an engineering crew working a 4-h night shift. The electrical checkout time averaged about four weeks per rack.

Most of the capacitors in the linear system were made by Sangamo for which the prior inspection performance was considerably below that of the Aerovox capacitors in the toroidal sector. However, the Sangamo units have generally operated satisfactorily during the checkout phase of the linear system.

The linear system will consist of seven operating racks. The five central racks will be used to create the plasma while the two end racks will drive mirror coils to inhibit end losses. The linear system with the toroidal sector in the background is shown in Fig. IX-1. Plasma experiments are scheduled to begin on the linear experiment in February 1972.

## B. General Engineering Support

1. Scyllac Prototype (A. Bailey, K. Hanks). In the early phases of the Scyllac development program, a prototype system was built to evaluate the new components and circuits that would be used in Scyllac. In 1971 the prototype was used to evaluate the high-voltage capabilities of the $\ell = 0$ coils that were installed in the Scylla IV feedback stabilization development system. The prototype was also used to evaluate and finalize the design of the bottom reach-through cartridges for the linear system. The linear Scyllac experiment will require 250-kG mirror coils. After considerable design study and calculations, a mirror coil was built and tested on the prototype system. The first test coil produced only 185 kG. Efforts are under way to modify the coil to produce 250 kG. Various configurations and coil materials will be investigated.

The prototype system can produce a respectable $\theta$-pinch plasma with an appropriate coil and discharge tube. This capability is being employed for an opacity experiment that is being performed on a not-to-interfere basis with the basic engineering uses of the bank. An 8.2 cm i.d. by 25-cm-long coil was attached to the prototype collector plates. A discharge tube was installed and filled with $D_2$ seeded with Ne and other gases. The VUV radiative emission spectrum of the $\theta$-pinch plasma is being investigated.

2. Capacitor Development (G. Boicourt). Over 4000 capacitors were purchased for Scyllac. Most of these were 1.85-$\mu$F, 60-kV units built by Aerovox, Sangamo, and McGraw-Edison. Incoming inspection consisted of 1500 to 4000 charge/discharge cycles on each unit before it was installed in the Scyllac system. The Aerovox units showed a failure rate of less than 3%. The Sangamo failure rate was 5 to 20%, the lower percentage corresponding to the later manufactured lots. The McGraw-Edison failure rate exceeded 50%.
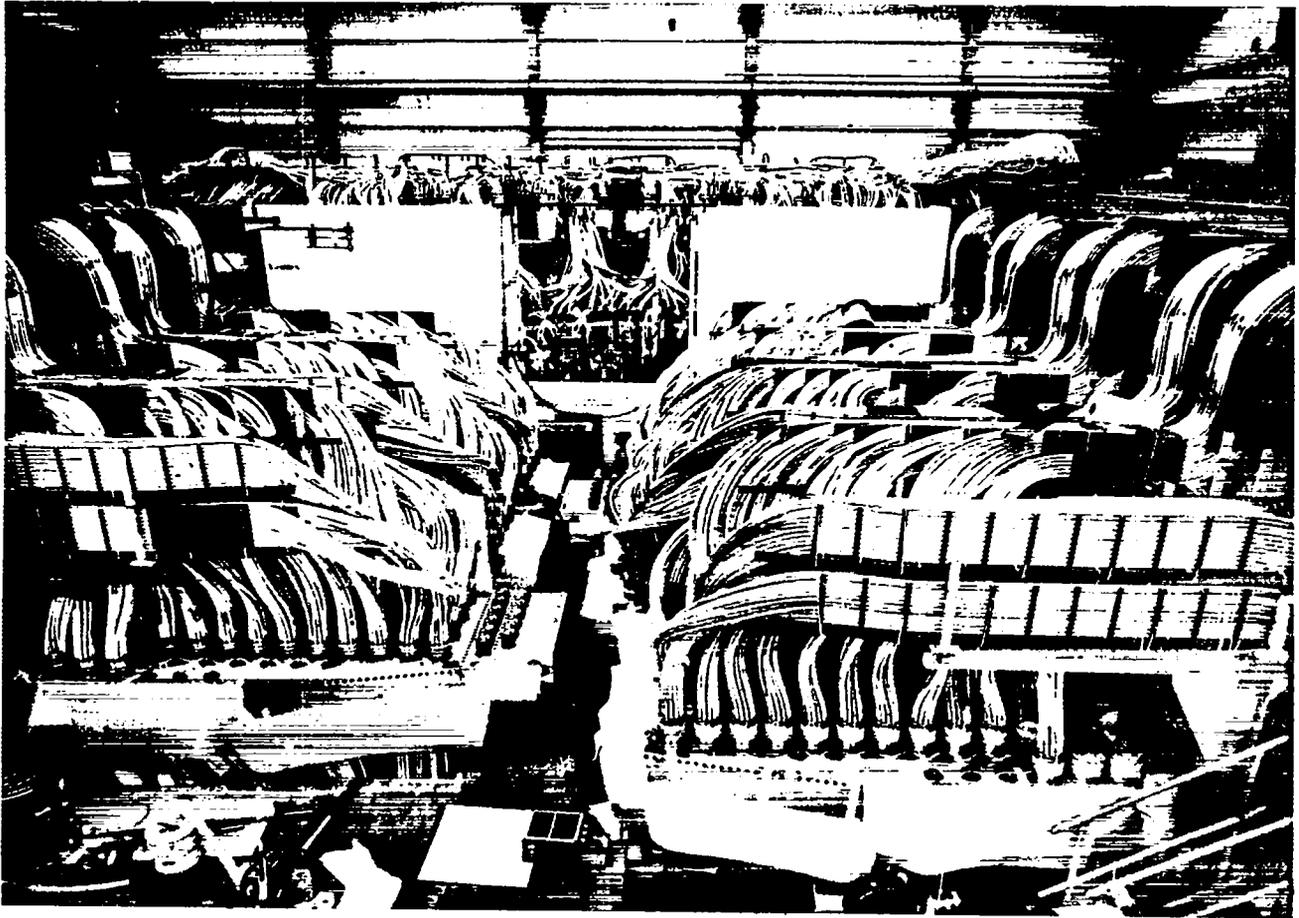
*Fig. IX-1.*
*Linear Scyllac with toroidal section in background.*

All units were under warranty and it was deemed essential to determine the cause of the early failures in the McGraw and Sangamo units so the manufacturers could correct the problem before building replacement units. In the case of Sangamo, a general upgrading of their swaging and impregnation processing seems sufficient to greatly improve the performance of their units.

The McGraw-Edison units exhibited a unique mode of failure. The first time their capacitors were tested about 13% of them failed. Then after a period of 4 to 6 months of storage they were again tested in the same test. This time over 40% failed. After considerable investigation, it is believed that the McGraw-Edison capacitors were not dried sufficiently before they were impregnated. Satisfactory replacements have been obtained.

3. Feedback Stabilization System (D. Call). A feedback stabilization system is being developed to stabilize the m = 1 instability on the toroidal Scyllac. The system includes a plasma position detector, a signal processor, a power amplifier, and load coils. P-16 efforts have been primarily on the power amplifier. The power amplifier consists of one transistor stage and three vacuum tube stages which are all transformer coupled. These coupling transformers were designed and built by Sherwood personnel to minimize the cost and procurement time. The final output stage uses two Machlett ML-8618 magnetically beamed triodes in a push-pull circuit. Technical details for the application and acceptance testing of the tubes were coordinated with Machlett. The 35-kV plate power supply for the ML-8618 includes a capacitor bank which must be discharged into a resistor when the ML-8618 arcs internally. A crowbar system for this purpose was designed and built.

A potential problem is that a fault in the load coils could generate a high voltage across the ML-8618 final

output tubes and destroy them. This problem has been studied with the help of the NET-2 network analysis computer program. A solution has been proposed which would use a voltage-dependent resistor (VDR) across the secondary of the output transformer. During proper operation, the voltage across the VDR will be low and therefore its resistance will be high. When a failure occurs, a high voltage will be placed across the VDR and its resistance will drop to a low value. This will divert the energy from feeding a high voltage back into the output tubes and destroying them.

4. Explosive-Driven Crowbar Switch (R. Dike and R. Kewish). The development of the detonator crowbar switch for use on ZT-1 has reached a stage where it is ready for actual test in a typical switching environment. Prior to its use on ZT-1, the switch will be proof-tested on the linear Z-pinch device where its reliability of operation with a system will be assured.

The basic design of the switching section, as shown in Fig. X-2, uses the expanding gases of a detonator discharge to achieve a metal to metal contact between the *driven plate* and the *die plate* as shown. The housing of the switch has been designed so that its incorporation within the ZT-1 experiment simply involves the removal of one through-bolt assembly and replacing it with the detonator switch assembly.

In its present design this switch has the following characteristics. With a peak voltage requirement of 40 to 50 kV and using a 0.030-in.-thick polyethylene insulator to hold off this pulsed voltage spike, the switch will carry about 400 kA. The total closure time, that is, the time between the igniting pulse and when contact is made, is ~ 12 $\mu$sec, involving a metal motion time of about 5 $\mu$sec. The resistance in the switch contacts is about 10 $\mu\Omega$ and the total inductance (including housing) is calculated to be about 20 nH.

5. Computer Analysis (G. Boicourt). Many of the circuits used in Sherwood generate high-voltage transients that cause electrical breakdowns with catastrophic results. A computer program, the NET-2 Network Analysis
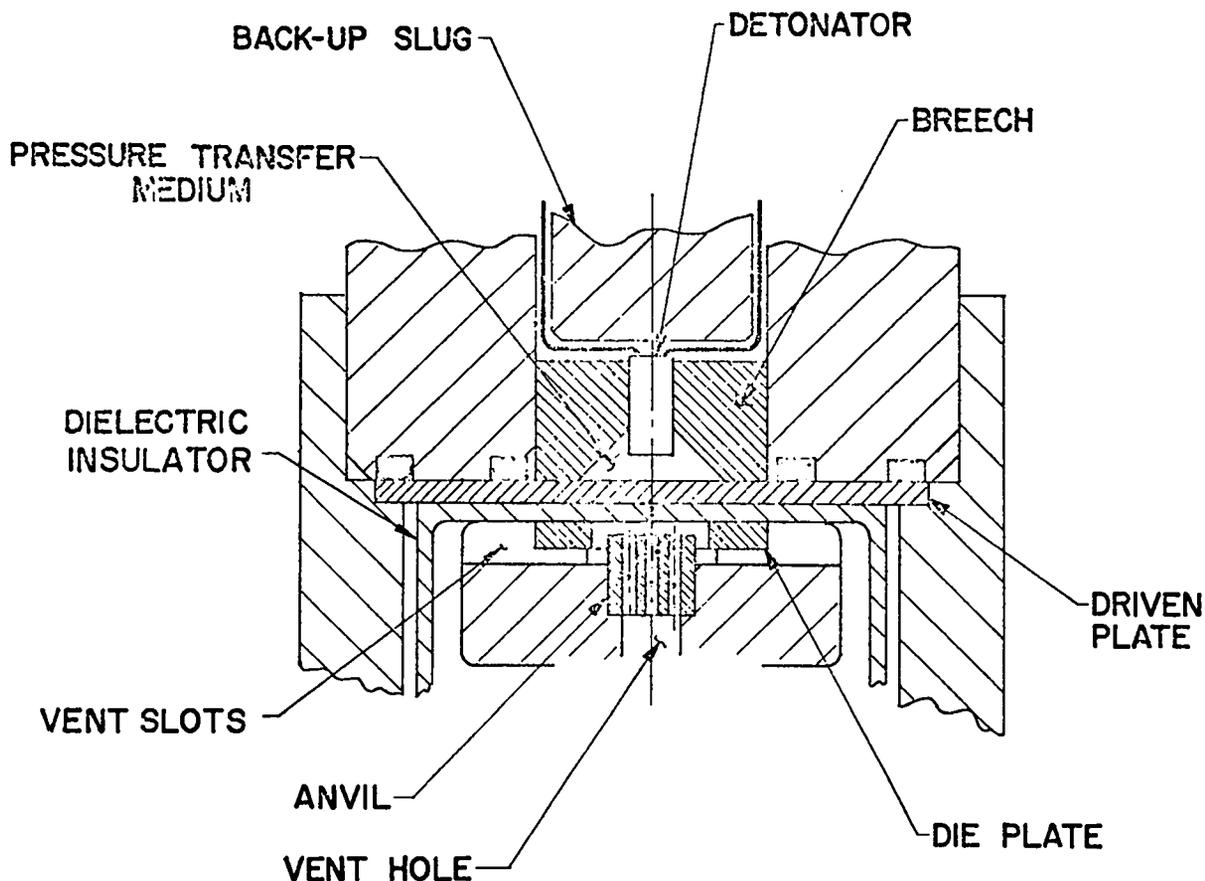


*Fig. IX-2.*
*Explosive-driven crowbar switching section.*

Program, has been effective in analyzing the transient voltages in actual hardware circuits. One of the laser groups in the Laboratory was losing capacitors well within their published ratings. Analysis showed high-voltage transients were the actual cause of failures. A simple solution has been proposed.

The toroidal Z pinch requires a circuit to reverse the bias field outside the plasma after compression. The NET-2 program was used to study a variety of circuits to accomplish the reverse bias. The NET-2 program was also used to analyze the crowbar circuit for the 2X-II mirror experiment at Livermore. The results were used in the design of a better crowbar system for the experiment.

The Scyllac mirror coils will be rather short in relation to their diameter. Consequently the field in the coil is a complex function of the coil current and the coil shape. A program code is being developed to design a coil that will produce a known field with a given coil shape.

# X. FEASIBILITY AND REACTOR TECHNOLOGY

## A. Introduction

There has been an increased interest and activity in the technological aspects of CTR during this past year. These activities include the extrapolation of high-$\beta$ pulsed systems to feasibility conditions and to reactor environments. Two reports that involve such matters are discussed in Sections X-B and -C. One of the basic considerations in reactor systems which should, ideally, be part of a feasibility demonstration, is how efficiently one can furnish the required energy to heat and confine the plasma. Present techniques for both $\theta$ and Z pinches involve capacitor banks to furnish the infrequent current pulse that both heats and compresses preionized deuterium. Much of the success and level of technical achievement attained today is due to the fine development that has been possible in rapidly and reliably switching millions of amperes and in furnishing the necessary high-quality capacitors. Nevertheless, such an energy source is not deemed to be well-suited to the economic requirements of a reactor, so a program of cryogenic energy storage has been initiated (see Section X-D). Although presently concerned with the basic properties of superconducting switches and coils, it is hoped that this approach will eventually permit a system to be devised with the required characteristics.

One cannot avoid the crucial question of how to understand the role of radiation damage in 14-MeV CTR energy sources; if an analogy is required the fission reactor program readily provides it. The problem is much more severe in the case of fusion in that the neutron energy distribution is fed by a 14-MeV source rather than a fission spectrum and that a much larger fraction of the energy released is in the form of fast neutrons. In addition, the radiation damage associated with full energy or slightly degraded 14-MeV neutrons, i.e.,energies over the $(n,\alpha)$ threshold in most materials, appears to be more serious than that associated with fission neutrons. It seems most appropriate, therefore, that careful consideration be given to the possibility of constructing an intense 14-MeV neutron source that might permit realistic and relevant material exposures within the next few years. Such a system has been conceived and is discussed in Section X-E.

Magnetic confinement represents a common base for all present approaches to CTR systems with one outstanding exception: laser heating. This radiation heating approach involves many very different basic physics concepts and technological requirements. Nevertheless, there is an important overlap concerning plasma physics,

especially on a short time scale. This overlap is probably most natural for the fast pinch systems and, indeed, the theoretical approaches to plasma simulation developed at Los Alamos are finding just such a role in calculations concerning laser-heated pellets as mentioned in Section VI-B. This basic, common plasma base is accentuated by the fact that LASL has a laser development program under way funded by the Division of Military Applications, wherein the technological aspects are under active study. A CTR-funded study has been initiated this year at LASL with the intent of investigating the general aspects of laser-ignited systems. This has been initially oriented toward a study of a specific reactor system proposed by another effort at Los Alamos, as discussed in Section X-F. In the process of attempting such a design, one inevitably uncovers many interesting aspects which may be limitations to such a design. Some of these are related to laser output energy and frequency, pellet design, and optical effects as well as to mechanical shock phenomena. Such considerations will be covered in the reactor system report being prepared and in future progress reports as well.

## B. Parameter Study of a Long, Separated-Shock $\theta$ Pinch with Superconducting Inductive Energy Storage (F. L. Ribe)

The following abstract summarizes a report (LA-4828-MS) which is being published. Figure X-1 summarizes plasma-heating parameters corresponding to a final temperature of 10 keV for a discharge-tube inner radius of 12 cm. In addition to a parameter study of the abiabatic-compression circuit, a cost estimate of the overall feasibility experiment is also given in the report.

Present $\theta$-pinch experiments involve high-$\beta$ plasmas with area compression ratios of the order of 40, using high-voltage capacitors to provide both the early shock heating (during the first few tenths $\mu$sec) and the later abiabatic compression, in a single-turn coil. In the separated-shock concept, the shock heating is done by high-voltage circuits whose energy content is only a few percent of that of the total system. The compression magnetic energy, which is preponderant, is contained in a muliturn coil with a slow risetime (of the order milliseconds) appropriate to abiabatic compression of the plasma in long systems. The area compression ratios are less than 10. Physical parameters and costs of a large system, appropriate to a scientific feasibility experiment at $kT_i \approx 10$ keV and $n\tau \approx 10^{14}$ cm$^{-3}$ sec are derived in this report. The shock heating is calculated on the basis of
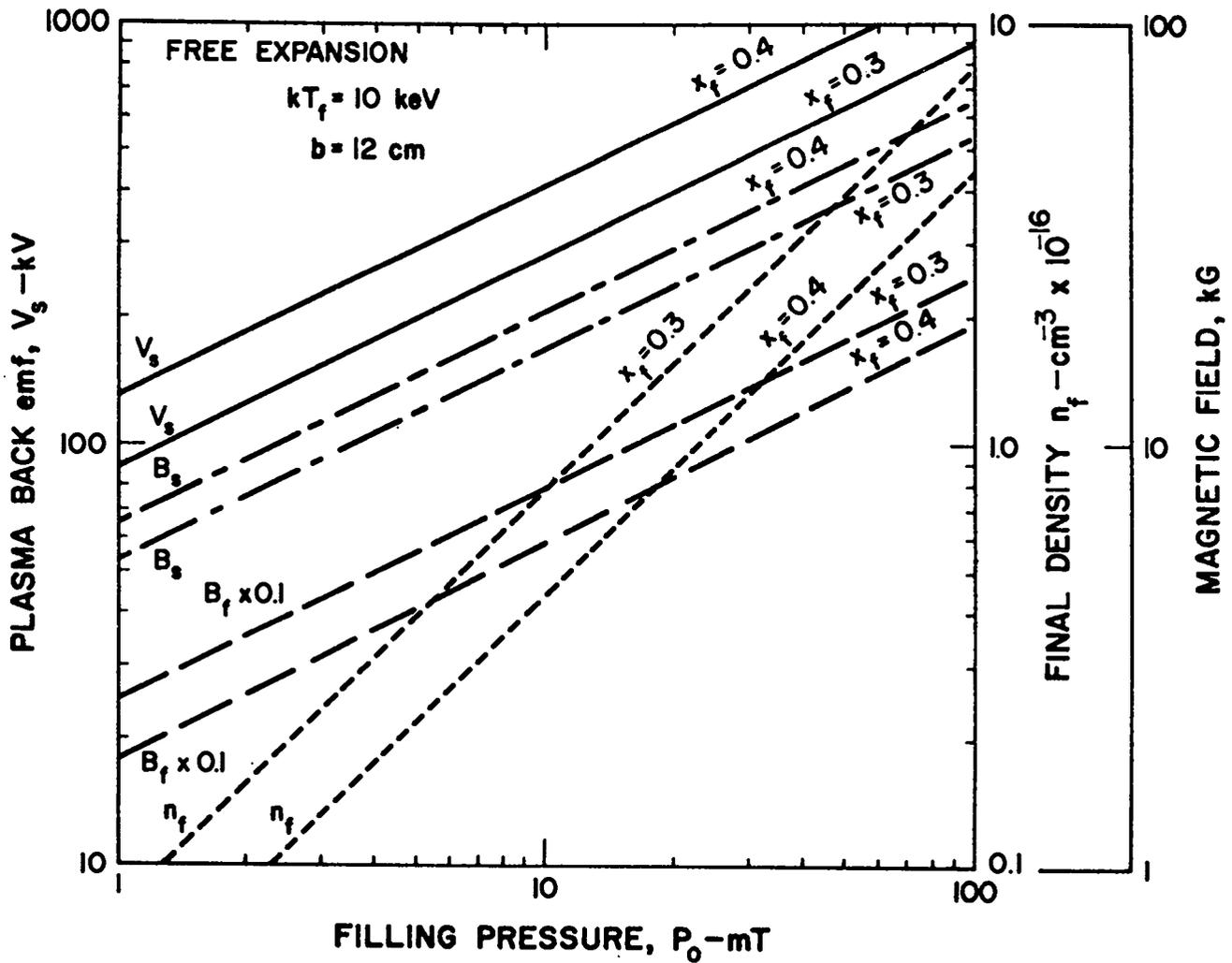
*Fig. X-1.*

*Plasma heating quantities vs filling pressure for various radial compression ratios $x_f$ corresponding to the final abiabatically compressed state. The ions are assumed to expand freely after their first acceleration by the magnetic piston.*

plasma sheaths driven by Blumlein transmission lines, although other electrical circuits might be used. The abiabatic compression field is assumed to be energized by

a superconducting inductive energy source, switched by normal-going superconductors.

C. Radiation and Wall Flux Calculations for a $\theta$-Pinch Scientific Feasibility Experiment and a **Prototype Reactor** (S. Burnett and W. Ellis)

A report (LA-4814-MS) has been written which summarizes the projected parameters for the next two generations of high-$\beta$ $\theta$-pinch devices: 1) a toroidal scientific feasibility experiment and 2) a prototype, pulsed D-T reactor. Table X-1 summarizes the projected parameters for these toroidal devices.

The parameters have been used to calculate reaction rates and the energy densities of charged particles, neutrons, and photons in the plasma. The effect of alpha particle heating and plasma expansion has been included by using a Fokker-Planck code of T. Oliphant to compute particle densities and temperatures as a function of time. The corresponding fluxes to be expected on the first-surface vacuum wall have been derived. Charged particle

fluxes have been estimated using a time dependent diffusion model suggested by J. Freidberg.

D. Cryogenic Energy Storage (H. L. Laquer, J. D. G. Lindsay, E. M. Little, and D. M. Weldon)

Some of the technological problems associated with magnetic energy storage were outlined in the 1970 annual report.[1] In the past year, our experimental program has concentrated on aspects of these problems bearing on storage systems using superconducting storage coils and high-current transfer switches which operate by changing from the superconducting to resistive state.[2,3] Although the exact mechanism of the transition from the superconducting to normal state is not known, some empirical understanding of the speed at which the transition occurs, as a function of the particular superconductor and its

TABLE X-1

PROJECTED PARAMETERS

| Quantity | Feasibility Experiment | Reactor[a] |
|---|---|---|
| Major radius | 28.6 m | 57 m |
| Circumference | 180 m | 360 m |
| Plasma radius | 3 cm | 8.3 cm |
| Wall radius | 10 cm | 20 cm |
| Plasma volume | $5.1 \times 10^5$ cm$^3$ | $7.8 \times 10^6$ cm$^3$ |
| Plasma line volume | 28.3 cm$^3$/cm | 216 cm$^3$/cm |
| Area of vacuum wall | $11.3 \times 10^5$ cm$^3$ | $4.5 \times 10^6$ cm$^2$ |
| Line area of vacuum wall | 62.8 cm$^2$/cm | 126 cm$^2$/cm |
| Plasma aspect ratio | $\sim 950$ | $\sim 700$ |
| Fuel | D-D or D-T | D-T |
| Filling pressure | 10 mTorr | 24.5 mTorr |
| $\beta$ | 0.8 | $\cong 1$ |
| Compression ratio | 3.3 | 2.4 |
| n | $8 \times 10^{15}$ cm$^{-3}$ | $10^{16}$ cm$^{-3}$ |
| $\tau_T$ | 12.5 msec | 50 msec |
| $T_i$ | 8.5 keV | 10.9 keV |
| $T_e$ | 7 keV | 14.0 keV |
| $n\tau_T$ | $10^{14}$ cm$^{-3}$ sec | $5. \times 10^{14}$ cm$^{-3}$ sec |
| $B_o$ | 80 kG | 110 kG |
| $B_i$ | 36 kG | 11 kG |
| Burnup fraction | 0.003% (D-D) <br> 0.35% (D-T) | 3-4% |
| Duty factor | - - - | $\cong 0.05$ |

[a]Reactor quantities refer to *average* values of the plasma parameters during the burn.

geometry, has been obtained from investigations of switching speeds of wires and braids of different materials and diameters. In most of these experiments, switching was accomplished by discharging a capacitor through the switch to exceed its critical current.

Switching times have been measured for various samples of multifilament superconductors in Cu-Ni matrix. Results obtained are similar to results obtained earlier by Laquer and Montgomery[4] for pure superconductor samples, i.e., the limiting switching times are a linear function of the sample diameters. Table X-2 shows the maximum current density, $J_c$, and the minimum switching time, $\tau_\varrho$, observed for several samples.

Figure X-2 shows a plot of switching time vs rate of change of current at time of switching. Some measurements have also been done on switches made in the form of ribbons and tubes of pure superconductor, but these proved to be unsatisfactory because of low limiting currents in the case of ribbons and mechanical problems with tubes.

The switch material employed so far in the model energy storage systems we have built is the same multifilament Nb-Ti investigated above, with a high-resistance matrix (90 wt% Cu, 10 wt% Ni) and a matrix-to-superconductor volume ratio of 2.8:1. A five-wire braider was built and a commercial 16-wire braider was obtained to produce up to 100-ft lengths of unbroken braid. Two-hundred-ampere and 600-ampere switches with normal resistances between 3 and 15 $\Omega$ were made in this fashion.

Braided superconductor should exhibit a critical current equal to the sum of the critical currents of the individual wires. This is true at fields above 30 kG; however, for the small 2- or 3-kG self-fields present in the switches at near critical currents, proximity effects become important, producing a degradation to about 50% of the sum of the single-wire currents in both pulsed and dc experiments. Fortunately, this degradation levels off between five and nine wires and the critical current densities in the Nb-Ti proper are then about $5 \times 10^5$ A/cm$^2$. This is in agreement with recent measurements on the steepness at low fields of the critical current vs field curves. Switching times for the switches in the model storage systems were in the range of five to ten $\mu$sec.

The largest energy storage coils constructed so far have been solenoids 8-in. long with a 5-in. inside diameter and an 8-in. outside diameter. These coils stored 1.5 kJ at 200 A and 4 kJ at 350 A and were wound with flat braids of multifilament Nb-Ti superconductor in a copper matrix. With additional mechanical stabilization of the storage coil windings and larger switches, all of these 8-in. coils should be capable of storing 20 kJ at 1000 A without exceeding the critical current of the superconductor. A nonconducting dewar capable of holding a 300 kJ storage system is being fabricated.

TABLE X-2

Nb-Ti SWITCH MATERIALS

| d (cm) | r | n | $J_c$ (A/cm$^2$) | $\tau_\varrho$ ($\mu$sec) | $\rho_n$ ($\mu \Omega$ cm) | Matrix |
|---|---|---|---|---|---|---|
| $1.40 \times 10^{-2}$ | 0 | 1 | $3.7 \times 10^5$ | 0.21 | -- | none |
| 2.39 | 0 | 1 | 3.9 | 0.3 | 40 | none |
| 3.68 | 0 | 1 | 2.0 | 0.5 | -- | none |
| 1.30 | 2.8 | 22 | 3.4 | 0.11 | 15 | 90/10 Cu-Ni |
| 2.49 | 2.8 | 22 | 2.5 | 0.22 | 16 | 90/10 Cu-Ni |
| 3.81 | 2.8 | 22 | 1.8 | 0.35 | 13 | 90/10 Cu-Ni |
| 7.62 | 2.5 | 467 | 2.8 | 1.6 | 20 | 80/20 Cu-Ni |
| 2.08 | 1.1 | 192 | 4.4 | 0.3 | 0.67 | 99/1 Cu-Ni |

d = wire diameter
r = ratio of matrix to superconductor
n = number of filaments of Nb-Ti
$J_c$ = measured switching current/total wire cross section (both matrix and superconductor)
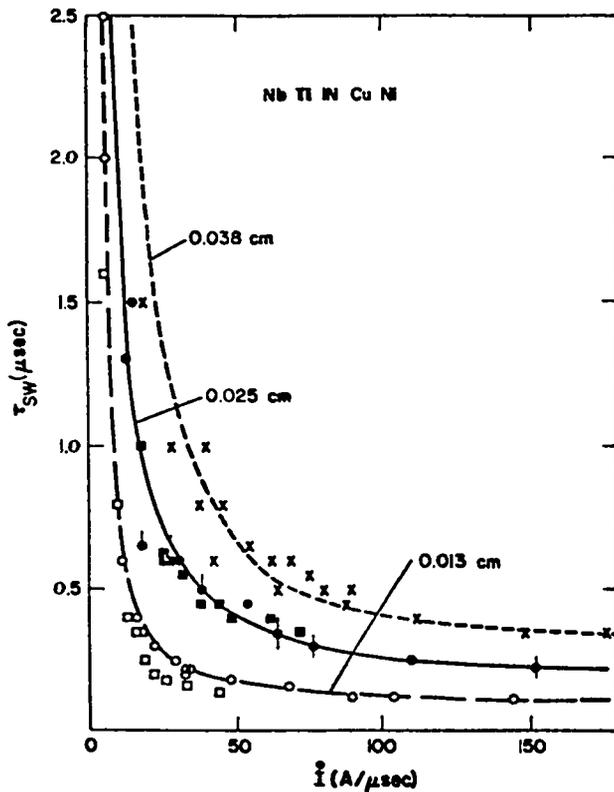
*Fig. X-2.*

*Variation of switching time with rate of current change (İ). The squares are from measurements on 8.5-cm long samples and the circles from 17.3-cm long samples. The x's include both short and long sample data.*

References:

1. Los Alamos Scientific Laboratory report LA-4585-MS, p. 28 , (1970).

2. H. L. Laquer, F. L. Ribe, and D. M. Weldon, Intersociety Energy Conversion Engineering Conference Proceedings, 38, 1089 (1971).

3. H. L. Laquer, D. B. Montgomery, and D. M. Weldon, XIII International Congress of Refrigeration, (1971).

4. H. L. Laquer and D. B. Montgomery, Bull. Am. Phys. Soc. 15, 1485 (1970).

E. A Possible Facility for Duplicating 14-MeV Neutron Effects in Fusion Power Reactors (H. Dreicer and D. B. Henderson)

We believe that an important ingredient of forthcoming technical fusion feasibility studies is the demonstration that reactor wall materials can maintain their structural integrity when bombarded by the intense flux of neutrons produced in a D-T fusion reactor. The main obstacle presently preventing such a demonstration is the nonexistence of a neutron source whose neutron flux and primary neutron spectrum are comparable to that emitted by a D-T burning fusion reactor, i.e., approximately $10^{15}$ neutrons-cm$^{-2}$-sec$^{-1}$ at 14 MeV.

Our recent survey of neutron sources[1] is summarized in Table X-3 and compared with a fusion power reactor. Of all possible sources considered and listed in Table X-3, only an ion accelerator, which utilizes a dense gas target for neutron production from the D-T reaction, can satisfy all of the conditions required for the demonstration and study of neutron effects. As one measure of the efficiency of each of the neutron sources listed, Table X-3 gives the rate of helium built-up due to $(n, x\alpha)$ reactions in niobium for each source and compares it with the helium production expected for fusion reactor neutrons. Table X-3 shows that only the gas target ion accelerator would be comparable to the fusion reactor in this respect. All other sources are several to many orders of magnitude too weak and may have an incorrect neutron spectrum as well.

Our conception of the gas target ion accelerator, shown schematically in Fig. X-3, utilizes a 1-A tritium ion beam from an ion source of the type developed at Oak Ridge National Laboratory (ORNL), a standard 300-keV accelerator column (design codes for which exist at LASL from the Meson factory (LAMPF) development), a dense ($\sim 10^{19}$ molecules-cm$^{-3}$) deuterium gas target in the form of a supersonic jet directed across the ion beam to minimize differential pumping requirements, and a tritium recovery dump which utilizes the existing LASL Tritium Facility for recovery and processing to allow reuse of the tritium (tritium cost = $10^4$/g). Our preliminary design of the target features a hypersonic wind tunnel at Mach 5 with entrance and exit holes for the tritium beam protected by differential pumping sections.

Although we have not yet optimized our design, we conclude that this neutron facility can produce 8 x $10^{14}$ neutrons-sec$^{-1}$ in a 1-cm$^3$ reaction volume by using a 500 horsepower wind tunnel compressor, 500 horsepower for the differential vacuum pumps, a 300-to 500-kW ion source power supply, and a cryosorb tritium recovery pump as a dump for the 50-keV tritium beam which emerges from the gas target. Assuming the sample subtends a third of the neutrons, this leads to the flux, 3 x $10^{14}$ neutrons-cm$^{-2}$-sec$^{-1}$, as given in Table X-3. Larger areas could be irradiated at this same flux by stacking up several ion beams.

The major technical developments required for the facility are the ion beam and the dense-gas target. The facility would profit strongly from the ongoing beam

## TABLE X-3

| Neutron Source | Spectrum D-T | Type | Flux (n/cm² sec) | Helium (ppm/month) |
|---|---|---|---|---|
| Fusion Power Reactor | Yes | -- | $1 \times 10^{15}$ | 30. |
| Ion Accelerator - Gas Target | Yes | -- | $3 \times 10^{14}$ | 9.0 |
|                - Metal Target | Yes | -- | $5 \times 10^{11}$ | 0.015 |
| LAMPF Beam Dump | No | Copper | $2 \times 10^{12}$ | 0.017 |
| Dense Plasma Focus at 5 MJ | Yes | -- | $1 \times 10^{12}$ | 0.030 |
| Experimental Breeder Reactor II | No | Fission | $3 \times 10^{15}$ | 0.008 |
| Electron Linac (e, $\gamma$, n) | No | Uranium | $6 \times 10^{11}$ | 0.0001 |
| Boosted Electron Linac | No | Fission | $6 \times 10^{12}$ | 0.0003 |
| Thermonuclear Bomb | Yes | -- | (n/cm²) $1 \times 10^{17}$ | (ppm) 0.0012 |
| Minimum needed for metallurgy | | | | 0.001 |
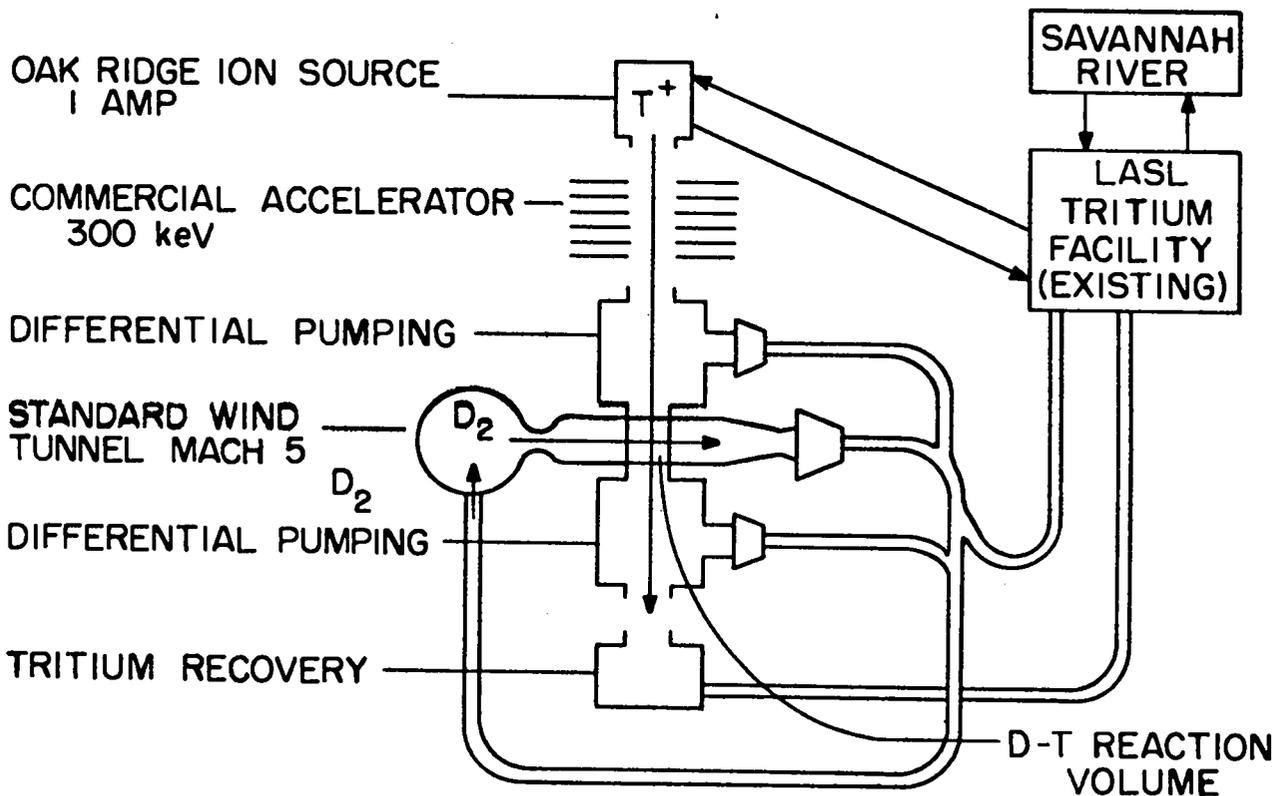


*Fig. X-3.*
*Concept of the gas target ion accelerator.*

development programs at ORNL and at the Lawrence Livermore Laboratory (LLL) which have already produced 1-A beams at several to several hundred keV. The primary development which therefore remains in this area involves the focusing of the beam through differential pumping ports of 1- to 2-cm diam, a development which is considered to be technically feasible. It is noteworthy that the neutral injection programs at ORNL and LLL depend upon focusing requirements which actually are more stringent than ours. The use of a 300-keV beam energy is expected to stiffen the beam and thus to simplify the problem. Hypersonic wind tunnels of the type described have already been built.

Reference

1. H. Dreicer and D. B. Henderson, A Facility for Duplicating 14-MeV Neutron Sources in Fusion Power Reactors, Los Alamos Scientific Laboratory report LA-4709-MS, 1970.

F. Reactor System

LASL has initiated the study of various methods by which stationary electrical power may be generated from pulses of energy released by laser-initiated fusion reactions. The immediate goal of this effort is an engineering analysis of a specific power-plant concept that holds promise for being both practical and useful. A special report summarizing the results of this work will be issued in early 1972.

Comparison of a laser-ignited fusion energy source with that of the traditional magnetic confinement controlled thermonuclear reactors (CTR) indicates a basic dissimilarity: in the laser-ignited source, the energy is produced in relatively infrequent large pulses from a very small volume which require a mechanical restraint, e.g., a pressure vessel, to contain the blast energy of the reaction. However, there are two outstanding areas of similarity with the traditional D+T-fueled CTR: a) the bulk of the energy produced (75 to 80%) is carried out of the thermonuclear reaction region by fast neutrons, and b) the power plant must breed, i.e., as much tritium must be produced as is consumed and lost.

These similarities dictate that either type of power plant must be designed with a thick blanket outside the reaction region (to convert the neutron energy) and this must consist to a great extent of lithium (to produce tritium). Also, the plant must contain facilities for extraction and recovery of tritium from the blanket.

The concept chosen for current study is the "wetted-wall" system. The assumed source of energy is a D+T fusion reaction releasing 200 MJ of energy per pulse

at the center of a spherical cavity of 1-m radius. The sphere is assumed to be evacuated to a pressure of < 1 mm Hg of lithium vapor. Energy pulses are released at the rate of one per sec. The boundary of the cavity is defined by a thin wall of porous metal, surrounded by a 1-m-thick spherical-shell blanket of liquid lithium. Before release of each energy pulse, liquid lithium is diffused through the wall to wet the inside surface of the sphere to a depth of ~ 1 mm. This lithium, which is vaporized by the energy release, is heated to a temperature of ~ 4000°K and a pressure of ~ 24 bar. The vapor escapes through a nozzle port (throat diameter, ~ 20 cm), which extends through both the wall and the blanket, and is condensed in a supersonic liquid-spray condenser. After one second, when the pressure in the sphere has been reduced again to < 1 mm Hg, another D+T-filled pellet is injected through a small port and initiated by a laser pulse. Electrical energy is generated by a conventional steam plant operating at a top temperature of 600°C. The bulk of the thermal energy to power the steam cycle is derived from the fast-neutron energy deposited in the spherical blanket of liquid natural lithium surrounding the pulse-reaction cavity. The heated liquid lithium in the blanket is pumped through a primary heat-exchange loop, which operates at a peak temperature of 750°C. Additional heat energy is obtained from the lithium-spray condenser system. The overall design is such that the tritium breeding ratio could be as high as 1.4; some poisoning of the blanket will therefore be allowed to reduce the breeding ratio to a value slightly exceeding unity.

A major question concerning the feasibility of this concept is the structural integrity of the wetted inner wall of the reaction vessel. The wall has two functions: 1) to define the spherical inner cavity and 2) to provide a porous passage for the lithium into the cavity. Because this sphere is not a pressure vessel, its walls will respond elastically to blast effects from the expansion of material generated by the pulse units. Neutron flux levels at the inner wall are comparable to those of steady-state CTR plants. Analysis indicates that by suitable deployment of pressure vessels within the blanket, the stresses in the inner wall could be kept low. These pressure vessels could be cooled by the lithium and could, in addition, serve as needed flow baffles to direct the radial flow of lithium. Thus, the inner wetted wall would be at a temperature comparable to the lithium inlet temperature, ~400°C, and therefore could be made of an ordinary material such as stainless steel. The inner wall could be either a perforated solid shell or a wire-wound shell.

The vessel described above is simple and easily fabricated. It could be clustered with several other units into a modular energy source for a fusion power plant. The

overall thermodynamic efficiency of such a plant would be 40 to 45%, with the output of one vessel being roughly 200 MW (thermal). The output of such a modular plant would not be impaired seriously by the downtime of one vessel for routine maintenance or emergency repair; the yearly replacement (if necessary) of metal liners would therefore not pose an unusual problem.

# PAPERS PUBLISHED OR PRESENTED

| | | |
|---|---|---|
| H. Dreicer<br>D. B. Henderson<br>J. C. Ingraham | Anomalous Microwave Absorption Near the Plasma Frequency | Phys. Rev. Letters 26, 1616 (1971). |
| H. Dreicer<br>D. B. Henderson<br>D. Mosher | Use of Radioactive Test Ions in the Measurement of the Spatial Distribution of Plasma Ion Drift Speeds | Phys. Fluids 14, 1289 (1971). |
| J. D. Thomas | An Anomalous Sturm-Liouville Problem | Submitted to SIAM Journal of Mathematical Analysis |
| P. R. Forman<br>A. Haberstich<br>H. J. Karr<br>J. A. Phillips<br>A. E. Schofield | Dynamic Stabilization of a Linear Z Pinch by a Magnetic Quadrupole | Physics of Fluids 14, 684 (1971). |
| P. R. Forman<br>F. C. Jahoda<br>R. W. Peterson | Two-D Interferometry with a Pulsed 10.6-$\mu$m Laser | Submitted to Applied Optics |
| R. F. Gribble<br>W. E. Quinn<br>R. E. Siemon | Plasma Experiments with a Three-Meter $\theta$ Pinch | Phys. Fluids 14, 2042 (1971). |
| C. R. Harder<br>F. L. Ribe<br>R. E. Siemon<br>K. S. Thomas | Demonstration of a Body Force Produced on a $\theta$-Pinch Plasma Column by Helical Magnetic Fields | Phys. Rev. Letters 27, 386 (1971). |
| F. C. Jahoda | Pulse Laser Holographic Interferometry | Published in Modern Optical Methods in Gas Dynamic Res.,Ed. by Kosanjh (Plenum Press, 1971). |
| R. W. Peterson<br>F. C. Jahoda | A New Method for Absolute Calibration of Electro-Optic Modulators | Rev. of Scientific Instruments 42, 532 (1971). |
| R. W. Peterson<br>F. C. Jahoda | A Far-Infrared Coupled-Cavity Interferometer | J. Appl. Phys. Letters 18, 440 (1971). |
| F. L. Ribe | Recent Developments in High-Beta Plasma Research on $\theta$ and Z Pinches | Article to be published in Comments on Plasma Phys. and Controlled Fusion, Sept. 1971. |
| T. P. Armstrong<br>C. W. Nielson | Initial Comparison of Transform and Particle-In-Cell Methods of Collisionless Plasma Simulation | Phys. Fluids 13, 1880 (1970). |
| G. Berge<br>J. P. Freidberg | Dynamic Stabilization of the Screw Pinch | Phys. Fluids 14, 1035 (1971). |
| J. Enoch | Constants of the Motion for Toroidal $\theta$ and Screw Pinches | Phys. Fluids 14, 1247 (1971). |
| D. W. Forslund<br>J. P. Freidberg | Theory of Laminar Collisionless Shocks | Phys. Rev. Letters 27, 1189 (1971). |
| D. W. Forslund<br>R. L. Morse<br>C. W. Nielson | Electron Cyclotron Drift Instability | Phys. Rev. Letters 25, 1266 (1970). |
| D. W. Forslund<br>R. L. Morse<br>C. W. Nielson | Nonlinear Electron-Cyclotron-Drift Instability and Turbulence | Phys. Rev. Letters 27, 1424 (1971). |

| D. W. Forslund<br>C. R. Shonk | Formation and Structure of Electrostatic<br>Collisionless Shocks | Phys. Rev. Letters 25,<br>1699 (1970). |
|---|---|---|
| J. P. Freidberg<br>B. M. Marder | High-Frequency Electrostatic<br>Plasma Instabilities | Phys. Rev. A4,<br>1549 (1971). |
| J. P. Freidberg | Resonant Absorption of Laser Light by<br>Plasma Targets | Submitted to Phys. Rev.<br>Letters |
| J. P. Freidberg | Stability of the Straight $\ell = 1$<br>Scyllac Configuration | Phys. Fluids 14,<br>2454 (1971). |
| J. P. Freidberg | A Vlasov-Fluid Model for Studying Gross<br>Stability of High-Beta Plasmas | Submitted to Physics of<br>Fluids |
| J. P. Freidberg<br>B. M. Marder | Stability of a High-$\beta$, Helically<br>Symmetric Pinch | Phys. Fluids 14,<br>174 (1971). |
| J. Freidberg<br>R. Mitchell<br>R. Morse<br>L. Rudsinski | Resonant Absorption of Laser Light by Plasma<br>Targets | Submitted to Phys. Rev.<br>Letters |
| S. J. Gitomer<br>D. W. Forslund<br>L. Rudsinski | Numerical Simulation of the Harris Instability<br>in Two Dimensions | Submitted to Physics of<br>Fluids |
| H. R. Lewis | Linearized Variational Analysis of Single-<br>Species, One-Dimensional Vlasov Plasmas | Submitted to Physics of<br>Fluids |
| H. R. Lewis | Variational Algorithms for Numerical Simula-<br>tion of Collisionless Plasma with Point<br>Particles Including Electromagnetic<br>Interactions | Submitted to Journal of<br>Computational Physics |
| H. R. Lewis<br>A. Sykes<br>J. A. Wesson | A Comparison of Some Particle-in-Cell Plasma<br>Simulation Methods | Submitted to Journal of<br>Computational Physics |
| B. Marder | A PIC-Type Fluid Code | Submitted to Journal of<br>Computational Physics |
| R. Morse<br>D. Forslund<br>C. Nielson | Electron Cyclotron Drift Instability<br>and Turbulence | Submitted to Physics of<br>Fluids |
| R. Morse<br>C. Nielson | Numerical Simulation of the Weibel Instabili-<br>ty in One and Two Dimensions | Phys. Fluids 14,<br>830 (1971). |
| R. L. Morse<br>C. W. Nielson | Studies of Turbulent Heating of Hydrogen<br>Plasma by Numerical Simulation | Phys. Rev. Letters 26,<br>3 (1971). |
| J. L. Tuck | Outlook for Controlled Fusion Power | Nature 233, No. 5322,<br>p. 593, October 29, 1971<br>and Nucl. Eng. Int'l,<br>Nov. 1971. |
| D. J. Dudziak | A Technical Note on D-T Fusion Reactor<br>Afterheat | Nuclear Technology 10,<br>391 (1971). |
| P. J. Bendt<br>M. G. Bowman<br>H. Dreicer<br>R. D. Fowler<br>E. F. Hammel<br>W. E. Keller<br>H. L. Laquer<br>F. L. Ribe<br>R. D. Taylor | Superconductivity at LASL: Research,<br>Development, and Applications | LA-4665-MS, May 1971. |

| | | |
|---|---|---|
| R. R. Hake | Single-Shot Pulsed Magnetic Fields from Inductive Energy Stores | LA-4617-MS, 1971 |
| H. Dreicer<br>D. B. Henderson | Facility for Duplicating 14-MeV Neutron Effects in Fusion Power Reactors | LA-4709-MS, 1971 |
| J. A. Phillips | Perhapsatron S-5 and S-5 Zeus Experiments Reviewed in Light of Current Technology | LA-4664, 1971 |
| W. R. Ellis<br>S. C. Burnett | Radiation and Wall Flux Calculations for a $\theta$-Pinch Scientific Feasibility Experiment and a Prototype Reactor | LA-4814-MS, 1971 |
| R. F. Gribble<br>E. M. Little<br>W. E. Quinn<br>R. E. Siemon | Plasma Experiments with a Three-Meter Theta Pinch | LA-4611-MS, 1971 |
| F. L. Ribe | Parameter Study of a Long, Separated-Shock $\theta$ Pinch with Superconducting Inductive Energy Storage | LA-4828-MS, 1971 |
| F. L. Ribe<br>W. H. Brokenhagen<br>W. R. Ellis<br>K. W. Hanks | Initial Equilibrium Configuration of the Scyllac 5 Meter Toroidal Sector Experiment | LA-4597-MS, 1971 |
| R. E. Siemon | $\Sigma$ 2 Least-Squares Fitting Program | LA-4619-MS, 1971 |
| K. I. Thomassen | Feedback Systems on Linear $\theta$ Pinches with Helical Fields | LA-4598-MS, 1971 |
| H. Weitzner | The Formulation of a Helically Symmetric Magnetohydrodynamic Theta-Pinch Problem | LA-4599-MS, 1971 |
| W. H. Borkenhagen<br>W. R. Ellis, Jr.<br>H. W. Harris<br>E. L. Zimmermann | $\ell$ - 1, 0 Coil System for Scyllac and Scylla IV | LA-4815-MS, 1971 |
| J. P. Freidberg<br>B. Marder | Laser-Induced Plasma Instability | LA-4604-MS, 1971 |
| Members of LASL<br>CTR Staff | Controlled Thermonuclear Research at LASL, Present Status and Future Plans for Feasibility and Reactor Experiments | LA-4656, 1971 |
| J. P. Freidberg | Resonant Absorption of Laser Light by Plasma Targets | LA-4852-MS |

## National Symposium on High Temperature Plasma Diagnostics, Sukhumi, USSR, May 13-21, 1970

| | |
|---|---|
| F. C. Jahoda | Laser Interferometry: A) Holographic and B) Coupled-Cavity |

## Symposium on Feedback and Dynamic Control of Plasmas, Princeton, New Jersey, June 18-19, 1970

| | |
|---|---|
| J. A. Phillips<br>P. R. Forman<br>A. Haberstich<br>H. J. Karr | Dynamic Stabilization of the Z-Pinch |
| F. L. Ribe | Feedback Stabilization of a High-Beta, Sharp-Boundaried Plasma Column with Helical Fields |

## International Symposium on Applications of Holography, Besancon, France, July 6-11, 1970
## Proceedings, Applications of Holography, J. C. Vienot, Ed., University of Besancon, 1970

F. C. Jahoda  
R. E. Siemon  
K. S. Thomas

Holographic Interferometry of Transient Plasmas

## AIAA Third Fluid and Plasma Dynamics Conference, Los Angeles, California, June 29-July 1, 1970

J. L. Tuck

Recent Progress in Controlled Thermonuclear Fusion Research

## Fifth Intersociety Energy Conversion Engineering Conference, Las Vegas, Nevada, September 21-25, 1970

E. R. Lady  
D. Call

High Voltage Test of a Large Cryogenic Coil for Magnetic Energy Storage System

F. L. Ribe

Economic Considerations and Magnetic Energy Storage for High Beta, Pulsed Reactors

## Sixth Symposium on Fusion Technology, Julich, Germany, September 22-26, 1970. Proceedings, Commission of the European Communities, Luxembourg, p. 227, 1970

E. L. Kemp Jr.  
G. P. Boicourt  
R. F. Gribble  
C. F. Hammer  
K. W. Hanks  
W. E. Quinn  
G. A. Sawyer

Design and Installation of Scyllac, a 15-Meter Theta-Pinch Experiment

## American Physical Society Meeting, Washington, D. C. Nov. 4-7, 1970. Bulletin of the American Physical Society, Ser. II, 15, No. 11 (1970)

H. Dreicer  
J. C. Ingraham  
D. B. Henderson

Anomalous Resistivity for Large Amplitude Electric Fields (E) Near The Electron Plasma Frequency (w)

D. B. Henderson  
H. Dreicer  
D. Mosher

Measurement of Ion Flux and Drift Speed Using Radioactive Ions

J. McLeod  
H. Dreicer

A Short Open Multi-mode Microwave Resonator for Plasma Density Measurement

J. A. Phillips

An All-Metal Discharge Tube for High E, Z-Pinch Experiments

J. N. DiMarco  
L. C. Burkhardt

A Fast Z Pinch

A. Haberstich

Numerical MHD Calculations of Shock-Heated Z Pinches

J. A. Phillips

The Z Pinch: Past and Future

K. I. Thomassen  
D. M. Weldon

Feedback Stabilization on Scylla IV

H. L. Laquer  
D. B. Montgomery

Superconductors as Fast Current Breakers

T. A. Oliphant  
F. L. Ribe  
H. Weitzner

A Numerical Study of the Helically Symmetric $\theta$ Pinch

A. R. Sherwood  
J. E. Hammel  
I. Henins  
J. Marshall  
R. W. Peterson

Interferometric Measurements of Plasma Densities in the LASL Toroidal Quadrupole Injection Machine

| | |
|---|---|
| W. E. Quinn<br>F. L. Ribe<br>K. S. Thomas | Helical Equilibrium and Stability Experiments in a 3-Meter<br>Theta Pinch |
| R. E. Siemon<br>H. Weitzner | Interferometric Measurements on a Helical Plasma Column |
| R. W. Peterson<br>F. C. Jahoda | A Double-Cavity Laser Interferometer Operating at $337\mu$ |
| G. Malesani<br>W. R. Ellis<br>A. A. Newton | Breakdown Behavior in Toroidal Pinches with Parallel Bias<br>Field |
| W. R. Ellis | Current Trapping in Toroidal Pinches as a Means of<br>Preionization |
| B. Marder<br>J. Freidberg<br>C. Nielson | A Laser-Induced Plasma Instability |
| J. P. Freidberg<br>B. M. Marder | Magnetohydrodynamic Stability of Scyllac<br>Configurations |
| J. Marshall<br>D. A. Baker<br>J. E. Hammel<br>I. Henins<br>R. W. Kewish, Jr.<br>L. W. Mann<br>A. R. Sherwood | Plasma Diagnostics in the LASL Toroidal Quadrupole Injection<br>Machine |
| J. E. Hammel<br>R. W. Kewish, Jr.<br>A. R. Sherwood | The Operation of a Toroidal Quadrupole with Kilovolt Plasma Energies |
| T. A. Oliphant<br>F. L. Ribe<br>H. Weitzner | A Numerical Study of the Helically Symmetric $\theta$ Pinch |
| S. J. Gitomer<br>D. W. Forslund<br>L. Rudsinski | Computer Simulation of an Electron Cyclotron Instability<br>Due to a Temperature Anisotropy |
| R. L. Morse<br>D. W. Forslund<br>C. W. Nielson | Electron Cyclotron Drift Instability |
| C. R. Shonk<br>D. W. Forslund | On the Formation and Structure of Strong Electrostatic<br>Collisionless Shocks |
| D. A. Baker<br>L. W. Mann | MHD Studies of Toroidal Z-Pinch and Related Equilibria |
| J. A. Phillips | An All-Metal Discharge Tube for High-E, Z-Pinch Experiments |

### Task Force on Research and Development Goals, Energy Research Council, San Diego, March 1, 1971

| | |
|---|---|
| F. L. Ribe | Status and Prospects of Pulsed, High-Beta Theta-Pinch Systems |

### Sherwood Theoretical Meeting at Courant Institute, New York University, March 22-23, 1971

| | |
|---|---|
| D. W. Forslund | Microscopic Instabilities in the Solar Wind |
| J. P. Freidberg<br>B. M. Marder | High Frequency AC Electrostatic Plasma Instabilities |
| J. P. Freidberg | Stability of the Straight $\ell = 1$ Scyllac Configuration |

# Fifty-Second AGU Meeting, Washington, D.C., April 12-16, 1971

D. W. Forslund  
G. Beeler

Helium-Rich Collisionless Shocks in the Solar Wind

# 1971 ANS Topical Meeting on Fast Reactor Fuel Element Technology, April 13-15, 1971, New Orleans, Louisiana

R. L. Cubitt

Thermal Irradiations of Sodium-Bonded Mixed Carbide Fuel

# Second SPIE Seminar in Depth on Holography, Boston, Massachusetts, April 14-15, 1971

R. E. Siemon  
F. C. Jahoda

Three-Frame Pulsed Holographic Interferometry of a Helical Plasma

# Fourth Symposium on Engineering Problems on Fusion Research, Washington, D.C., April 20-23, 1971. Proceedings, IEEE Trans. Nucl. Science, NS-18, No. 4 (1971)

D. L. Call  
R. F. Gribble  
R. E. Siemon

The Linear Feedback Stabilization System for Scyllac

W. H. Borkenhagen  
W. R. Ellis, Jr.  
H. W. Harris  
E. L. Zimmermann

Auxiliary Coil Systems for Scyllac

G. P. Boicourt

Analysis of a Capacitor Failure Problem Using Partially  
Ordered Sets

E. L. Kemp

Summary of the 4th Symposium on Engineering Problems of Fusion  
Research

# American Physical Society Division of Plasma Physics Symposium in Washington, D.C., April 26-28, 1971. Bulletin of the American Physical Society, Ser. II, 16 (1971)

B. M. Marder

A Review of Plasma and MHD Simulation at  
Los Alamos

# International Symposium of the National Helium Society, Washington, D.C., May 2-4, 1971

J. L. Tuck

On the Outlook for Controlled Fusion Power with Notes on Its Relation  
to Helium Consumption

# IAEA Fourth Conference on Plasma Physics and Controlled Nuclear Fusion Research, June 17-23, 1971, University of Wisconsin, Madison, Wisconsin

D. A. Baker  
L. C. Burkhardt  
J. N. DiMarco  
P. R. Forman  
A. Haberstich  
H. J. Karr  
L. W. Mann  
J. A. Phillips  
A. E. Schofield

Z-Pinch Experiments with Shock Heating

J. E. Hammel  
Ivars Henins  
R. W. Kewish  
John Marshall  
A. R. Sherwood

High-Energy Gun-Injected Toroidal Quadrupole

R. L. Morse  
D. W. Forslund  
C. W. Nielson

Theory of Turbulent Heating and Anomalous Diffusion in Pinch Plasmas

T. A. Oliphant

Simulation of Binary Collisional Dissipative Effects in CTR Plasmas

| | |
|---|---|
| S. C. Burnett<br>W. R. Ellis<br>C. F. Hammer<br>C. R. Harder<br>H. W. Harris<br>F. C. Jahoda<br>W. E. Quinn<br>A. S. Rawcliffe<br>F. L. Ribe<br>G. A. Sawyer<br>R. E. Siemon<br>K. S. Thomas<br>E. L. Zimmermann | Theta-Pinch Experiments with Helical Equilibrium Fields in a Five-Meter Toroidal<br>Sector and in a Three-Meter Linear Device |
| D. A. Baker<br>L. W. Mann | MHD Studies of Finite Beta Toroidal Equilibria |
| J. P. Freidberg<br>T. A. Oliphant<br>H. Weitzner | Survey of Scyllac Theory |

## Gordon Research Conference, Proctor Academy, Andover, New Hampshire, June 28-July 2, 1971

| | |
|---|---|
| C. W. Nielson | Studies of Anomalous Resistivity by Numerical Simulation |
| R. L. Morse | Electron Cyclotron Drift Instability and Turbulence |
| H. Dreicer<br>D. B. Henderson<br>J. C. Ingraham | Anomalous Microwave Absorption Near the Plasma Frequency |

## International Working Session on Fusion Reactor Technology, Oak Ridge National Laboratory, Oak Ridge, Tennessee, June 28-July 2, 1971

| | |
|---|---|
| H. L. Laquer<br>F. L. Ribe | Energy Storage and Switching With Superconductors |
| H. Dreicer<br>D. B. Henderson | Facility for Duplicating 14-MeV Neutron Effects in Fusion Power Reactors |

## Fifteenth International Union of Geodesy and Geophysics General Assembly, August 2-14, 1971, Moscow, USSR. "Instabilities in the Magnetosphere" session

| | |
|---|---|
| D. W. Forslund | Instabilities in Finite Beta Plasmas |

## 1971 Intersociety of Energy Conversion Engineering Conference, Boston, Massachusetts, August 3-6, 1971

| | |
|---|---|
| H. L. Laquer<br>D. M. Weldon | Energy Storage and Switching with Superconductors as a Power Source<br>for Magnetic Fields in a Pulsed Thermonuclear Reactor |
| H. L. Laquer<br>F. L. Ribe<br>D. M. Weldon | Energy Storage and Switching With Superconductors as a Power Source for<br>Magnetic Fields in Pulsed Thermonuclear Experiments and Reactors |

## Gordon Research Conference, Beaver Dam, Wisconsin, August 23-27, 1971

| | |
|---|---|
| R. L. Morse | Absorption of Laser Light in Plasmas |

## XIIIth International Congress of Refrigeration, Washington, D.C., August 27-Sept. 3, 1971

| | |
|---|---|
| H. L. Laquer<br>D. B. Montgomery<br>D. M. Weldon | Superconductive Energy Storage and Switching Experiments |

## Fourth United Nations Conference, Geneva, Switzerland, September, 1971

| | |
|---|---|
| F. L. Ribe | Research on High-Beta, Theta-Pinch Plasmas |

## Third International Conference on Quiescent Plasmas, Risø, Denmark, September 20-24, 1971

| H. Dreicer<br>D. B. Henderson<br>J. D. Thomas | Kinetic Theory of Plasma Ion Drift Speed in the Presence of Resonant<br>Charge Exchange |

| H. Dreicer<br>D. B. Henderson<br>D. Mosher | Use of Radioactive Test Ions in the Measurement of the Spatial Distribution<br>of Plasma Ion Drift Speeds |

## ANS Winter Meeting, Miami Beach, Florida, October 17-21, 1971.
## Translations of the American Nuclear Society 14, 442 (1971)

| E. L. Kemp | A Review of the Major Containment Systems in the U.S. Controlled<br>Thermonuclear Research Program |

## Conference on Computational Physics, Naval Research Laboratory, November 2-3, 1970

| R. W. Mitchell | PIC Codes on the Control Data 7600 |

| R. L. Morse<br>C. W. Nielson | An Electromagnetic Particle-in-Cell Simulation Method |

## Hearings on Controlled Thermonuclear Research before the Joint Committee on Atomic Energy, Washington, D.C., November 10-11, 1971

| F. L. Ribe | The High-Beta Pulsed Pinch Program |

## American Physical Society Division of Plasma Physics Meeting, Madison, Wisconsin, November 15-18, 1971.
## Bulletin of the American Physical Society, Ser. II, 16,No. 11 (1971)

| D. B. Henderson<br>H. Dreicer<br>J. D. Thomas | Q-Machine Ion Drift Speed and Resonant Charge Exchange Near the Hot Plate |

| H. Dreicer<br>D. B. Henderson<br>J. C. Ingraham | Anomalous Microwave Absorption Near the Plasma Frequency |

| J. C. Ingraham<br>H. Dreicer<br>D. B. Henderson | Interpretation of Anomalous Microwave Absorption Measurements |

| R. W. Peterson<br>P. R. Forman<br>F. C. Jahoda<br>S. T. Kush<br>F. L. Yarger | Two-Dimensional Interferometry at $10.6\mu$ |

| L. Burkhardt<br>J. DiMarco<br>P. Forman<br>A. Haberstich<br>H. Karr<br>J. Phillips<br>A. Schofield | The Toroidal Z-Pinch Experiment with Shock Heating |

| S. C. Burnett<br>W. R. Ellis | A Parameter Study of Next Generation Theta-Pinch Experiments |

| H. L. Laquer<br>J.D.G. Lindsay<br>E. M. Little<br>D. M. Weldon | Experimental Study of Magnetic Energy Storage for $\theta$-Pinch Experiments |

| F. L. Ribe | The Separated-Shock Concept for Large-Scale $\theta$-Pinch Experiments |

| | |
|---|---|
| F. C. Jahoda<br>S. C. Burnett<br>W. R. Ellis<br>M. Kaufmann<br>R. E. Siemon | Plasma Measurements on the Scyllac 5-Meter Toroidal Sector |
| G. A. Sawyer<br>R. F. Gribble<br>C. F. Hammer<br>W. E. Quinn<br>D. M. Weldon | Initial $\theta$-Pinch Experiments in the Scyllac 5-Meter Toroidal Sector |
| W. E. Quinn<br>W. R. Ellis<br>F. L. Ribe<br>E. L. Zimmermann | Experiments on the $\ell = 1,0$ Helical Equilibria in the Scyllac 5-Meter $\theta$-Pinch Toroidal Sector |

## Fifth Annual Conference on Numerical Simulation of Plasmas, Iowa City, Iowa, November 19-20, 1971

| | |
|---|---|
| R. W. Mitchell<br>L. E. Rudsinski | PIC Codes on Advanced Computers |
| R. L. Morse<br>C. W. Nielson | Electromagnetic Particle-in-Cell Methods |
| B. M. Marder | A PIC-Type Fluid Code |
| C. W. Nielson<br>B. L. Buzbee<br>L. I. Rudsinski | Elliptic Equation Solution Using Combined Direct and Interative Methods |
| D. W. Forslund<br>R. W. Mitchell | On the Formation and Structure of Strong Electromagnetic Collisionless Shockwaves |

## AAS Symposium on Energy Production from Nuclear Fusion, Philadelphia, Pennsylvania, December 27, 1971

| | |
|---|---|
| F. L. Ribe | Nuclear Fusion-Pulsed-Magnetic-Confinement and Laser-Fusion Research |